DOCTORAL THESIS

Ionospheric Aerodynamics in Low Earth Orbit

Author:
Christopher CAPON

Supervisor:
Prof Russell BOYCE
Dr Melrose BROWN

A thesis submitted in fulfillment of the requirements
for the degree of Doctor of Philosophy

in the

School of Engineering and Information Technology

September 12, 2017

THE UNIVERSITY OF NEW SOUTH WALES
Thesis/Dissertation Sheet

Surname or Family name: Capon

First name: Christopher

Other name/s: Jack

Abbreviation for degree as given in the University calendar: PhD

School: School of Engineering and Information Technology

Faculty: Space

Title: Ionospheric Aerodynamics in Low Earth Orbit

Abstract 350 words maximum:

Understanding perturbing forces takes on new significance as the Low Earth Orbit (LEO) environment becomes increasingly congested and the risk of collision events that threaten access to space infrastructure grows. The perturbation caused by the charged aerodynamic interaction of LEO objects with the ionosphere (``ionospheric aerodynamics") is currently poorly understood and not modelled accurately. The work presented in this thesis provides quantitative insight into the physics underpinning ionospheric aerodynamics and its influence on the orbital motion of LEO objects.

By deriving the set of scaling parameters that describe the electrostatic interaction of a K-species plasma with a charged object, this work has reduced the 4+5K quantities that define plasma interactions to 1+4K independent scaling parameters, and in doing so has helped make the study of charged ionospheric aerodynamics feasible. These scaling parameters represent a significant generalisation of previous work, including linking high and low surface potential plasma phenomena through a new general plasma shielding length parameter. Plasma interaction phenomena that influence charged aerodynamics are then represented in a two-dimensional phase-space P defined by two key dimensionless scaling parameters: the ion deflection parameter "alpha" and the general shielding ratio "chi". A map of plasma interaction phenomena within P was developed and related to charged aerodynamic forces providing new insights into phenomena that govern direct and indirect charged aerodynamic forces. This map was then applied to develop a physics-based framework to predict the influence of ionospheric aerodynamics on LEO objects.

This work predicts that ionospheric aerodynamic forces may represent up to 0.05-18% of the total aerodynamic force vector experienced by a cylindrical object with a surface potential between -0.75 V and -30 V at 500 km altitude, increasing to 0.9-78% at 1500 km. This work, therefore, concludes that ionospheric aerodynamics can have a significant influence on the motion of LEO objects.

FOR OFFICE USE ONLY   Date of completion of requirements for Award:

ORIGINALITY STATEMENT

'I hereby declare that this submission is my own work and to the best of my knowledge it contains no materials previously published or written by another person, or substantial proportions of material which have been accepted for the award of any other degree or diploma at UNSW or any other educational institution, except where due acknowledgement is made in the thesis. Any contribution made to the research by others, with whom I have worked at UNSW or elsewhere, is explicitly acknowledged in the thesis. I also declare that the intellectual content of this thesis is the product of my own work, except to the extent that assistance from others in the project's design and conception or in style, presentation and linguistic expression is acknowledged.'

Signed ....

Date .... 29/3/2017 ....

"So much universe, and so little time."

Terry Pratchett

UNIVERSITY OF NEW SOUTH WALES CANBERRA

Abstract

School of Engineering and Information Technology

Doctor of Philosophy

Ionospheric Aerodynamics in Low Earth Orbit

by Christopher CAPON

Understanding perturbing forces takes on new significance as the Low Earth Orbit (LEO) environment becomes increasingly congested and the risk of collision events that threaten access to space infrastructure grows. The perturbation caused by the charged aerodynamic interaction of LEO objects with the ionosphere ("ionospheric aerodynamics") is currently poorly understood and not modelled accurately. The work presented in this thesis provides quantitative insight into the physics underpinning ionospheric aerodynamics and its influence on the orbital motion of LEO objects.

By deriving the set of scaling parameters that describe the electrostatic interaction of a K-species plasma with a charged object, this work has reduced the $4 + 5K$ quantities that define plasma interactions to $1 + 4K$ independent scaling parameters, and in doing so has helped make the study of charged ionospheric aerodynamics feasible. These scaling parameters represent a significant generalisation of previous work, including linking high and low surface potential plasma phenomena through a new general plasma shielding length λ_ϕ. Plasma interaction phenomena that influence charged aerodynamics are then represented in a two-dimensional phase-space $\mathcal{P}$ defined by two key dimensionless scaling parameters: the ion deflection parameter α and the general shielding ratio χ. A map of plasma interaction phenomena within $\mathcal{P}$ was developed and related to charged aerodynamic forces providing new insights into phenomena that govern direct and indirect charged aerodynamic forces. This map was then applied to develop a physics-based framework to predict the influence of ionospheric aerodynamics on LEO objects.

This work predicts that ionospheric aerodynamic forces may represent up to $0.05 - 18\%$ of the total aerodynamic force vector experienced by a cylindrical object with a surface potential between -0.75 V and -30 V at 500 km altitude, increasing to $0.9 - 78\%$ at 1500 km. Therefore, this work concludes that ionospheric aerodynamics can have a significant influence on the motion of LEO objects.

Acknowledgements

First and foremost, I would like to thank my supervisors, Prof Russell Boyce and Dr Melrose Brown, whose attention to detail drove me to learn how to punctuate prose (most of the time). More importantly, you have both provided me with support and mentorship, which has helped me grow both as an academic, and as a person. Whilst frustrating at times, you have challenged me to question my own ideas, which has led me to deeper insights and new questions that have undeniably shaped both this work and the way I approach problems. Without your tireless help, this work would not have been possible.

I would like to acknowledge the support provided by Dr Tom Scanlon, Dr Craig White, Prof Richard Brown who provided both the code, dsmcFOAM, which formed the basis of the code pdFOAM developed in this work. Without your advice and knowledge, I would probably still be debugging C++ errors. Special thanks also to everyone at the James Weir Fluid Laboratory, the University of Strathclyde Mountaineering Club, and Canoe Club, all of who kept me (mostly) sane during my time in Glasgow.

I am grateful to my father Robert and mother Deborah for your love and support through what has, at times, been a tough journey. Most of all, I would thank you both for inspiring me to try and make the science fiction, which I have always avidly consumed, into non-fiction. Your advice and humour have helped me make it this far and, I'm sure, with whatever comes next.

And finally, last but by no means least, I would like to thank all of my friends. Throughout this journey it is the small things that you have done that have meant the most to me. Whether you have provided encouragement, shared a meal, laughed at a bad joke, joined me on an ill-conceived adventure or provided a couch to fall onto, I wouldn't have made it without you all, and you all have my sincere thanks.

Contents

List of Figures

xx

List of Tables

List of Abbreviations

CIRA	COSPAR International Reference Atmosphere
CLV	Composite Linear Volume
DSMC	Direct Simulation Monte Carlo
ESA	European Space Agency
EOS	Earth Observation System
FK	Fully Kinetic
FVM	Finite Volume Method
GEO	Geosynchronous Earth Orbit
HS	Hard Sphere
HK	Hybrid fluid-Kinetic
IRI	International Reference Ionosphere
ISS	International Space Station
JSpoC	Joint Space Operations Center
LEO	Low Earth Orbit
MSIS	Mass Spectrometer Incoherent Scatter
NGP	Nearest Grid Point
NTC	No Time Counter
SSA	Space Situational Awareness
OM	Orbital Motion
OML	Orbital Motion Limited
PCG	Pre-conditioned Conjugate Gradient
PIC	Particle-In-Cell
PIP	Plasma Interaction Phase-Space
TCC	Transient Conglomerated Cell
VHS	Variable Hard Sphere
VSS	Variable Soft Sphere

Physical Constants

Permittivity of Free Space	$\epsilon_0 = 8.85 \times 10^{-12} \, \mathrm{m}^{-3} \, \mathrm{kg}^{-1} \, \mathrm{s}^4 \, \mathrm{A}^2$
Boltzmann Constant	$k_B = 1.38 \times 10^{-23} \, \mathrm{m}^2 \, \mathrm{kg} \, \mathrm{s}^{-2} \, \mathrm{K}^{-1}$
Elementary Charge Unit	$q_e = 1.602 \times 10^{-19} \, \mathrm{A} \, \mathrm{s}^{-1}$

List of Symbols

Operators

X_e	electron species quantity
X_i	ion species quantity
X_n	neutral species quantity
$X_{(0)}$	property at arbitrary location
X_B	body property
X_∞	freestream property
$X_{(r)}$	property at rarefaction wave edge
$X_{D,N}$	neutral drag quantity
$X_{D,C}$	total charge drag quantity
$X_{D,d}$	direct charge drag quantity
$X_{D,m}$	indirect charge drag quantity
$\hat{X}$	normalised parameter
$\langle X \rangle$	average quantity
∇_x	spatial gradient operator
∇_X	dimensionless spatial gradient operator
∇_c	velocity gradient operator
∇_C	dimensionless velocity gradient operator
t	time

Dimensionless Parameters

Φ	dimensionless potential
α_k	ion deflection parameter of species k
β_k	ion coupling parameter of species k
Ω_k	temporal parameter
S_d	thermal drift ratio
$S_{d,k}$	thermal drift ratio of species k
μ_e	electron energy coefficient
χ	general shielding ratio
$\mathbf{C}_{\text{Aero}}$	aerodynamic force coefficient
$C_{D,N}$	total neutral drag coefficient
$C_{D,C}$	total charged drag coefficient
$C_{D,d}$	total direct charge drag coefficient
$C_{D,m}$	total indirect charge drag coefficient
$c_{D,N}$	local neutral drag coefficient
$c_{D,C}$	local charged drag coefficient
$c_{D,d}$	local direct charge drag coefficient
$c_{D,m}$	local indirect charge drag coefficient
c_P	local pressure coefficient

c_H	local heat flux coefficient	
Λ	coulomb collision parameter (plasma parameter)	
Kn	knudsen number	
M_i	ion acoustic Mach number	
U_{eff}	effective potential energy	
θ_r	rarefaction wave angle	
γ_k	adiabatic index of species k	
n	degrees of freedom	
$\mathcal{P}$	plasma interaction phase-space	
$\mathcal{B}$	ballistic coefficient	

Physical Parameters

f_k	particle distribution function of species k	m^{-3}
$\lambda_{D,e}$	electron Debye length	m
λ_D	general Debye length	m
λ_ϕ	general sheilding length	m
λ	mean free path	m
$\mathbf{x}$	particle position	m
ϕ	electric potential field	$\mathrm{kgm^2s^{-3}A^{-1}}$
ϕ_k	electric potential field at k	$\mathrm{kgm^2s^{-3}A^{-1}}$
ρ_c	space-charge density	$\mathrm{Cm^{-1}}$
ρ_m	mass density	$\mathrm{kgm^{-3}}$
$\mathbf{c}_k$	flow speed of k	$\mathrm{ms^{-1}}$
n_k	number density of k	$\mathrm{m^{-3}}$
q_k	charge of k	C
m_k	mass of k	kg
T_k	temperature of k	K
I_k	current of k	$\mathrm{As^{-1}}$
j_k	current density of k	$\mathrm{As^{-1}m^{-2}}$
p_k	pressure of k	$\mathrm{kgm^{-1}s^{-2}}$
Γ_k	flux of species k	$\mathrm{s^{-1}}$
$\mathbf{c}$	particle velocity vector	$\mathrm{ms^{-1}}$
$\mathbf{F}$	force vector	$\mathrm{kgms^{-2}}$
$\mathbf{v}$	velocity vector	$\mathrm{ms^{-1}}$
$\mathbf{a}$	acceleration vector	$\mathrm{ms^{-2}}$
$\mathbf{E}$	electric field	$\mathrm{kgms^{-3}A^{-1}}$
$\mathbf{B}$	magnetic field	$\mathrm{Nm^{-1}A^{-1}}$
$\bar{\mathbf{T}}$	maxwell stress tensor	$\mathrm{Nm^{-2}}$
p_k	thermal pressure of species k	$\mathrm{Nm^{-2}}$
ω_p	plasma frequency	$\mathrm{s^{-1}}$
$\omega_{p,e}$	electron plasma frequency	$\mathrm{s^{-1}}$
$\omega_{p,i}$	ion plasma frequency	$\mathrm{s^{-1}}$
σ	collision cross-section	$\mathrm{m^2}$
b	impact parameter	m
b_*	critical impact parameter	m
b_{90}	impact parameter for 90° deflection	m
r_B	cylinder body radius	m

r_c	distance of closest approach	m
r_M	distance of local maximum in U_{eff}	m
σ_{pq}	scattering cross-section between p and q	m^2
A	area	m^2
V	volume	m^3
Numerical Parameters		
Δt	numerical time step	s
Δx	spatial discretisation length in x	m
Δy	spatial discretisation length in y	m
S	shaping function	
$F_{10.7}$	solar activity indices	
A_p	geomagnetic activity indices	
ρ_{part}	super-particle density	

To my loving Grandfather Walter Howse,
for helping inspire another generation
to bounce off of the ionosphere.

Chapter 1
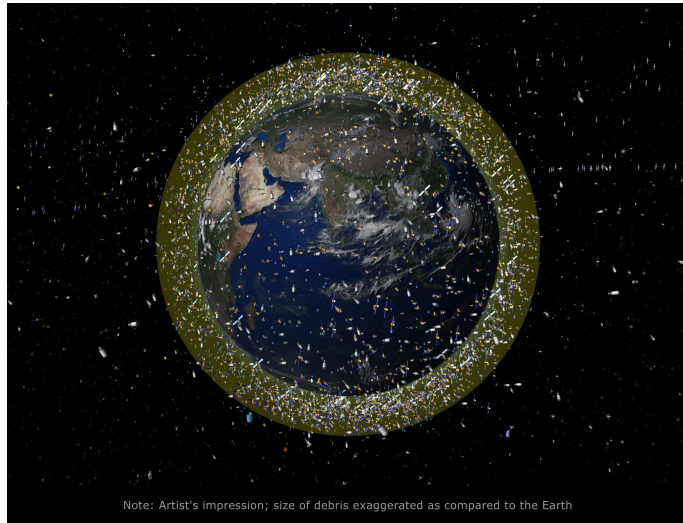
Introduction:
The Space Situational Awareness
Problem in Low Earth Orbit

1.1   Overview

Low Earth Orbit (LEO) infrastructure with an altitude between 100 km and 2000 km plays an increasingly important role in everyday life, ranging from tasks as simple as weather observations and crop monitoring to complex capabilities supporting telecommunications, emergency response and national security (Pelton, 2016). Current trends indicate that LEO infrastructure will only become more important (Amos, 2015; Selding, 2015).

By as early as 2018 OneWeb aims to place 648 washing machine sized small satellites weighing 150 kg in a LEO constellation with a nominal altitude of 1200 km to provide worldwide access to the internet (Amos, 2015). A mere two days after OneWeb's announcement, SpaceX upped the ante, proposing a competing constellation composed of 4000 satellites with an altitude of 1100 km (Selding, 2015). Meanwhile, Planet reached its mission of being able to image all of the Earth's landmass every day with the addition of 88 3U Cube Satellites (CubeSats) on 14 February 2017, each satellite a 10 cm x 10 cm x 30 cm rectangular prism (10 cm x 30 cm x 30 cm with solar panels extended). These 88 satellites comprise almost 1/10th of the 1000 active satellites currently in LEO and demonstrate how the CubeSat platform is increasingly becoming the go-to platform for satellite development in LEO. Gone are the days of the bus size behemoths in LEO like ENVISAT, overwhelmingly LEO infrastructure is taking advantage of the miniaturisation systems to deliver more capabilities at a reduced cost. The rapid increase in satellite population in LEO brings new challenges for the international space community as the local space environment becomes increasingly congested with not only satellites but debris.

On 7th January 2017, the Joint Space Operations Center (JSpoC) issued a notification that two non-manoeuvrable satellites in sun-synchronous orbits had a 44% chance of colliding (Blau, 2017). While the satellites passed each other safely this time, there were almost 50-50 odds of another major collision event like that seen on 10th February 2009 between the active Iridium-33 telecommunications satellite and the defunct military communications satellite, Kosmos-2251. The Iridium-Kosmos collision emphasised to the international space community the importance of being able to both reliably and accurately predict the orbit of objects. While much progress has been made since 2009, precise prediction of orbits in LEO remains difficult; small errors in force modelling integrating up to large errors in position. This represents a critical problem for maintaining the safe and secure access to space technologies in a congested LEO environment. The most important outcome of the Iridium-Kosmos collision was not the event itself; it was the debris that were left behind.

Note: Artist's impression; size of debris exaggerated as compared to the Earth

Figure 1.1: Visualisation of the LEO debris environment. Highlighted region corresponds to LEO. Reproduced from (ESA, 2008)

In LEO alone there are currently in the order of $20,000$ debris being tracked with a characteristic length (r_B) greater than 10 cm. This number is expected to increase to around $200,000$ objects with $r_B > 1$ cm when the new S-band Space Fence system comes online (Pelton, 2016). To illustrate the cluttered nature of the LEO environment, Figure 1.1 provides a visualisation of objects currently tracked by the European Space Agency (ESA) in LEO, each piece of debris representing a potentially mission critical risk to LEO infrastructure (ESA, 2008). Without the ability to accurately and reliably predict the orbits of LEO objects, including both spacecraft and debris, it is hard for satellite operators to make informed decisions about performing collision avoidance maneuvers. Space Situational Awareness (SSA) activities seek to resolve this problem.

SSA research aims to develop the capability to view, understand and predict the location of objects orbiting the Earth to avoid collisions. Predicting the location of Earth orbiting objects is made difficult by uncertainties in force modelling. Orbiting the Earth once every 90 minutes, small uncertainties in force modelling integrate into large uncertainties in position over a relatively small time frame in LEO. Forces experienced by LEO objects fall into one of two categories; gravitational $\mathbf{F}_G$ or non-gravitational $\mathbf{F}_{NG}$ perturbations.

Gravitational perturbations are (Andrés de la Fuente, 2007),

$$\mathbf{F}_G = \mathbf{F}_{\text{Geo}} + \mathbf{F}_{\text{SET}} + \mathbf{F}_{\text{OT}} + \mathbf{F}_{\text{RD}} + \mathbf{F}_{\text{SMP}} + \mathbf{F}_{\text{Rel}} \qquad (1.1)$$

$\mathbf{F}_{\text{Geo}}$ is the geopotential force due to gravitational attraction. $\mathbf{F}_{\text{SET}}$ is the perturbation caused by third bodies to the Earth mass distribution. $\mathbf{F}_{\text{OT}}$ is the perturbation caused by ocean tides. $\mathbf{F}_{\text{RD}}$ accounts for the rotational deformation of the Earth. $\mathbf{F}_{\text{SMP}}$ is the gravitational perturbation of solar bodies in a Newtonian framework. $\mathbf{F}_{\text{Rel}}$ is a term to account for effects arising from general relativity.

Non-gravitational forces acting on LEO objects are (Andrés de la Fuente, 2007),
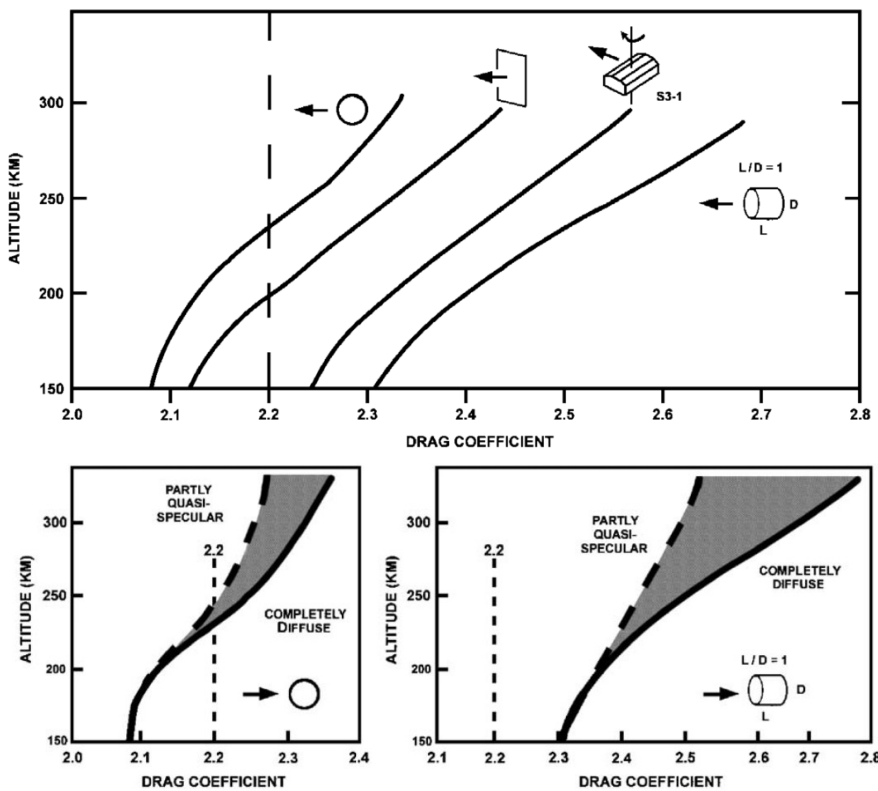
$$\mathbf{F}_{\text{NG}} = \mathbf{F}_{\text{Aero}} + \mathbf{F}_{\text{Solar}} + \mathbf{F}_{\text{Earth}} + \mathbf{F}_{\text{Thermal}} \qquad (1.2)$$

$\mathbf{F}_{\text{Aero}}$ is the aerodynamic exchange of momentum between body and the local space environment. $\mathbf{F}_{\text{Solar}}$ is the force exerted by solar radiation pressure. $\mathbf{F}_{\text{Earth}}$ is the radiation pressure imparted by the Earth. $\mathbf{F}_{\text{Thermal}}$ is the force due to a net thermal radiation imbalance caused by non-uniform temperature distributions on an object surfaces.
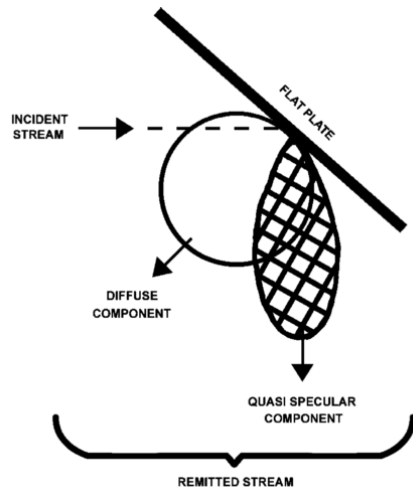
Among the non-gravitational forces in Eqn. 1.2, $\mathbf{F}_{\text{Aero}}$ is the largest non-conservative force on LEO objects, second only in magnitude to $\mathbf{F}_{\text{Geo}}$. Unfortunately, measurements associated with LEO aerodynamics also have the largest associated uncertainties; errors accumulating as the result of assumptions regarding drag coefficients, atmospheric properties, satellite velocity (atmospheric winds) and the nature of the gas-surface interaction (Moe and Moe, 2005; Doornbos and Klinkrad, 2006; Pilinski, 2011; Prieto, Graziano, and Roberts, 2013; Emmert, 2015). LEO aerodynamic accelerations can be written as,

$$\mathbf{F}_{\text{Aero}} = m_B \mathbf{a}_{\text{Aero}} = 1/2 \rho_m \mathbf{v}_B^2 \mathbf{C}_{\text{Aero}} A_B \qquad (1.3)$$

where $\mathbf{a}_{\text{Areo}}$ is the body acceleration vector, $\mathbf{C}_{\text{Aero}}$ is the aerodynamic force coefficient vector, A_B is the cross-sectional area of the object, m_B is the mass of the object, ρ_m is the atmospheric mass density, and $\mathbf{v}_B$ is the relative velocity vector.

Figure 1.2: Uncertainties in drag coefficient caused by geometry (top) and reflection model (bottom). Solid curves represent drag coefficients calculated using (Sentman, 1961) with completely diffuse reflections. Dashed curves represent upper bound estimates from (Moe and Moe, 2005) on the effect of quasi-specular reflections. Reprinted from (Moe and Moe, 2005) with permission from Elsevier.

Figure 1.3: Visualisation of diffuse and quasi-specular reflection models. Reprinted from (Moe and Moe, 2005) with permission from Elsiver.

The aerodynamic perturbation to LEO orbits is largest in the along-track direction, while lift forces (orthogonal to along-track velocity) are relatively small in most cases. As such, the contribution of aerodynamics to LEO objects is usually approximated as a drag acceleration (a_D), where $\mathbf{C}_{\text{Aero}}$ assumed to be the neutral drag coefficient $C_{D,N}$ and the relative velocity vector becoming the orbit velocity of the object (v_B). Eqn. 1.3 then becomes,

$$a_D = -\frac{1}{2}\frac{C_{D,N}A}{m_B}\rho_m v_B^2 \tag{1.4}$$

where a positive $C_{D,N}$ represents a deceleration, hence the negative sign.

In the early 1960s, Cook, (1965) applied rarefied gas dynamics theories (detailed in Sentman, (1961)) to estimate $C_{D,N}$ for LEO objects. For a compact object, Cook, (1965) justified the now common practice of using a constant $C_{D,N}$ of 2.2 in Eqn. 1.4 in order to estimate the atmospheric mass density ρ_m. A historical consequence of this constant $C_{D,N}$ has been to induce drag biases into many atmospheric models e.g. CIRA (COSPAR International Reference Atmosphere), Jacchia, and MSIS (Mass Spectrometer Incoherent Scatter) (see discussion in Emmert, (2015)). Motivated in part by a desire to improve SSA capabilities, it is only relatively recently (within the past decade) that the ubiquitous use of $C_{D,N} = 2.2$ has been called into question (Moe and Moe, 2005; Doornbos and Klinkrad, 2006; Pilinski, 2011; Pilinski, Argrow, and Palo, 2011; Mclaughlin, Mance, and Lechtenberg, 2011; Walker, Mehta, and Koller, 2013; Mehta, Walker, and Koller, 2014; Walker, Mehta, and Koller, 2014; Vallado and Finkleman, 2014; Emmert, 2015). As an example, Figure 1.2, reproduced from Moe and Moe, (2005), emphasises the break down of a constant $C_{D,N}$ for a range of geometries (top), along with the uncertainties in $C_{D,N}$ caused by assuming a completely diffuse or quasi-specular gas-surface interaction model (bottom) - the nature of these reflection models is illustrated in Figure 1.3.

The range of adjustable parameters that have resulted from *"improvements"* in aerodynamic modelling has led to other challenges. Vallado and Finkleman, (2014) presented a critical assessment of the effect of satellite drag and atmospheric model parameters on the propagation of near-Earth objects. Among their conclusions, Vallado and Finkleman, (2014) found that:

> *"Attempting to use one or two fixed parameters may result in improved results, but unless the underlying assumptions and conventions are precisely known and based on an <u>understanding of the physics (which they are often not)</u>, you simply shift the problem from one variable to another. Depending on your solution technique, this may make certain problems unobservable and give you false outcomes."* - Vallado and Finkleman, (2014) page 23.

Emphasis has been added to highlight the identified need for an understanding of the physics involved in both the atmosphere and its aerodynamic interaction with orbiting objects. Similar conclusions can be found throughout the literature.
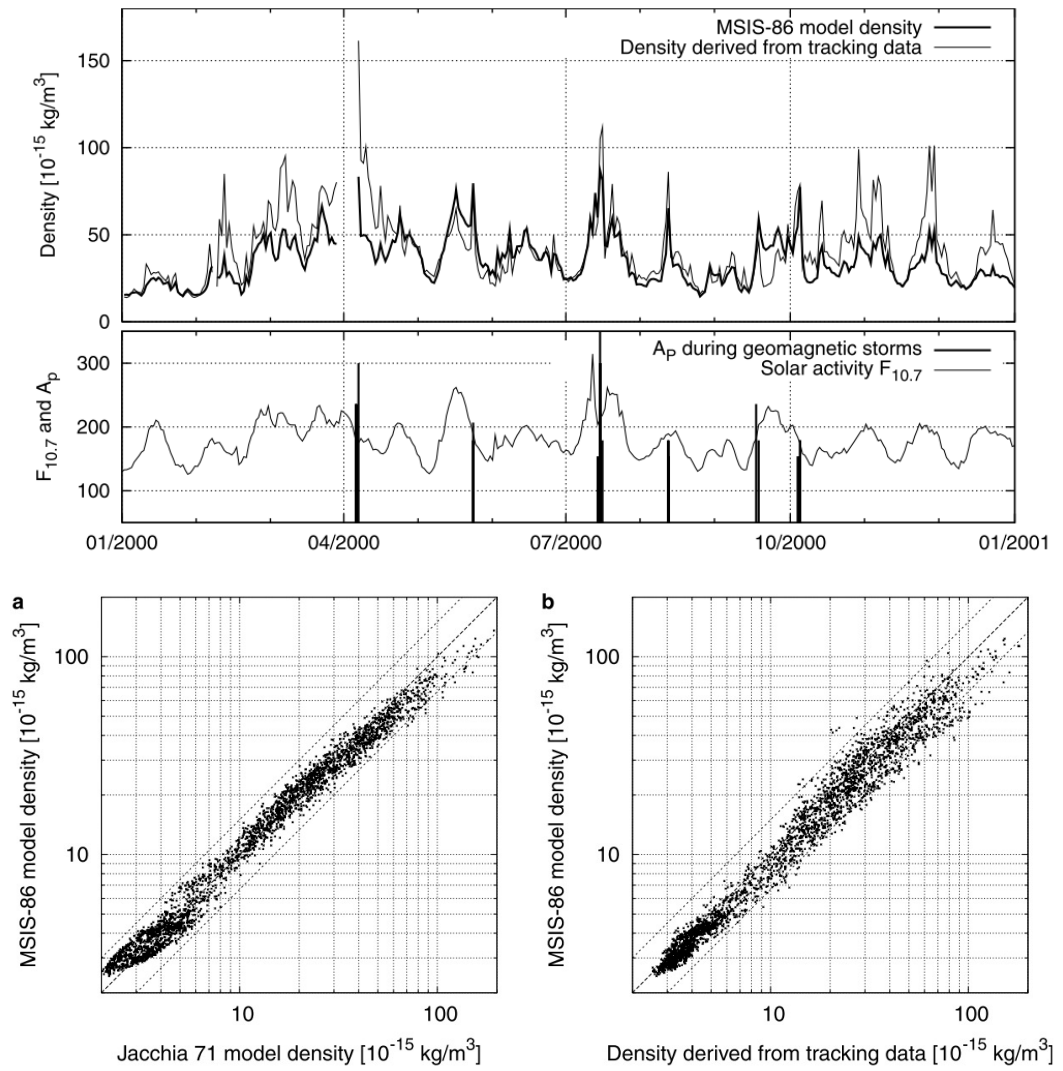
For example, while studying the effect of space weather on satellite drag, Doornbos and Klinkrad, (2006) compared two thermospheric density models (the Jacchia-71 and MSIS-86 models) with densities derived from the ERS-2 satellite. These densities were based on the accelerations of ERS-2, where ρ_m was derived from Eqn. 1.4 after correcting for the perturbations described in Eqns. 1.1 and 1.2. Assuming a maximum error in $C_{D,N}$ of 5%, Doornbos and Klinkrad, (2006) compared MSIS-86 and Jacchia-71 densities against these derived densities. Figure 1.4 reproduces a selection of the results from Doornbos and Klinkrad, (2006), the top two frames comparing derived densities against the MSIS-86 thermospheric model and the concurrent space weather indices - the $F_{10.7}$ index, which describes the solar intensity and the A_p index, which describes the geomagnetic activity (Emmert, 2015).

Doornbos and Klinkrad, (2006) attributed errors greater than 5% between derived densities and MSIS-86 predictions seen in Figure 1.4 (top) to atmospheric model uncertainties. In comparing the prediction errors between the Jacchia-71 and MSIS-86 atmospheric models (models based on independent datasets) and ERS-2 derived densities, shown in Figure 1.4 (bottom), Doornbos and Klinkrad, (2006) concluded that both models:

> ...are affected by similar limitations in the model formulation or the scope of the underlying observation databases. In other words, the models are likely making similar extrapolation errors or similar errors due to imperfect correlation between space weather proxies and density." - Doornbos and Klinkrad, (2006) page 8.

Mclaughlin, Mance, and Lechtenberg, (2011) obtained a similar conclusion in their study of $C_{D,N}$ for the Stella, Starlette and Geosat Follow-On (GFO) satellites. Both Stella and Starlette are spherical satellites. Stella is on a near-circular 800 km orbit with an inclination of 98.6^o, Starlette is orbiting between 800 km and 1100 km with an inclination of 49.83^o. Figure 1.5 plots the derived $C_{D,N}$ for Stella (top) and Starlette (bottom) over the year 2001 overlaid with the theoretical $C_{D,N}$. There are two main features in Figure 1.5. The first is the disagreement between $C_{D,N}$ predictions from the MSIS-86 and NRLMSISE-00 atmospheric models (the NRLMSISE-00 atmospheric model being the MSIS-(20)00 model at 800 km). The second is that there are periods of high $C_{D,N}$ predicted by both models that are well above the theoretical $C_{D,N}$.
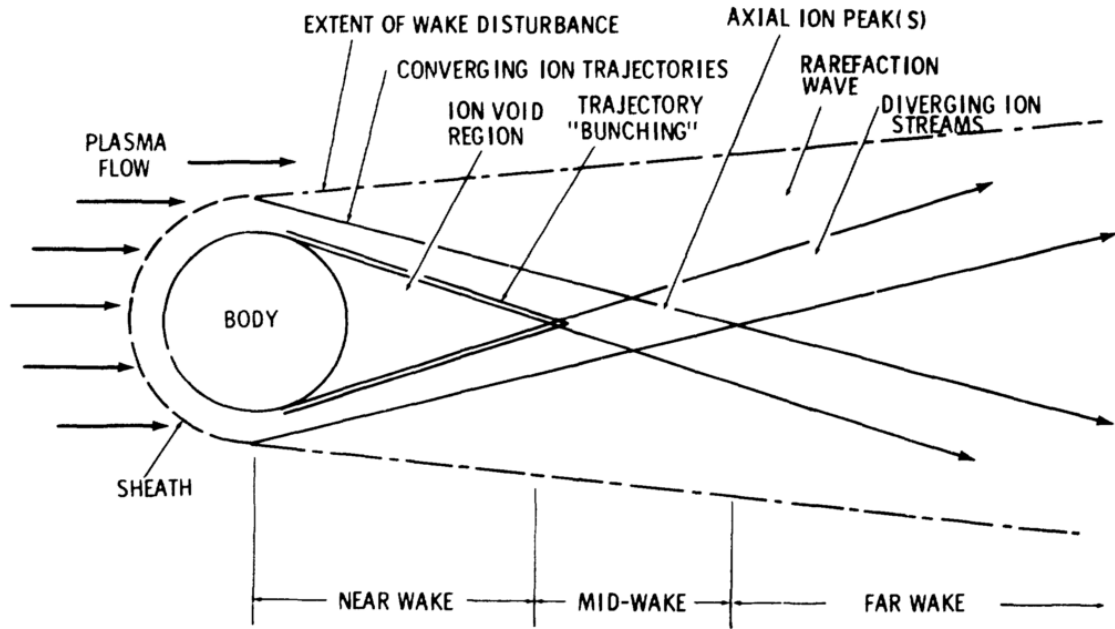
Both the errors in Figures 1.4 and 1.5 were primarily attributed to uncertainties in atmospheric models. Following from Vallado and Finkleman, (2014), this seems plausible since the uncertainty in $C_{D,N}$ caused by the nature of gas-surface interactions are not sufficient

Figure 1.4: Top: Average daily densities encountered by the ERS-2 during the year 2000 and the concurrent daily $F_{10.7}$ and A_p values. Bottom: Scatter plots showing the daily average density along ERS-2 orbit for days between 1995 until 2002. Reprinted from (Doornbos and Klinkrad, 2006) with permission from Elsivier.

Figure 1.5: Variation of daily average $C_{D,N}$ for the Stella (top) and Starlette (bottom) satellites over the year 2001. Adapted from (Mclaughlin, Mance, and Lechtenberg, 2011)

Figure 1.6: Plasma-body interaction phenomena observed experimentally in (Stone, 1981a). Reproduced from (Stone, 1981a) with permission.

to fully explain the extreme variations in $C_{D,N}$ during solar weather events. There may however be other (unmodelled) physical effects in additional to changes in neutral density that generate an increased drag. For example, a key assumption made in the original work by Cook, (1965) was that the primary source of drag in LEO was a result of interaction with the thermosphere (the neutral LEO environment). The contribution of the ionosphere (the charged LEO environment) to the satellite aerodynamics, or *"ionospheric aerodynamics"*, was assumed to be negligible based on conclusions in Brundin, (1963).

The aerodynamic interaction between a LEO object and the ionosphere is fundamentally different from the aerodynamic interaction between the object and the thermosphere. Whenever an object is immersed in a plasma, it acquires a floating potential (ϕ_B) with respect to the freestream plasma based on the sum of currents to the surface. In LEO, the electron thermal velocity is orders of magnitude larger than an object's orbital velocity, which is in turn larger than the surrounding ion thermal velocity. This velocity distribution (known as a *"mesothermal flow"*) results in a negative floating potential and sets up a region of charge discontinuity about the body where ions are accelerated toward the body and electrons are repelled such that the ion and electron currents are equal. This region of charged discontinuity is known as the *"plasma sheath"*. Figure 1.6 is reproduced from Stone, (1981a) to illustrate the main features of mesothermal plasma-body interactions.

The plasma sheath has two key effects: the first is to increase the effective collection area of the object beyond the wetted area of the body; the second is to deflect (scatter) ions into (or away from) the wake of the object. The increase in effective collection area allows direct charged aerodynamic forces resulting from gas-surface interactions to be enhanced compared to an equivalent rarefied gas dynamic interaction. The deflection of ions causes an indirect exchange of momentum between the object and ions also known as *"dynamic friction"* (Chandrasekhar, 1943; Brundin, 1963). Hence, while neutral aerodynamics in LEO is well described by rarefied gas mechanics (Sentman, 1961)[1], ionospheric aerodynamics calculations must account for both the direct and indirect exchange of momentum between the object and the surrounding plasma through field effects (see discussion in Section 2.2.3).

In essence, charged aerodynamic mechanisms cause an increased drag compared to equivalent neutral aerodynamic interactions. This raises the question, *why did Cook, (1965), and Brundin, (1963), assume that charged aerodynamic forces in LEO were negligible*? The answer to this question revolves around three critical assumptions (Brundin, 1963):

1. That the surface potential of LEO objects is never more negative than -0.75 V with respect to a quasi-neutral freestream plasma ($\phi_\infty = 0$).

2. That the maximum ion number density is approximately 10% of the neutral number density in LEO.

3. That monotonic oxygen ions (O^+) are the dominant source of charged aerodynamic forces (monotonic hydrogen ions (H^+) were not considered).

Based on these assumptions, Brundin, (1963) concluded that neglecting ionospheric aerodynamic forces would cause a maximum possible over-prediction of neutral density by 20% when based on satellite accelerations. With advances in knowledge of the LEO space environment and the increasing complexity of LEO satellites and their orbits, the validity of each of these assumptions has become questionable.

It is now recognised that LEO objects can naturally achieve floating potentials more negative than -100 V (albeit for short periods), while the use of high voltage power systems can cause large artificial surface potentials (Hastings, 1995; Olsen and Purvis, 1983; Gussenhoven et al., 1985; Evans et al., 1989; Garrett and Whittlesey, 2000; Anderson, 2012). Advances in atmospheric models mean that regions where the ion number density approaches the neutral number density are well recognised (see discussion in Section 2.2.1). Meanwhile, LEO objects now regularly orbit above $700 - 900$ km altitude where H^+ ions dominate the ionosphere.

---

[1]Uncertainties in neutral aerodynamics are primarily caused by the nature of the gas-surface interaction (Moe and Moe, 2005)

While there has been relatively little work done on ionospheric aerodynamics since Brundin, (1963), a recent study by Andrés de la Fuente, (2007) offers *in-situ* evidence that charged aerodynamic forces[2] can be significant. Andrés de la Fuente, (2007) applied the dusty plasma theory described in Hutchinson, (2002) and Hutchinson, (2005) to predict the contribution of charged aerodynamics to the anomalous along-track accelerations experienced by the LAGEOS-I and LAGEOS-II satellites with nominal altitudes of 5900 km (Medium Earth Orbit). Andrés de la Fuente, (2007) concluded that the contribution of charged aerodynamics to along-track accelerations increases from -0.5 pms^{-2} when not in eclipse to -85 pms^{-2} and -70 pms^{-2} respectively in eclipse - the larger eclipse charged aerodynamic acceleration for the LAGEOS-I a reflection of its orbit which brought it over the auroral and polar zones where larger negative floating potentials occur. Compared to a neutral drag acceleration of -0.5 pms^{-2}, Andrés de la Fuente, (2007) demonstrated that charged aerodynamics can have a significant and complex effect on the dynamics of the LAGEOS spacecraft in MEO. However, the structure of plasma-body interactions differs significantly between LEO and MEO.

LEO plasma-body interactions are characterised by anisotropic, thin plasma sheaths compared to whereas MEO plasma-body interactions which are thick and relatively symmetric compared to those in LEO (see discussion in Section 2.2.2). As a result, the flow physics, and therefore charged aerodynamic interactions, are likely to be different between the two cases. The important question then arises: *can ionospheric aerodynamics have an appreciable effect on the non-conservative force vector experienced by a LEO object?* Herein lies the motivation for the research presented in this thesis.

By developing a physics-based understanding of charged aerodynamics, this work helps address whether the underlying limitations in atmospheric models are in part a reflection of unmodelled perturbations caused by ionospheric aerodynamics.

---

[2]Ionospheric aerodynamics referring to charged aerodynamic forces in an ionosphere.

1.2   Statement of the Problem

Establishing the sources of uncertainty in atmospheric and aerodynamic perturbations in LEO requires a physical understanding of the interaction between LEO objects and the space environment. The perturbation to LEO objects resulting from charged aerodynamic interaction with the ionosphere (ionospheric aerodynamics) is not currently considered nor even well understood. By developing a physical understanding of charged aerodynamics, this work aims to quantify the significance of ionospheric aerodynamics to LEO objects compared to neutral aerodynamics. The main objective of this work can thus be formulated as determining the answer to the question:

> *"How does the electrostatic interaction generated when a negatively charged body orbits through the ionosphere affect the body's non-conservative force vector?"*

To develop a cohesive argument supporting the thesis that ionospheric aerodynamics can have an appreciable effect on the motion of LEO objects, the following progression is taken in this work:

1. Review the charged aerodynamics literature and related field (i.e. dusty plasmas, charging theory, etc.) to identify the state-of-the-art.

2. Revisit early studies of ionospheric aerodynamics to ascertain the validity of past assumptions and conclusions given the current state-of-the-art.

3. Develop and validate a method to test whether these assumptions/conclusions are appropriate for LEO plasma-body interactions.

4. Identify important physical phenomena that contribute to charged aerodynamics.

5. Develop a framework to explore the range/bounds of possible ionospheric aerodynamic plasma-body interactions

6. Use this framework to assess where ionospheric aerodynamics could become significant compared to neutral aerodynamics in LEO.

By developing a physical understanding of charged aerodynamics in general, this work provides a platform for future work to bring in additional phenomena. Therefore, the scope of this work is limited to studying the unmagnetised, electrostatic interaction of a flowing plasma with uniformly charged objects with a fixed surface potential relative to the local plasma environment. Additional physical phenomena, such as secondary electron emission, photoelectron emission, sputtering, etc. are considered to be higher-order phenomena that perturb this underlying flow interaction. The primary goal of this work is to quantify the significance of ionospheric aerodynamics to LEO objects to demonstrate both when and where such high-fidelity analysis is required.

1.3   Summary of Chapters

An outline of this dissertation is as follows:

Chapter 2   introduces relevant background theory that informs a comprehensive review of literature investigating the influence of ionospheric aerodynamics to LEO objects. Key limitations of past ionospheric aerodynamic investigations are identified. To address these limitations, the applicability of numerical methods to the modelling of ionospheric aerodynamics is discussed, resulting in the selection of the Particle-in-Cell (PIC) method used throughout this work.

Chapter 3   outlines the implementation of an electrostatic PIC method in OpenFOAM as part of the new hybrid PIC- Direct Simulation Monte Carlo (DSMC) code, *pdFOAM*, developed in the present work by the author in collaboration with the University of Strathclyde. Code-to-code comparisons with the established DSMC code *MONACO* and PIC code *PICLas* are presented to verify the ability of pdFOAM to reproduce fundamental phenomena. Additional validation studies are included in Appendix B.

Chapter 4   explores the effect of surface potential, ion mass and body radius on plasma-body interaction phenomena and their influence on ionospheric aerodynamics. Past analytical predictions of ionospheric aerodynamics are compared against numerical predictions using pdFOAM to investigate the break down of assumptions underlying prior conclusions regarding the significance of ionospheric aerodynamics to LEO objects.

Chapter 5   applies kinetic theory to determine the dimensionless system that governs multi-species plasma-body interactions in LEO. The identified set of dimensionless parameters that govern this system are compared with those obtained via the Buckingham Pi theorem, demonstrating that the identified dimensionless parameters represent physically relevant scaling laws. The validity of these scaling parameters is demonstrated through their ability to predict self-similar transformations.

Chapter 6   determines the parametric relationship between scaling parameters and plasma-body interaction phenomena. Based on observed physical relationships, the plasma interaction phase-space $\mathcal{P}$ is introduced as a framework within which to study charged aerodynamics in general - ionospheric aerodynamics spanning a particular region within $\mathcal{P}$.

Chapter 7 applies this framework to construct a physics-based response surface to predict the influence of ionospheric aerodynamics on the motion of LEO objects. This model overcomes identified limitations in past work, allowing the identification of regions in LEO where ionospheric aerodynamics becomes significant compared to neutral aerodynamics.

Chapter 8 concludes by summarising the original contributions of this work and its limitations. This chapter also makes recommendations for future work to address both the limitations of this work and its implications.

1.4 A Comment on Notation

To allow a concise and general description of equations governing plasma interactions, the following notational rules are applied throughout this work.

Rule 1: Plasma quantity X of species k is defined with respect to location (y) as,

$$X_{k,(y)} \tag{1.5}$$

k will either describe ions i, electrons e or the kth ion species. In general, (y) will either refer to the freestream[3] ∞, a body property B or an arbitrary location (0) (the exception being the rarefaction wave edge (r) discussed in Section 5.4). Properties at an arbitrary location (0) can be applied at any location in the flowfield, including B and ∞ - the choice of which is dependent on the analysis.

Rule 2: Naming subscripts N come before k and (y) e.g.

$$X_{N,k,(y)} \tag{1.6}$$

Rule 3: No additional subscripts are included on properties derived from a combination of plasma and body properties (other than naming subscripts) e.g. the total space-charge density ρ_c.

Rule 4: Ion species subscripts k are replaced with i for single species cases for simplicity.

---

[3]Undisturbed plasma upstream of the body.

1.5 Publications

Table 1.1: List of published material.

Journal Paper:	C. J. Capon, M. Brown, C. White, T. Scanlon and R. R. Boyce, *pdFOAM: A PIC-DSMC Code for Near-Earth Plasma-Body Interactions* Computers & Fluids (2017).
Description	This paper describes the implementation and validation of the hybrid PIC-DSMC code *pdFOAM*.
Relation to this Work:	pdFOAM is the principle research tool used throughout this work. Content from Chapter 3 describing the implementation and validation of pdFOAM is included in this paper. Additional validation cases in Appendix B are included in this paper.
Author Contribution:	The Author developed and implemented the PIC portion of pdFOAM, which used the DSMC code *dsmcFOAM* as a framework. The Author was responsible for all of the validation studies. The Author wrote this paper.
Journal Paper:	C. J. Capon, M. Brown and R. R. Boyce, *Scaling of Plasma-Body Interactions in Low Earth Orbit* Physics of Plasmas (2017)
Description:	This paper describes the derivation of scaling parameters that describes the electrostatic interactions of a multi-species plasma with a body at an arbitrary surface potential with respect to a quasi-neutral plasma.
Relation to this Work:	These scaling parameters form the framework developed in this work to investigate ionospheric aerodynamics. Content from Chapter 5 is presented in this paper.
Author Contribution:	The Author derived the scaling parameters and demonstrated their validity through self-similar transformations. The Author wrote this paper.
Conference Paper:	Capon, C.J., Brown, M. and Boyce, R.R., 2016, November. *Charged aerodynamics of a Low Earth Orbit cylinder.* AIP Conference Proceedings (Vol. 1786, No. 1, p. 190004). AIP Publishing.
Description:	This conference paper presents preliminary observations of the influence of plasma interaction phenomena on the direct charged aerodynamics of a LEO cylinder.
Relation to this Work:	Content from Chapter 4 is presented in this paper.
Author Contribution:	The Author wrote and presented this paper at the 40th International Rarefied Gas Dynamics Symposium 2016.

Chapter 2

Background:
Ionospheric Aerodynamics Literature

2.1   Introduction
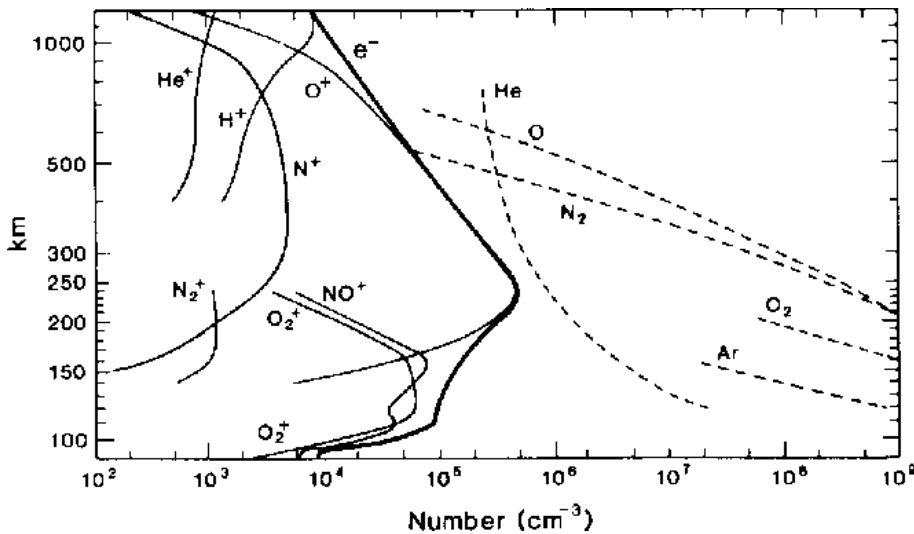
The size of a beach ball and with about the same shape, Sputnik made history on October 4, 1957 when it become the first artificial satellite. Sputnik is a typical example of early satellites; simple in geometry with very low power requirements. The neutral drag coefficient $C_{D,N}$ of 2.2 proposed in Cook, (1965) was largely accurate for these early satellites. Modern satellites are different: modern satellites vary drastically in structure, ranging from large complex installations with characteristic dimensions (r_B) on the order of 10 m to small 10 cm cubes (i.e. CubeSats); they employ a wide range of electrical equipment with power requirements that dwarf those early satellites; and their orbits are more varied, ranging from polar to equatorial, near-circular to highly elliptic. Much as the constant $C_{D,N}$ of 2.2 became outdated as the complexity of satellite structures increased, the use of high voltage power systems, dramatic variation in size and changes in orbits brings into question past conclusions regarding the significance of ionospheric aerodynamics in LEO.

The purpose of this chapter is to explore the argument that ionospheric aerodynamics may have an appreciable effect on the motion of LEO objects. Section 2.2 begins by presenting background information into the nature of the LEO environment, the structure of LEO plasma-body interactions and the physical basis of charged aerodynamic mechanisms. This then informs the discussion in Section 2.3, which presents a critical review of past ionospheric aerodynamic literature. The focus of this discussion is on literature directly related to ionospheric aerodynamics, literature in parallel fields, such as dusty plasma physics and *in-situ* measurements in MEO, are discussed where appropriate. Based on the identified limitations of previous ionospheric aerodynamic literature (or *"gaps"*), Section 2.4 justifies the selection of the numerical approach used throughout this work.

2.2 Plasma-Body Interactions in Low Earth Orbit: A Primer

2.2.1 The Low Earth Orbit Space Environment

Compared to Geostationary Earth Orbit (GEO), the LEO space environment is a cold, dense, quasi-neutral, partially ionised plasma primarily composed of N_2, O_2, O, He and H and their ionised analogues. Description of the environment is often broken into the neutral domain, comprising the thermosphere ($90 - 600$ km) and exosphere (> 600 km)[1], and the charged domain, also known as the ionosphere. The structure of the thermosphere and ionosphere are significantly different. Figure 2.1 plots representative variations in neutral and ion composition with altitude during a representative international quiet solar year (Cairns, 1999).
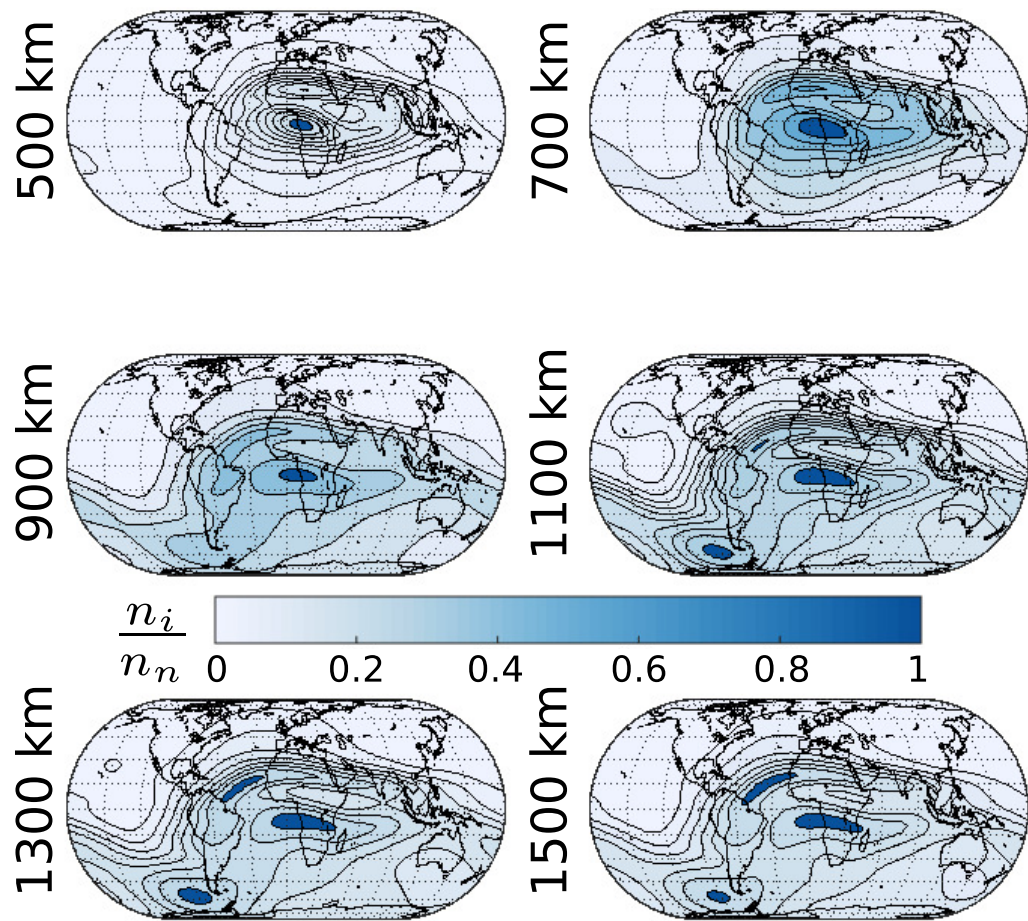
Figure 2.1: Representative daytime atmosphere structure during an international quiet solar year. Reproduced from (Cairns, 1999).

The temperature of the thermosphere asymptotes to a common exospheric temperature with increasing altitude. A consequence of this common temperature is the stratification of constituents by molecular mass, the driving force being gravity (Emmert, 2015). Extreme ultraviolet (EUV) solar radiation provides the primary direct day-side heat source, producing large thermal gradients with the night-side and causing upper atmospheric winds ranging from 1 km/s to 100 km/s (Doornbos, Klinkrad, and Visser, 2005; Emmert, 2015). Solar EUV production exhibits an 11-year cycle that results in density variations of an order of magnitude, while dinural[2] variations are typically on the order of 10% (Emmert,

---

[1]Hereafter referred to as the thermosphere for convenience.
[2]24 hour

Figure 2.2: Comparison of total ion and neutral number densities in LEO based on the NRLMSISE-00 (Picone et al., 2002) and IRI-2012 (Bilitza et al., 2014) atmospheric models. Conditions are for 4/1/2007 UT 12:00:00 with solar indices $f_{10.7} = 87.7$, $f_{10.7a} = 83.35$ and using the daily magnetic index $a_p = [17.3750, 15.0, 20.0, 15.0, 27.0, 18.125, 21.75]$.

2015). EUV is also the primary ionisation mechanism maintaining the day-side ionisation of the charged environment (Bilitza et al., 2014).

While the thermosphere is gravity and temperature dependent, the Earth's magnetic field and self-induced local electromagnetic inhomogeneities govern the ionosphere. As a result, the ionosphere exhibits a greater latitudinal variation than the thermosphere (Bilitza et al., 2014). Similarly, the distribution of ionospheric constituents with altitude is non-linear and coupled with global and local electromagnetic perturbations. The injection/precipitation of energetic plasma species into polar auroral regions during solar weather events, such as coronal mass ejections, along with increased EUV fluxes can significantly disturb the ionosphere (Hastings, 1995; Garrett and Whittlesey, 2000; Anderson, 2012; Bilitza et al., 2014).

During these events, energy input can increase by an order of magnitude compared to local EUV input, increasing ionisation, temperature, and other key parameters (Hastings, 1995; Anderson, 2012). The redistribution of this energy to the thermosphere occurs through transfer mechanisms, significantly disturbing global circulation patterns and generating phenomena such as travelling ionospheric disturbances and gravity waves (Emmert, 2015). It is perhaps not surprising then that the modelling of the LEO environment has been, and remains, difficult (Emmert, 2015).

Two established atmospheric models are the Naval Research Laboratory Mass Spectrometer Incoherent Scatter Radar Extended (NRLMSISE-00) (Picone et al., 2002) and International Reference Ionosphere (IRI-2012) (Bilitza et al., 2014) atmospheric models. For a comprehensive review of atmospheric models see Vallado and Finkleman, (2014) and Emmert, (2015).

One of the principle arguments described in Chapter 1 for neglecting ionospheric aerodynamics was the assertion that ion number densities (n_i) are orders of magnitude less than neutral number densities (n_n). While true below 300 km altitude, as altitude increases so does the proportional ionisation of the environment. Figure 2.2 plots n_i/n_n slices through altitude based on NRLMSISE-00 and IRI-2012 atmospheric models. Conditions are for the 4th of January 2007 UT 12:00:00 with solar indices $f_{10.7} = 87.7$, $f_{10.7a} = 83.35$ and using the daily magnetic index $a_p = [17.3750, 15.0, 20.0, 15.0, 27.0, 18.125, 21.75]$[3]. Figure 2.2 illustrates that above 500 km there exist regions where $n_i/n_n \to 1$. The question then is whether the total force of the ions remains sufficient in regions where $n_i/n_n \to 1$ to have an appreciable effect on the motion of LEO objects. To answer this question requires knowledge about how charged species interact with LEO objects.

---

[3]Relevant solar and magnetic data can be obtained from `ftp://ftp.ngdc.noaa.gov/STP/space-weather/solar-data/solar-features/solar-radio/noontime-flux/penticton/` and `ftp://ftp.ngdc.noaa.gov/STP/GEOMAGNETIC_DATA/INDICES/KP_AP/`

2.2.2 Structure of Mesothermal Plasma-Body Interactions

The physics of a conducting body immersed in a stationary, collisionless, quasi-neutral plasma is well established (Godd and Laframboise, 1983; Laframboise and Luo, 1989; Allen, 1992; Hutchinson, 2005). The most probable ion ($v_{t,i}$) and electron ($v_{t,e}$) thermal velocity in three dimensions is given by Bird, (1977),

$$v_{t,i(e)} = \sqrt{\frac{2k_B T_{i(e)}}{m_{i(e)}}} \tag{2.1}$$
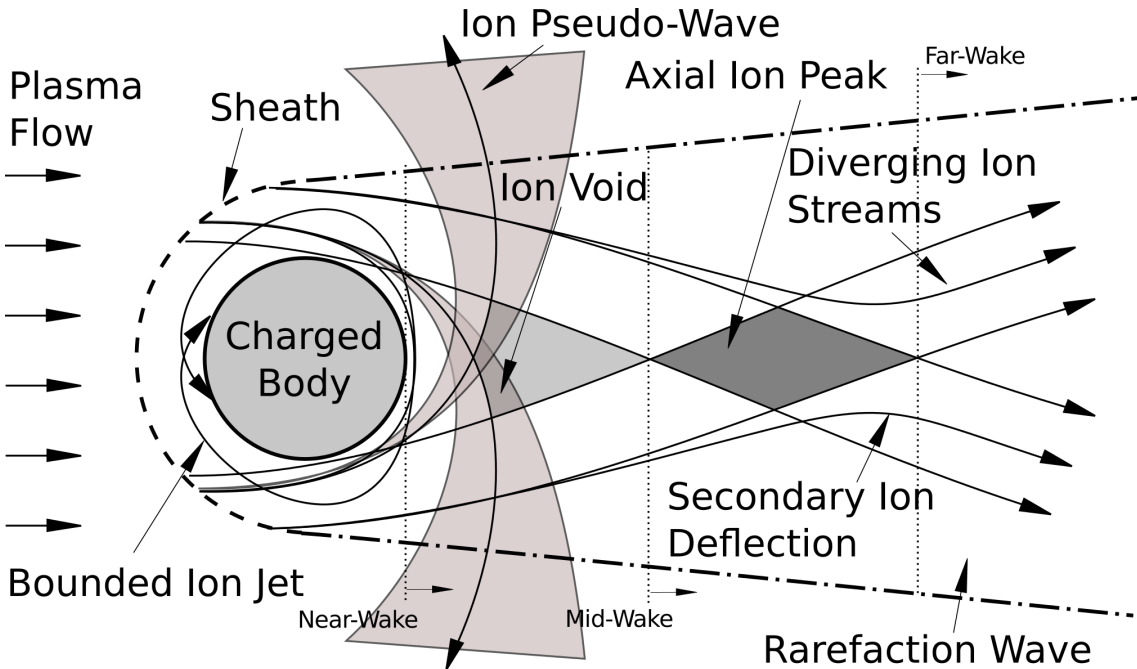
where k_B is the Boltzmann constant, subscripts i and e refer to ion and electron properties, and T and m are the ion and electron temperature and mass respectively.

From Eqn. 2.1 it is clear that, except for the conditions where $T_i \gg T_e$, the relative mass of ions and electrons results in $v_{t,i} \ll v_{t,e}$. Consequently, when an object is immersed in the plasma, the surface initially experiences a larger flux of electrons than ions and the body gains a macroscopic negative charge relative to the surrounding plasma. Plasmas tend to work to neutralise charge discontinuities, hence the body surface potential (ϕ_B) caused by the build-up of charge on the body's surface tends to accelerate and repel nearby ions and electrons. The body is said to have achieved a *"floating potential"* when the ion and electron currents (I) have achieved some dynamic equilibrium i.e. $I_i = I_e$. Ions are not accelerated from infinity however, instead there exists a region of charge discontinuity surrounding the body known as the *"plasma sheath"*, beyond which the plasma is electrically shielded from the influence of the body. While the structure of plasma sheaths in quiescent plasmas are well understood, when there exists relative motion between the plasma and body, such as in LEO, the sheath structure becomes significantly more complex (Stone, 1981a; McMahon, Xu, and Laframboise, 2005).

The structure of LEO plasma-body interactions has been studied extensively[4]. In general, these studies fall into one of two categories: studies that investigate the floating potential of LEO objects by calculating the self-consistent ion and electron surface currents (Whipple, 1965; Parker, 1978; Deforest, 1972; Laframboise and Luo, 1989; Shaw, 1993; Whipple, 1981; Gussenhoven et al., 1985; McMahon, Xu, and Laframboise, 2005; Barrie, 2006; Wang, Qiu, and Qin, 2008); and the study of wake phenomena from a charging context or physics perspective (Stone, 1981a; Stone, 1981b; Samir, Wright, and Stone, 1983; Wang and Hastings, 1992a; Wang and Hastings, 1992b; Wang et al., 1994; Meassick et al., 1991; Engwall, Eriksson, and Forest, 2006; Choinière and Gilchrist, 2007). Charging studies are intrinsically related to charged aerodynamics, the difference being the prediction of ion/electron surface fluxes (charging) compared to momentum exchange

---

[4]The study of floating potentials and surface potentials in LEO.

Figure 2.3: Illustration of relationship between collective phenomena observed in mesothermal plasma-body interactions and ion trajectories.

(charged aerodynamics). Charging studies are not interested momentum exchange, but instead the distribution of ion current collection and the equilibrium condition where ion current equals electron current ($I_i = I_e$). Similarly, studies focusing on the characterisation of plasma interaction phenomena, while providing important physical insights to plasma-body interaction phenomena, do not consider the influence of these phenomena to momentum exchange - the justification for the characterisation of phenomena generally related to charging. Nevertheless, it is instructive to review the general structure of LEO plasma-body interactions based on this literature.

Figure 2.3 illustrates the general anatomy of LEO plasma-body interactions, linking observed collective phenomena with representative ion trajectories based on the findings by Stone, (1981a), Wang and Hastings, (1992b), McMahon, Xu, and Laframboise, (2005) and Choinière and Gilchrist, (2007). The LEO plasma interaction phenomena illustrated in Figure 2.3 arise primarily from the relative velocity between LEO objects and the ionosphere. The orbital velocity (v_B) of LEO objects is on the order of 7.5 km/s. As a result, LEO objects move hyperthermally ($v_B \gg v_{t,i}$) relative to the ion thermal velocity ($v_{t,O^+} \approx 1.25$ km/s) and subthermally ($v_B \ll v_{t,i}$) relative to the electron thermal velocity ($v_{t,e} \approx 246$ km/s). This bi-thermal velocity distribution is referred to as a *"mesothermal"* flow. As illustrated in Figure 2.3, characteristic features resulting from this velocity distribution are a compressed forebody (or *"ram"*) sheath and an elongated *"wake"* sheath surrounded

by a *"rarefaction wave"* (Stone, 1981a). Two important additional features are shown in Figure 2.3 compared to those shown previously in Figure 1.6; bounded ion jets and ion pseudo-waves. These are discussed below.

The compression of the ram sheath and elongation of the wake sheath seen in Figure 2.3 is a product of the hyperthermal ion velocity where ions are unable to populate the near-wake region immediately behind the body. The electron mobility allows an initial population of the ion void region labelled in Figure 2.3 causing a localised negative disturbance trailing behind the body. The negative region then attracts ions into the wake region and deflects incoming electrons, re-populating the wake region significantly faster than equivalent neutral flow interactions where re-population is a function of gas temperature.

The re-population of the wake region by deflected ions causes an ion density gradient as ions move to fill the wake. This density gradient causes a collective response in the plasma in the form of a *"rarefaction wave"*, defined by the leading edge of the density gradient travelling perpendicularly outwards to the flow direction. As illustrated in Figure 2.3, in the frame of the body this rarefaction wave angle (θ_r) appears physically similar to a continuum Mach wave where its angle relative to the flow direction is defined by the ion acoustic Mach number (M_i)[5], e.g. (Burgess and Scholer, 2015)

$$\theta_r = \sin^{-1}\left[\frac{1}{M_i}\right], \qquad M_i = \frac{v_B}{\sqrt{k_B(T_e + \gamma_i T_i)/m_i}} \tag{2.2}$$

where the ion adiabatic index γ_i refers to the ability of real gases to store energy in higher energy rotational and vibrational states (degrees of freedom n),

$$\gamma_i = 1 + 2/n \tag{2.3}$$

In a collisionless plasma $n = 1$ and $\gamma_i = 3$ (Burgess and Scholer, 2015).

Within the wake, the confluence point of deflected ions may then create a positive space-charge region of sufficient intensity to cause the secondary deflection of incoming ions[6] (Stone, 1981a). Finally, depending on where they enter the sheath, ions within particular energy bands are deflected through the near wake on unbounded (hyperbolic orbit) or bounded (impact the body) trajectories (see discussion in Section 2.3). Together, these ions form bounded and unbounded ion jets, the latter appearing as the ion pseudo-waves illustrated in Figure 2.3.

McMahon, Xu, and Laframboise, (2005) investigated the effect of ion drift speed on plasma-body interaction phenomena, in particular the sheath and pre-sheath structure,

---

[5]The speed at which electrostatic information travels through a plasma.
[6]This primarily occurs in the wake of compact objects e.g. spheres, cubes.

to determine its effect on ion current collection i.e. a charging study. The method used by McMahon, Xu, and Laframboise, (2005) to simulate plasma-body interactions involved the tracing of particle trajectories through a computational domain to build-up a space-charge distribution. This space-charge distribution was then used to solve Poisson's equations for the electrostatic field $\phi(\mathbf{x})$, whereupon particle trajectories were traced through this potential field according to Newton's laws and the Lorentz force. This process was iteratively repeated until the average of the square of differences in normalised densities between two repetitions was smaller than a specified tolerance i.e. the solution had converged (numerical methods for simulating plasma-body interactions are discussed in more detail in Section 2.4). Figure 2.4, reproduced from McMahon, Xu, and Laframboise, (2005), provides an illustrative example of the general plasma interaction phenomena described above. Here contours are of normalised number density $(\hat{n}_= n_i(\mathbf{x})/n_\infty)$ at various ion drift velocities normalised against thermal velocity $(S_d = v_B/\sqrt{2k_B T_i/m_i})$, where $\Phi = q_e \phi_B/k_B T_e = -25$ and $\lambda_{D,e}/r_B = 1$[7].
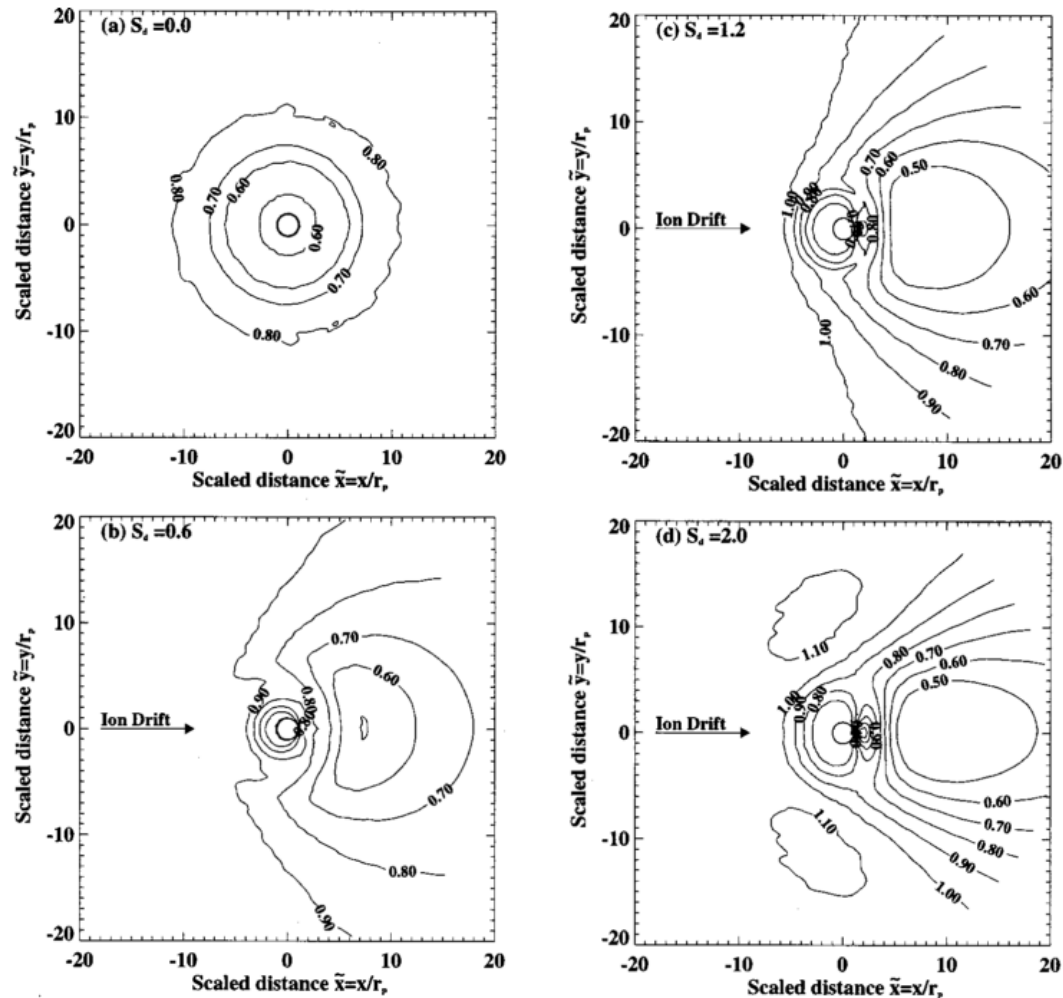
The top left frame shows the stationary case, the plasma sheath causing a (near) uniform density gradient around the body i.e a symmetric plasma sheath. The bottom left frame shows the sub-thermal $(S_d < 1)$ case, where ion drift velocity causes the formation of a rarefaction wave while the low kinetic energy of the freestream ions compared to the body results in bounded orbits that cause the apparent forebody density discontinuity (this feature is discussed further in Chapter 6). The top and bottom right panels show hyperthermal flows $(S_d > 1)$, the peak in ion density in the immediate wake of the bodies caused by the confluence of deflected ions. Overdense regions outside the rarefaction wave in the bottom right panel are representative of unbounded ion jets, the super-position of unbounded ion jets and freestream ions causing an over-dense region.

It is also worth noting that the above phenomena assume unmagnetised plasma interactions. This is a common assumption whereby the gyration radius of ions[8] is orders of magnitude larger than object sizes in LEO (with the exception of the International Space Station) and therefore, in the frame of the body, the ions travel in straight lines. The unmagnetised assumption is also employed in this work.

---

[7]Here $\lambda_{D,e}$ is the electron Debye length and is generally used to describe the distance required to electrostatically shield an ion (see discussion in Section 2.3)

[8]The radius about which an ion gyrates when moving parallel to a magnetic field

Figure 2.4: Contours of equal ion density $\hat{n}_i$ around a probe for various drift speed ratios S_d. Plasma parameters are $\Phi_B = -25$, $\lambda_{D,e}/r_B = 1$, $T_e/T_i = 1$. Reprinted from McMahon, Xu, and Laframboise, (2005) with the permission of AIP Publishing.

2.2.3 Charged Aerodynamics Mechanisms

Aerodynamics refers to the exchange of momentum between a fluid and an immersed body with some relative velocity; drag forces being the manifestation of momentum losses tending to reduce the relative velocity between fluid and body. Therefore, when an object is immersed in a flowing plasma, there will be some charged aerodynamic exchange of momentum. Plasmas differ from conventional fluids however, in that momentum is exchanged both directly, through gas-surface interactions, and indirectly, through field effects. Direct charged aerodynamics refers to the direct exchange of momentum between body and plasma environment due to gas-surface interactions. Indirect charged aerodynamics refers to the indirect exchange of momentum between the body and plasma due to ion deflections; the indirect momentum exchange is transmitted through field effects.

To illustrate the theoretical basis of direct and indirect charged aerodynamics contributions to LEO bodies, it is instructive to consider arguments developed in the analysis of dusty plasmas (Fortov et al., 2005; Hutchinson, 2005; Hutchinson, 2006; Allen, 2007), in particular the control volume approach outlined by Allen, (2007) - the charged aerodynamics of dusty plasmas and LEO objects is a physically similar problem, with the differences being a matter of scale (see Section 2.3.6). Allen, (2007) begins by treating positive ions as a cold gas[9]. Discarding the ion stress tensor by assuming that the drift motion is much greater than thermal motion, the ion momentum equation may be written as (Allen, 2007),

$$n_i m_i \left(\mathbf{v} \cdot \nabla \right) \mathbf{v} + \cancelto{0}{\nabla p_i} = n_i q_i \mathbf{E} \tag{2.4}$$

Conversely, assuming that the electron thermal motion is much greater than its drift motion, the electron momentum can be written in the form (Allen, 2007),

$$\cancelto{0}{\underline{n_e m_e \left(\mathbf{v} \cdot \nabla \right) \mathbf{v}}} + \nabla p_e = -n_e q_e \mathbf{E}, p_e = n_e k_B T_e \tag{2.5}$$

where p_e is the thermal electron pressure, q_e is a fundamental charge unit and $\mathbf{E}$ is the electric field vector.

These two assumptions take advantage of the mesothermal nature of the plasma flow and are applicable in LEO. By assuming that the system is at a steady-state, the electric field $\mathbf{E}$ is given by Poisson's equation. Written in divergence form, Possion's equation is,

$$\nabla \cdot \mathbf{E} = \frac{\rho_c}{\epsilon_0} = \frac{q_e \left(n_i - n_e \right)}{\epsilon_0} \tag{2.6}$$

---

[9]Note that the fluid treatment of this problem is not applicable to all cases in LEO, where the mean-free path between particles becomes large (continuum/fluid assumptions breakdown). This is discussed further in Section 2.4

where ρ_c is the space-charge density and ϵ_0 is the permittivity of free-space.

Adding Eqns. 2.4 and 2.5 and substituting Eqn. 2.6 gives (Allen, 2007),

$$n_i m_i \left(\mathbf{v} \cdot \nabla\right) \mathbf{v} + \nabla p_e = \epsilon_0 \left(\nabla \cdot \mathbf{E}\right) \mathbf{E} \tag{2.7}$$

Considering a volume V of plasma that does *not* contain a body, Eqn. 2.7 becomes,

$$\underbrace{\int_V n_i m_i \left(\mathbf{v} \cdot \nabla\right) \mathbf{v} dV + \int_V \nabla p_e dV}_{\text{mechanical}} - \overbrace{\int_V \epsilon_0 \left(\nabla \cdot \mathbf{E}\right) \mathbf{E} dV}^{\text{electrical}} = 0 \tag{2.8}$$

In words, the variations in mechanical forces and (net) electrical forces acting within the volume causes the flow of mechanical momentum entering the volume to differ from the flow of mechanical momentum out of the volume i.e. conservation of momentum in an electromagnetic field must account for the momentum stored by the fields (Allen, 2007). This interpretation can be made explicit by applying Gauss's divergence theorem to express Eqn. 2.8 in terms of surface integrals,

$$\underbrace{\int_S n_i m_i \left(\mathbf{v} \cdot \mathbf{n}\right) \mathbf{v} dS}_{\text{ion momentum}} + \overbrace{\int_S p_e \mathbf{n} dS}^{\text{electron pressure}} - \underbrace{\int_S \bar{\mathbf{T}} \cdot \hat{\mathbf{n}} dS}_{\text{Maxwell stress}} = 0, \tag{2.9}$$

where $\hat{\mathbf{n}}$ is the outward unit vector normal to the surface S that encompasses the volume V and $\bar{\mathbf{T}}$ is the Maxwell stress tensor whose divergence becomes a vector of electric force per unit area i.e. an electric pressure and shear force.

The (electrostatic) Maxwell stress term can be written as (Miller, Vandome, and John, 2010),

$$\int_S \bar{\mathbf{T}} \cdot \hat{\mathbf{n}} dS = \int_S \left(\epsilon_0 \left(\mathbf{E} \cdot \hat{\mathbf{n}}\right) \mathbf{E} - \frac{1}{2}\epsilon_0 E^2 \hat{\mathbf{n}}\right) dS \tag{2.10}$$

For completeness, the derivation of the Maxwell stress tensor is detailed in Appendix A. The physical interpretation of the Maxwell stress is reflected by the terms in Eqn. 2.10, the electric field exerting a tension of $\epsilon_0 E^2$ in the direction of the electric field together with an isotropic pressure of $1/2\epsilon_0 E^2$ (Allen, 2007). On a surface, off-diagonal components cause a symmetric shear force while diagonal components reflect a pressure force.

Defining S_1 as the body surface and S_2 as any surface enclosing S_1, Eqn 2.9 becomes (Allen, 2007),

$$\int_{S_1} \left(n_i m_i \left(\mathbf{v} \cdot \mathbf{n}\right) \mathbf{v} + p_e \hat{\mathbf{n}} - \bar{\mathbf{T}} \cdot \mathbf{n}\right) dS + \int_{S_2} \left(n_i m_i \left(\mathbf{v} \cdot \hat{\mathbf{n}}\right) \mathbf{v} + p_e \hat{\mathbf{n}} - \bar{\mathbf{T}} \cdot \hat{\mathbf{n}}\right) = 0 \tag{2.11}$$

The implicit assumption in Allen, (2007) being that the system is steady. If transient phenomena exist, the right-hand side of Eqn. 2.11 is non-zero.

Note that the integral of S_1 is the force exerted on the body by the plasma $\mathbf{F}_C$. Taking S_2 on an equipotential surface, such as a conducting body's surface, the contribution of the electron pressure can be neglected. Eqn. 2.11 can then be written as,

$$\mathbf{F}_C = -\underbrace{\int_{S_2} n_i m_i \left(\mathbf{v} \cdot \hat{\mathbf{n}} \right) \mathbf{v} dS}_{\text{direct force}} - \int_{S_2} p_e \hat{\mathbf{n}} dS^{\,0} + \underbrace{\int_{S_2} \bar{\mathbf{T}} \cdot \hat{\mathbf{n}} dS}_{\text{indirect force}} \qquad (2.12)$$
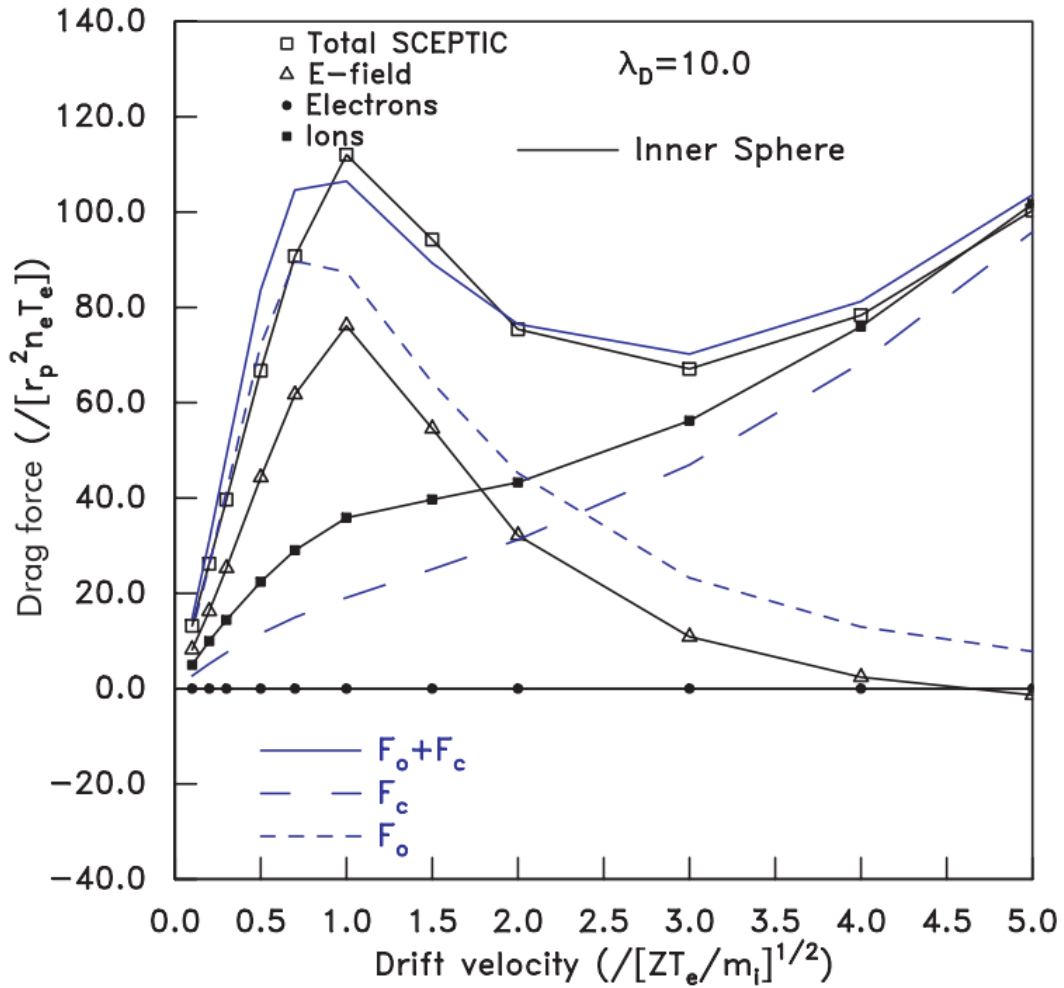
Based on Eqn. 2.12, direct charged aerodynamics is readily conceptualised as the net momentum exchanged between the body and plasma due to direct gas-surface collisions. Eqn. 2.12 however provides a different but consistent interpretation of indirect charged aerodynamics compared with previous scattering models, which focus on calculating the momentum exchanged between body and scattered ions, where electric stress on the surface captured by the Maxwell stress tensor causes a force on the body to reflect the deformation of electric fields required to deflect ions. The advantage of this approach over the scattering interpretation is that the Maxwell stress includes the indirect force caused by the acceleration of both collected and non-colliding ions i.e. ions may contribute to both direct and indirect charged aerodynamic forces (and they do).

Note that for drag calculations, $\mathbf{F}_C$ is transformed into total charged drag force $F_{D,C}$. To be consistent with $F_{D,N}$, a positive $F_{D,C}$ causes a drag i.e. the negative of Eqn. 2.12.

Figure 2.5 illustrates results from Hutchinson, (2005), which employs this approach to study the effect of drift velocity on the charged aerodynamics of dusty plasmas. For the case shown in Figure 2.5, as ion drift approaches the ion acoustic Mach number the relative contribution of indirect charged drag dominates the total charged drag, while above that the influence of indirect charged drag decays. As Hutchinson, (2005) and Hutchinson, (2006) concluded in the study of dusty plasmas, to quantify the contribution of ionospheric aerodynamics to LEO objects requires the *self-consistent*[10] calculation of this sheath in order to capture the direct and indirect exchange of momentum between plasma and body.

---

[10]Self-consistent plasma interactions refer to a system that accounts for the electrical coupling between plasma distribution and object without imposing assumptions regarding the sheath structure i.e. at steady-state the sheath structure created by the motion of the ions through the sheath doesn't change the ion trajectories.

Figure 2.5: Variation of direct and indirect charged drag forces with ion acoustic Mach number for a probe with $r_B = 10\lambda_{D,e}$ and $T_i = 0.1T_e$. Reprinted from (Hutchinson, 2006) with permission.

2.3 Review of Ionospheric Aerodynamics Literature

While the aerodynamics of LEO objects resulting from interactions with neutral particles has matured since the early 1960s, study of the equivalent charged particle interaction has languished. In the 1963 review of the effect of charged aerodynamics on the motion of LEO bodies, Brundin, (1963) concluded that the error caused by neglecting direct charged aerodynamics in O^+ dominated LEO plasmas would result in a 20% over-prediction of neutral density based on satellite accelerations when $n_{O+}/n_O < 10\%$. The conclusion in Brundin, (1963) had a large impact on the field of LEO charged aerodynamics, best reflected by the following quotes:

> *"On the basis of present evidence,(Brundin, (1963), Knechtel and Pitts, (1965)) charged drag appears to be negligible up to at least the altitude where helium becomes the main constituent."* - Cook, (1965)

> *"...charged particle drag (which was ultimately shown to be of less importance than errors in the neutral drag coefficient (see reviews by Brundin, (1963) and Leeuw, (1966)[11]) was still of primary concern, and self-consistent solutions of particle trajectories and fields had not been carried out."* - Garrett, (1981)

The first quote is from the work by Cook, (1965), which proposed the use of a constant $C_{D,N}$ of 2.2 for compact objects in LEO. The seminal nature of the work by Cook, (1965) is clear, $C_{D,N} = 2.2$ remaining in operational use until the past decade, when, spurred by the Iridium-Kosmos collision, higher-order physical models were used to demonstrate the importance of gas-surface interactions, wetted area, molecular species, etc. on $C_{D,N}$ (see Moe and Moe, (2005), Pilinski, (2011), Pilinski, Argrow, and Palo, (2011), and Mehta, Walker, and Koller, (2014) for examples). The second quote is from the 1981 review of the then state-of-the-art of spacecraft charging by Garrett, (1981), this and their follow-up review (Garrett and Whittlesey, 2000) being some of most highly referenced treatments of the subject (see also Hastings, (1995) and Hastings, (1995)).

The impact of the conclusions by Brundin, (1963) is reflected in the focus of LEO ionospheric aerodynamics research; work prior to Brundin, (1963) investigating the forces on LEO objects (Jastrow and Pearse, 1957; Kraus and Watson, 1958; Wyatt, 1960; Chopra, 1961b; Davis and Harris, 1961; Bird, 1962), later work investigating the structure of LEO interactions (Hall et al., 1963; Al'Pert, Gurevich, and Pitaevskii, 1965; Hester and Sonin, 1969; Vaglio-Laurin and Miller, 1969; Gurevich, Pitaevskii, and Smirnova, 1970; Martin, 1974; Liu, 1972; Liu, 1975; Senbetu and Henley, 1989). Fundamental to the conclusions by Brundin, (1963) is the assertion that the surface potential of LEO objects (ϕ_B) never

---

[11]Note that no copy of Leeuw, (1966) was found.
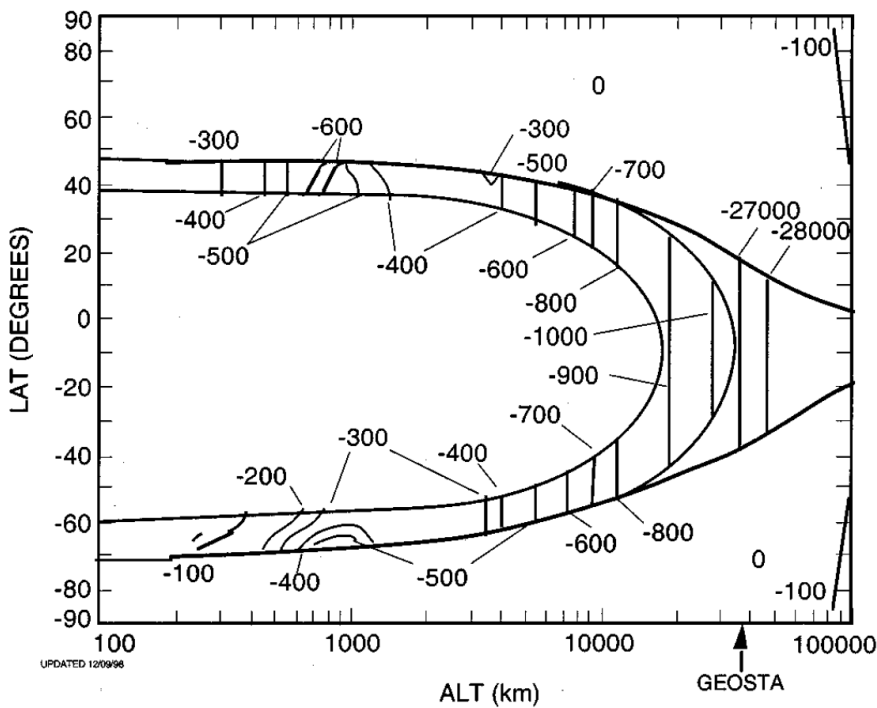
becomes more negative that -0.75 V compared to the surrounding plasma. While this assertion was supported by major works of the era (Whipple, 1965; Whipple, 1981; Garrett, 1981), modern LEO charging literature illustrates that this assertion is not appropriate for all conditions in LEO.

The purpose of this section is to review ionospheric aerodynamic literature from a modern context to establish: (1) what is the current state-of-the-art and its limitations and (2) whether early conclusions regarding the significance of ionospheric aerodynamics to LEO objects remain valid and if not, to establish why not. In turn, this discussion will help focus this work to addresses the limitations in the current state-of-the-art of ionospheric aerodynamics. To achieve this, the discussion is broken into four parts. Section 2.3.1 provides a brief discussion of charging in LEO to establish representative surface potentials of LEO objects. Section 2.3.2 discusses two recent works, the study by Andrés de la Fuente, (2007) of the LAGEOS spacecraft in Medium Earth Orbit (MEO) and the work by Li, (2011) on the perturbation to LEO objects based on charged aerodynamic predictions by Chopra, (1961a) (predictions based on an unshield, stationary plasma interaction inappropriate for ionospheric aerodynamics). The use of relationships in Chopra, (1961a) by Li, (2011) further motivates a comprehensive review of early ionospheric aerodynamics literature in Section 2.3.3 to establish the state-of-the-art of ionospheric aerodynamics to act as a reference for future work. Section 2.3.4 follows the review of early ionospheric aerodynamic literature by considering relevant experimental results, which in turn leads to a discussion in Section 2.3.5 of established plasma-body interaction scaling relationships and their suitability to ionospheric aerodynamics. Leading on from the discussion of scaling in Section 2.3.5, Section 2.3.6 discusses relevant work in dusty plasma physics, where the study forces on charged dust grains in a flowing plasma provides a physically relevant basis to develop an understanding of ionospheric aerodynamics.

2.3.1   Charging in Low Earth Orbit

As outlined in (Hastings, 1995) and (Garrett and Whittlesey, 2000), there have been significant advances in LEO charging literature in the past two decades. Complex structures resulting from the mesothermal interaction of LEO bodies with the plasma environment combined with the desire to operate increasingly high voltage solar arrays, has made the analysis of LEO plasma-body interactions historically difficult. With the continuing growth in computing capabilities and advances in numerical methods the simulation of these interactions has now become feasible.

It is now recognised that LEO objects, particularly those in polar orbits, can naturally achieve floating potentials more negative than -100 V, albeit sometimes for short periods (Olsen and Purvis, 1983; Gussenhoven et al., 1985; Evans et al., 1989; Hastings, 1995;

Figure 2.6: Surface charging potential contours (in the absence of sunlight) as a function of altitude and latitude for a conducting aluminium sphere. Reprinted from (Garrett and Whittlesey, 2000) IEEE (see also (Evans et al., 1989)).

Garrett and Whittlesey, 2000; Anderson, 2012). Figure 2.6, reproduced from Garrett and Whittlesey, (2000), illustrates a first-order prediction of the worst-case floating potential of a conducting, spherical, aluminium satellite without photoemission[12] through a range of altitudes and latitudes. Intended to serve as a simple tool to illustrate charging threat levels to satellites orbiting Earth, below 2000 km altitude, Figure 2.6 predicts floating potentials as high as -600 V in LEO near the poles. This is consistent with observations from by Anderson, (2012) who presented a statistical study of 1600 charging events (defined as spacecraft charges exceeding -100 V) on the DMSP spacecraft at 840 km during auroral crossings (surface charges of up to -2000 V were observed) (see also Gussenhoven et al., (1985)).

Perhaps more significant to ionospheric aerodynamics however, is the use of high voltage power systems e.g. solar panels, which may couple with the charged space environment to induce large artificial surface potentials (Wang, 1991; Wang and Hastings, 1992b; Hastings, 1995; Garrett and Whittlesey, 2000). An examples include the calculations presented by Hastings, (1995) that predicted that the International Space Station (ISS) surface potential

---

[12]A positive current source that tends to suppress negative floating potentials.

would range between -110 V and -160 V due to its power systems[13]. Other examples include the work by Wang, (1991) and Wang and Hastings, (1992b), who investigated plasma structures about a highly charged plate at different angles of attack i.e. a solar panel, and the applications outlined by Choinière and Gilchrist, (2007), who presented a study of high voltage objects outside the scope of previous works limited to surface potentials less than 25 times the electron temperature.

Hence, the conclusions regarding charged aerodynamics in (Brundin, 1963) based on a maximum negative ϕ_B of -0.75 V, while appropriate in the 1960s, may not accurately represent the influence of charged aerodynamics to LEO objects in a modern context. It is therefore appropriate to survey recent literature applicable to charged aerodynamics in LEO and review the basis of conclusions in Brundin, (1963). Before this however, we consider the more recent works by Li, (2011) and Andrés de la Fuente, (2007).

2.3.2 Modern Ionospheric Aerodynamics Literature

Li, (2011) applied the theory in (Chopra, 1961a) and (Chopra and Singer, 1958) to orbit perturbation equations to quantify the effect of ionospheric aerodynamics on the orbital elements of LEO objects. Unfortunately the analyses by Chopra and Singer, (1958), Chopra, (1961a), and Chopra, (1961b) suffered from a variety of inappropriate assumptions (discussed in detail in (Brundin, 1963)). Chopra, (1961a) estimated the contribution of direct charged aerodynamics to LEO objects by considering the unshielded stationary interaction of an object with a plasma. Neither the unshielded nor stationary assumptions are appropriate LEO for objects, resulting in extreme (inaccurate) charged aerodynamic predictions. Chopra and Singer, (1958) also estimated the contribution of indirect charged aerodynamics to LEO objects by applying a modification of equations (Chandrasekhar, 1943) for gravitational *"dynamic friction"* applied to Coulomb forces. The resulting indirect charged drag expression is,

$$F_{D,M} = 8\pi r_B^2 n_{i,\infty} \frac{(Z_k q_k)^2 \phi_B^2}{m_i v_B^2} \ln\left[\Lambda\right] \tag{2.13}$$

where $\ln\left[\Lambda\right] = \int_{b_{min}}^{b_{max}} db/b$ is the Coulomb logarithm and b_{max} and b_{min} are the maximum and minimum impact parameters.

Highlighted by both Chandrasekhar, (1943) and Brundin, (1963), Eqn. 2.13 was obtained under the restriction that $\ln\left[\Lambda\right] \ll 1$. In place of $\ln\left[\Lambda\right]$ Chopra and Singer, (1958) and Chopra, (1961a) used $\ln\left[\lambda_{D,e}/b_{90}\right]$ where b_{90} is the impact parameter for a 90° deflection in a collision between singly charged ions. While Chopra, (1961a) describes $\lambda_{D,e}/b_{90}$ as a *"more plausible parameter"*, no argument is made to support this statement, specifically

---

[13]To mitigate ESD hazards, the ISS surface potential is artificially maintained at -30 V

why a quantity derived for a singly charged ion would be appropriate for a body with a macroscopic charge (Brundin, 1963). A more comprehensive treatment of this problem can be found in the dusty plasma literature (see discussion in Section 2.3.6). To summaries, there remain significant ambiguities and uncertainties in the treatment of this term when applied to finite-size objects (Hutchinson, 2006). To address these ambiguities requires the calculation of the full self-consistent charge distribution about the object e.g. the work in (Hutchinson, 2005; Hutchinson, 2006) and the references therein. Hence, while interesting, we do not consider the results from Li, (2011) further. Investigations into the accelerations of the LAGEOS-I and LAGEOS-II spacecraft, however, are more insightful.

The LAGEOS-I and LAGEOS-II spacecraft are low area-to-mass ratio spherical satellites with nominal altitudes of 5900 km designed for geodetic measurements (Andrés de la Fuente, 2007). While outside the ionosphere, a consequence of their use in geodetic measurements is that their motion has been well studied, in particular, the anomalous along-track deceleration of the spacecraft causing a decay of the semimajor axis of the orbit at a rate of approximately 1.1 mm/day (Andrés de la Fuente, 2007; Rubincam, 1980; Mignard et al., 1985; Rubincam, 1990; Gilles, Vokrouhlick, and Eanes, 1997). Early studies dedicated to quantifying the effect of charge aerodynamics on the motion of the LAGEOS spacecraft did not account for important perturbations, such as thermal forces, resulting in large inaccuracies when compared to observations (Andrés de la Fuente, 2007) i.e. empirical accelerations, which represent a host of tiny forces from direct causes, were inappropriately grouped by not modelling all force mechanisms.

Primary limitations in early LAGEOS charged aerodynamics studies cited by Andrés de la Fuente, (2007) include: the use of fluid dynamic expressions for charged aerodynamics which exclusively depend upon the orbital velocity of the satellite without taking into account the ion thermal speed and spacecraft potential (Rubincam, 1980); the use of a first approximation in evaluating the charged drag coefficient for the latter fluid dynamics expression (Rubincam, 1980; Mignard et al., 1985); approximations of indirect charge aerodynamics as an empirical expression, or as a percentage of direct charge aerodynamics (Rubincam, 1980; Mignard et al., 1985); the application of cylindrical based charged aerodynamics approximations applied to spherical bodies (Fournier, 1970).

Andrés de la Fuente, (2007) applied dusty plasma theory developed in Hutchinson, (2002) and Hutchinson2005 to estimate the contribution of direct and indirect drag to the LAGEOS-I and LAGEOS-II spacecraft. Hutchinson, (2005) calculated the Orbit Motion Limited (OML) momentum flux rate integrated over a shifted Maxwellian velocity distribution to predict the direct charged drag on a sphere (see also Uglov and Gnedovets, (1991)). Similarly, Hutchinson, (2002) applied OML assumptions of conservation of energy and angular

momentum to develop an analytical expression for the indirect charged drag due to dynamic friction on a spherical dust particle (see also the more recent work in (Hutchinson, 2006)). OML theory is discussed in detail in Section 2.3.3, in brief, is revolves around the assumption that the plasma sheath structure is spherically/cylindrically symmetric, much larger than the body, and that the variation of potential structures with radial distance from a central point is slower than $1/r^2$ (Allen, 1992; Fortov et al., 2005). The first assumption implies conservation of ion angular momentum, which, when combined with the second and third assumptions, allows the estimation of ion collection without requiring a solution of Poisson's equation.

At 5900 km, the sheath surrounding the LAGEOS spacecraft is similar to that of a stationary probe, the relative velocity no longer being mesothermal ($v_B \approx 5.7$ km/s, $v_{t,i} \approx 9.8$ km/s) and the shielding distance comparable to body dimensions ($r_B = 0.3$ m, $\lambda_{D,e} = 0.136$ m) (Andrés de la Fuente, 2007). As a result, the theory developed in Hutchinson, (2002) and Hutchinson, (2005) is largely appropriate when applied to the LAGEOS spacecraft.

In their study of the LAGEOS-I and LAGEOS-II spacecraft, Andrés de la Fuente, (2007) concluded that the contribution of charged aerodynamics to along-track accelerations increases from -0.5 pms^{-2} when not in eclipse to -85 pms^{-2} and -70 pms^{-2} respectively in eclipse - the larger eclipse charged aerodynamic acceleration for the LAGEOS-I a reflection of its orbit which brings it over the auroral and polar zones, causing higher floating potentials. Figure 2.7 is reproduced from Andrés de la Fuente, (2007), plotting instantaneous charged drag accelerations of LAGEOS-II in cross-track (a_{YCT}), along-track (a_{AT}) and radial (a_{R}) directions along with predicted body floating potentials ϕ_p, and solar ($F_{10.7}$) and geomagnetic (A_p) indices from launch until 4th June, 2006. Figure 2.7 supports the argument made that unmodelled charged aerodynamics forces may explain large uncertainties in $C_{D,N}$ and ρ_m observed in Doornbos and Klinkrad, (2006) and Mclaughlin, Mance, and Lechtenberg, (2011) during solar weather events: the maximum along-track acceleration a_{AT} in Figure 2.7 corresponding to large $F_{10.7}$ and A_p indices. The reason for the increase in charged aerodynamic accelerations in eclipse is a reflection of the increase in negative floating potential due to the absence of a positive photo-electric current and drop in total ion density (Hastings, 1995; Garrett and Whittlesey, 2000; Andrés de la Fuente, 2007).

Compared to a neutral drag acceleration of -0.5 pms^{-2}, Andrés de la Fuente, (2007) demonstrated that charged aerodynamics can have a significant and complex effect on the dynamics of the LAGEOS spacecraft in MEO. Unfortunately, the anisotropic, thin-sheath structure characteristic of LEO plasma interactions break down underlying assumption in OML theory employed in Andrés de la Fuente, (2007). As a result, the approach in Andrés de la Fuente, (2007), while appropriate for MEO objects, is not transferable to all LEO objects.

Figure (Text/Chart/Diagram etc.) has been removed
due to copyright restrictions. This figure may be found in
the reference listed in the caption.

Figure 2.7: Instantaneous charged drag accelerations over time with predicted floating potentials and space weather indices for the LAGEOS-II from launch until June 4,2006. Red lines have been added to highlight period of high along-track acceleration a_{AT} caused by charged aerodynamic forces. Adapted from Andrés de la Fuente, (2007).

2.3.3 Early Ionospheric Aerodynamics Literature

Of early ionospheric aerodynamics investigations, this discussion shall focus on three notable works (Jastrow and Pearse, 1957; Brundin, 1963; Knechtel and Pitts, 1965). The works by Jastrow and Pearse, (1957) and Brundin, (1963) summarise the approaches and different points of view of the time, whereas the work by Knechtel and Pitts, (1965) is the only experimental investigation to date to directly measure the forces on a objects immersed in a mesothermal plasma with application to ionospheric aerodynamics in LEO. The following comprise a majority of works that directly consider ionospheric aerodynamics, those before Brundin, (1963) focused on aerodynamic forces, while those that followed focused on flow features (Jastrow and Pearse, 1957; Kraus and Watson, 1958; Beard and Johnson, 1960; Wyatt, 1960; Chopra, 1961b; Davis and Harris, 1961; Bird, 1962; Brundin, 1963; Hall et al., 1963; Knechtel and Pitts, 1965; Al'Pert, Gurevich, and Pitaevskii, 1965; Kiel and Gey, 1968; Call, 1969; Hester and Sonin, 1969; Vaglio-Laurin and Miller, 1969; Fournier, 1970; Gurevich, Pitaevskii, and Smirnova, 1970; Martin, 1974; Liu, 1975). Jastrow and Pearse, (1957) and Brundin, (1963) explored the significance of charged aerodynamics to LEO dynamics compared to neutral aerodynamics by estimating the ratio of charged to neutral drag forces $F_{D,C}/F_{D,N}$.

Applying a hyperthermal ion approximation ($v_B \gg v_{t,i}$), Jastrow and Pearse, (1957) and Brundin, (1963) began by considering the free molecular drag on a sphere given as (Sentman, 1961),

$$F_{D,k} = \pi m_k n_k v_B^2 b_k^2 \tag{2.14}$$

where k refers to species and b_k is a species dependent impact parameter (illustrated in Figure 2.8).

Neutral drag is calculated simply by considering the wetted area defined by the body radius r_B ($b_n = r_B$),

$$F_{D,N} = \pi m_n n_n v_B^2 r_B^2 \tag{2.15}$$

Both Jastrow and Pearse, (1957) and Brundin, (1963) then made arguments regarding the nature of b_i by considering the motion of an ion with total energy $\mathcal{E}$ and angular momentum $\mathcal{L}$ given by,

$$\mathcal{E} = \frac{1}{2}m_i\left(v_r^2 + v_\theta^2\right) + q_i\phi(r), \quad \mathcal{L} = m_i b v_\theta \tag{2.16}$$

where v_θ and v_r are the transverse and radial components of particle velocity centered about the body.

Importantly, both Jastrow and Pearse, (1957) and Brundin, (1963) assumed a symmetric sheath structure, making the physical system considered in Jastrow and Pearse, (1957) and Brundin, (1963) equivalent to that considered by Orbital Motion (OM) theory.

A Note on Orbital Motion Theory

OM theory revolves around predicting the motion of ions and electrons in a central force field. By assuming a spherically or cylindrically symmetric sheath, it follows from conservation laws that the radial motion of an ion is fully determined by the effective potential energy (U_{eff}) (Al'Pert, Gurevich, and Pitaevskii, 1965; Allen, 1992; Fortov et al., 2005). Here U_{eff} is the difference between the total energy $\mathcal{E}$ and the radial kinetic energy $1/2 m_i v_r^2$. Re-arranging Eqn. 2.16, substituting $\mathcal{L}$ to eliminate v_θ and normalising against the total freestream energy ($\mathcal{E}_\infty = (1/2) m_i v_\infty^2$), U_{eff} can be written as,

$$U_{eff}(r, b(v)) = \frac{2\mathcal{E}}{m_i v_B^2} - \frac{v_r^2}{v_B^2} = \frac{b(v_B)^2}{r^2} + \frac{2 q_i \phi(r)}{m_i v_B^2} \tag{2.17}$$

where ion motion is restricted to the region where $U_{eff}(r, b) \leq 1$ i.e. if $U_{eff}(r, b) = 1$ has root(s), the largest root determines the distance of closest approach (r_c) (Al'Pert, Gurevich, and Pitaevskii, 1965; Fortov et al., 2005).
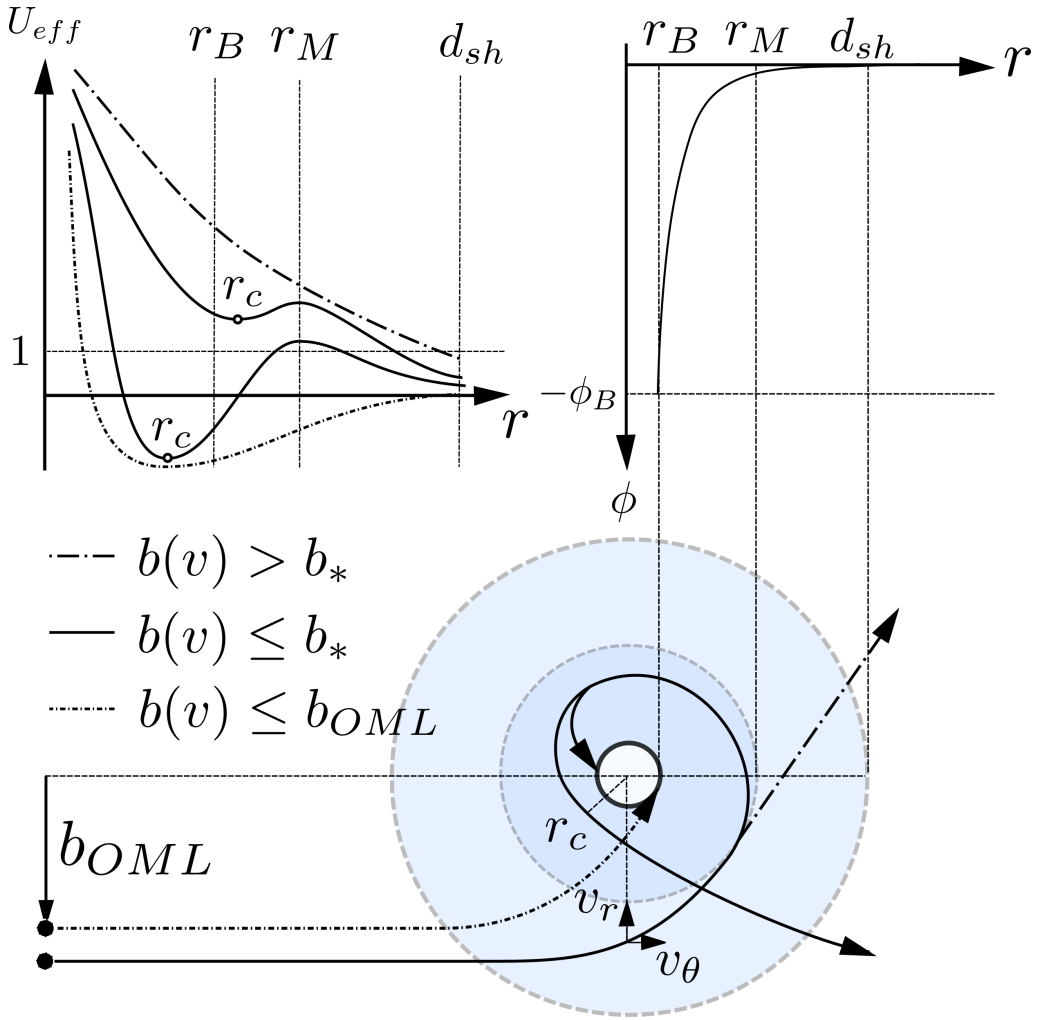
For a sphere/cylinder with radius r_B, an ion is collected when $r_c \leq r_B$ (it hits the surface), whilst for $r_c > r_B$, the ion will be elastically scattered by $\phi(r)$. Eqn. 2.17 demonstrates that ion collection depends on sheath structure through $\phi(r)$. In a stationary plasma with a symmetric sheath (as was seen in Figure 2.4 top left), the collection of ions by an attractive body ($\phi_B < 0$) is governed by the gradient in potential $d\phi(r)/dr$.

Figure 2.8 illustrates the representative trajectories of ions through a symmetric sheath. Three different trajectories are considered. The first two are based on a Debye-Huckle type $d\phi(r)/dr$ potential profile. At large values of r (light blue), the potential varies slower than $1/r^2$ ($d\phi(r)/dr < 1/r^2$), while near the body (dark blue) the potential varies faster than $1/r^2$ ($d\phi(r)/dr > 1/r^2$) (Fortov et al., 2005). As illustrated in Figure 2.8, a physical consequence of this sheath structure is the existence of a velocity dependent critical impact parameter b_* within which particles are deflected through an orbit about the body - this is known as an *"ion absorption barrier"* or *"potential barrier"* (Al'Pert, Gurevich, and Pitaevskii, 1965; Allen, 1992; Fortov et al., 2005).

Taking the derivative of Eqn 2.17 with respect to r, the implications of different sheath structures becomes clearer by examining extrema in U_{eff} (dU_{eff}/dr), given as,

$$r^3 (d\phi(r)/dr) = m_i v^2 b^2 \tag{2.18}$$

In other words, local maxima in Eqn. 2.18 (illustrated in Figure 2.3) correspond to orbital inflection points where ions are deflected onto trajectories about the body at the critical radius r_M, while local minima in Eqn. 2.18 correspond to the closet approach r_c of the

Figure 2.8: Illustration of ion orbital motion about a charged cylinder in a central force field.

particle's orbit (perigee). If the perigee is less than the body radius ($r_c < r_B$), the ion is collected.

The last trajectory in Figure 2.8 is based on the Orbit Motion Limited (OML) case; OML theory is a subset of OM theory where the sheath structure is assumed to vary slower than $1/r^2$ ($d\phi(r)/dr \leq 1/r^2$). Consequently, Eqn. 2.18 grows monotonically and there exists a single solution corresponding to a minimum U_{eff}. The critical or maximum impact parameter in the OML limit b_{OML} for a grazing incidence ($r_M = r_B$) occurs at this minimum. This was the approach taken in Brundin, (1963).

Orbital Motion Theory Applied to Charged Aerodynamics

Brundin, (1963) predicted the direct contribution of charged aerodynamics by applying OML type arguments about the sheath structure. Equating the freestream effective potential energy with the effective potential energy at the body surface and solving for the maximum impact parameter b_{OML} gives,

$$(b_*)_{\text{Brundin}} = b_{\text{OML}} = r_B \left(1 - \frac{2q_i \phi_B}{m_i v^2} \right)^{1/2} \tag{2.19}$$

In essence, b_{OML} is equivalent to that used in Brundin, (1963) [14].

Jastrow and Pearse, (1957), on the other hand, numerically integrated Poisson's equation to obtain a 1D sheath structure which was assumed to uniformly surround a LEO body. Based on this sheath structure, Jastrow and Pearse, (1957) argued that b_* should have the form,

$$(b_*)_{\text{Jastrow}} = r_B \left(1 + \kappa(\phi_B) \frac{\lambda_{D,e}}{r_B} \right) \tag{2.20}$$

where $\kappa(\phi_B)$ is a case dependent function of ϕ_B and incorporates the negative sign seen in Eqn. 2.19.

As illustrated in Figure 2.9, Eqns. 2.19 and 2.20 predict the increase (or decrease) in effective ion collection area caused by a plasma sheath. Applying the hyperthermal assumption ($v_B \gg v_{t,i}$), the incident direct charged drag force $F_{D,d}$ on a sphere was calculated as in Eqn. 2.15, substituting b_* for r_B (Jastrow and Pearse, 1957; Brundin, 1963),

$$(F_{D,d})_{\text{Brundin}} = \pi m_i n_i v_B^2 r_B^2 \left(1 - \frac{2q_e \phi_B}{m_i v_B^2} \right)$$

$$(F_{D,d})_{\text{Jastrow}} = \pi m_i n_i v_B^2 r_B^2 \left(1 + \kappa(\phi_B) \frac{\lambda_{D,e}}{r_B} \right)^2 \tag{2.21}$$
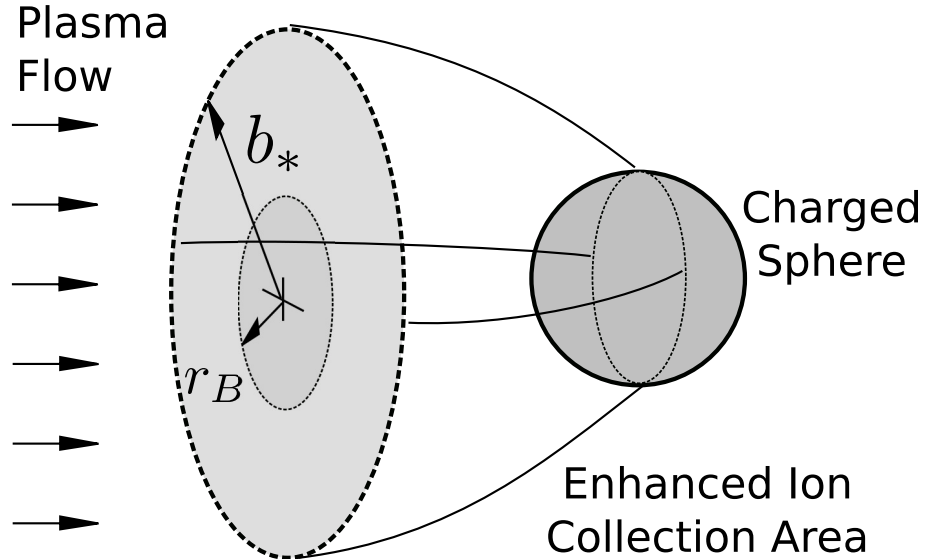
Taking the ratio of equations in Eqn. 2.21 with Eqn. 2.15 gives,

$$\left(\frac{F_{D,d}}{F_{D,N}} \right)_{\text{Brundin}} = \frac{m_i}{m_n} \frac{n_i}{n_n} \left(1 - \frac{2q_e \phi_B}{m_i v_B^2} \right)$$

$$\left(\frac{F_{D,d}}{F_{D,N}} \right)_{\text{Jastrow}} = \frac{m_i}{m_n} \frac{n_i}{n_n} \left(1 + \kappa(\phi_B) \frac{\lambda_{D,e}}{r_B} \right)^2 \tag{2.22}$$

Note that neither approach considered the sheath driven ion acceleration, the argument being that momentum is conserved between the freestream and the body. A simple energy

---

[14]Note that for positive ϕ_B, $b_{\text{OML}} < r_B$, the sheath deflects ions away from the body and reduces the effective ion collection area

Figure 2.9: Illustration of the physical relationship between b_* and the drag on a charged sphere. The plasma sheath is not shown for simplicity.

balance between the freestream shows that ions arrive at the surface (v_S) with a velocity,

$$v_S = v_B \left(1 - \frac{2q_i\phi_B}{m_i v_B^2}\right)^{1/2} \tag{2.23}$$

For the -0.75 V case considered in Brundin, (1963) with $v_B = 7.5$ km/s, this corresponds to a 7.74% increase in incident O^+ velocity and an 88.62% increase in incident H^+ velocity. However, we saw in Section 2.2.3 that momentum in an electric field is conserved when considering both the mechanical momentum (particles) and field momentum (Maxwell stress) (Hutchinson, 2005; Allen, 2007). As will be shown in Chapter 4, this ion acceleration induces an indirect thrust force on the body that counters the increase in direct charged drag caused by the ion acceleration i.e. the general concept of ion collection enhancement holds (though is more complicated than implied in either equation in Eqn. 2.22). Other assumptions in Eqn. 2.22 include a symmetric sheath and the assumption that all momentum is transferred in the along-track (drag) direction. The most important difference between the approaches (and therefore conclusions) in (Jastrow and Pearse, 1957) and (Brundin, 1963) were assumptions regarding ϕ_B.

Jastrow and Pearse, (1957) predicted LEO surface potentials between -10 V and -60 V, while, as mentioned, Brundin, (1963) predicted maximum negative surface potentials of -0.75 V. Based on their potentials Jastrow and Pearse, (1957) concluded that charged aerodynamics varies from 10% to 150% of neutral drag at an altitude of 482.80 km (300

miles). Taken another way, *calculations of atmospheric density based on satellite acceler-*
ations that do not account for charged aerodynamics would be substantially over-estimated
above ≈ 500 km.

Brundin, (1963), meanwhile, argued that the $T_e \gg T_i$ assumption made by Jastrow and
Pearse, (1957), which resulted in high surface potential predictions, is more appropriately
$T_e \approx T_i$ in LEO i.e. they argued that Jastrow and Pearse, (1957) over-predicted ϕ_B and
therefore charged aerodynamics forces. Based on a maximum negative floating potential
of -0.75 V, Brundin, (1963) concluded that the error induced by neglecting O^+ direct
charged aerodynamics would always be less than 20% when the ratio of charged to neutral
monatomic oxygen is less than 10%.

In Section 2.2.1, however, we established that there exist conditions in LEO where $n_i/n_n \rightarrow$
1, while Section 2.3.1 discussed how it is now recognised that high surface potentials,
whether natural or artificial, may occur in LEO. Therefore, while the justification for high
floating potentials made by Jastrow and Pearse, (1957) may have been incorrect, their
conclusions regarding the significance of ionospheric aerodynamics may prove valid for
certain cases.
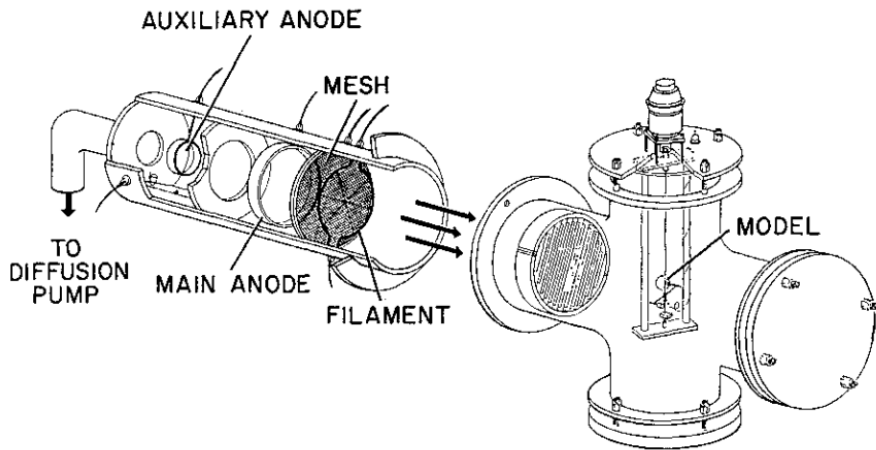
2.3.4   Experimental Measurements of Charged Aerodynamics

So far, the above sections have primarily presented theoretical arguments supported by
a selection of numerical works to assess the state-of-the-art for ionospheric aerodynamics
and to argue that prior conclusions regarding the significance ionospheric aerodynamics in
LEO may no longer be accurate when applied to modern satellites and orbits. This section
focuses on ionospheric aerodynamics measurements made in laboratory experimental test
facilities.

As with the theoretical literature, the experimental and in-situ literature is best considered
by separating into works that considered the force on a macroscopic body in a flowing
plasma and works that focus on characterising the phenomena associated with plasma-body
interactions. There exists a wide area of literature in the latter category, in part because
it is directly related to plasma probe measurements - plasma probes used to measure the
surrounding plasma environment must correct for sheath effects as measurements at the
surface are of sheath properties, not plasma properties. Here, we shall focus our discussion
to works directly related to LEO plasma-body interactions. Scaling relationships applied
by these works are discussed in Section 2.3.5 and are not discussed here.

Aerodynamic Force
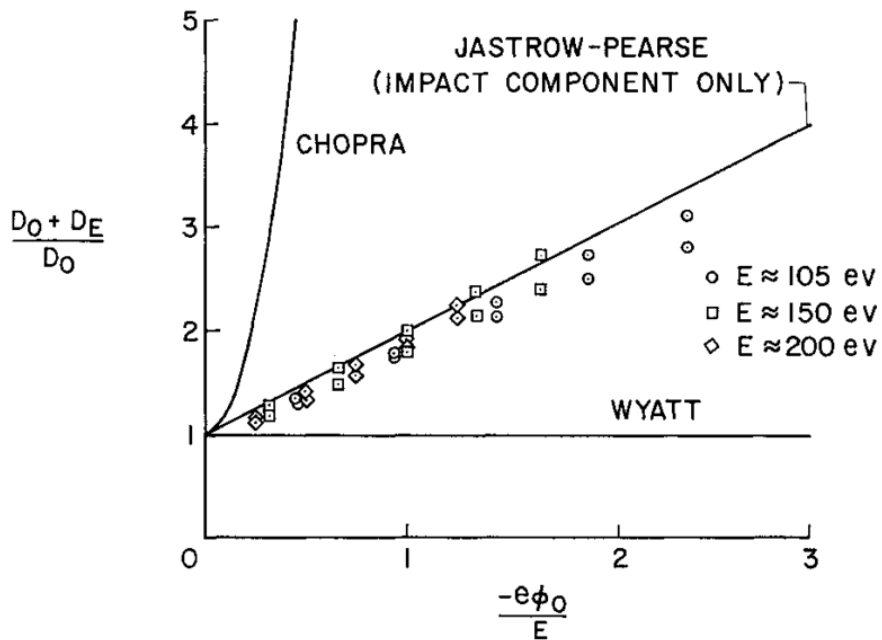
The only readily available experimental study of charged aerodynamics forces applied to a LEO context are those in Knechtel and Pitts, (1965). Knechtel and Pitts, (1965) investigated the effect of ϕ_B on the charged drag of a sphere in an attempt to resolve the disagreements in charged drag predictions between (Chopra, 1961a), (Jastrow and Pearse, 1957) and (Brundin, 1963) caused by different assumptions regarding the physical nature of the interaction. Figure 2.10 is reproduced from (Knechtel and Pitts, 1965) showing their experimental setup.
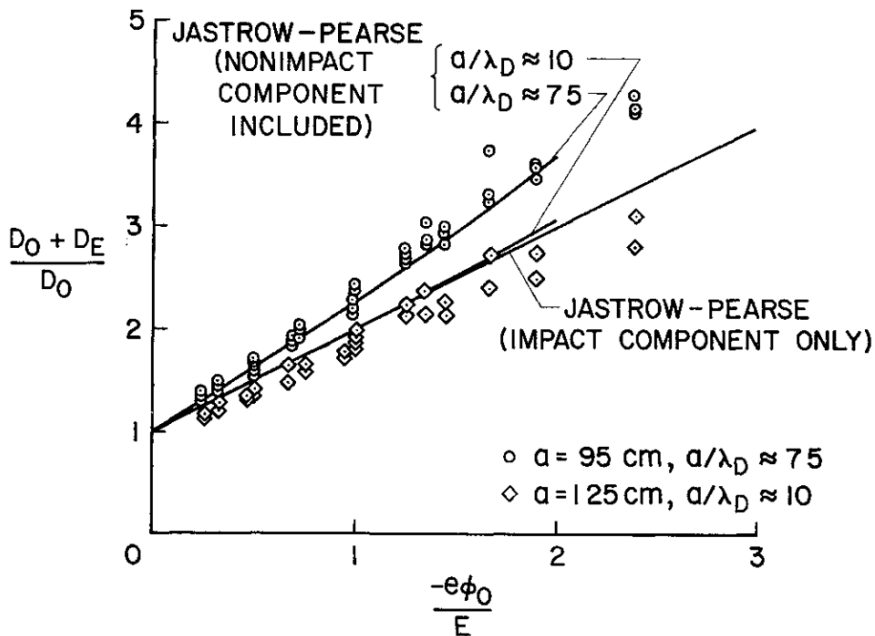
Figure 2.10: Illustration of experimental setup in Knechtel and Pitts, (1965). From Knechtel and Pitts, (1965): reprinted with permisson of the American Institude of Aeronautics and Astronautics, Inc.

Experimental measurements were made by placing conducting spherical models in a broad beam of singly ionised Mercury plasma with a streaming (drift) velocity ranging between $8 - 16$ km/s. The usable beam core was stated to have a diameter of 5 cm and an ion number density of approximately 10^{12} m^{-3}, while the background density was stated to be kept sufficiently low by pumping and refrigeration to assure background number densities were in the free-molecular (collisionless) regime. Force measurements were made using a null-type quartz-fibre micro-balance, sensitive to three μg up to several hundred μg. A 4μg diameter wire was connected to the balance to control the sphere potential externally. No additional details other than those above regarding experimental setup, such as source characterisation measurements, are provided in (Knechtel and Pitts, 1965).

Two figures have been reproduced from (Knechtel and Pitts, 1965). Figure 2.11 compares theoretical charged to neutral drag ratio from (Jastrow and Pearse, 1957) (seen in Eqn. 2.22), (Chopra, 1961a) and (Wyatt, 1960) with experimental results for a 2.5 cm diameter model. Here $F_{D,C}/F_{D,N} = (D_O + D_E)/D_O$, where D_O is neutral drag and D_E is the

Figure 2.11: Comparison of experimental measurements of the ratio of charged and neutral drag with neutral drag compared with theory. From (Knechtel and Pitts, 1965): reprinted with permisson of the American Institude of Aeronautics and Astronautics, Inc.

Figure 2.12: Ratio of charged and neutral drag with neutral drag for a 0.95 cm and 1.25 cm diameter sphere compared with theoretical predictions. From (Knechtel and Pitts, 1965): reprinted with permisson of the American Institude of Aeronautics and Astronautics, Inc.

charged drag, while $-e\phi_0/E = -2q_e\phi_B/m_i v_B^2$ i.e. the ratio of body potential energy to ion kinetic energy. The theory by Wyatt, (1960) under-predicts $F_{D,C}$ because it does not account for hard collisions between the satellite surface and ions (i.e. gas-surface interactions) and, as discussed previously, the theory by Chopra, (1961a) drastically over-predicts $F_{D,C}$ because it does not consider the shielding by the plasma sheath i.e. ions contribute to drag from infinity.

Figure 2.12 then investigates whether indirect charged drag has a significant effect on the total charged drag by investigating two spheres with diameters 0.95 cm and 1.25 cm [15]. Using the ratio of body diameter r_B to electron Debye length $\lambda_{D,e}$ as a proxy for sheath thickness, (Knechtel and Pitts, 1965) found the ratio of total drag (including both neutral and charged drag) to neutral drag for smaller model was consistently higher than the large model. This was attributed to the increased contribution from indirect charged drag caused by the relative increase in sheath thickness.
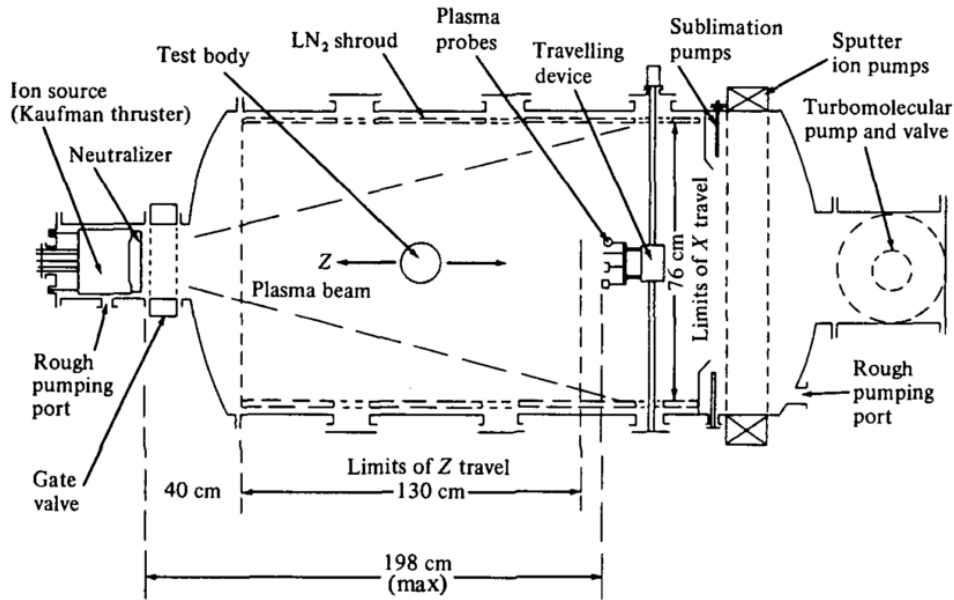
Overall, *Knechtel and Pitts, (1965) concluded that a theory for charged aerodynamics must include both direct and indirect momentum exchange mechanisms and that their appears to be conditions where the indirect drag dominates the total drag* (such as the West Ford needle experiment (Wiedemann et al., 2001)). Unfortunately, the work in (Knechtel and Pitts, 1965) was not explored further. Though it is worth noting that modern facilities, such as that described in Maldonado and Ketsdever, (2015), may be used for such measurements.

Plasma-Body Interactions Phenomena

The experimental and *in-situ* study of LEO plasma-body interaction phenomena has generally focused on the characterisation of wake structures (Hall et al., 1963; Hester and Sonin, 1969; Kiel and Gey, 1968; Troy, Maier, and Samir, 1975; Stone, 1981a; Stone, 1981b; Enloe et al., 1995). Experimental setups are generally similar to that in Knechtel and Pitts, (1965), the primary difference being the use of plasma probes on a slider in the wake. Figure 2.13 illustrates the experimental setup from Stone, (1981a) and Stone, (1981b), which is similar to that shown in Hester and Sonin, (1969) and Hall et al., (1963). Much like the approach taken in (Knechtel and Pitts, 1965), models were placed in a beam of ions and electron and the surface charge of the model is either allowed to float, or is controlled externally.
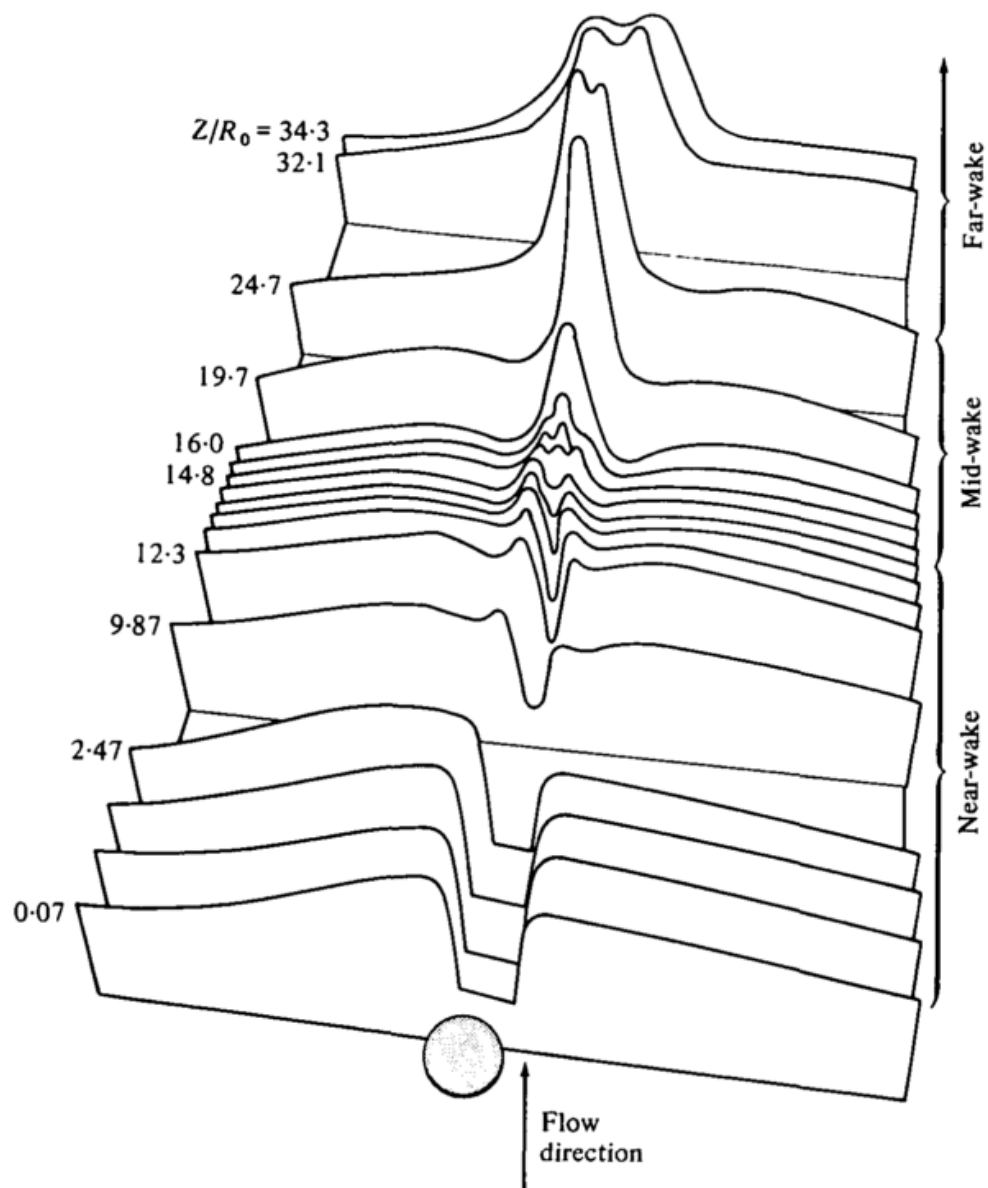
The comprehensive experimental investigation of the parametric relationship between interaction conditions and plasma-body interaction wake phenomena by Stone, (1981a) brings together many of the observations made in prior works (Hall et al., 1963; Kiel and Gey,

---

[15]Note that the available copy of (Knechtel and Pitts, 1965) is of a poor quality and we assume the "." have not correctly scanned as seen in Figure 2.12 because the maximum core size is only 5 cm.

Figure 2.13: Illustration of experimental setup in (Stone, 1981a). Reproduced from Stone, (1981a) with permission.

1968; Hester and Sonin, 1969; Troy, Maier, and Samir, 1975). In particular, Stone, (1981a) studied the structure of the ion density peak formed in the wake-core of a variety of geometries (cylinders, spheres and cubes) caused by the confluence of deflected ion beams. An example wake structure for a sphere is shown in Figure 2.14, reproduced from (Stone, 1981b). Figure 2.14 shows ion current density profiles downstream from a conducting sphere with $r_B = 3$ cm, $r_B/\lambda_{D,e} = 1$, $S_k = 16.5$ and $\Phi = -5$. An important result from Stone, (1981a) for this work, which focuses on the interaction of long (2D) objects, is that the large axial ion peak seen in mid to far-wake in Figure 2.14 was significantly reduced for the flow around cylinders. Specific relationships observed between plasma interaction phenomena and flow parameters are discussed further in Chapter 6.

Figure 2.14: Ion current slices through the wake of a 3 cm radius sphere in a flow with $r_B/\lambda_{D,e} = 1$, $S_k = 16.5$ and $\Phi = -5$. Reproduced from Stone, (1981a) with permission.

2.3.5   Scaling of Plasma-Body Interaction Phenomena

Critical to the experimental study of aerodynamics is the concept of scaling. In this context, scaling refers to the relationship between flow parameters and phenomena. Scaling parameters are generally dimensionless functions of several flow parameters, whereby two flows can be considered identical if the scaling parameters are equal (even if the primitive flow quantities are different). The theoretical basis of scaling parameters and their derivation is described in detail in Chapter 5. The purpose here is to identify the scope and limitations of current scaling parameters.

Scaling parameters listed in Table 2.1 represent a sample of those most relevant to this work. More examples of scaling parameters can be found throughout the literature that include magnetic effects, see for example Beiser and Raab, (1961) and Lacina, (1971).

Table 2.1: Scaling (similarity) parameters used in ionospheric aerodynamic and plasma-body interaction studies.
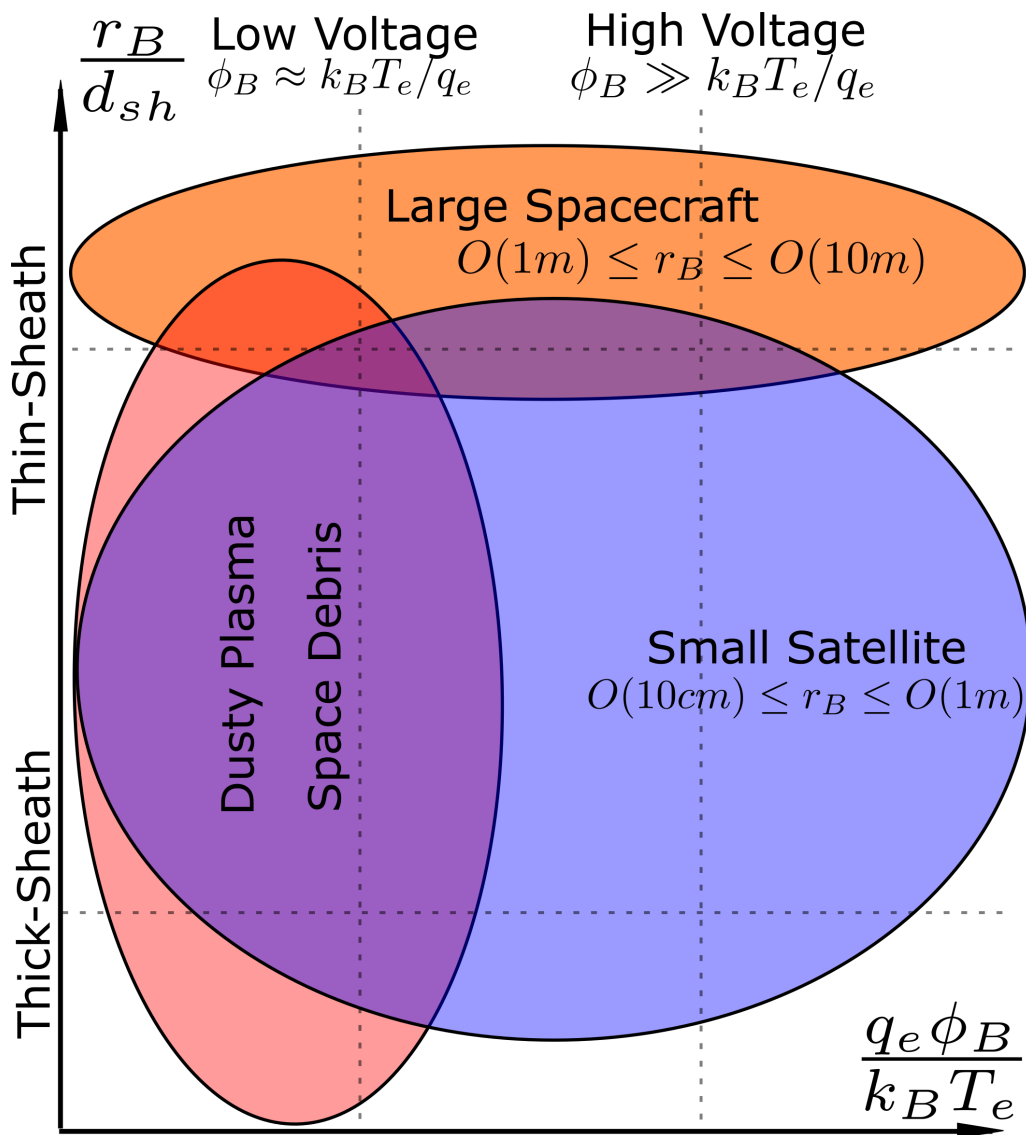
Author(s)	Scaling Parameters	Assumptions
Knechtel and Pitts, (1965)	$2q_e\phi_B/m_i v_B^2$	$T_i << T_e$
	$r_B/\lambda_{D,e}$	$q_e\phi_B \ll k_B T_e$
	$\Phi = q_e\phi_B/k_B T_e$	$\phi_\infty = 0$
Hester and Sonin, (1969)	$v_B\left(k_B T_e/m_i\right)^{-1/2}$	$T_i << T_e$
	$r_B/\lambda_{D,e}$	$q_e\phi_B \ll k_B T_e$
	$\Phi = q_e\phi_B/k_B T_e$	$\phi_\infty = 0$
	T_i/T_e	
Gurevich, Pitaevskii, and Smirnova, (1970)		
	$v_B\left(k_B T_i/m_i\right)^{-1/2}$	$\phi_B \to 0$
	$v_B\left(2k_B T_e/m_i\right)^{-1/2}$	$T_i << T_e$
	T_e/T_i	
Liu, (1975)	$r_B/\lambda_{D,e}$	$q_e\phi_B \ll k_B T_e$
	$Kn = r_B/\lambda$	
Stone, (1981a)	$v_B\left(2k_B T_e/m_i\right)^{-1/2}$	$T_i << T_e$
	$r_B/\lambda_{D,e}$	$q_e\phi_B \ll k_B T_e$
	$\Phi = q_e\phi_B/k_B T_e$	$\phi_\infty = 0$
Choinière and Gilchrist, (2007)		
	$v_B\left(k_B T_e/m_i\right)^{-1/2}$	$T_i << T_e$
	$r_B/\lambda_{D,e}$	$q_e\phi_B \ll k_B T_e$
	$\Phi = q_e(\phi_B - \phi_\infty)/k_B T_e$	
	T_i/T_e	

Table 2.1 shows the inconsistent emergence of the ion acoustic Mach number in the $T_i/T_e \ll 1$ limit, some derivations including a factor of 2, and the ion thermal velocity ratio. This is discussed further in Chapter 5. Table 2.1 demonstrates that there exists a common underlying assumption for all scaling parameters shown; that the electron Debye length ($\lambda_{D,e}$) describes the relative shielding of a body through $r_B/\lambda_{D,e}$. The electron Debye length $\lambda_{D,e}$ arises through the linearisation of Poisson's equation by applying the high-temperature assumption $q_e\phi_B \ll k_B T_e$ for cold ions ($T_e \gg T_i$). This is not necessarily true for high-voltage objects. For example, as Choinière and Gilchrist, (2007) point out, cylindrical-sheath theories for current collection break down at voltages where $\phi_B > 25 k_B T_e/q_e$ i.e. the $q_e\phi_B \ll k_B T_e$ assumption becomes invalid. In these cases, the Child-Langmuir law provides a more accurate prediction of sheath thickness d_{sh}, which can be written as,

$$d_{sh} = \frac{2}{3}\frac{2q_e}{m_i}^{1/4}\frac{|\phi_B|^{3/4}}{2\sqrt{\pi j_{\text{ion}}^{\text{sat}}}} \tag{2.24}$$

where $j_{\text{ion}}^{\text{sat}}$ is the ion saturation current. Given that LEO objects may achieve surface potentials much larger than the surrounding electron temperature (Hastings, 1995; Garrett and Whittlesey, 2000), Table 2.1 suggests there is a need for a general set of scaling parameters that links both low and high-voltage systems. To emphasis this, Figure 2.15 illustrates the relationships between LEO objects local plasma parameters, specifically the ratio of body dimension to sheath thickness r_B/d_{sh} and body potential to electron thermal energy $q_e\phi_B/k_B T_e$. $d_s h$ is approximated based on the electron Debye length $\lambda_{D,e}$ of representative ionospheric conditions for low voltage LEO objects, d_{sh} approximated for high voltage LEO objects using Eqn. 2.24. The electron Debye length $\lambda_{D,e}$ ranges between 1 mm to 10 cm in LEO based on the IRI-2012 data shown previously in Figure 2.2 (Bilitza et al., 2014). Three groups of LEO objects are shown; large satellites with characteristic dimensions ranging between 1 m to 10 m, small satellites with dimensions ranging between 10 cm to 1 m, and space debris, which range from 1 μm to 10 m. Here thick-sheaths are defined are defined where $r_B/d_{sh} \geq 1$ and thin-sheaths where $r_B/d_{sh} \leq 1$ i.e. the sheath is larger or smaller than the body dimension.

Figure 2.15 shows that, in general, large satellites are characterised by thin-sheaths. Small satellites, space debris and dusty plasmas, on the other hand, span the spectrum of shielding, ranging from thin-sheaths to thick-sheaths. Here dusty plasmas occupy a similar region to space debris, both systems electrically floating at the plasma potential, the increased density in dusty plasmas (and therefore smaller $\lambda_{D,e}$) offset by the reduction in characteristic length $O(1\mu m - 1mm)$. Meanwhile, small satellites differentiate themselves from space debris and dusty plasmas in that they may achieve high surface potentials relative to the surrounding environment as a consequence of active electrical systems.

Figure 2.15: Illustration of the relative shielding (r_B/d_{sh}) and body potential ($q_e\phi_B/k_BT_e$) of LEO objects overlaid with dusty plasmas. Note: Highlighted regions are representative only.

It is important to note that Figure 2.15 is a simplification. As has been discussed in Section 2.3.1, space debris (and dusty plasmas) may achieve large floating potentials relative to the bulk plasma environment if there exist complicating factors e.g. a population of high energy electrons (e.g. auroral electron beams), multi-body charging (Fortov et al., 2005). Figure 2.15 also does not account for the coupling of flow velocity with sheath thickness, nor the interrelationship of surface potential and sheath thickness. Instead, the purpose of Figure 2.15 is simply to highlight that small satellites and space debris share a physical region in dimensionless space with dusty plasmas and that this regions is characterised by plasma sheaths with thickness appreciable to the dimensions of the immersed object. While small satellites also occupy a high-voltage regime in Figure 2.15 compared to dusty plasmas, the overlap with space debris and small satellites suggests that a review of dusty plasma literature, specifically the forces on dusty particulates immersed in flowing plasmas (e.g. dusty plasma aerodynamics), would be useful.

2.3.6 Charged Aerodynamics in Dusty Plasmas

Thus far, discussions have focused on literature directly relating to the study of plasma-body interactions in LEO. As implied by the scaling discussion above, literature significant to ionospheric aerodynamics is not limited to these studies, but should also include physically equivalent systems in dimensionless space e.g. dusty (complex) plasmas.

Unlike ionospheric aerodynamics, the ion (plasma) drag on particulates suspended in flowing plasmas has received extensive attention. Applications are wide ranging, spanning astrophysical phenomena such as planetary rings and comet trails (Horányi, 1996) to the transport of contaminants in plasma systems (Choi and Kushner, 1994). A full review of dusty plasmas is beyond the scope of this work, such a review can be found in Fortov et al., (2005). Some aspects of dusty plasma aerodynamics literature have already been discussed, such as the application of OML (Section 2.3.3) and the control surface approach to charged aerodynamic calculations (Section 2.2.3). Others aspects, such as multi-body charging effects (Miloch, Kroll, and Block, 2010; Ikkurthi et al., 2010; Hutchinson, 2011; Ikkurthi et al., 2010) and collisional effects (Khrapak, 2008; Khrapak, Chaudhuri, and Morfill, 2009; Hutchinson and Haakonsen, 2013), while relevant to ionospheric aerodynamics, are outside the scope of this work, which focuses on the ionospheric aerodynamics of single LEO objects in the collisionless regime. The inclusion of such phenomena, along with secondary electron emission, photoelectron emission, out-gassing, etc., are discussed as future work in Section 8.3. Here, we shall focus on outlining important results from dusty plasma aerodynamic studies significant to ionospheric aerodynamics.

In general, the study of dusty plasma aerodynamic focuses on the charged drag on electrically floating spherical grains immersed in flowing plasmas (Northrop and Birmingham,

1990; Barnes et al., 1992; Khrapak et al., 2005; Khrapak, 2008; Khrapak and Morfill, 2009; Khrapak, Chaudhuri, and Morfill, 2009; Hutchinson, 2006). Drag forces are separated into direct and indirect components, also referred to as the *"collection"* and *"orbital"* forces e.g. (Khrapak, Chaudhuri, and Morfill, 2009) As with early ionospheric aerodynamic work, direct (collection) drag forces are calculated by predicting the *"collection cross-section"* using the OML method outlined in Section 2.3.3 for the case where the sheath thickness is much larger than the grain size ($r_B/d_{sh} < 1$) (Hutchinson, 2006; Hutchinson, 2005; Khrapak, Chaudhuri, and Morfill, 2009). Applying the OML impact parameter b_{OML}, analytical expressions for direct charged aerodynamics forces can be expressed in terms of the ion thermal ratio S_i (see for example (Hutchinson, 2006)). Similarly, attempts are made to analytically predict indirect (orbital) drag using the extension of Chandresekhar's equation for dynamic friction to electrodynamic systems (Hutchinson, 2006),

$$F_{D,M} = 8\pi r_B^2 n_{\infty,i} \frac{(Z_k q_e)^2 \phi_B^2}{m_i v_{t,i}^2} G\left[S_d\right] \ln\left[\Lambda\right] \qquad (2.25)$$

where $G\left[S_d\right]$ is the Chandrasekhar function,

$$G\left[S_d\right] = \frac{1}{2S_d^2} \left(\mathrm{erf}\left[S_d\right] - 2S_d e^{-S_d^2}/\sqrt{\pi}\right) \qquad (2.26)$$

In essence, Eqn 2.25 is a more general form of Eqn. 2.13 used by Chopra, (1961b) and Li, (2011), where $G(S_d)$ takes into account finite flow velocities (Eqn. 2.13 assumes $v_B > v_{t,i}$). The form taken by the Coulomb logarithm $\ln\Lambda$ is the primary source of uncertainty in Eqn. 2.25. As alluded to in Section 2.3.2, the Coulomb logarithm arises from the integral of small-angle deflections experienced by a particle between the cut-off impact parameter b_{max} and the minimum impact parameter b_{min}, i.e.

$$\ln\Lambda = \int_0^\infty db/b \approx \int_{b_{min}}^{b_{max}} \frac{db}{b} \qquad (2.27)$$

Here, the cut-offs b_{max} and b_{min} are introduced in Eqn. 2.27 as the integral diverges as $b \to 0$ (deflection angle approaches 90°) and $b \to \infty$ (deflection angle approaches 0°). The upper cut-off b_{max} of an *ion* is therefore reasonably the Debye length λ_D,

$$\lambda_D = \sqrt{\frac{\epsilon_0 k_B/q_e^2}{n_e/T_e + \sum_k^K Z_k^2 n_k/T_k}} \qquad (2.28)$$

which physically describes the sheath thickness around an ion, including both electron and ion thermal effects i.e. it is the distance outside which an ion or electron will be electrically screened from another ion.

Similarly, the lower cut-off is plausibly the impact parameter that corresponds to deflection of the test particle by 90° i.e. b_{90}. This was the argument employed by Chopra, (1961a) and Li, (2011) with the assumptions of cold ions such that $\lambda_D \to \lambda_{D,e}$. As noted by (Brundin, 1963), $\ln\Lambda = \ln[\lambda_{D,e}/b_{90}]$ does not apply to LEO objects as: a) the sheath thickness of a macroscopic object is not given by $\lambda_{D,e}$ (particular when $\phi_B \gg k_B T_e/q_e$), and b) $T_i \approx T_e$ in LEO, hence λ_D is more appropriate. A physically plausible extension of Eqn. 2.27 to finite-sized particles cited in Hutchinson, (2006) is,

$$\ln\Lambda = \frac{1}{2}\ln\left[\frac{b_{90}^2 + d_{sh}^2}{b_{90}^2 + b_{OML}^2}\right] \tag{2.29}$$

where the upper cut-off is expressed in terms of the sheath thickness d_{sh}[16] and the lower cut-off is expressed in terms of the OML collection impact parameter b_{OML} as ions with $b(v) < b_OML$ are collected by the surface of the object.
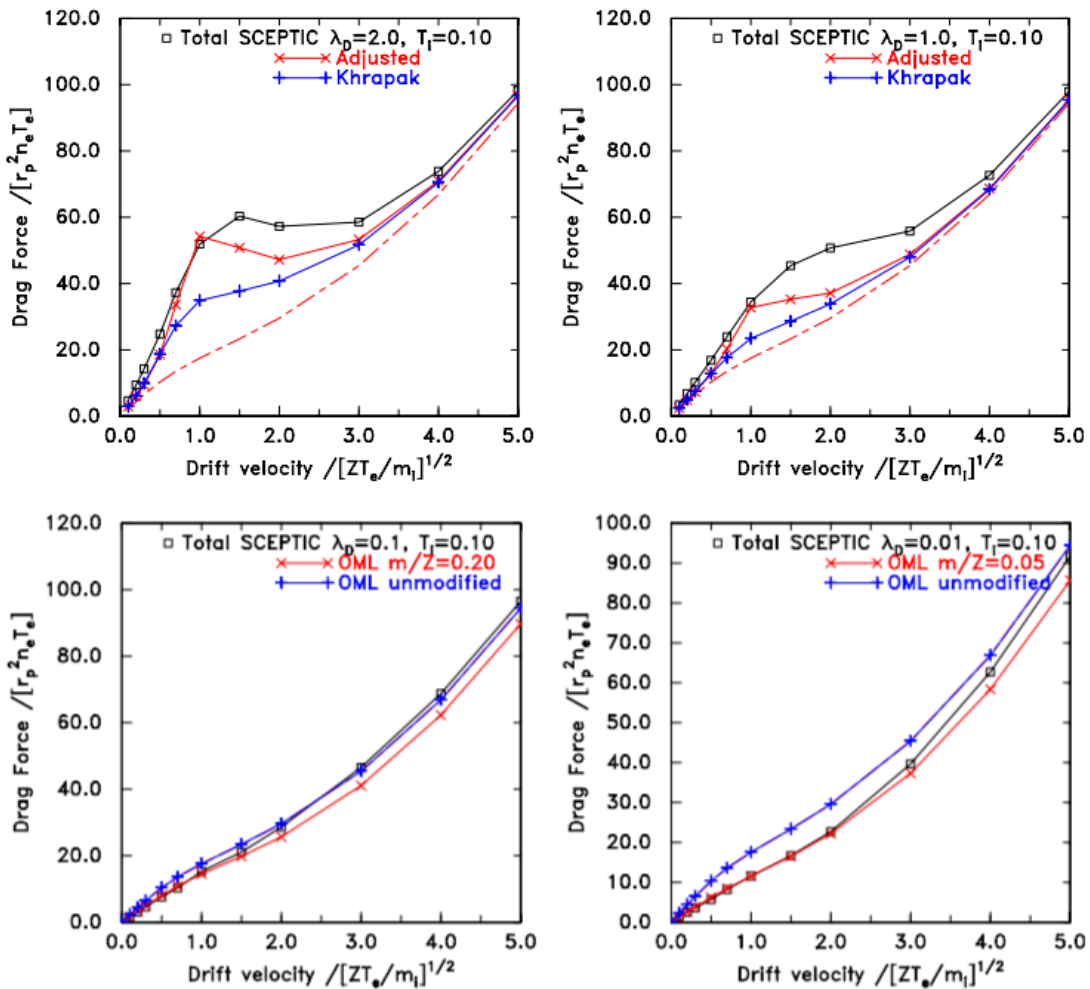
While this expression has the correct asymptotic form for large d_{sh}, it breaks down when $d_{sh} \approx b_{OML}$ (Hutchinson, 2006). Further, ambiguities remain in Eqn. 2.29, such as what to take as d_{sh} and the velocity/energy used to calculate b_{90} and b_{OML}. To avoid these ambiguities, Hutchinson, (2006) presents a series of numerical investigations for a range of particle sizes (e.g. $r_B/\lambda_{D,e}$) and flow velocities using Particle-in-Cell (PIC) simulations with rotational symmetry (the PIC method is discussed in more detail in Section 2.4 and Chapter 3).

Using the self-consistent flowfields calculated with the PIC method, Hutchinson, (2006) applied the control surface approach described in Section 2.2.3 to determine indirect and direct charge drag contributions (see also Hutchinson, (2005)). Figure 2.16 shows the variation of charged drag with ion acoustic Mach number ($M_i = v_B/\sqrt{k_B T_e/m_i}$) for $r_B/\lambda_{D,e} = 1/2$ (top left), $r_B/\lambda_{D,e} = 1$ (top right), $r_B/\lambda_{D,e} = 10$ (bottom left) and $r_B/\lambda_{D,e} = 100$ (bottom right). Here, the surface potential of the grain is floating (calculated based on the self-consistent the numerical ion and electron current) and electron temperature is $0.1eV$ i.e. the cases shown in Figure 2.16 are similar to those experienced by debris in LEO.

Based on the results in Figure 2.16, Hutchinson, (2006) concludes that the physical arguments used to derive expressions for indirect (orbital) drag do not hold for this regime. For example, for the top frames in Figure 2.16, the analytical predictions significantly under-predict the charged drag for $1 \leq M_i \leq 3$. As the sheath becomes thin ($r_B/\lambda_{D,e} > 1$, bottom frame), direct (collection) drag dominates and is predicted by OML theory (as outlined previously). However, as Figure 2.16 shows, OML predictions over-estimated direct

---

[16]Note that Hutchinson, (2006) uses $d_{sh} = \lambda_D$ which is appropriate for the floating case they consider. d_{sh} has been substituted here to reflect the uncertainty in sheath thickness for LEO objects where $\phi_B > k_B T_e/q_e$.

Figure 2.16: Comparison of numerical and analytical charge drag on a spherical grain with $r_B/\lambda_{D,e} = 1/5$ with different flow velocities. Reprinted from (Hutchinson, 2006) with permission.

charged drag forces. This over-prediction is attributed to the formation of ion absorption barriers, not accounted for in OML theory, which tend to reduce actual ion collection (Hutchinson, 2006).

The results from (Hutchinson, 2006) in Figure 2.16 demonstrate the need for a numerical approach to studying ionospheric aerodynamics, where object size is finite compared to the Debye length. Further, these results support the conclusions in previous sections that charged aerodynamic mechanisms tend to increase drag and therefore equivalent neutral drag calculations will under-predict the actual force experienced by the objects in LEO. A key difference between the above studies and ionospheric aerodynamics is that objects may not be electrically floating, but instead at artificial surface potentials relative to the surrounding space environment. Nevertheless, the above results provide a good basis for the charged aerodynamics of space debris and a starting point for investigations into ionospheric aerodynamics.

2.4   Applicability of Numerical Methods in Low Earth Orbit

A key limitation in previous ionospheric aerodynamics analyses identified in Section 2.3 has been the approximation of mesothermal plasma sheath structures using OML type assumptions. As has been identified in previous work (Stone, 1981a; Wang and Hastings, 1992b; Garrett and Whittlesey, 2000; Hastings, 1995; McMahon, Xu, and Laframboise, 2005), these assumptions do not capture the complexities of LEO plasma-body interactions. To achieve the objectives outlined in Section 1.2 requires a self-consistent numerical approach that accounts for the coupling between the body and local ion and electron distributions to provide a realistic sheath structure and, hence, prediction of charged aerodynamics. The purpose of this section is to review the applicability of numerical methods for this task.
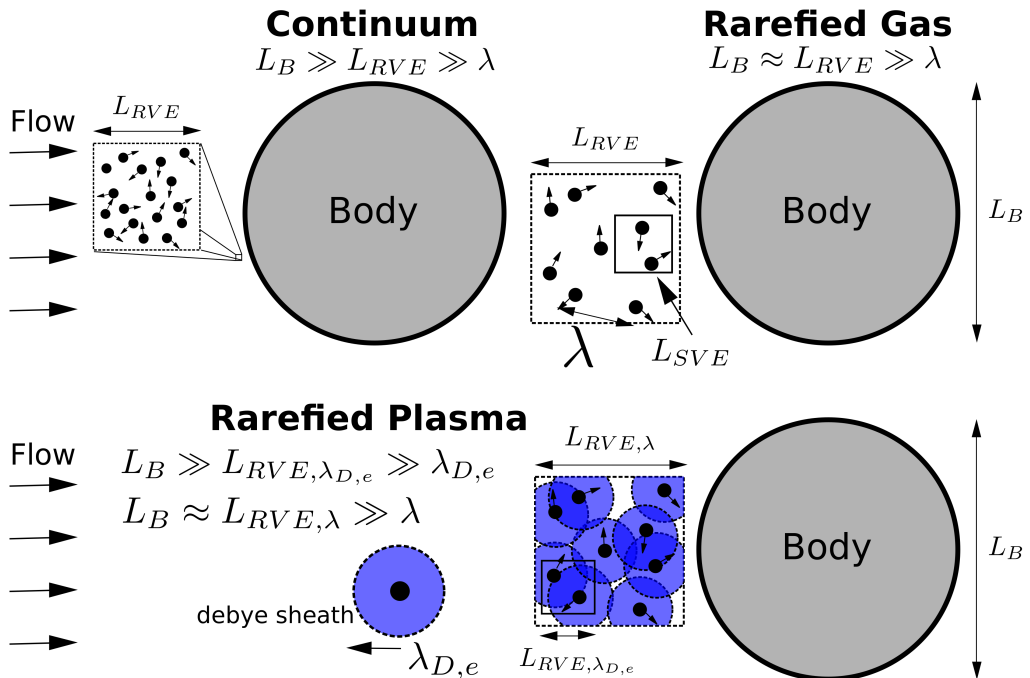
2.4.1   Continuum Verses Kinetic Methods

Numerical methods used to simulate fluid dynamics fall into one of two categories, continuum based methods and kinetic approaches. Both categories attempt to determine solutions to the Boltzmann equation, which describes the evolution of the particle distribution of a system resulting from external and internal forces (Boltzmann, 1872; Fehske, Schneider, and Weibe, 2008). Continuum approaches revolve around macroscopic properties, attempting to determine solutions to gradient based expressions that arise as moments of the Boltzmann equation. Kinetic methods take a microscopic point of view, attempting to identify solutions to the Boltzmann equation by directly simulating particles by tracing the trajectory of particles using Newtonian mechanics (hence the kinetic nomenclature). Each category has its drawback and advantages. The principle advantage of continuum based methods being speed, the cost being the physical fidelity, physical fidelity being where kinetic approaches excel at a considerable computational cost (Fehske, Schneider, and Weibe, 2008). Regardless of the type of method, it is vital to understand the limitations and applicability of a numerical method to a system.

Fundamental to continuum methods is the concept of a Representative Volume Element (RVE) - the smallest volume over which a measurement yields a value representative of the whole (Bachmat and Bear, 1987). As the REV becomes vanishingly small, a continuous function provides a good approximation of the system. The physical dimensions of the REV in a neutral gas are related to the mean distance between binary particle collisions (λ) (Bird, 1994). When λ becomes finite compared to a characteristic dimension of the system (L), the system is defined as *"rarefied"* [17]. In a rarefied system, fluctuations within the REV become significant, and the domain cannot be approximated as a continuum. The physical equivalent of the REV in a rarefied system is the Statistical Volume Element (SVE),

---
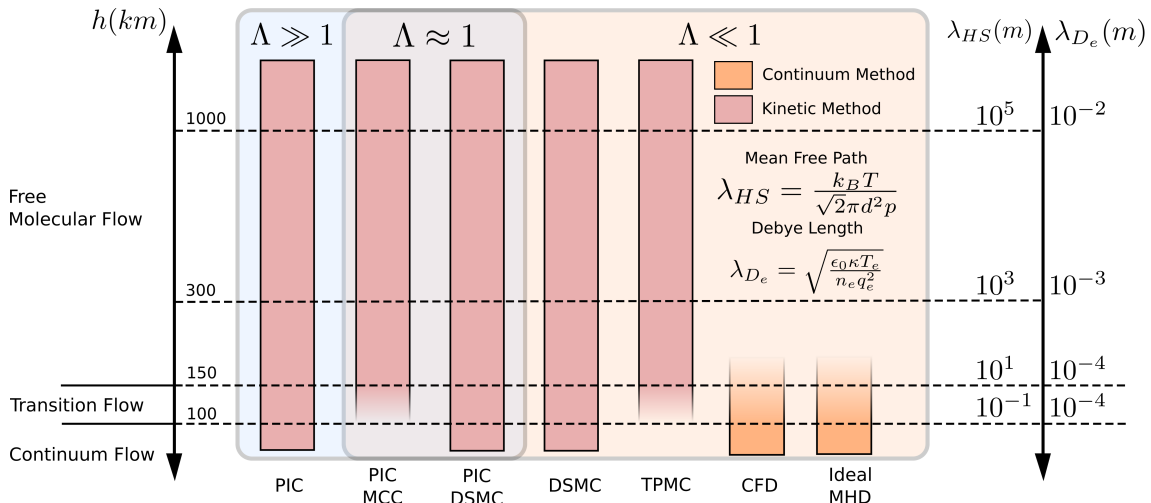
[17]The rarefaction of a system is identified by the Knudsen number $Kn = L/\lambda$

Figure 2.17: Illustration of the RVE and SVE concepts in the context of gas and plasma dynamics.

which accounts for stochastic fluctuations in volume properties. Figure 2.17 illustrates the concept of RVE and SVE in a neutral gas and its relationship to continuum and rarefied flow scales, the mean free path approaching some characteristic dimension of the system ($\lambda \to L_B$) as the flow becomes increasingly rarefied. Figure 2.17 also illustrates a fundamental difference between neutral gas dynamics and plasmas; that the flow information is not limited to travelling via particle-particle collisions in a plasma but can also travel through electromagnetic fields.

A key principle in plasma is the concept of shielding. In a plasma, shielding limits the transmission of electrical information on both a micro and macroscopic scale. The concept of the macroscopic, *"collective"* shielding of objects immersed in a plasma via the plasma sheath was introduced Chapter 1. As illustrated in Figure 2.17, the electron Debye length $\lambda_{D,e}$ defines the electrical shielding of an ion; from a computational perspective, the Debye length defines the plasma RVE. As $\lambda_{D,e}$ becomes large compared to a system length scale L, assumptions regarding quasi-neutrality assumptions that plasma continuum methods are based on breakdown e.g. Magnetohydrodynamic (MHD) methods (Fehske, Schneider, and Weibe, 2008). The *"plasma parameter"* Λ is often used to quantify the breakdown of an ideal plasma (Fehske, Schneider, and Weibe, 2008). Physically, Λ describes whether a system is dominated by binary particle collisions ($\Lambda \ll 1$) or collective interactions ($\Lambda \gg 1$) - hence its appearance previously in Eqn. 2.29.

Figure 2.18: Illustration of breakdown and applicability of computational methods to plasma-body interactions in LEO.

In general, Computational Fluid Dynamic (CFD) methods that revolve around the gradient based Navier-Stokes equations breakdown in LEO (Anderson et al., 2009). Similarly, while Magnetohydrodynamic (MHD) methods can be applied to global ionospheric models (Ridley, Deng, and To, 2006), the introduction of length scales on the order of LEO objects breaks down the underlying continuum assumption ($\lambda_{D,e} \to L_B$). As a result, kinetic methods such as the Direct Simulation Monte Carlo (DSMC) and Test Particle Monte Carlo (TPMC) are generally used to model systems dominated by binary particle collisions in LEO (Pilinski, Argrow, and Palo, 2011; White et al., 2013; Mehta, Walker, and Koller, 2014; Turansky and Argrow, 2014), while Particle-in-Cell (PIC) methods have been used extensively to study satellite charging and wake phenomena (Wang et al., 1994; Hutchinson, 2005; Fortov et al., 2005; McMahon, Xu, and Laframboise, 2005; Engwall, Eriksson, and Forest, 2006; Choinière and Gilchrist, 2007; Wang, Qiu, and Qin, 2008; Jeong, 2008; Barrie, 2006). Figure 2.18 illustrates the breakdown and applicability of these numerical methods through altitude with representative λ and $\lambda_{D,e}$ values.

A more concise argument for the use of kinetic methods is that, almost without exception, continuum approaches to plasma dynamics are limited to solutions of linearised sets of equations. Including non-linear terms in continuum methods prevents the decoupling of equations, and hence, the advantages of a closed, analytical solution are lost e.g. OML. There is little reason then not to take advantage of the more exact results from kinetic methods, the disadvantage of increased computational cost outweighed by gains in physical fidelity i.e. there is no point getting an answer quickly if that answer is wrong. For plasma-body interactions in the LEO environment, this argument is a reasonable summary of the problem.

2.4.2   Selection of Kinetic Method

Plasma kinetic methods can be divided into two basic groups, *"outside-in"* and *"inside-out"* approaches. As the names imply, the outside-in approaches trace ion trajectories through time from the undisturbed medium upstream (or *"freestream"*) of the body through regions of disturbance to either the body or a simulation boundary (Parker, 1976). The inside-out approach reverses this process, tracing ion trajectories from a point of interest within the disturbed zone back upstream to the freestream - the underling assumption being that the interaction is ergodic[18] (Parker, 1976). Outside-in methods are more appropriate in the context of plasma-body interactions, the aim being to understand the entire flow interaction compared to a small region. Outside-in methods can then be further divided into two types, *"flux-tube"* techniques and *"super-particle"* techniques.

Flux-Tube Techniques

The flux-tube technique assumes that the flux of particles in a small tube is constant. By considering two neighbouring ion trajectories and defining the cross-sectional area of the tube with an ion velocity along the trajectory, the ion density can be calculated anywhere within the flux tube. This technique was applied to early charged aerodynamics calculations by several authors (Davis and Harris, 1961; Al'Pert, Gurevich, and Pitaevskii, 1965; Call, 1969; Martin, 1974). The advantage of the flux-tube approach is that it significantly reduces the number of trajectories that must be simulated compared to super-particle techniques. The caveat is that it is *invalid if ion trajectories cross or reverse direction* making it unsuitable for LEO plasma-body interactions where ion trajectories may both cross and reverse direction.

Super-Particle Techniques

The super-particle, or weighted depositing, approaches (such as the PIC method) account for both crossing particles and time-dependent phenomena. Super-particle methods divide the plasma in a region of interest into a large number of packets or *"super-particles"* representing a significant number of real particles. The trajectories of these super-particles are determined by dividing the region of interest into spatial cells (i.e. SVE) and calculating the Lorentz forces on each super-particle by weighting particle properties to the surrounding cells to allow the calculation of electric ($\mathbf{E}$) and magnetic ($\mathbf{B}$) fields. By considering the contribution of all super-particles to each cell, macroscopic properties of the region of interest that arise from the distribution of particles can be constructed by sampling the cell

---

[18]Time reversible.

through time (steady-state) or over a large number of statistically independent simulations (time-dependent). The drawback of super-particle type approaches is the need to calculate many particle trajectories to obtain useful statistics (the method is computationally expensive).

Despite these drawbacks, super-particle methods, particularly the PIC (Parker, 1976; Wang, 1991; Wang and Hastings, 1992b; Wang and Hastings, 1992a; Hutchinson, 2005) and DSMC (Pilinski, Argrow, and Palo, 2011; White et al., 2013; Mehta, Walker, and Koller, 2014; Turansky and Argrow, 2014) methods, have proven ideal in the study of LEO environment interactions; the low number density of LEO systems combined with the increasing computational power of modern computers making kinetic simulations viable. The DSMC and PIC methods are complimentary, the DSMC method used to study collision dominated systems ($\Lambda \ll 1$) and the PIC method used to study collective dominated systems ($\Lambda \gg 1$) e.g. plasmas. This work applies the PIC method to study plasma-body interactions in LEO above 300 km where the system may be considered collisionless. The PIC and DSMC methods, and their implementation this work are discussed in detail in the following chapter.

2.5   Summary

Throughout the above discussion, various arguments have been made to support the thesis that charged aerodynamic interaction of LEO objects with the ionosphere, termed *"ionospheric aerodynamics"*, can become significant compared to neutral aerodynamics forces. Section 2.2 began by outlining background theory relating to nature of the LEO environment, the physics of plasma-interaction phenomena in LEO and an outline of charged aerodynamic mechanisms based on a control surface analysis of momentum flux.

Section 2.3 provided a comprehensive review of ionospheric aerodynamic literature. Starting with a discussion of charging in LEO, recent recent *in-situ* evidence presented by Andrés de la Fuente, (2007) in MEO was cited to demonstrated that charged aerodynamics may an appreciable effect on orbital motion. Motivated by this discussion, critical review of the seminal work by Brundin, (1963) found that conclusions that ionospheric aerodynamics forces are negligible compared to neutral aerodynamics may not be appropriate for all cases considering advances in our understanding of the LEO environment and the change in scope of LEO infrastructure. This was further highlighted by a comparison with another major work of the era, (Jastrow and Pearse, 1957), which concluded that ionospheric aerodynamic forces can be significant in LEO.

Predictions from (Jastrow and Pearse, 1957) were found to provide the most accurate prediction of experimental charged drag measurements in the work by (Knechtel and

Pitts, 1965). A brief review of scaling parameter literature however highlighted limitations, specifically the implicit application of the high-temperature (weakly-coupled) assumption $q_e\phi_B/k_B T_e$ through the *ad hoc* addition of the electron Debye length $\lambda_{D,e}$ to non-dimensionalise system length scales. As a consequence, conclusions in Knechtel and Pitts, (1965) cannot be applied to LEO objects until a general set of scaling parameters that capture both low and high voltage objects has been derived.

Nevertheless, applying these scaling parameters, the argument was made that the study of charged aerodynamics applied to dusty plasmas is physically similar to the interaction experienced by electrically floating space debris. A brief survey of dusty plasma aerodynamics literature illustrated the non-linear relationship between flow velocity and charge drag forces and highlighted the need for a numerical approach capable of capture indirect charged aerodynamic forces for finite-size objects. Similar to the scaling literature, dusty plasma aerodynamics studies have (reasonably) focused on the interaction of floating grains. With the increasing us of small spacecraft in LEO with high voltage power systems, the study of high voltage objects in LEO with thick plasma sheaths represents both an important class of system and a gap in the literature.

Hence, the principle gaps in the ionospheric aerodynamic literature are that,

1. There is no general understanding of how self-consistent plasma-body interaction phenomena affect charged aerodynamic force, including both direct and indirect components, when applied to objects in LEO.

2. There does not exist a general set of scaling parameters capable of describing the range of possible plasma-body interactions in LEO, including both high and low voltage objects.

The first gap can be addressed using high-fidelity self-consistent numerical methods, by-passing assumptions regarding sheath structure and the ambiguities present in analytical calculations of indirect charged drag. The second gap can be addressed by determining the dimensionless parameters that scale the interaction of a multi-species plasma with a body with an arbitrary surface potential. These gaps are addressed in this work by developing a physical understanding of the influence of plasma-body interaction phenomena on charged aerodynamics forces numerically using the Particle-in-Cell (PIC) method. By removing ambiguities and unnecessary complexity caused by these phenomena, this work isolates key physical phenomena and their influence to charged aerodynamics by focusing on the charged aerodynamics of a 2D, perfectly conducting cylinder (a flat plate is also considered in Chapter 5).

Chapter 3

Research Tool: The Implementation and Validation of pdFOAM

3.1 Introduction

The PIC-DSMC code, pdFOAM, has been developed here to investigate the interaction of LEO objects with the space environment (including both charged and neutral environments) and is the principle research tool used throughout this work. pdFOAM has been developed in the open-source C++ CFD library, *OpenFOAM* (Jasak, Jemcov, and Tukovic, 2007), extending the DSMC code, *dsmcFOAM*[1], to include a PIC method.

The purpose of this chapter is to detail the implementation and validation of pdFOAM. As such, this chapter is broken down as follows: Section 3.2 provides a brief introduction to kinetic theory and its relationship to the PIC and DSMC methods. Section 3.1 then describes the numerical realisation of the PIC method in pdFOAM. Section 3.4 presents two validation cases; the replication of results in Lofthouse, (2008) for the rarefied flow of Argon at Mach 10 over a cylinder, and the self consistent charging of a flat plate and cylinder in a flowing plasma compared with the PIC code, PICLas (Auweter-Kurtz et al., 2005). The first case demonstrates the ability of pdFOAM to accurately predict surface force distributions, while the second case demonstrates the ability of pdFOAM to capture the self-consistent interaction of an object immersed in a flowing plasma. Together these cases demonstrate the suitability of pdFOAM to investigate charged aerodynamics. Additional validation cases can be found in Appendix B and include studies of the one-dimensional sheath structure in a flowing plasma, replication of the two-stream instability phenomenon in Birdsall and Langdon, (1991), the one-dimensional oscillation of an electron about an ion, and a study of collision rates.

---

[1] See Scanlon et al., (2010) for a description of the implementation and validation of dsmcFOAM

3.2 Kinetic Theory and Super-Particle Methods

This section presents an overview of the relationship between kinetic theory and the PIC and DSMC methods. While this work is primarily focused on the collisionless plasma regions described by the PIC method, a discussion of the DSMC method is included for two reasons. The first is that the gas-surface interactions model used throughout this work was primarily developed within DSMC methods and all collisions are handled using the DSMC portion of pdFOAM. The second is that an avenue for future study is considering regimes or situations where particle-particle collisions are non-negligible e.g. below 300 km, out-gassing structures or objects employing mass based thrusters (either gas or ion).

3.2.1 The Vlasov-Maxwell Equations

The near-Earth space environment is a collection of positive ions, negative electrons, and neutral atoms and molecules. To describe this system, let us define the phase space distribution function f of particles of species k within the volume element $dx_1 dx_2 dx_3$ as $f_k(\mathbf{x}, \mathbf{c}_\alpha, t)$, where $\mathbf{c}_k$ and $\mathbf{x}$ are the particle velocity and position respectively at time t. Given a particular f_k, macroscopic mean properties arise from the moments of f_k e.g. number density (n_k) and velocity (v_k) Feller, (1940),

$$n_k = \int f_k d\mathbf{c}, \qquad \mathbf{v}_k = \frac{1}{n_k} \int \mathbf{c}_k f_k d\mathbf{c} \tag{3.1}$$

At its most general, the evolution of f_k through t is described by the Boltzmann equation (Boltzmann, 1872),

$$\frac{\partial f_k}{\partial t} + \mathbf{c}_k \cdot \nabla_x f_k + \frac{\mathbf{F}_k}{m_k} \cdot \nabla_c f_k = \left(\frac{\partial f_k}{\partial t} \right)_{coll} \tag{3.2}$$

From left to right, the terms on the LHS of Eqn. 3.2 describe: the rate of change of f_k with time; the diffusion of f_k; and the influence of external forces $\mathbf{F}_k$ acting on f_k. The RHS of Eqn. 3.2 describes the rate of change of f_α as a result of particle collisions.

In a plasma, Eqn. 3.2 describes the interaction of particles of mass m_k and charge q_k through their mutual electric ($\mathbf{E}$) and magnetic ($\mathbf{B}$) fields via the Lorentz force ($\mathbf{F_k}$) (Boltzmann, 1872; Fehske, Schneider, and Weibe, 2008),

$$\mathbf{F}_k = q_k \left(\mathbf{E}(\mathbf{x}, t) + \mathbf{c}_k \times \mathbf{B}_k(\mathbf{x}, t) \right) \tag{3.3}$$

In the context of LEO plasma-body interactions, the interaction may be considered electrostatic and unmagnetised (Whipple, 1981; Stone, 1981a; Wang, Qiu, and Qin, 2008;

Lapenta, 2011). Under these assumptions, Maxwell's equations reduce to Poisson's equation for the electric potential ϕ,

$$\mathbf{E} = -\nabla\phi, \qquad \nabla^2\phi = -\frac{\rho_c}{\epsilon_0} \tag{3.4}$$

where ϵ_0 is the permittivity of free space and ρ_c is the macroscopic space-charge density,

$$\rho_c \quad = \sum_k q_k \int f_k d\mathbf{c}_k = \sum_k q_k n_k \tag{3.5}$$

Determining the general particle distribution of a system with multiple reacting species in the presence of external and self-consistent forces is the challenge posed by kinetic theory. Direct solutions of the Boltzmann equation are intractable for practical systems. PIC (Birdsall and Langdon, 1991) and DSMC (Bird, 1994) methods avoid solving the Boltzmann equation directly by simulating the microscopic interactions of super-particles.

3.2.2 The Direct Simulation Monte Carlo Method

The DSMC method describes collision dominated systems ($\Lambda \ll 1$) i.e. systems where the collision kernel $(\partial f_k/\partial t)_{coll}$ drives the evolution of f_k (Bird, 1994). Applying the *"molecular chaos"* assumption[2], the basis of the DSMC method is the *ad hoc* assumption that particle motion and collisions are decoupled over the small time-step Δt (Bird, 1994). During a DSMC *"push"* step, simulated macro-particles are moved ballistically over Δt. During the collision step, Markov processes, implied by the molecular chaos assumption, describe the interaction of super-particles according to kinetic theory (Fehske, Schneider, and Weibe, 2008; Wagner, 1992). Phenomenological collision models[3] approximate the physical interaction to varying degrees of fidelity (see Hard Sphere (HS), Variable Hard Sphere (VHS), and Variable Soft Sphere (VSS) described in (Bird, 1994)). Macroscopic properties are then sampled directly from the particle distribution, as in Eqn. 3.1, by applying time-averaging or ensemble-averaging for steady-state or transient systems respectively.

A common feature in most DSMC collision procedures involves the sorting of macro-particles into *"collision cells"* (Scanlon et al., 2010; Bird, 2013), the exception being gridless DSMC methods (Olson and Christlieb, 2008; Pfeiffer, Mirza, and Fasoulas, 2013). In collision cell approaches, candidate collision pairs are selected from a computational cell based on collision rates described by kinetic theory (Bird, 1994). Collision pairs then undergo an acceptance-rejection test e.g. the No-Time-Counter (NTC) method (Bird, 1994). The basis of the NTC method lies in determining the differential scattering cross-section (σ)

---

[2]The molecular chaos assumption is that *"velocities of colliding particles are uncorrelated, and independent of position"* (Maxwell, 1867)
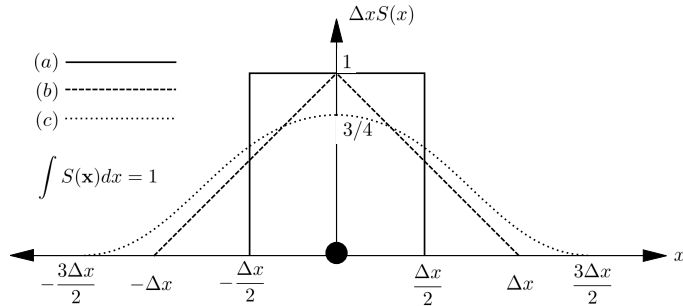
[3]Semi-empirical models with physical arguments designed to reproduce macroscopic properties from microscopic interactions.

between particles p and q i.e. σ_{pq}. Calculation of σ_{pq} is through a phenomenological model, where semi-empirical coefficients are tuned to match collision rates and viscosity coefficients at a reference temperature $((T_{ref})_{pq})$. A list of VHS and VSS coefficients may be found in Bird, (2013).

3.2.3 The Particle-in-Cell Method

The PIC method determines solutions to the Vlasov-Maxwell system where the contribution of collisions in Eqn. 3.2 are neglected i.e. collective dominated systems ($\Lambda \gg 1$). The numerical realisation of the PIC method is similar to the DSMC method. Super-particle trajectories are traced through time using appropriate integration techniques e.g. the Leapfrog or Boris methods (Hockney and Eastwood, 1988). ρ_c is calculated by weighting the contribution of macro-particles p to a computational mesh with nodes n according to some shaping function S (Birdsall and Langdon, 1991) and *vice versa*. The processes of determining ρ_c and $\mathbf{E}$ at a super-particle are referred to as the *"assignment"* and *"interpolation"* steps respectively. Figure 3.1 illustrates the concept of charge assignment in one dimension, higher order shaping functions available to reduce numerical fluctuations in ρ_c as particles traverse cells (Birdsall and Langdon, 1991).

$$\rho_c(n) = \sum_p q_p S(\mathbf{x}_n - \mathbf{x}_p) \tag{3.6}$$

Figure 3.1: Shaping functions for charge and fields: (a) nearest grid point; (b) linear; (c) second-order.
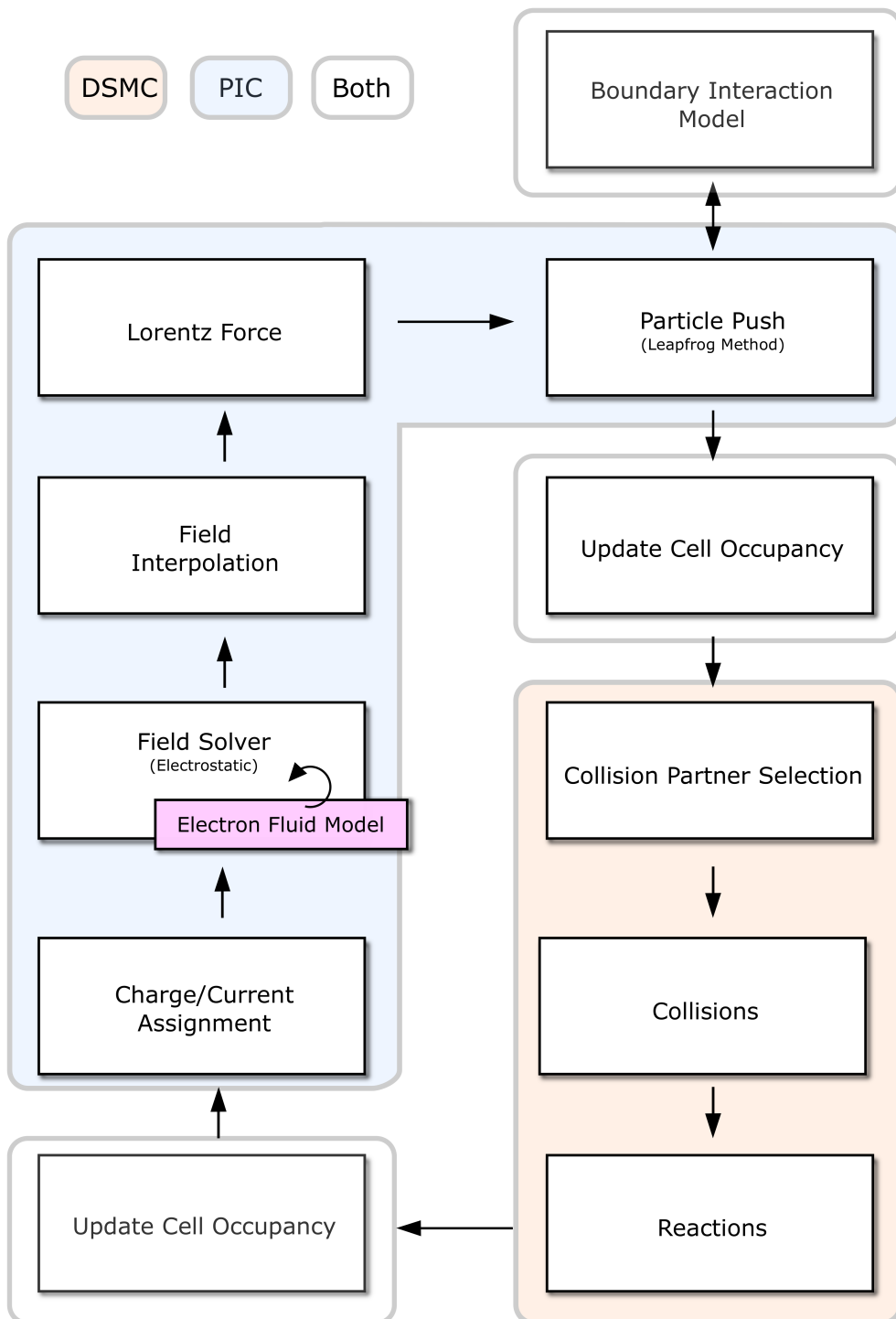
While a variety of approaches have been developed to capture increasingly higher order shaping effects with reduced computational cost necessary for electromagnetic and relativistic PIC codes (see for example Sentoku and Kemp, (2008), Vay and Godfrey, (2014), and Belyaev, (2015)), the comprehensive review of numerical issues inherent in coupling particle and field domains through S by Birdsall and Langdon, (1991) remains the relevant

treatise on the subject for electrostatic PIC codes, such as that used in this work. The key points are: the shaping functions must conserve charge between assignment and interpolation steps; and the same shaping function should be applied between the assignment and interpolation steps to avoid numerical self-forcing (self-forcing being a purely numerical force on a particle caused by its own charge (Birdsall and Langdon, 1991)).

3.3 Overview of pdFOAM

pdFOAM supports both fully-kinetic (FK) and hybrid-fluid kinetic (HK) simulations. FK simulations model neutral, ion, and electron particle distributions directly; HK simulations approximate the electron particle distribution by a non-linear Boltzmann electron fluid (EF) (see Section 3.3.1). The advantage of the HK approach is a significant reduction in computational expense compared to FK simulations, but at the expense of physical fidelity i.e. electron kinetic phenomena. Both HK and FK simulations begin by solving for $\mathbf{E}$ given an initial particle distribution and use this field to set up the Leapfrog method, a time-centered particle integration technique (Birdsall and Langdon, 1991). At this point the computational cycle outlined in Figure 3.2 begins (the italicised processes are those that have been developed and implemented here):

1. Particles are pushed to a new position and boundary models are applied. The particle tracking algorithm is described in Macpherson, Niklas, and Weller, (2009).

2. Cell occupancy is updated to include boundary interactions e.g. particle injection, deletion, reaction.

3. Collision partners are selected. *To reconcile disparate spatial discretisation requirements of the PIC and DSMC methods pdFOAM implements a new collision selection procedure developed here (the Transient Conglomerated Cell (TCC) method, see Section 3.3.1).*

4. Collision pairs are collided. pdFOAM supports HS, VHS and VSS phenomenological collision models, including reactions, with the Larsen-Borgnakke and Quantum-Kinetic (Q-K) energy redistribution models (Scanlon et al., 2015).

5. Particle cell occupancy is updated to account for the creation/annihilation of reacting particles.

6. *Charge is weighted to the mesh domain to determine ρ_c. pdFOAM supports nearest volume (NV) and Composite Linear Volume (CLV) shaping functions (see Section 3.3.1).*

Figure 3.2: Standard computational cycle in pdFOAM with DSMC, PIC and PIC-DSMC methods colored

7. *Poisson's equation is solved using a preconditioned conjugate gradient (PCG) Finite Volume Method (FVM) supplied in OpenFOAM (Jasak, Jemcov, and Tukovic, 2007). Newton's method is used in HK simulations to solve the non-linear contribution of the Boltzmann electron fluid (see Section 3.3.1).*

8. *Fields are weighted to particles using the inverse shaping function of step 6.*

The above process is repeated until the system either achieves a *steady-state*, is identified as *transient*, or reaches a predefined end condition e.g. end time. *In this work, we define steady-state as when the total number of particles, charge in the system, and the linear kinetic and potential energy of the system achieves a dynamic equilibrium.* Simulations are performed in two stages: a HK simulation to quickly reach a steady-state, followed by an FK simulation that uses the HK electron fluid to initialise the electron distribution. This allows consideration of the effect of electron kinetics on plasma-body interactions as a perturbation instead of requiring FK simulations started from a homogeneous solution.

3.3.1 Numerical Methods in pdFOAM

Composite Linear Volume Method

The composite linear volume method applies multiple linear weighting functions to transform from particle to cell nodes and then cell nodes to cell volumes in logical space (l). The physical to logical space transformation uses the tri-linear interpolation method described in (Sadarjoen et al., 1994). The concept of performing particle assignment and interpolation in PIC codes has been successfully demonstrated by the CPIC (Delzanno et al., 2013) and DEMOCRITUS (Lapenta, 2011) codes.

The charge assignment step determines the inverse linear volume weighting centered at the particle position to cell verticies. The charge is then distributed to surrounding cell verticies and weighted to the surrounding volumes. After solving for the field distribution, fields are interpolated back to particle positions using the inverse the the charge assignment process e.g given the cell occupied by the particle, the surrounding cell nodes gather volume weighted fractions of surrounding field quantities and then interpolate these back onto the particle using a linear volume gather (summation instead of decomposition). Figure 3.3 illustrates the charge assignment and field interpolation processes with the linear weighting function shown in Eqn. 3.7,

$$\rho_{c_n}(i,j) = \frac{q_i}{A_c}\frac{(\Delta x - x)(\Delta y - y)}{\Delta x \Delta y}, \quad \rho_{c_n}(i+1,j) = \frac{q_i}{A_c}\frac{x(\Delta y - y)}{\Delta x \Delta y}$$
$$\rho_{c_n}(i,j+1) = \frac{q_i}{A_c}\frac{(\Delta x - x)y}{\Delta x \Delta y}, \qquad \rho_{c_n}(i+1,j+1) = \frac{q_i}{A_c}\frac{xy}{\Delta x \Delta y} \tag{3.7}$$

The advantage of the composite linear volume method is that it allows the use of cell-centered numerical methods without needing to employ co-located or staggered meshes, while also facilitating parallelisation in OpenFOAM. The composite linear volume method fills the niche for cell-centered data on a single grid at the expense of an increased computation cost compared to the co-located grid approach - OpenFOAM does not currently support co-located or staggered grids. As an alternative, pdFOAM also includes a nearest volume approach were charge is assumed to be uniformly distributed within the cell occupied by the particle - equivalent to a Nearest-Grid-Point (NGP) approach. At the expense of physical fidelity, the nearest volume offers a significantly faster alternative to the CLV method in pdFOAM.

To illustrate the effect of the composite linear volume and nearest volume shaping functions on particle motion (also know as *"aliasing"*), Figure 3.4 plots the oscillation of an electron about a stationary ion in position-velocity phase space compared against theory predicted by pdFOAM and compared against theory. Details on theory and numerical setup can be found in Appendix B. Motion in X demonstrates that neither method adds a significant amount of numerical energy over the simulated period i.e. the oscillation amplitude remaining constant. Motion in u_x illustrates the aliasing effect of the nearest volume method, the x-axis acceleration a_x constant throughout each cell and 0 in the central cell. Comparatively, the CLV method provides a significantly better approximation of the electron's motion.
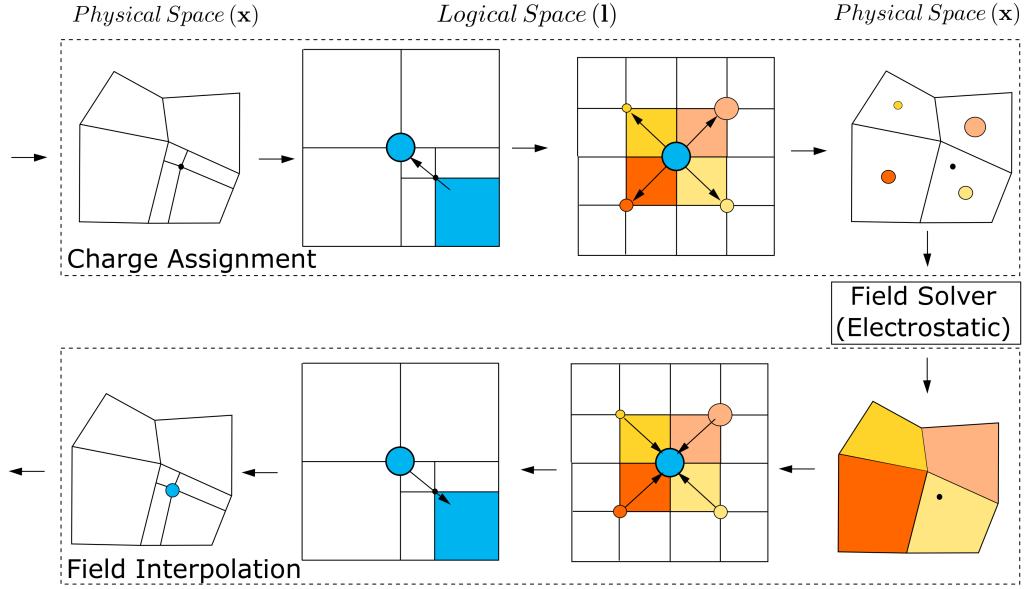
It should be noted that Figure 3.4 shows the best case where the ion is at a cell center. Disagreements between the nearest volume method and theory increase when the ion is not at a cell center (the composite linear volume method still provides a good match with theory). It should also be noted that PIC methods are generally not used to study single particle motion but instead plasma collective phenomena. The main purpose of Figure 3.4 is to demonstrate that the shaping functions do not add numerical energy to the system, which they do not.

Non-Linear Boltzmann Electron Fluid Model
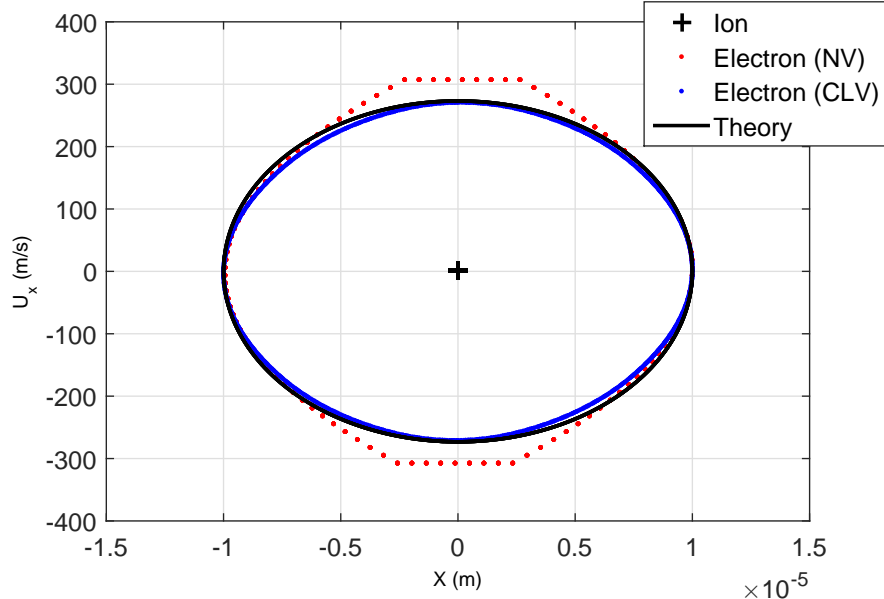
Directly simulating electrons comes at a significant computational cost. To maintain numerical stability, Δt must be smaller than the fastest plasma frequency ω_p i.e. $\Delta t < \omega$ (Fehske, Schneider, and Weibe, 2008) [4]. In a similar manner, the stability requirements of the Leapfrog method (see Hockney and Eastwood, (1988)) require a spatial discretisation (Δx) of $\Delta x < \lambda_{D,e}/2$. As a result, the numerical requirements of FK-PIC simulations are limited by electron length and time scales i.e. the electron Debye length $\lambda_{D,e}$ and plasma

---

[4] $\Delta t < 0.01\omega$ is often used in FK-PIC simulations to avoid numerical heating of the electron distribution (Birdsall and Langdon, 1991).

Physical Space (**x**)   *Logical Space* (**l**)   *Physical Space* (**x**)

Charge Assignment

Field Solver
(Electrostatic)

Field Interpolation

Figure 3.3: Illustration of Composite Linear Volume (CLV) method applied in charge assignment and field interpolation steps. Only the process for a single node/particle is shown for brevity.

Figure 3.4: Theoretical 1D electron oscillation about stationary ion compared to observed oscillation in pdFOAM for the Composite Linear Volume (CLV) and Nearest Volume (NV) methods in position-velocity phase-space.

frequency $\omega_{p,e}$. Hence, the numerical cost of PIC simulations can be significantly reduced if the electron distribution can be approximated by a fluid i.e. a Hybrid Fluid-Kinetic PIC simulations (HK-PIC). HK-PIC simulations benefit from an increase in allowable time-step, cell-size and reduction in simulated particles (no electrons) at the expense of solving an extra set of equations to capture the electron fluid. In most cases, the benefits of HK-PIC simulations outweigh the cost of solving for the electron fluid distribution.

The approach taken here for HK-PIC simulations is to assume that the electron distribution function can be described by an isothermal, currentless (electrostatic), unmagnetised ($\mathbf{B} = 0$), inertia-less ($m_e/m_i \rightarrow 0$) electron fluid; this approach has been used successfully for the study of plasma-body interaction in a charging/arcing context (Wang and Hastings, 1992b) and in the analysis of plasma thrusters (Boerner and Boyd, 2007). Under these assumptions, magnetohydrodynamic equations of continuity, momentum, and energy reduce to (Boerner and Boyd, 2007),

$$n_e = n_{e,\infty}\exp\left[\frac{q_e\phi(\mathbf{x}) - \phi_\infty}{k_B T_e}\right] \tag{3.8}$$

where k_B is the Boltzmann constant, T_e is the electron temperature, $n_{e,\infty}$ is the freestream electron number density and ϕ_∞ is the freestream potential (assuming a quasi-neutral freestream $\phi_\infty \approx 0$).

Poisson's equation then becomes a non-linear function of potential,
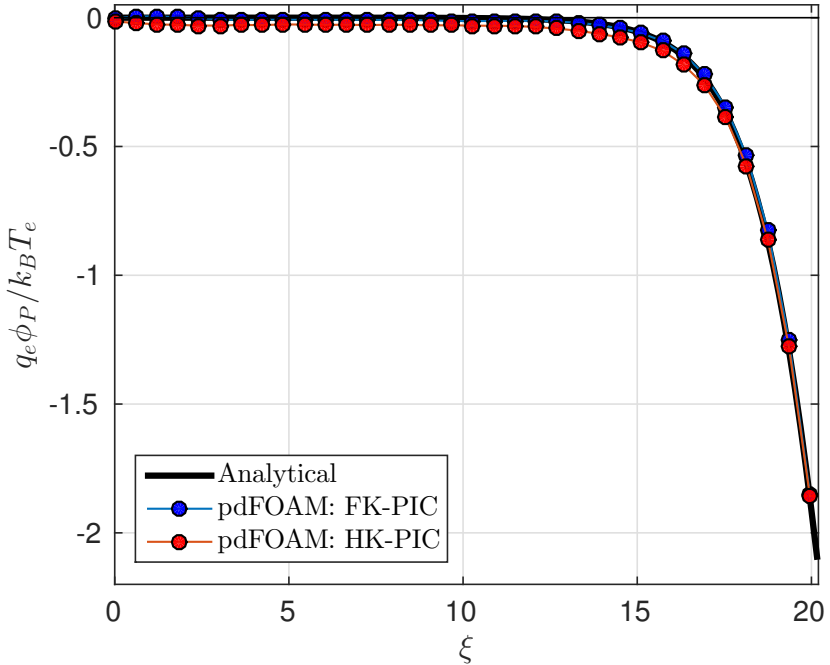
$$\epsilon_0\nabla^2\phi - q_e n_{e,\infty}\exp\left[\frac{q_e\phi}{k_B T_e}\right] = -q_i n_i \tag{3.9}$$

Applying Newton's method, solutions to Eqn. 3.9 become an iterative process in t,

$$\left(\epsilon_0\nabla^2 - \frac{\epsilon_0}{\lambda_{D,e}^2}\exp\left[\frac{q_e\phi^{(t)}}{k_B T_e}\right]\right)\phi^{(t+1)} = -q_i n_i + \left(q_e n_{e,\infty} - \frac{1}{\lambda_{D,e}^2}\phi^{(t)}\right)\exp\left[\frac{q_e\phi^{(t)}}{k_B T_e}\right] \tag{3.10}$$

Note that the electron Debye length $\lambda_{D,e}$ appears in Eqn. 3.10 from the derivative of the exponential term, not from the linearisation assumption seen previously - the importance of this is seen in Chapter 5.

Hockney and Eastwood, (1988) demonstrated that the convergence of Eqn. 3.10 is quadratic provided the initial guess is sufficiently near the solution; this is the case for time-stepping simulations, such as the PIC method, where the initial solution t at time-step n is taken as the converged solution at $n - 1$.
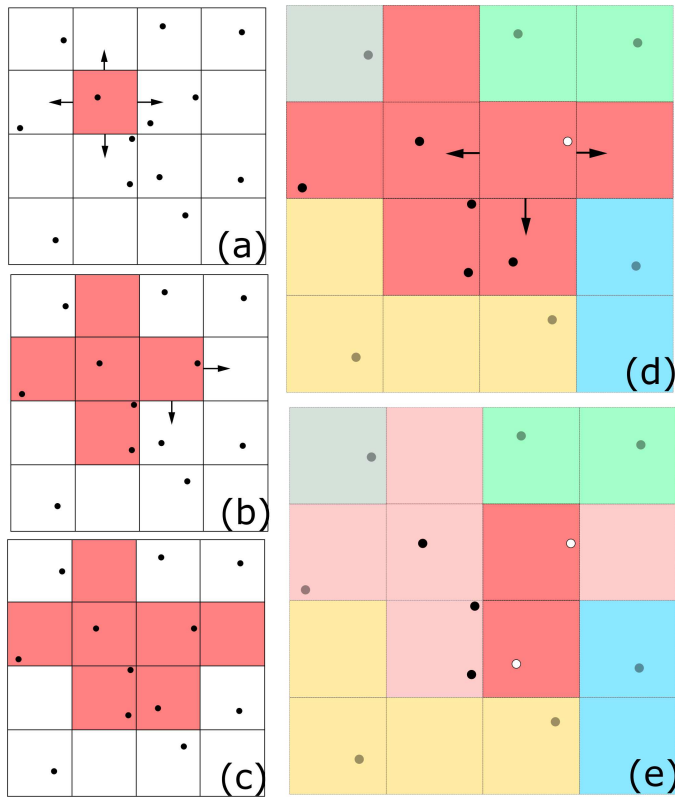
Figure 3.5: Comparison of numerical sheath structure, calculated by FK-PIC and HK-PIC simulations in pdFOAM, and analytical sheath structure, calculated using the method described in Appendix appdendixA. Ion acoustic Mach number M_i is 2.1.

Figure 3.5 is reproduced from Appendix B and compares the one-dimensional sheath structure formed near a flat plate in a flowing plasma predicted by HK-PIC and FK-PIC simulations against theory. Details can be found in Appendix B. Figure 3.5 demonstrates that the structure of FK-PIC and HK-PIC simulations closely match theoretical predictions, the FK-PIC simulation exhibiting a source sheath structure caused by the refluxing electrons (electrons repelled by the sheath) meeting the inflowing electrons at the boundary i.e. the source sheath is a numerical boundary phenomena. A detailed investigation of this phenomenon can be found in Birdsall and Langdon, (1991).

Transient Conglomerated Cell Method

The numerical requirements of DSMC and PIC methods differ. While both approaches are stochastic as a result of their particle nature, the acceptance/rejection scheme in the DSMC collision step applies a further stochastic method compared to the PIC method. DSMC best practice is to maintain a constant number of particles per cell throughout the flowfield to avoid numerically biasing a particular region (Bird, 2013). Furthermore, the size of collision cells should not exceed $\lambda/3$ (Bird, 2013). PIC cells must satisfy the requirement
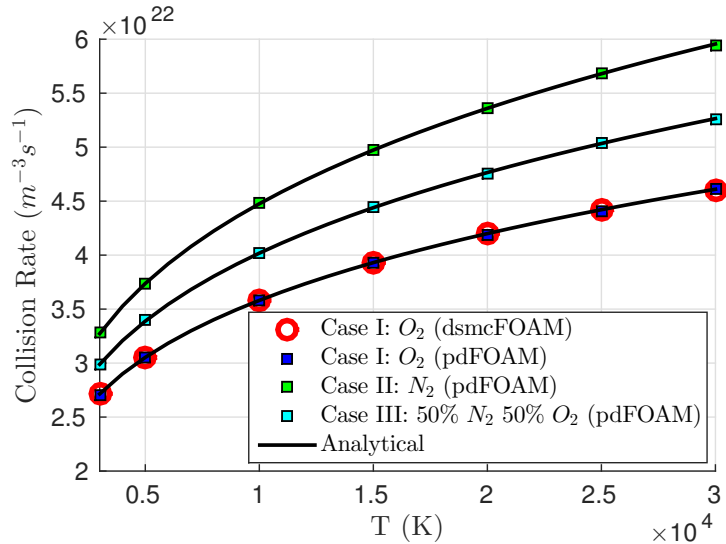
Figure 3.6: TCC collision cell procedure: (a) Collision cell construction begins, (b) Cells with common faces are added to collision cell, (c) Cells are iteratively added until construction requirements are met, (d) Cells surrounding candidate are searched (e) Closest cell containing collision candidates is selected and a partner randomly chosen.

$\Delta x < \lambda_{D,e}/2$ in order for the leapfrog method to remain stable (Hockney and Eastwood, 1988). Hence, in general, PIC requirements limit PIC-DSMC simulations. As a result, PIC-DSMC simulations using a single mesh require orders of magnitude more particles than pure DSMC simulations to satisfy both the particles per cell and $\Delta x < \lambda_{D,e}/2$ requirements.

Several approaches have been proposed to reconcile the numerical requirements of the PIC and DSMC method (Pfeiffer, Mirza, and Fasoulas, 2013; Kolobov and Arslanbekov, 2012). The Transient Conglomerated Cell (TCC) method developed and implemented here in pdFOAM has been adapted from the approach taken in the DSMC codes DS2V/3V (Bird, 2013). DS2/3V uses a fine background mesh to construct collision cells from a conglomeration of sub-cells about randomly scattered node points. Similarly, the TCC method constructs collision cells from the PIC mesh based on the instantaneous particle distribution at each time-step. Cell clusters are built by iterating out through cells with common face indices as illustrated in Figure 3.6 (a) - (c).

The TCC method promotes nearest neighbour collisions by preferentially searching the collision cell decomposition to minimise mean collision distance. Figure 3.6 (d) and (e) illustrates the TCC collision partner selection procedure. First, a collision candidate p is selected randomly from the collision cell. Next, adjacent collision sub-cells are iteratively searched to find the nearest cell containing particles. A collision candidate q is then randomly selected from this sub-cell.

As only an integer number of collisions may occur during a time-step, the remainder is isotropically distributed over the collision cell's sub-cells and carried forward to the next time-step. By linking the collision remainder to the mesh instead of collision cell index, the random motion of the collision cell index compared to physical location does not cause the transport of collisions to non-physical locations.

Figure 3.7: Comparison of numerical and theoretical collision rates using the TCC method.

Figure 3.7 is reproduced from Appendix B and compares theoretical collision rates for three gases with increasing temperature calculated using the standard collision selection procedure in dsmcFOAM and the TCC method implemented here in pdFOAM. Figure 3.7 demonstrates the ability of the TCC method to correctly reproduced analytical collision rates in both single species and gas mixtures. The advantages of the TCC method are detailed further in Section 3.4.

3.3.2   Guidelines for PIC simulations in pdFOAM

Birdsall and Langdon, (1991) and Hockney and Eastwood, (1988) presented extensive studies into numerical effects caused by the discretization of a plasma into super-particles (see also Melzani et al., (2013). These studies include the stability of the particle movers, aliasing effects caused by particle shaping functions, and the effect of statistical fluctuations caused by an insufficient number of simulation particles. To minimise numerical effects the following general rules guide PIC simulations presented in this work:

1. The time-step Δt must be smaller than the time-scales scales of studied phenomena e.g. the electron plasma frequency ω_{pe} that describes the oscillation frequency of electrons in FK-PIC simulations.

2. The time-step Δt must be sufficiently small such that particles do not jump multiple cells i.e. $\Delta t < \Delta x / v_i$

3. Δx must both resolve length scales of studied phenomena and satisfy the stability requirement $\Delta x < \lambda_{D,e}/2$.

4. If thermal effects are considered, ensure there is a sufficient representation of high energy species by demonstrating the independence of results on super-particle density.

5. The plasma should remain collisionless i.e. if collision rates become significant ion-neutral collisions must be modelled with the DSMC portion of the code.

6. A sufficient number of particles per cell should be maintained to minimise numerical fluctuations. This should be tested case by case by demonstrating the independence of results the on the number of particles per cell (achieved by varying the number of real particles represented by each simulated particle).

7. Demonstrate independence of numerical solution from mesh topology.
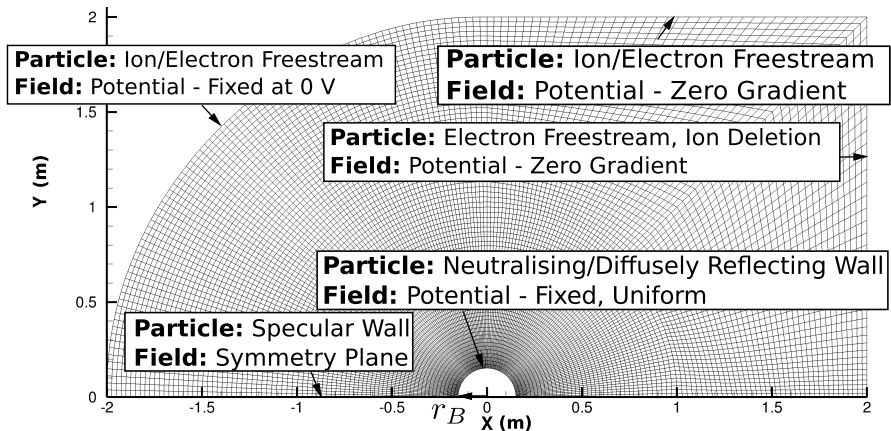
All simulations presented in this work assume a steady-state solution. Steady-state is defined as having been reached when the number of super-particles, charge in the system and linear kinetic energy of the system reach some dynamic equilibrium. In the case of self-consistent charging simulations, floating potential is also used to identify when dynamic equilibrium (steady-state) has been achieved.

3.4   Validation of pdFOAM

Section 3.1 described the implementation of the PIC method in pdFOAM and presented the validation of several novel numerical methods implemented here. This Section further develops confidence in the ability of pdFOAM to model the interaction of LEO objects with the space environment with two studies that verify the ensemble implementation of the PIC and DSMC methods in pdFOAM:

1. The Mach 10 $Kn = 0.25$ cylinder case from Lofthouse, Boyd, and Wright, (2007) is repeated and compared with data from MONACO (Dietrich and Boyd, 1996), an established DSMC code.

2. The self-consistent charging of a flat plate and a cylinder in a flowing, collisionless, unmagnetised plasma is compared to theoretical predictions of floating potential at different ion drift velocities.

3.4.1   Simulation Topology

Figure 3.8: Domain topology and boundary conditions. Every 10th grid node displayed for clarity.

The following simulations are 2D and use a common cylinder topology with body radius r_B as illustrated in Figure 3.8. Figure 3.8 lists particle and field boundary conditions, while case specific boundary conditions are described in the appropriate sections. Mesh density is based on the mean plasma conditions experienced by the Earth Observation System (EOS) satellite during a period of mean sunspot activity (Hastings, 1995); these conditions are listed in more detail in Section 3.4.3.

3.4.2 Hypersonic Cylinder

Lofthouse, Boyd, and Wright, (2007) investigated the breakdown of the continuum assumption on the aerothermodynamics of a hypersonic cylinder in a reacting flow. They investigated a Mach (M) 10 flow of Argon (Ar) over a two-dimensional, 12 in (0.3048 m) diameter cylinder with a fixed surface temperature of 500 K for a variety of Kn by varying the freestream number density (n_∞). The purpose of this validation case is to demonstrate that pdFOAM retains the ability of its underlying DSMC capability to predict rarefied gas dynamics and in particular gas-surface interactions. While the nature of these gas-surface interactions will likely differ from plasma-surface interactions, they serve as an appropriate approximation in the context of this work. The assumption being that, upon colliding with the object surface they are neutralised and re-emitted diffusely (as a normal neutral gas-surface interaction). Additional plasma effects may include the secondary emission of electrons (ion collisions cause the secondary ejection of electrons from the surface) and sputtering (ion collisions cause the secondary emission of surface atoms/molecules). As outlined in Chapter 1, these phenomena are not considered in this work to isolate the underlying physics of plasma-body interactions in LEO to quantify whether ionospheric aerodynamic is significant compared to neutral aerodynamics. The influence of this assumption and recommendations for future work to incorperate these phenomena is discussed in Section 8.3).
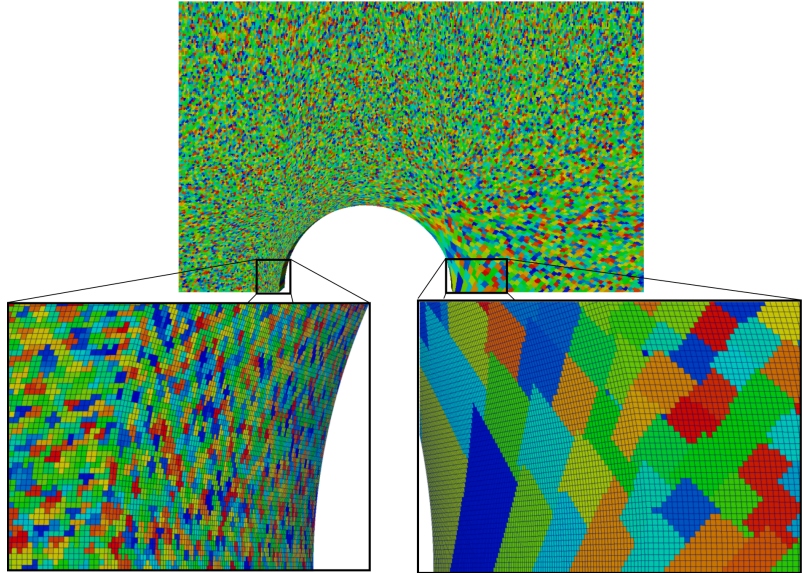
Numerical Setup

Freestream number density, temperature and velocity are $1.699 \times 10^{19} m^{-3}$, $200 K$ and $2634.1 m/s$ respectively. Gas-surface interactions are that of a diffusely reflecting wall with complete thermal accommodation to a fixed surface temperature of $500 K$. VHS coefficients are $T_{ref} = 1000 K$, $d_{ref} = 3.959 \times 10^{-10} m$, and $\omega = 0.734$ to be consistent with Lofthouse, Boyd, and Wright, (2007).

Results and Discussion

The total linear kinetic energy and number of simulated macro-particles achieved a dynamic equilibrium (steady-state) after $10,000$ time-steps, with 1.6 million macro-particles in the system. At steady-state there were ≈ 1500 collision cells and a 99.9% reduction in calls to the collision partner selection procedure compared to the full mesh (≈ 4 million cells). Results were sampled over $60,000$ time-steps after the steady-state had been reached to reduce statistical fluctuations. Figure 3.9 visualises the conglomerated collision cells constructed in the fore-body (bottom left) and rear (bottom right) of the cylinder on the

full mesh. Clustering of collision cells in Figure 3.9 demonstrates the ability of the TCC method to capture high and low-density regions as well as the transition region with no *a priori* knowledge of the flow.

Figure 3.9: Visualisation of collision cells. Colours are random.

Figure 3.10 compares contours of temperature between pdFOAM (top) and MONACO (bottom). Figure 3.11 compares the surface pressure (c_P) and heat flux (c_H) coefficients.

$$c_P = \frac{2\left(P - P_\infty\right)}{\rho_\infty u_\infty^2} \qquad c_H = \frac{2Q}{\rho_{m_\infty} u_\infty^3} \tag{3.11}$$

where P is pressure, Q heat flux and ρ_m is the mass density.

There is good agreement between pdFOAM and MONACO - differences being a small increase in peak translational temperature in the ram position in the pdFOAM simulation and an extension of the warm wake region. Both the small increase in peak heating and extension of the wake region are believed to be a reflection of different collision selection procedures causing a small difference in localised viscosity. A drawback of the TCC method is the use of small cells resulting in higher numerical fluctuations caused by a comparatively lower number of particles per sampling cell than in MONACO. However, as the basis of the TCC method is to reconcile PIC and DSMC spatial requirements, PIC being significantly smaller than DSMC, this is expected.

Comparing surface properties, pdFOAM over-predicts peak c_P by 2.27% and under-predicts peak c_H by 2.7% compared to MONACO. A comparison of MONACO with other established DSMC codes for the $Kn = 0.002$ case in Lofthouse, Boyd, and Wright, (2007) shows that a 2.7% under-prediction of peak c_H is within the code-to-code uncertainty reported
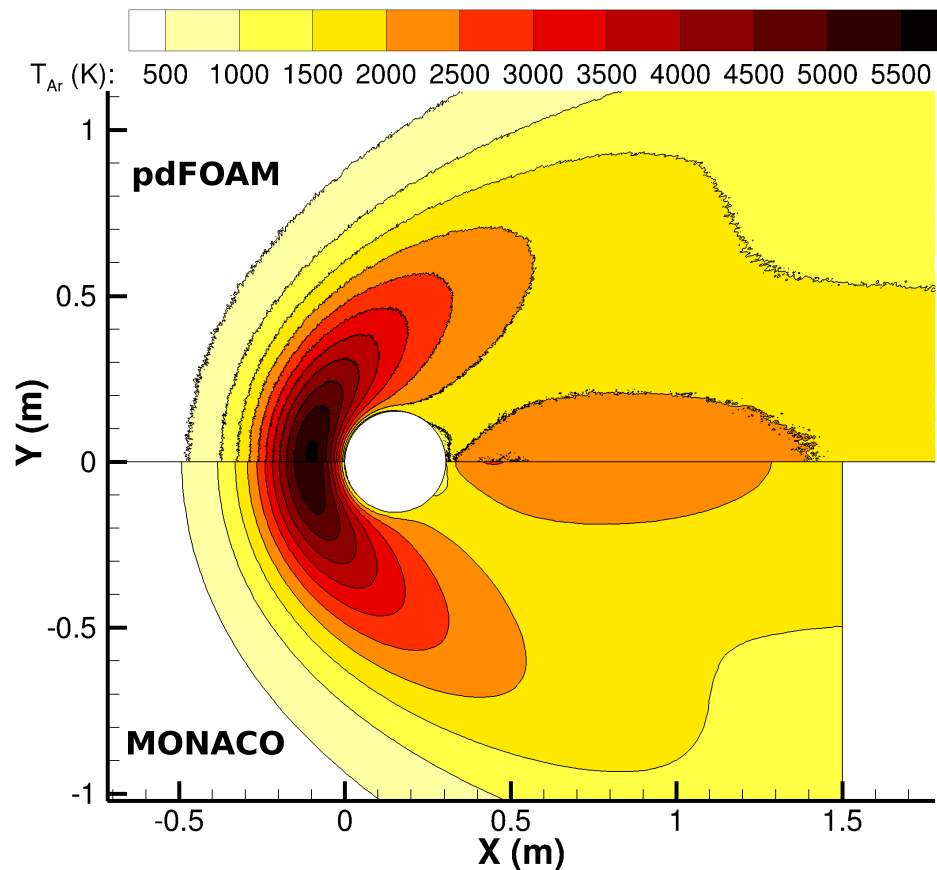
in Bird, (2007). Similarly, the distribution of coefficients is similar, the over-prediction of c_P likely due to the different apparent viscosity caused by different collision selection procedures. Overall, pdFOAM is able to reproduce the interaction from Lofthouse, Boyd, and Wright, (2007) and in particular the surface force distribution. This later result is important in a charged aerodynamic context, the purpose of this validation case primarily being to demonstrate the ability of pdFOAM to correctly predict forces due to gas-surface interactions. Based on results in Figure 3.11, confidence can be placed in pdFOAM's ability to accurately capture diffusely reflecting gas-surface interactions.

3.4.3   Self-Consistent Charging in a Flowing Plasma
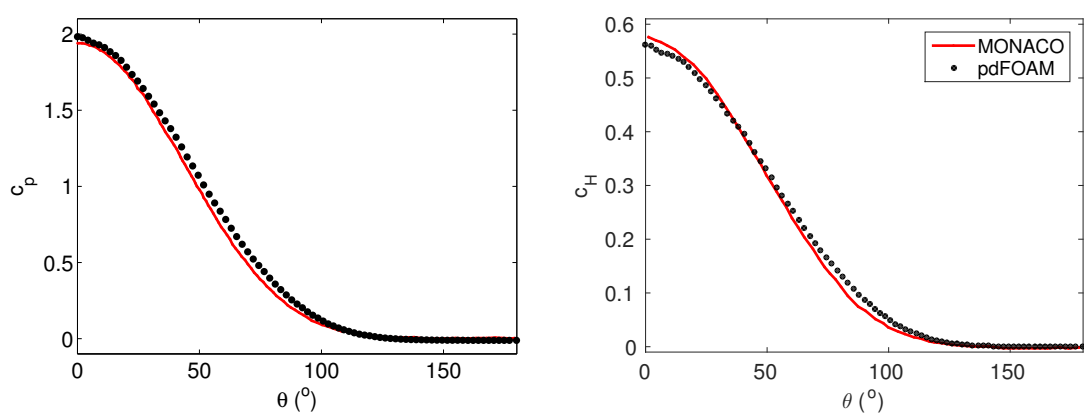
The self-consistent charging of a body immersed in plasma is a complex problem in plasma physics (Garrett and Whittlesey, 2000; Hastings, 1995; Garrett, 1981). Validation of pdFOAM's PIC method has included unbounded plasma kinetic phenomena (two-stream instability) and bounded plasma-body interactions (planar sheath structure) (see Appendix B). Self-consistent charging requires accurate replication of both kinetic and boundary phenomena to reproduce the electron and ion current balance needed to achieve a dynamic equilibrium at floating potential ϕ_B.

pdFOAM supports both absorbing and catalytic walls - the former deleting incident particles, the latter transforming them into one or more particles. Reflected particles may be re-emitted in either a diffuse or specular manner with a degree of thermal accommodation to the wall. pdFOAM treats wall charging in one of three ways: as a perfectly conducting wall where charge is distributed evenly across the surface before calculating fields (the effect of surface currents on the system is neglected); as a perfectly insulating wall where charge accumulates on wall cell faces and does not transport about the surface (arcing is not currently considered); as a fixed potential wall where charge is absorbed, and the surface potential remains fixed based on initial conditions.

The following validation cases compare the numerical floating potential of a conducting flat plate (one-dimensional) and cylinder (two-dimensional) in a drifting plasma predicted by pdFOAM with established theoretical relationships developed to analyse plasma probe measurements. As such, Section 3.4.3 provides a more detailed discussion of charging theory than that outlined in Section 2.2.2, Section 3.4.3 outlines the numerical setup and Section 3.4.3 presents the results. The implementation of more advanced wall boundary conditions to include effects such as secondary electron emission and sputtering is the subject of ongoing work. The above boundary conditions sufficient for enabling the study of LEO plasma-body interactions in this work.

Figure 3.10: Contours of temperature: pdFOAM (top) and MONACO (bottom)

Figure 3.11: Comparison of pdFOAM and MONACO surface distributions.

Background: Charging in a Flowing Plasma

Consider the charging of a large, perfectly conducting, flat plate in a collisionless, unmagnetised, single ion species plasma, with ion drift velocity u_∞. The electron current (I_e) from random particle flux per unit surface area to a surface with potential ϕ_B can be written as (Whipple, 1981),

$$I_e = q_e n_{e_\infty} \left(\frac{8T_e k_B}{\pi m_e} \right)^{1/2} \exp\left[-\frac{q_e \phi(\phi_B)}{k_B T_e} \right] \tag{3.12}$$

As ion thermal velocity $u_{t,i} \to u_\infty$, the ion velocity distribution is described by a shifted-Maxwellian function (Bird, 1976),

$$f_i(v) = \left(\frac{m}{2\pi k_B T_i} \right)^{1/2} \exp\left[-\frac{m (v - u_\infty)^2}{2k_B T_i} \right] \tag{3.13}$$

where ion current (I_i) is given by,

$$I_i = q_e n_{i_\infty} \int_0^\infty v f_i(v) d^3 v \tag{3.14}$$

For a flat plate, Eqn. 3.14 becomes (Whipple, 1981),

$$I_i = q_e n_{i_\infty} u_\infty \frac{1}{2} \left(1 + \mathrm{erf}[y] + \frac{1}{\sqrt{\pi} S_i} \exp\left[-S_i^2 \right] \right), \quad S_i = u_\infty \left(\frac{2k_B T_i}{m_i} \right)^{-1/2} \tag{3.15}$$

Here S_i is the ion drift ratio, and the system reaches an electrical dynamic equilibrium when $I_i = I_e$. Equating Eqn. 3.12 and Eqn. 3.15, the floating potential of a large flat plate in a drifting plasma is described by,

$$\begin{aligned} \phi_p &= \frac{k_B T_e}{q_e} \left(\ln(f) - \ln\left(\sqrt{\frac{m_i}{2\pi m_e}} \right) \right), \\ f &= \frac{S_i}{\sqrt{2}} \left(1 + \mathrm{erf}(S_i) + \frac{1}{S_i \sqrt{\pi}} \exp\left[-S_i^2 \right] \right) \end{aligned} \tag{3.16}$$

The charging of a cylinder in a collisionless, unmagnetised, single species plasma, with drift velocity u_∞, is similar to the flat plate case but must also take into account conservation of angular momentum of ions about the body. In the OML regime, Hoegy and Wharton, (1973) demonstrated that I_i can be approximated as,

$$I_i = I_{i,t} \frac{2}{\pi^{1/2}} \left(|\Phi| + S_i^2 + \frac{1}{2} \frac{|\Phi| + 1/2 S_i^2}{|\Phi| + S_i^2} \right)^{1/2}, \quad |\Phi| + S_i^2 > 0, \Phi = \frac{q_e \phi_B}{k_B T_e} \tag{3.17}$$

where $I_{i,t}$ is the random ion thermal current to the surface with area A,

$$I_{i,t} = Aq_e n_i \sqrt{\frac{k_B T_i}{2\pi m_i}} \tag{3.18}$$

The electron current, similar to Eqn. 3.12, is given by,

$$I_e = Aq_e n_e \sqrt{\frac{k_B T_e}{2\pi m_e}} \exp\left[-\frac{q_e \phi(\phi_B)}{k_B T_e}\right] \tag{3.19}$$

Equating Eqn. 3.17 and Eqn. 3.19, the floating potential for a given condition may be solved numerically - Newton's method is used in this work (Hockney and Eastwood, 1988).

Numerical Setup

Flow and numerical properties for the flat plate and 0.3 m radius cylinder charging cases are listed in Table 3.1. Cylinder flow conditions are taken from Hastings, (1995) and represent the average conditions experienced by the EOS during a period of mean sunspot activity. Flat plate conditions are based on similar work in Delzanno et al., (2013). Gas-surface interactions used in both flat plate and cylinder charging simulations are those of a perfectly conducting, absorbing wall, where incident particles are neutralised and removed from the simulation; this is appropriate as the system is collisionless. All simulations are fully-kinetic. At steady-state, simulations are time-averaged over $10,000$ time-steps to reduce the statistical scatter of the data. Simulated floating potentials are then compared against analytical predictions calculated using the methods described above, the floating potential occurs at the point where $I_i = I_e$.
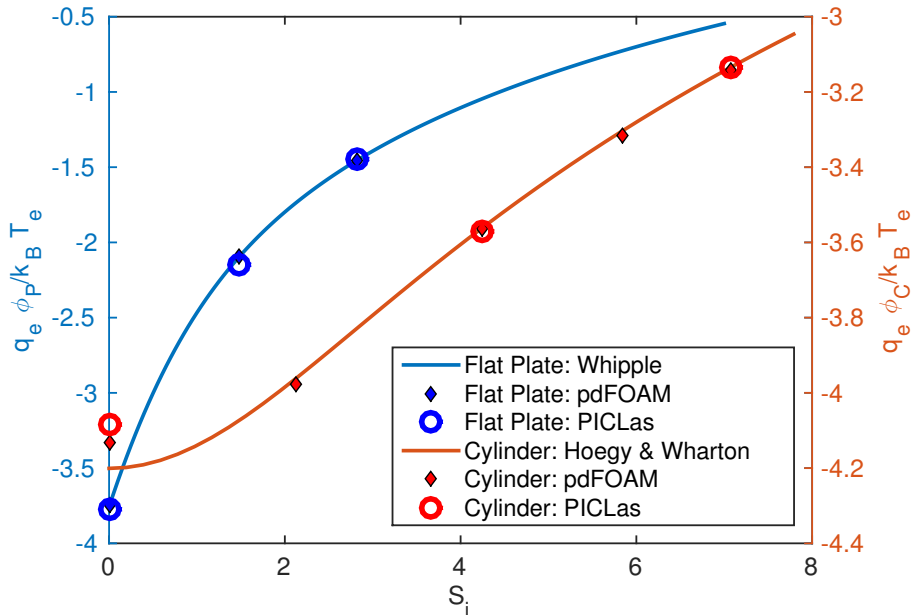
Results and Discussion

Figure 3.12 compares theoretical floating potentials for a flat plate and a 0.03 m radius cylinder with those predicted by pdFOAM. Charging simulations using the conditions listed in Table 3.1 using PIC-DSMC code, *PICLas*, provided by T. Binder (personal communications, 13/12/2016) are included for comparisons. There is excellent agreement between theory and simulated floating potentials for all flat plate cases. Cylinder floating potential are well predicted for all $S_i > 2$, the maximum disagreement between pdFOAM and PICLas being 0.25%. The mean floating potential at $S_i = 0$ is under-predicted by both pdFOAM and PICLas when compared to Hoegy and Wharton, (1973). However, fluctuations in floating potential were observed in both pdFOAM and PICLas for the $S_i = 0$ case suggesting either the presence of time-dependent phenomena or that the system is

Table 3.1: Computational parameters for charging simualtions

	Flat Plate	Cylinder
Plasma Parameters		
$n_{i/e,\infty}$ (m^{-3})	1×10^{12}	4×10^{10}
T_i (K)	1000	1537
T_e (K)	1000	1997
Gas Properties		
Species	H^+	O^+
m (kg)	1.67×10^{-27}	26.55×10^{-27}
Computational Parameters		
ρ_{part}	2	45
Δt (s)	2.5×10^{-9}	5×10^{-9}
Case	$u_{H^+,\infty}$ (m/s)	$u_{O^+,\infty}$ (m/s)
I	0	0
II	6038	2722
III	11501	5445
IV	-	7500
V	-	9076

numerically sensitive. One explanation for the under-prediction of floating potential for the stationary case is the presence of ion absorption barriers.

Figure 3.12: Comparison of floating potential in a flowing plasma predicted by pdFOAM (diamonds) and PICLas (circles) for the flat plate (blue) and cylinder (red) cases compared against theory.

For example, Delzanno et al., (2013) performed a similar charging simulation on an axisymmetric sphere using the PIC code, CPIC. Delzanno et al., (2013) observed a 1.6% over-prediction in floating potential when compared to OML based predictions (compared to a 1.6% under-prediction by pdFOAM for the cylinder case seen in Figure 3.12). As noted in Section 2.3, OML assumptions do not capture the absorption barrier phenomena discussed (for example) in Al'Pert, Gurevich, and Pitaevskii, (1965), Allen, (1992) and Fortov et al., (2005). This is reflected in Delzanno et al., (2013) and the stationary cylinder case presented here as the over and under-prediction of the floating potential. As the relative kinetic energy of the flow increases, the effect of ion absorption barriers decreases and the floating potential approaches Eqn. 3.17, supporting the assertion in Hoegy and Wharton, (1973) that Eqn. 3.17 is valid for $\Phi + S_i^2 > 0$ (see also McMahon, Xu, and Laframboise, (2005)). We therefore conclude that pdFOAM accurately reproduces the self-consistent charging interaction of a perfectly conducting flat plate and a cylinder in a flowing plasma and, therefore, the underling plasma sheath structure required to achieve this floating potential.

3.5 Summary

The use of OML type assumptions regarding sheath structure was identified in Chapter 2 as a key limitation of ionospheric aerodynamic literature. To address this limitation, the Particle-in-Cell (PIC) method was identified as an appropriate numerical method for capturing the self-consistent sheath structure surrounding an object immersed in a mesothermal plasma flow. The purpose of this chapter was to describe the implementation of the PIC method within the hybrid PIC-DSMC code, pdFOAM, developed here as the primary research tool used throughout this work.

pdFOAM is limited to electrostatic, non-relativistic plasma simulations; sufficient for the scope of this work. To demonstrate that pdFOAM can be used confidently to capture the underlying physics of charged aerodynamics, two validation cases were presented in this chapter. The first validation case demonstrated the ability of pdFOAM to predict the forces on a body caused by diffusely reflecting gas-surface interactions thermalised to a 500 K wall when compared with the established DSMC code, MONACO i.e. direct aerodynamics forces. A 2.2% over-prediction of peak surface pressure coefficient when compared to MONACO was observed. This over-prediction is within the uncertainty seen in similar DSMC code-to-code comparisons and pdFOAM was concluded to correctly capture direct aerodynamic surface forces to the same level of accuracy as other DSMC codes, and to the level needed to be able to explore flow physics and extract underlying phenomena.

The second validation case demonstrated the ability of pdFOAM to predict the self-consistent floating potential of a flat plate and a cylinder in a flowing plasma when compared against both probe theory and the PIC code, PICLas. By reproducing the self-consistent floating potential, this validation case developed confidence in the ability of pdFOAM to capture the physical structure of the plasma sheath of mesothermal plasma-body interactions and, therefore, address one of the limitation of past charged aerodynamic analyses. While excellent agreement was observed for mesothermal flows, the floating potential was under-predicted by both pdFOAM and PICLas for a quiescent plasma when compared against probe theory. Comparisons with a similar floating potential study of a sphere suggest this under-prediction is caused by ion absorption barriers not captured in the OML based floating potential predictions. As the flow velocity increased into the range where the OML equations are valid, the numerical and theoretical floating potential showed excellent agreement. Therefore, it was concluded that *pdFOAM captures the self-consistent sheath structure about a conducting body.*

In summary, based on these two results as well as those presented in Appendix B, pdFOAM can be confidently used for high-fidelity physics-based studies of the effect of ionospheric aerodynamics on LEO objects.

Chapter 4

Observations of Flow Physics: Identification of Ionospheric Aerodynamic Phenomena

4.1   Introduction

Employing the research tool, pdFOAM, the purpose of this chapter is to explore flow phenomena resulting from the self-consistent interaction of a representative ionospheric plasma with cylindrical geometries at a range of surface potentials. The methodology and numerical setup used in this chapter is described in Section 4.2. Section 4.3 begins to address the identified gaps by presenting initial observations of LEO plasma-body interaction phenomena caused by both high and low voltage objects without making an assumption regarding the sheath structure. The relationship of these phenomena to charged aerodynamic surface forces is then studied in Section 4.4 where the influence of OML assumptions on ionospheric aerodynamic predictions is determined. In doing so, challenges that this work must overcome to make the study of ionospheric aerodynamics feasible are identified.

4.2   Methodology and Numerical Setup

The following simulations are two-dimensional, employ hybrid-kinetic (HK-PIC) assumptions and focus on the flow over a cylinder - mesh topology is similar to that seen in Section 3.4.1. A cylindrical geometry was chosen to aid unnecessary flow complexity and minimised computation costs, thereby allowing this work to focus on isolating key physical phenomena. The principle advantage of the cylindrical flow is to allow a direct comparisons with Orbital Motion (OM) theory, which is based on the motion of an ion through a

central force field - this is not true for a flat plate for example as the potential field is not
a function of radius from a central point.

Reference flow conditions are outlined in Table 4.1 and correspond to those in Hastings,
(1995) for the EOS satellite during a period of mean sunspot activity. The simulations
take advantage of flow symmetry and only model the top half of the geometry. To adhere
to the best practice guidelines outlined in Section 3.3.2 for PIC simulations, the maximum
dimension (Δx) of each cell was less than 0.5 mm, satisfying the stability requirement
$\Delta x < \lambda_{D,e}/2 = 7.7$ mm. Similarly, the simulation time-step (Δt) was 5×10^{-8} s. Note
that this time-step is significantly smaller than strictly required, the hybrid-kinetic nature
of the simulations meaning that only $\Delta t < 2\omega_{pi}^{-1}$ and $\Delta t < \Delta x/v_i$ need to be satisfied. The
chosen time-step however, satisfies the latter requirement, accounting for the clustering of
cells near the body surface (≈ 0.08 mm) and the acceleration of ions through the plasma
sheath e.g. an ion accelerated from 7.5 km/s to 15 km/s takes 5.3×10^{-8} s to traverse a
0.08 mm cell.

Steady-state was defined as when the total linear kinetic energy and charge contained in
the system reached an equilibrium. Each simulated particle represents 2500 real parti-
cles ($\rho_{part} = 2500$ real particles/simulated particles). Simulations reached steady-state
at approximately 0.002 s (40000 steps), taking around 12 hours on 60 2.2 GHz CPUS [1].
For simplicity, cases are numbered sequentially from here on. Table 4.1 listing interaction
quantities used in Cases 1-24 seen in this section.

All gas-surface interactions considered are for a neutralising, diffusely reflecting surface
with complete thermal accommodation to a 500 K wall.

4.2.1   Numerical Effects on Flow Physics.

Particle Density: At steady-state each simulation contains approximately 1.4 million
simulated particles (including both ions and neutrals), each particle representing 2500
real particles. After achieving steady-state simulations were time-averaged over 10, 000
steps to reduce statistical fluctuations in flow properties and resolve flow structures. Flow
structures were seen to be independent of particle weight. To demonstrate this, Figure
4.1 compares the flow of an O^+ plasma over a 0.3 m radius cylinder with a uniform fixed
surface potential of -50 V (Case 6) for simulations with numerical particle densities (ρ_{part})
of 2500 (bottom) and 625 (top) i.e. a four-fold increase in simulated particles. Flowfields
show the ratio of ion potential energy to kinetic energy α. The reason for this is discussed
later. Case 6 was chosen as it contains a variety of important flow phenomena that will be
described in detail in subsequent discussions.

---

[1]Exact time to steady-state was case dependent, indicated values are representative.

Table 4.1: Reference conditions and case parameters investigating the coupling of ϕ_B, r_B and m_i. Reference conditions are from (Hastings, 1995) and correspond to the mean ionospheric conditions experienced by the EOS satellite during a period of mean sunspot activity. Cases 1-6 and Cases 7-8 correspond to the flow of an O^+ and H^+ plasma over a 0.3 m radius cylinder at different fixed surface potentials. Cases 13-18 and Cases 19-24 investigate the same plasma flows over a 0.03 m radius cylinder. Total computation time for Cases 1-24 was approximately 360 hrs (15 days) on 60 CPUs.

Reference Conditions				
v_B (m/s)	n_i (m^{-3})	n_e (m^{-3})	T_i (K)	T_e (K)
7500	4×10^{10}	4×10^{10}	1531	1997
Case #.	ϕ_B (V)	r_B (m)	Species	
1	0	0.3	O^+	
2	-1	0.3	O^+	
3	-5	0.3	O^+	
4	-10	0.3	O^+	
5	-25	0.3	O^+	
6	-50	0.3	O^+	
7	0	0.3	H^+	
8	-1	0.3	H^+	
9	-5	0.3	H^+	
10	-10	0.3	H^+	
11	-25	0.3	H^+	
12	-50	0.3	H^+	
13	0	0.03	O^+	
14	-1	0.03	O^+	
15	-5	0.03	O^+	
16	-10	0.03	O^+	
17	-25	0.03	O^+	
18	-50	0.03	O^+	
19	0	0.03	H^+	
20	-1	0.03	H^+	
21	-5	0.03	H^+	
22	-10	0.03	H^+	
23	-25	0.03	H^+	
24	-50	0.03	H^+	
Total Computational Time $\approx$ 360hrs (15days)				

The general plasma interaction features are independent of numerical particle density in Figure 4.1. Two regions of dissimilarity are labelled at a) and b).

The feature at a) is a bounded ion jet predicted by Orbital Motion (OM) theory caused by the deflection of a specific energy band of ions by ion absorption barriers into bounded orbits about the body. By increasing the number of simulated particles in Figure 4.1 (top), the resolution of ions in this energy band is increased and as a result statistical effects are reduced compared to Figure 4.1 i.e. more particles reduce the amplitude of numerical fluctuations in field measurements.
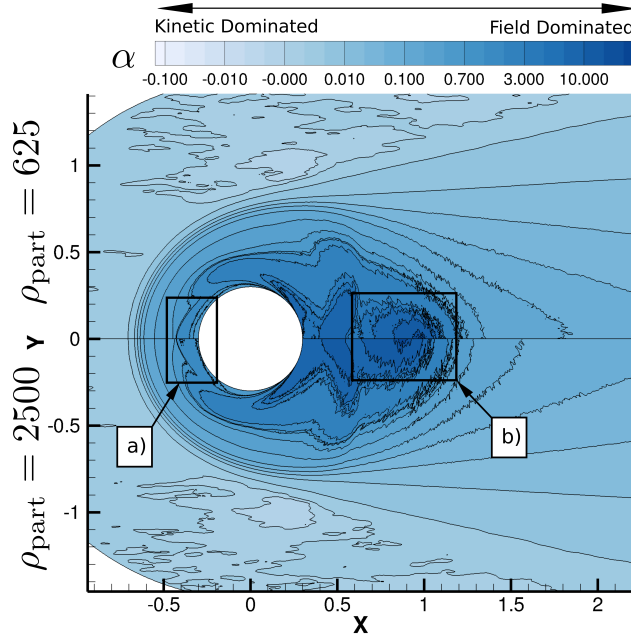
The difference seen at b) reflects a flow region occupied by relatively few simulated particles. Again, by increasing the number of simulated particles in Figure 4.1 the statistical fluctuations in field properties are reduced.

The underlying physical interactions shown in Figure 4.1 are therefore independent of the numerical particle density. The $\rho_{\text{part}} = 2500$ took approximately 15 hrs on 60 CPUS to process, while the $\rho_{\text{part}} = 625$ case took approximately 40 hrs. Therefore presented simulations use $\rho_{\text{part}} = 2500$ to reduce numerical costs.
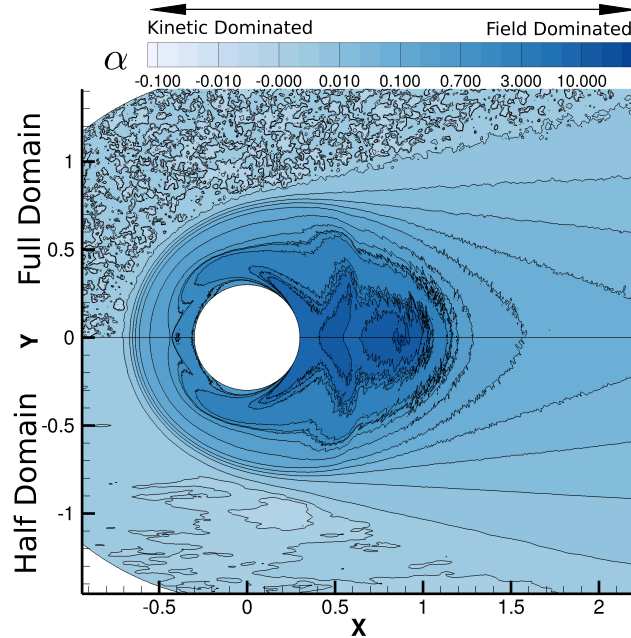
Symmetry Plane: To demonstrate that the symmetry plane used in this work does not affect the structure of flow phenomena, Figure 4.2 compares the flow of an O^+ plasma over a 0.3 m radius cylinder with a uniform fixed surface potential of -50 V (Case 6) for a full domain (top) and half domain (bottom).

The primary difference between the cases shown in Figure 4.2 is the increased noise in the full domain case, particularly in the freestream. This is a reflection of the increased computational time required by the full domain simulations, where both the number of particles and number of cells have doubled compared to the half domain simulation. As a consequence, the full domain simulation was only averaged over $5,000$ steps after achieving steady-state (compared to the $10,000$ in the half domain case). The total time required to achieve steady-state and average the full domain simulation was approximately 40 hrs, compared to 15 hours in the half domain simulation.
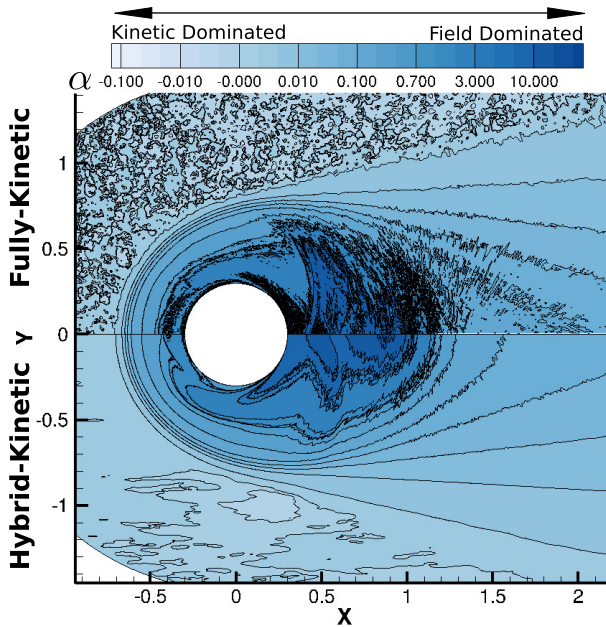
Half domain simulations are used in this work unless otherwise stated. The independence of solutions on mesh structure is demonstrated in Section 5.5.3.

Figure 4.1: Comparison of Case 6 α flowfields for with numerical particle density (ρ_{part}) of 2500 (bottom) and 625 (top). α is the ratio of ion potential energy to kinetic energy. a) and b) correspond to regions where high statistic resolution of features in the top case effect the resolution of flow features.

Figure 4.2: Comparison of full domain (top) and half domain (bottom) simulations for the flow of O^+ over a 0.3 m cylinder with a uniform, fixed surface potential of -50 V (Case 6).

Figure 4.3: Comparison of full domain FK-PIC (top) and half domain HK-PIC (bottom) simulations for the flow of O^+ over a 0.3 m cylinder with a uniform, fixed surface potential of -50 V (Case 6).

Hybrid-Kinetic: Finally, the effect of hybrid-kinetic assumptions on the flow was tested against fully-kinetic simulations. The FK simulation was performed on the full domain mesh used in the previous example with a time-step of 1×10^{-9} s. Simulations were initialised based on the steady-state HK flowfield and run for an additional 0.001 s (1000000 steps) to allow electron kinetic effects to influence flow characteristics. Simulations were then averaged over another 0.0002 s (200000 steps).

Figure 4.3 shows that the half-domain HK-PIC simulation (bottom) is similar to the full domain FK-PIC simulation (top). Electron heating in the wake was observed but this does not appear to have significantly influenced the near-body flowfield.

4.2.2   A Note on Drag Force Calculations

Two sources of drag are considered in this work; direct charged drag ($F_{D,d}$), and indirect charged drag ($F_{D,m}$). Both direct and and indirect charged drag surface forces include a surface *normal* and *tangential* component. The convention in this work is to express local direct and indirect charged drag forces as $f_{D,d}$ and $f_{D,m}$ and forces as $F_{D,d}$ and $F_{D,m}$,

$$F_{D,d} = \sum_{i}^{n} f_{D,d}, \quad F_{D,m} = \sum_{i}^{n} f_{D,m} \tag{4.1}$$

where $f_{D,d}$ and $f_{D,m}$ correspond to the drag force on a surface element with area A_i and $F_{D,d}$ and $F_{D,m}$ correspond to the total force on an object with area A_B (the sum of n surface elements).

The total charged drag force ($F_{D,C}$) is then the sum of indirect and direct drag components,

$$F_{D,C} = F_{D,d} + F_{D,m} \tag{4.2}$$

The charged drag coefficient is then written as,
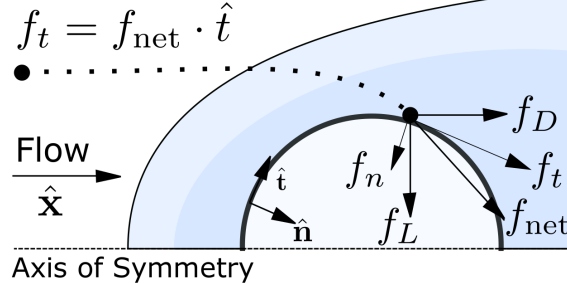
$$C_{D,C} = \frac{F_{D,C}}{1/2 m_i n_i v_B^2 A_B} \tag{4.3}$$

Figure 4.4 illustrates the vector breakdown of the net force (f_net) contributed by a particle to the local normal (f_n) and tangential (f_t) forces. The vector breakdown of the indirect drag is the same as in Figure 4.4, the diagonal elements of the Maxwell stress tensors representing a pressure (normal force) and the off-diagonal elements representing a symmetric shear force (tangential force). Indirect aerodynamic forces are therefore numerically calculated by integrating the Maxwell stress tensor about the surface of the object and taking the drag component. Given the axisymmetric nature of the flows considered in this work, the lift component (f_L) sums to zero and are not considered here further. It should be noted however that the symmetry plane *enforces* flow symmetry. While it was shown above that this does not appear to have influenced the flow, it is possible that this is not true for all cases. The ramifications of this are discussed as future work in Section 8.2.

Figure 4.4: Breakdown of incident force vector components of a particle into normal (f_n), tangential (f_t) and drag (f_D) components.

4.3 Observations of Plasma-Body Interaction Phenomena

The parameters that govern single species plasma-body interactions for geometrically similar objects include: the ion number density (n_i), ion mass (m_i), ion temperature (T_i), ion charge (q_i), electron temperature (T_e), electron number density (n_e), body velocity (v_B), body scale (r_B) and the body potential (ϕ_B) (the multi-species case is discussed in Chapter 5). The set of these parameters are referred to as the *interaction quantities*[2] in this work. This section focuses on investigating the effect of m_i and r_B on plasma interaction phenomena for a range of surface potentials (ϕ_B).

The reason for investigating m_i, r_B and ϕ_B stems back to the limitations in previous ionospheric aerodynamic studies discussed in Chapter 2, in particular those in Brundin, (1963) and Jastrow and Pearse, (1957). As we established in Chapter 2, the seminal nature of the conclusions in Brundin, (1963) was reflected by a shift in focus within the ionospheric aerodynamic literature from forces to phenomena (and later charging). A fundamental difference between the expressions for direct charged aerodynamic forces in Brundin, (1963) and Jastrow and Pearse, (1957) was the independence of the expression in Brundin, (1963) on body radius r_B. While the expression in Jastrow and Pearse, (1957) that incorporated r_B was later shown to provide a reasonable approximation of experimental measurements in Knechtel and Pitts, (1965), the conclusions by Brundin, (1963) regarding the significance of ionospheric aerodynamics to LEO objects were never reviewed.

Brundin, (1963) concluded that the charged aerodynamic forces would, at most, be on the order of 20% the total neutral aerodynamic forces. Brundin, (1963) did not draw conclusions regarding H^+ dominated plasmas that occur above 900 km altitude, instead focusing on O^+ dominated plasmas below 700 km - this was in part a reflection of the range of satellite orbits in the 1960s. Further, conclusions in (Brundin, 1963) regarding the significance of ionospheric aerodynamics in LEO were focused around the assumption that the surface potential of LEO objects is never more negative than -0.75 V. As Section 2.3.1 established, this is not true, large surface potentials are now recognised to occur both naturally and artificially in LEO (Hastings, 1995; Garrett and Whittlesey, 2000; Anderson, 2012).

By investigating the relationship between m_i, r_B and ϕ_B, plasma interaction phenomena, and their influence on charged aerodynamic forces, this section begins to address the limitations of prior ionospheric aerodynamic studies by allowing the identification of plasma interaction phenomena significant to ionospheric aerodynamics in LEO.

---

[2]Quantities referring to their dimensional nature.

4.3.1 Effect of Ion Mass on Ionospheric Aerodynamics: Low Voltage

Plasma-Body Interaction Phenomena

Section 2.2.2 outlined the general structure of LEO plasma-body interactions. To summarise, the mesothermal flow velocity results in a compressed fore-body sheath and elongated wake sheath to reflect the directed ion velocity. The immediate wake forms a negative ion void region populated by electrons. The negative wake region caused by these electrons in the ion void sets up an electric field that deflects ions into the wake which appears physically as an ion gradient ("rarefaction wave") moving outward at the ion acoustic wave speed i.e. electrostatic compression wave. In the frame of the body, this appears as a Mach wave defined by the ion acoustic Mach number M_i, which is the ratio of body velocity v_B to ion acoustic wave speed $v_{i,s}$. The leading edge of the rarefaction wave is then defined by the angle θ_r as,
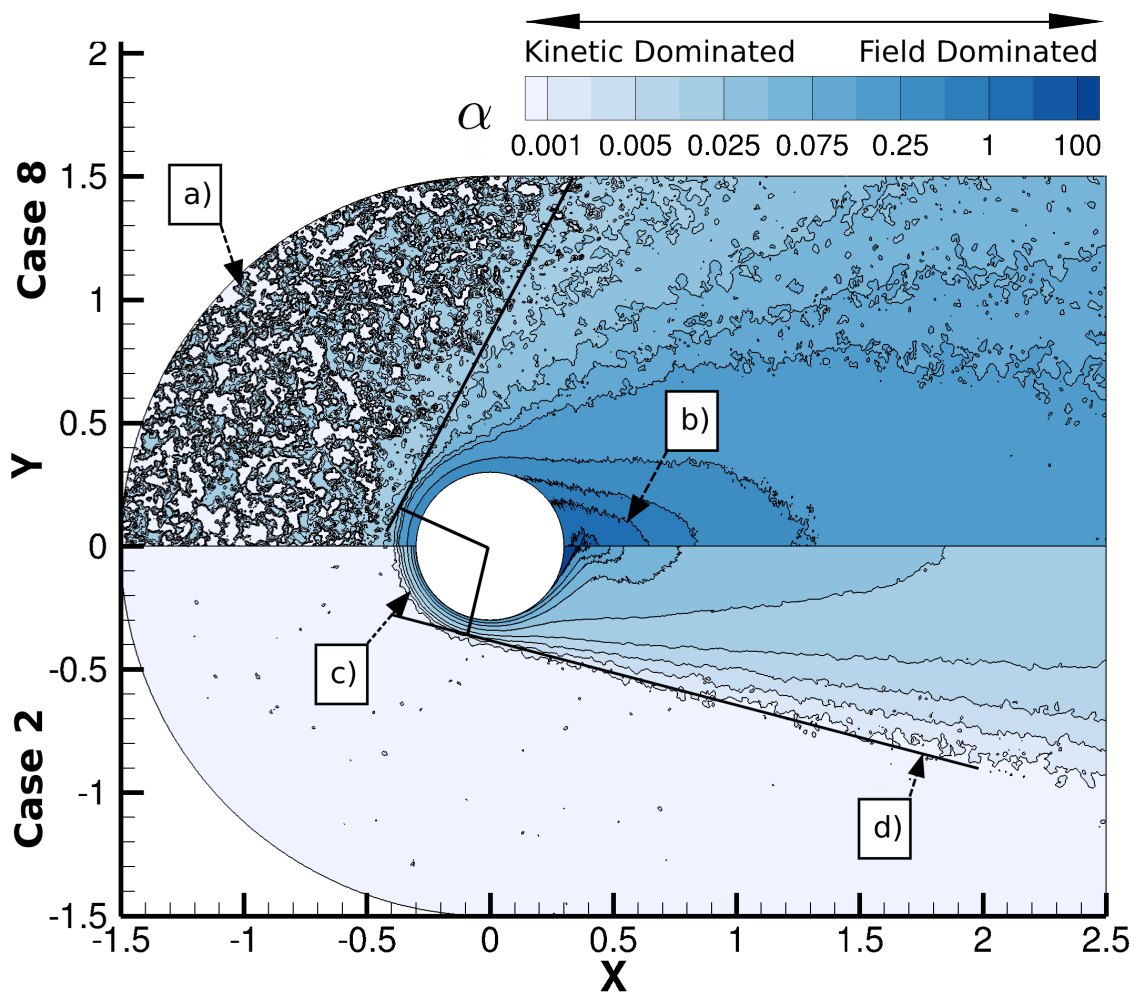
$$\theta_r = \sin^{-1}\left[\frac{1}{M_i}\right], \quad M_i = \frac{v_B}{v_{i,s}} = \frac{v_B}{\sqrt{k_B\left(T_e + \gamma_i T_i\right)/m_i}} \tag{4.4}$$

where γ_i is the adiabatic index that describes the ability of a real gas to distribute energy to rotational and vibrational modes (degrees of freedom). In a collisionless plasma $\gamma_i = 3$ (Burgess and Scholer, 2015).

This section investigates the effect of ion mass on low voltage plasma-body interactions. Specifically, this section compares flow phenomena arising from the interaction of a 0.3 m radius cylinder with a surface potential of -1 V with identical O^+ (Case 2) and H^+ (Case 8) plasmas. Eqn. 4.4 predicts that the reduced mass in the H^+ flow will increase the ion rarefaction wave angle θ_r. The physical explanation of this is that the H^+ ions are lighter and therefore have a lower momentum than the O^+ ions. As result, the force required to influence the motion of the H^+ is proportionally lower the O^+ ions (Newton's first law of motion) making them more susceptible to field effects. Similarly, the ion and electron temperature terms in Eqn. 4.4 reflect the thermal energy of the flow. As the thermal energy of the plasma increases, the average ion velocity increases (momentum) and therefore the resistance of the plasma to disturbances such as ion acoustic waves.

To demonstrate the effect of ion mass, Figure 4.5 plots to the ratio of potential energy $(q_i\phi(\mathbf{x}))$ to kinetic energy $(1/2m_i v_i(\mathbf{x})^2)$ α,

$$\alpha = -\frac{q_i\phi(\mathbf{x})}{m_i v_i(\mathbf{x})^2} \tag{4.5}$$

Figure 4.5: Comparison of Case 2 and 8 corresponding to a -1 V, 0.3
m radius cylinder in O^+ (bottom) and H^+ (top) plasmas. Features are
labelled as follows: a) Residual numerical noise; b) Elongated wake sheath;
c) compressed fore-body sheath; d) rarefaction wave.

Note that the factor of 1/2 has been dropped from the kinetic energy term. The reason for this is discussed in Chapter 5. The physical meaning of α is to highlight regions dominated by field effects ($\alpha > 1$) (e.g. the plasma sheath and rarefaction wave) and kinetic effects ($\alpha < 1$) (e.g bounded ion jets and ion pseudo-waves).

Figure 4.5 compares the interaction of an O^+ plasma (bottom) and H^+ plasma (top) with a 0.3 m cylinder with a fixed, uniform surface potential of -1 V compared to a quasi-neutral freestream plasma. General mesothermal plasma-body interaction features described above are reproduced in Figure 4.5. The ion acoustic Mach number M_i for the O^+ flow (Case 2) is 4.61, Eqn. 4.4 predicting a θ_r of 14.3^o. Comparatively, M_i for the H^+ flow (Case 8) is 1.16, Eqn. 4.4 predicting a θ_r of 80°.

Lines indicating the identified wake edge are shown in Figure 4.5, an example of which is labelled as d). A more detailed description of these measurements is found in Chapter 6. Based on the indicated rarefaction wave angle measurements in Figure 4.5, $\theta_r = 14.0^o \pm 1^o$ for the O^+ flow (Case 2) and $\theta_r = 69.8^o \pm 10^o$ in the H^+ flow (Case 8). Hence, there is excellent agreement seen between Eqn. 4.4 and the O^+ flow in Figure 4.5, while the large uncertainty in the H^+ flow makes it difficult to assess the fit of the H^+ flow with Eqn. 4.4. To understand the H^+ flow, it is instructive to consider the source of the noise seen in Figure 4.5.

There are two principal sources of noise in the H^+ flow. One source is residual noise left over after averaging the simulation to reduce statistical fluctuations. This noise is also evident in the O^+ flow in Figure 4.5 but to a significantly smaller degree. Another source of noise is due to ion thermal effects.

Previous work that considered ion thermal effects on mesothermal plasma-body interactions determined that ion thermal effects tend to diffuse mesothermal plasma phenomena (Davis and Harris, 1961; Martin, 1974; Stone, 1981b) - this work comes to a similar conclusion in Chapter 5. Ion thermal effects can be described by the ion thermal ratio (S_i), defined as the ratio of body velocity to ion thermal velocity can be written as,

$$S_i = v_B/v_{t,i} = v_B/\sqrt{2k_B T_i/m_i} \tag{4.6}$$

The ion thermal ratio of the O^+ and H^+ flows is 5.89 and 1.48 respectively. As S_i approaches unity, ion thermal effects cannot be ignored (the mesothermal assumption breaks down). As will be shown in Chapter 5, this is the case in the H^+ flow.

Influence of Phenomena on Surface Coefficients

Figures 4.6 and 4.7 plot the distribution of the normalised direct ($\hat{f}_{D,d}$), indirect ($\hat{f}_{D,m}$) and total charged drag ($\hat{f}_{D,C}$) forces about the surface of the cylinder in Case 2 and 8 respetively. $\theta = 0$ corresponding to the fore-body and the normalisation is with respect to the total charged drag $F_{D,C}$ in each flow e.g. $\hat{f}_{D,d} = f_{D,d}/F_{D,C}$. This normalisation allows the influence of direct and indirect charged aerodynamic forces on phenomena governed by ion mass observed directly.
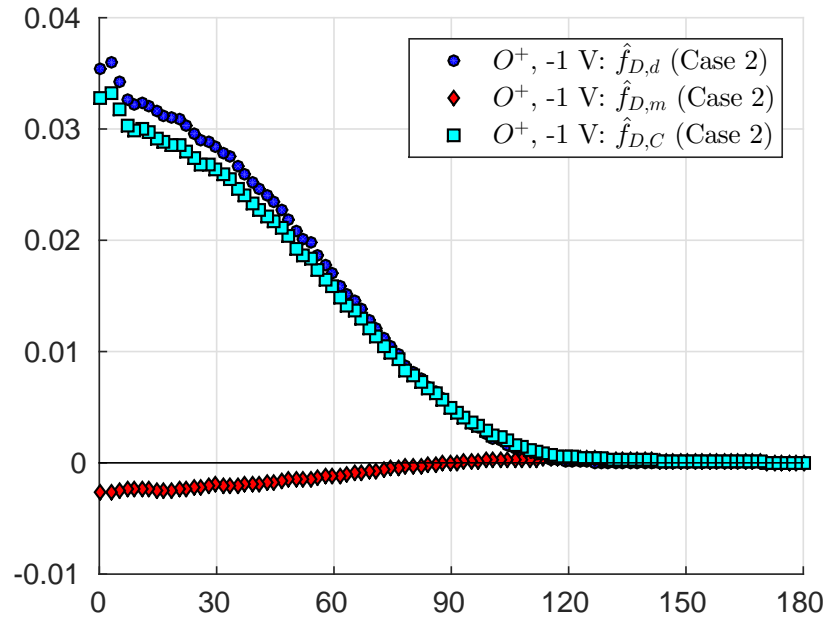
Figures 4.6 and 4.7 shows that, as ion mass decreases, the direct charged drag contribution in the fore-body increases. This was predicted in the expression for direct charged particle drag in Brundin, (1963) through the use of the OML impact parameter (Fortov et al., 2005),

$$(b_*)_{\text{OML}} = r_B \left(1 - \frac{2q_i\phi_B}{m_i v^2} \right)^{1/2} = r_B \left(1 + 2\alpha \right)^{1/2} \tag{4.7}$$
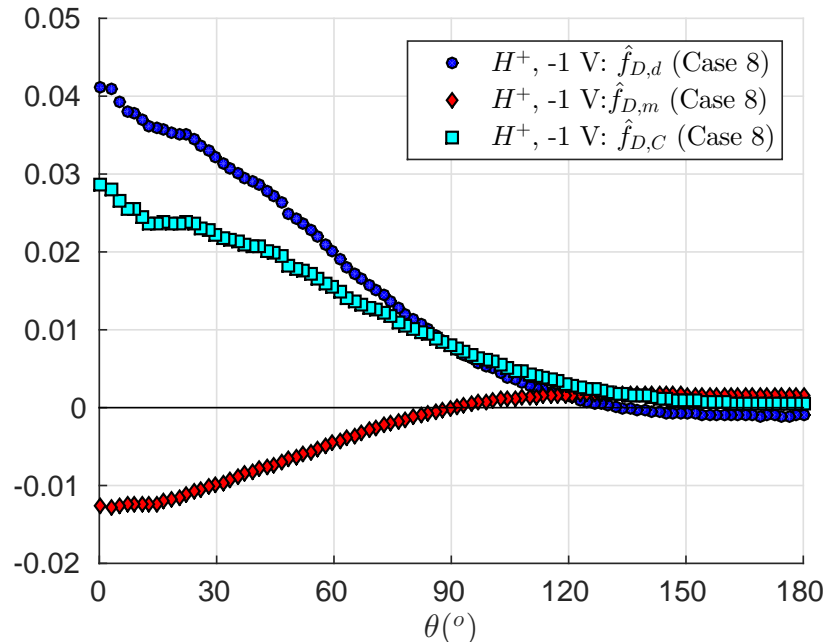
Eqn. 4.7 predicts that as the ion kinetic energy becomes small compared to the potential energy of the object (or the potential energy becomes large compared to the kinetic energy), the effective capture area of the object increases and therefore so does the direct charged drag. Eqn. 4.7 does not account for the sheath driven ion acceleration, where ions arrive at the object surface after falling through a potential well with an incident velocity,

$$v_S = v_B \left(1 - \frac{2q_i\phi_B}{m_i v_B^2} \right)^{1/2} = v_B \left(1 + 2\alpha \right)^{1/2} \tag{4.8}$$

The acceleration of the ions through the sheath must exert a force on the body (Newton's third law). The body feels this acceleration as an indirect electrostatic thrust i.e. accelerated ions pull the body forward. Figures 4.6 and 4.7 shows that, while the direct charged drag force on the fore-body increases with decreasing ion mass, the indirect thrust force also increases to counter the increase caused by ion accelerations. As a result, the direct drag caused by ion accelerations is largely cancelled by this indirect thrust. In other words, the concept of enhancement of the effective ion collection area as a principle mechanism describing direct charged drag holds. This is an important insight into charged aerodynamics, demonstrating that even for systems where indirect scattering effects are minor (such as those presented here), indirect effects cannot be neglect otherwise calculations based on direct charged aerodynamics will over-predict total charged aerodynamic forces.

Figure 4.6: Normalised surface direct ($\hat{f}_{D,d}$), indirect ($\hat{f}_{D,m}$) and total charged ($\hat{f}_{D,C}$) drag force distributions about cylinder surface with a uniform surface potential of -1 V in an O^+ (Case 2).

Figure 4.7: Normalised surface direct ($\hat{f}_{D,d}$), indirect ($\hat{f}_{D,m}$) and total charged ($\hat{f}_{D,C}$) drag force distributions about cylinder surface with a uniform surface potential of -1 V in an H^+ (Case 8) plasma.

4.3.2 Effect of Ion Mass on Ionospheric Aerodynamics: High Voltage
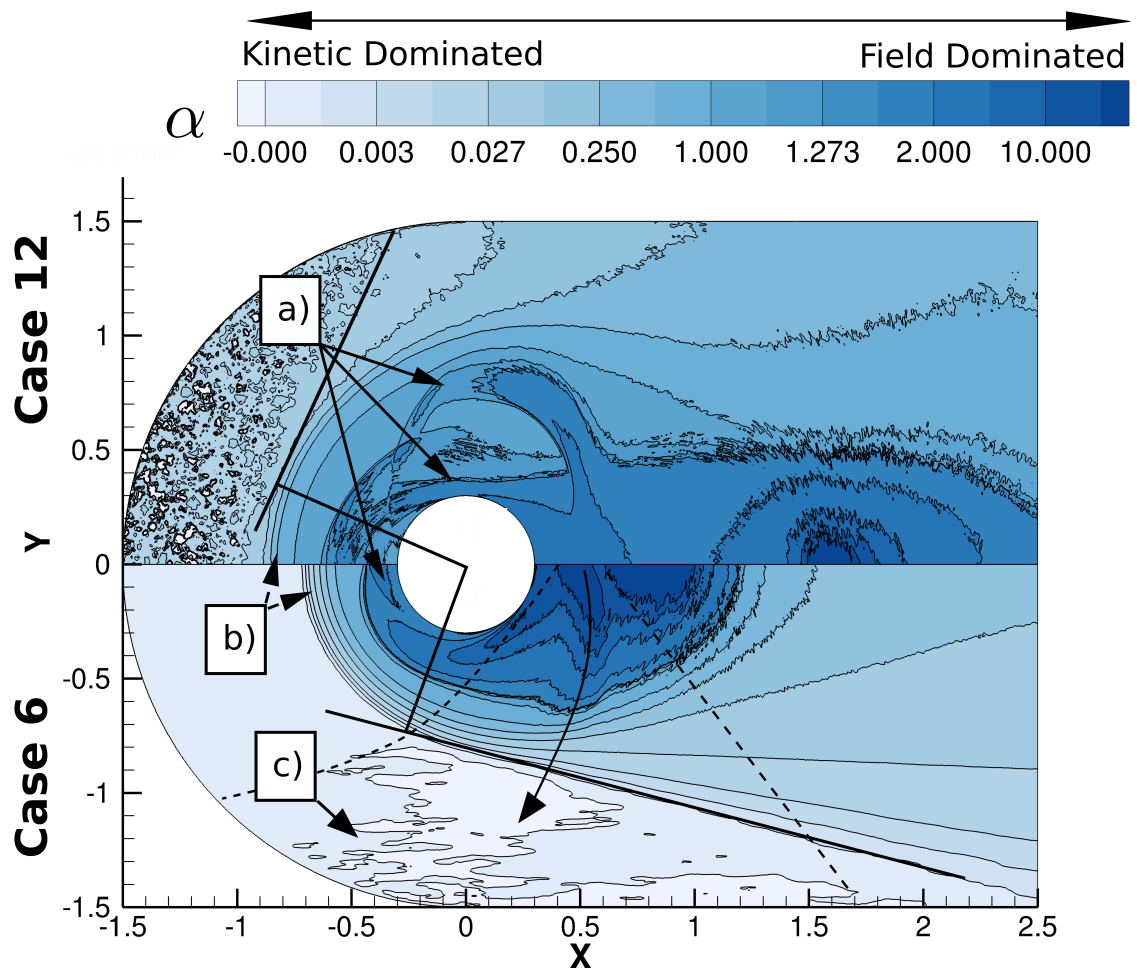
Plasma-Body Interaction Phenomena

The previous section presented the flow of an O^+ and H^+ plasma over a 0.3 m radius cylinder with a fixed, uniform surface potential of -1 V. General features of LEO plasma-body interactions were observed. The principle effect of the ion mass was reflected in the rarefaction wave angle. Important from a charged aerodynamics perspective, the sheath was thin compared to the body. As a result, direct charged aerodynamic forces dominated the total charged drag. This section considers the same O^+ and H^+ plasma flow about a uniformly charged -50 V cylinder with a radius of 0.3 m.

The reason for considering this case is two-fold. First, as mentioned at the start of this section, previous ionospheric aerodynamic studies focused on low-voltage objects. It is now well recognised that LEO objects may achieve large surface potentials with respect to the environment for a variety of reasons. It is therefore instructive to determine whether there exist phenomena significant to high-voltage objects that would not be observed (or obvious) for low-voltage objects. This leads to the second reason. The previous section did not discuss the indirect drag evident in the H^+ flow or the net increase in charged drag with θ in the H^+ flow compared to the O^+ flow. By increasing the potential energy of the body which holding the kinetic energy of the surrounding plasma constant, these effects should be enhanced.

Figure 4.8 compares the interaction of an O^+ plasma (bottom) and H^+ plasma (top) with a 0.3 m cylinder at a fixed, uniform surface potential of -50 V with respect to a quasi-neutral freestream plasma (Case 6 and Case 12). Contours are of α to highlight kinetic and field dominated phenomena. While the general structure of mesothermal plasma-body interactions is evident, two additional phenomena can also be seen in Figure 4.8. These phenomena are referred to as bounded ion jets and ion pseudo-waves.

Bounded ion jets refer to the bunching of ions within an energy dependent critical impact parameter (b_*) such that they enter bounded (they are collected) orbits about the body as predicted by OM theory (Al'Pert, Gurevich, and Pitaevskii, 1965). Ion pseudo-waves refer to the scattering of a subset of ions within a critical impact parameter range such that they are deflected into fan-like structures about the body outside of the rarefaction wave. These phenomena are *kinetic* in nature (are caused by specific ion trajectories through a self-consistent electric field) compared to *collective* phenomena such as the plasma sheath and rarefaction wave, which are the electrical response of the *system* to an electrical disturbance.
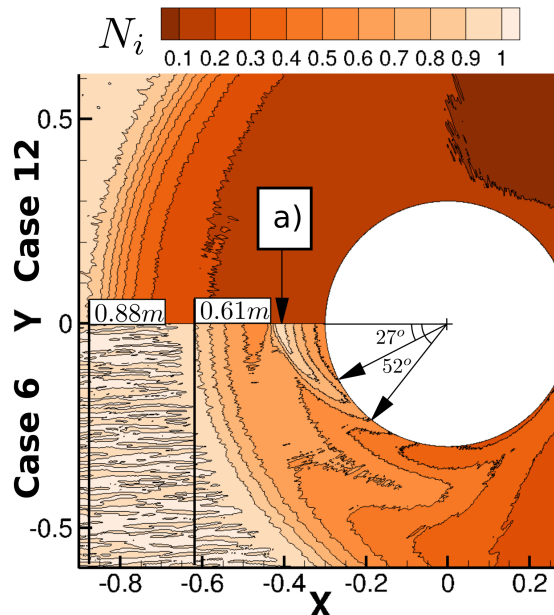
Figure 4.8: Comparison of Case 6 and 12 corresponding to a -50 V, 0.3 m radius cylinder in O^+ and H^+ plasmas respectively. Features are labelled as follows: a) bounded ion jets; b) compressed fore-body region; c) ion pseudo-wave.

A tenuous ion pseudo-wave is evident in the O^+ flow in Figure 4.8 (bottom). Dashed lines have been added to highlight the ion pseudo-wave labelled at c). Bounded ion jets are seen in both the O^+ (Case 6) and H^+ (Case 12) in Figure 4.8 labelled at a). However, the intensity of the bounded ion jets differs between the O^+ and H^+ case. To demonstrate this, Figure 4.9 plots ion number density contours normalised by the freestream ion number density ($N_i = n_i(\mathbf{x})/n_{i,\infty}$).

Figure 4.9 shows that the bounded ion jet in the O^+ flow is sufficiently dense to cause a localised over-dense region in the fore-body sheath created by the superposition of the ion jet and ions collected by the fore-body sheath. Based on the N_i contours, this ion jet connects to the fore-body of the cylinder between 27° and 52°.

Another feature evident in both Figures 4.8 and 4.9 is the expansion of the sheath with decreased ion mass, the O^+ and H^+ flows having a sheath thickness of 0.31 m and 0.58 m respectively. This is significantly larger than the sheaths seen in the -1 V cases previously, which were 0.09 m thick. In other words, *for high-voltage LEO objects, the sheath cannot be assumed to be thin compared to the body.* Another important conclusion that can be drawn from the above discussion is that *bounded ion jets and ion pseudo-waves may be present in LEO plasma body interactions.* To date, the influence of these phenomena on charged aerodynamic forces has not been studied (however ion pseudo-wave phenomena have been observed, for example in McMahon, Xu, and Laframboise, (2005)).

Figure 4.9: Normalised ion density contours for the O^+ (Case 6) and H^+ (Case 12) plasma flow over a 0.3 m radius cylinder at $-50V$. Features are labelled as follows: a) intense bounded O^+ jet.

Influence of Phenomena on Surface Coefficients
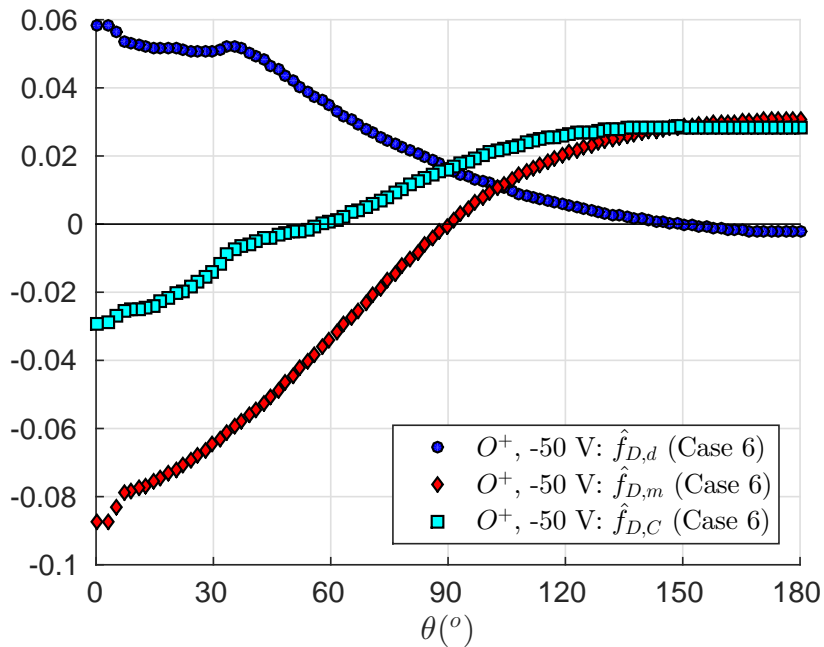
Figures 4.10 and 4.11 plot the distribution of the normalised direct ($\hat{f}_{D,d}$), indirect ($\hat{f}_{D,m}$) and total charged drag ($\hat{f}_{D,C}$) about the surface of a -50 V cylinder in O^+ (Case 6) and H^+ (Case 12) plasma. The direct and indirect charged aerodynamic trends are significantly different in both Figures 4.10 and 4.11 compared to those seen previously for the -1 V cases.

Unlike the -1 V cases, which were dominated by direct charged aerodynamic forces, the -50 V cases here are dominated by indirect charged aerodynamics forces. This is clearly evident in the fore-body, where the direct charged drag forces are outweighed by indirect thrust forces. While the effective ion collection area has increased with surface potential (hence the increase in sheath thickness), there now exists a portion of ions which are accelerated by the sheath but not collected. As a result, the indirect thrust outweighs the ram portion of the direct charged drag force. This is studied in more detail in Chapter 6.
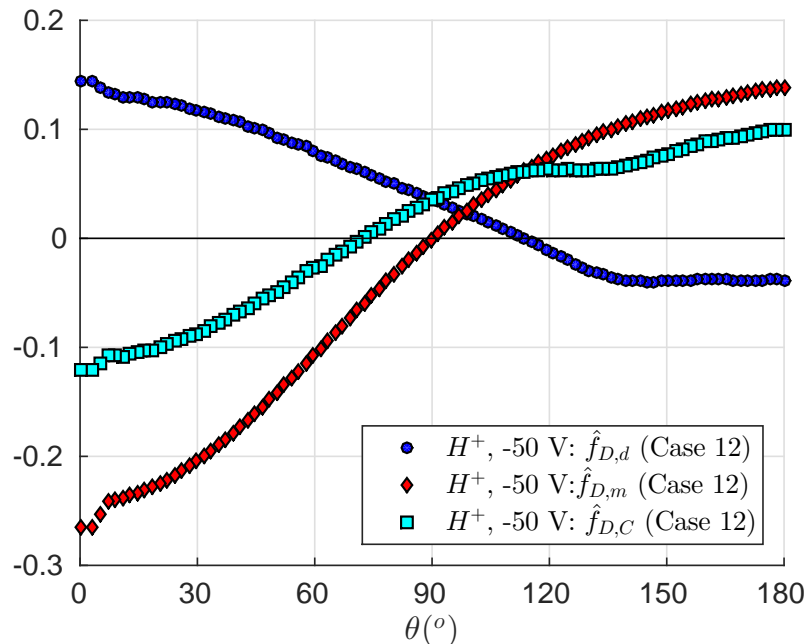
Two important features are evident in the direct charged drag force distribution in Figures 4.10 and 4.11. The first is the discontinuous jump in $f_{D,d}$ between approximately 28° to 40° seen in Figure 4.10 (Case 12). This jump corresponds to the dense ion jet highlighted in Figure 4.9, which connects to the cylinder surface between 27° and 52°. The second feature is the direct ion thrust on the rear of the cylinders (particularly evident in the H^+ flow). This thrust is caused by the deflection of ions into orbits that connect to the cylinder wake surface and are explored in more detail in Chapter 6.

While the indirect thrust outweighs the direct drag on the ram surface of the cylinder, the increase in sheath thickness also increases the proportion of scattered ion in the wake. The elongated nature of the wake sheath means that these ions experience an along-track deceleration force. As with the accelerated ions, this deceleration is experienced as an (electrostatic) drag by the body. This indirect drag is the primary component of the total charged aerodynamic force in Figures 4.10and 4.11.

These observations are important as they demonstrate that previous ionospheric aerodynamic studies that assert that the indirect charged aerodynamic force is small compared to the direct contribution are not always valid (Jastrow and Pearse, 1957; Brundin, 1963). These observations further strengthen the argument in the previous section that charged aerodynamics requires treatment of both the indirect and direct forces.

Figure 4.10: Normalised surface direct ($\hat{f}_{D,d}$), indirect ($\hat{f}_{D,m}$) and total charged ($\hat{f}_{D,C}$) drag force distributions about cylinder with a surface potential of -50 V in a O^+ (Case 6).

Figure 4.11: Normalised surface direct ($\hat{f}_{D,d}$), indirect ($\hat{f}_{D,m}$) and total charged ($\hat{f}_{D,C}$) drag force distributions about cylinder with a surface potential of -50 V in a H^+ (Case 12) plasma.

4.3.3 Effect of Body Radius on Ionospheric Aerodynamics: High Voltage
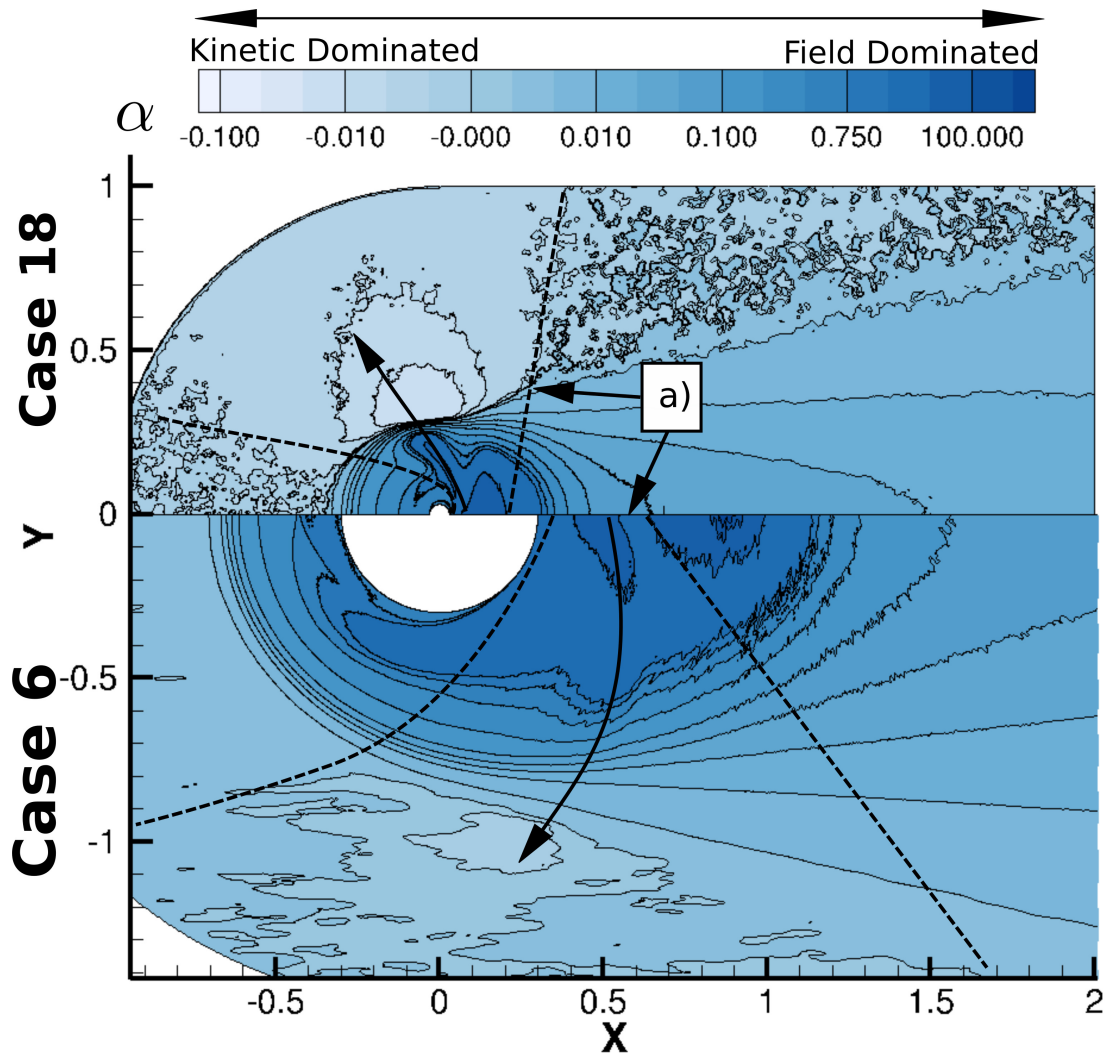
Plasma-Body Interaction Phenomena

As the name implies, OML based predictions of ion collection revolve around the ion motion being *"orbit limited"* i.e. the orbital dynamics of an ion through a plasma sheath limits ion collect. However, if the sheath is not sufficiently thick, then the structure of the sheath limits ion collect i.e. *"sheath-limited"* ion collection. As shall be shown in Chapter 6, as the sheath becomes very thin compared to the body, the ion collection approaches that of an equivalent neutral flow.

A key assumption in Brundin, (1963) was that ion collection was OML. Jastrow and Pearse, (1957) attempted to account for the relative sheath thickness compared to the body through the shielding ratio $\lambda_{D,e}/r_B$. The previous section demonstrated that the sheath thickness is related to the surface potential of an object. This relationship is not accounted for in Brundin, (1963) but is well recognised in the literature (Beiser and Raab, 1961; Laframboise and Parker, 1973; Samir, Wright, and Stone, 1983; Whipple, 1981; Choinière and Gilchrist, 2007). This section considers whether body scale has an effect on the relative shielding i.e. does the sheath thickness scale linearly with body radius.

Figure 4.12 compares the interaction of an O^+ plasma with a 0.3 m radius cylinder (bottom) and 0.03 m radius cylinder (top) with a fixed, uniform surface potential of -50 V compared to a quasi-neutral freestream plasma (Case 18 and Case 24). Ion pseudo-waves are outlined in Figure 4.12 (dashed lines) with a solid arrow indicating the approximate centre of the unbounded ion jet that forms the observed pseudo-waves.

The most important feature of Figure 4.12 for this discussion is that the sheath thickness has clearly not scaled linearly with the body radius. Measuring the sheath thickness about the 0.03 m radius cylinder (Case 18) gives a thickness of 0.308 m. Therefore Figure 4.12 shows that sheath has not scaled with r_B between Case 6 and Case 18, both having a forebody sheath thickness of ≈ 0.31 m. Hence, the relative thickness of the sheath compared to the body (d_{sh}/r_B) in Case 18 is ten times that of Case 6. In other words, an object in a given plasma with a given surface potential will experience a different charged aerodynamic interaction compared to an identical scaled object.

Figure 4.12: Comparison of Case 6 and 18 corresponding to a -50 V, 0.3 m radius cylinder (bottom) and 0.03 m radius cylinder (bottom) in O^+ plasma. Features are labelled as follows: a) ion pseudo-waves

Influence of Phenomena on Surface Coefficients

To confirm the assertion that the relative sheath thickness will influence the charged aerodynamics of an object, Figures 4.13 and 4.14 compare the normalised direct, indirect and total charged drag surface force distributions about the 0.3 m and 0.03 m radius cylinders. Figures 4.13 and 4.14 demonstrate that as the relative thickness of the sheath increased between the 0.3 m and 0.03 m cylinder, the influence of indirect drag became increasingly dominant.
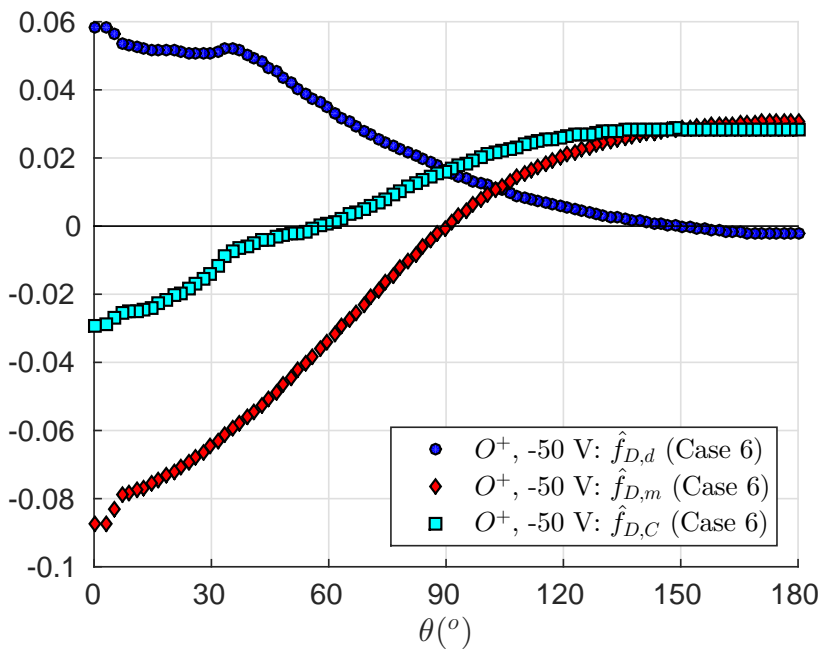
Physically, the increased contribution of indirect aerodynamic forces with decreasing radius reflects the thickening of sheath compared to the body radius. As a consequence, the contribution of accelerated ions (indirect thrust) and scattered ions (indirect drag) becomes proportionally larger as sheath thickness increases. At the same time, direct charged aerodynamic forces plateau as ion collection becomes limited by their orbital motion (OML). A more detailed physical investigation of these phenomena is presented in Chapter 6.

4.3.4 Summary of Observations
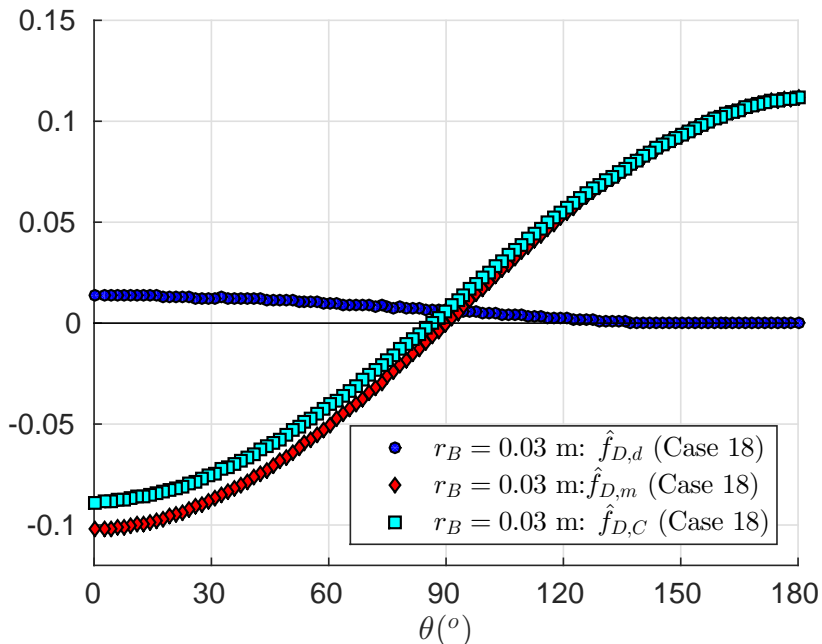
The purpose of the above observations was to begin addressing limitations in the prior ionospheric aerodynamic literature by identifying plasma-body interaction phenomena significant to charged aerodynamics. Three interaction quantities were studied: ion mass (m_i), body potential (ϕ_B) and body radius (r_B). By studying the effect of ion mass on low and high voltage objects and the effect of body radius on high voltage objects, the following conclusions were drawn:

1. *Low-voltage plasma-body interactions with thin sheaths are dominated by direct charged aerodynamics. Direct charged aerodynamic forces are primarily governed by the enhanced ion collection area caused by the sheath structure surrounding the body. The increase in direct charged aerodynamic forces caused by sheath driven ion acceleration is largely countered by an indirect thrust force experienced by the body.*

2. *High-voltage plasma-body interactions exhibit both bounded ion jets and ion pseudo-waves.*

3. *Sheath thickness does not scale with body size. Indirect charged aerodynamic forces are strongly dependent on the sheath thickness and increase at a greater rate than direct charged aerodynamic forces. As a result, indirect charged aerodynamic forces may dominate total ionospheric aerodynamic forces.*

These observations are important as they contradict previous assertions regarding ionospheric aerodynamics, specifically that indirect charged aerodynamic will only be a perturbation to the direct charged aerodynamic force (Jastrow and Pearse, 1957; Brundin, 1963;

Figure 4.13: Normalised surface direct ($\hat{f}_{D,d}$), indirect ($\hat{f}_{D,m}$) and total charged ($\hat{f}_{D,C}$) drag force distributions about a0.3 m radius cylinder (Case 18) with a surface potential of -50 V in a O^+ plasma.

Figure 4.14: Normalised surface direct ($\hat{f}_{D,d}$), indirect ($\hat{f}_{D,m}$) and total charged ($\hat{f}_{D,C}$) drag force distributions about a 0.03 m radius cylinder (Case 18) with a surface potential of -50 V in a O^+ plasma.

Knechtel and Pitts, 1965) (this conclusion is consistent with prior dusty plasma aerodynamic observations (Hutchinson, 2005; Hutchinson, 2006)). Further, the observation that the ion acceleration is largely cancelled by an indirect thrust felt by the body is a contribution to ionospheric aerodynamics that wasn't considered in early works (again this observation is similar to that made by Hutchinson, (2005) in the analysis of dusty plasmas). However, by performing an energy balance between the freestream and the body surface, early ionospheric aerodynamic studies correctly predicted the concept of an enhanced ion collection area as the principle direct charged drag contribution. It is therefore appropriate to compare early analytical ionospheric aerodynamics predictions against those in pdFOAM to determine the significance of the above observations to conclusions regarding the influence of ionospheric aerodynamics to LEO objects.

4.4 Preliminary Assessment of Ionospheric Aerodynamics

This section takes the observations above and considers their implications by comparing the ratio of the total charged to neutral drag ($F_{D,C}/F_{D,N}$) predicted by pdFOAM against analytical predictions to assess the validity of previous conclusions regarding the significance of ionospheric aerodynamics to LEO objects. To facilitate this comparison, the approach employed by Brundin, (1963) to predict direct charged drag is re-derived for a cylinder in Section 4.4.1 to obtain an analytical expression for $F_{D,d}/F_{D,N}$. This, in turn, allows a direct assessment of the validity of their conclusions regarding the significance of ionospheric aerodynamics in LEO.

4.4.1 Charged Aerodynamics: An Orbital Motion Limited Approach

As established in Section 2.3, the ratio of charged to neutral drag for a sphere can be expressed as (Jastrow and Pearse, 1957; Brundin, 1963),

$$\left(\frac{F_{D,d}}{F_{D,N}} \right)_{\text{Jastrow}} = \frac{m_i}{m_n} \frac{n_i}{n_n} \left(1 + \kappa(\phi_B) \frac{\lambda_{D,e}}{r_B} \right)^2 \tag{4.9}$$

$$\left(\frac{F_{D,d}}{F_{D,N}} \right)_{\text{Brundin}} = \frac{m_i}{m_n} \frac{n_i}{n_n} \left(1 - 2 \frac{q_e \phi_B}{m_i v_B^2} \right) \tag{4.10}$$

Eqn. 4.9 was developed by first solving from the one-dimensional (1D) sheath structure near a flat plate with surface potential ϕ_B in a flowing plasma (see Appendix B for example). By assuming a spherically symmetric plasma sheath, Jastrow and Pearse, (1957) applied this 1D sheath structure to predict the critical impact parameter b_* as a function of the relative shielding thickness $\lambda_{D,e}/r_B$ and the parameter $\kappa(\phi_B)$ calculated based on the 1D sheath. Unfortunately a direct comparison with Eqn. 4.9 is not possible without using the same sheath structure calculation. Eqn. 4.9 has several important implications, namely that both ϕ_B and the relative sheath thickness scale direct charged drag. The latter being the primary difference with Eqn. 4.10, which implies the independence of direct charged drag on r_B.

The independence of Eqn. 4.10 with r_B is a reflection of the OML assumption that the sheath does not limit ion collection. Starting with neutral drag, the free molecular drag on a cylinder is similar to that for a sphere, the main difference being the wetted area (Sentman, 1961),

$$F_{D,d,k} = 2l_B b_* m_k n_k v_B^2 \tag{4.11}$$

where l_B is the cylinder length and b_* is the impact parameter equal to r_B for neutral drag.

The incident direct charged drag is calculated by recalling the OML impact parameter,
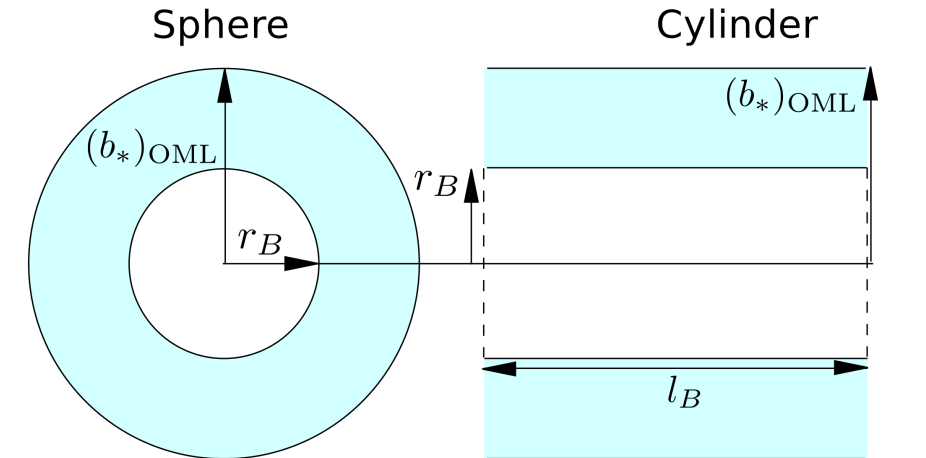
$$(b_*)_{\text{OML}} = r_B \left(1 - 2\frac{q_i \phi_B}{m_i v^2}\right)^{1/2} \tag{4.12}$$

Substituting Eqn. 4.12 into Eqn. 4.11, the OML ratio of direct charged to neutral drag $(F_{D,d}/F_{D,N})$ for a cylinder can be expressed as,

$$\left(\frac{F_{D,d}}{F_{D,N}}\right)_{\text{OML}} = \frac{2l_B r_B m_i n_i v_B^2}{2l_B r_B m_n n_n v_B^2}\left(1 - 2\frac{q_i \phi_B}{m_i v^2}\right)^{1/2} = \frac{m_i}{m_n}\frac{n_i}{n_n}\underbrace{\left(1 - 2\frac{q_i \phi_B}{m_i v_B^2}\right)^{1/2}}_{\text{ion collection enhancement}} \tag{4.13}$$

The only difference between Eqns. 4.10 and 4.13 being the power of $1/2$ for the ion collection enhancement term - a reflection of a reduction in degrees of freedom between sphere and cylinder as illustrated in Figure 4.15. Note also that we have allowed for multiply charged ions, this will be discussed in Chapter 5.

Eqn. 4.13 suffers the same limitations as Eqn. 4.10, in particular, it assumes that: (1) ion collection is not limited by sheath thickness; (2) the affect of ion absorption barriers phenomena has no effect on direct charged drag; (3) ion acceleration does not contribute to direct charged drag; (4) all momentum is transferred into drag.

Sphere   Cylinder

$$A_{\text{sphere}} = \pi r_B^2 \left(1 - 2\frac{q_i \phi_B}{m_i v_B^2}\right) \qquad A_{\text{cylinder}} = 2l_B r_B \left(1 - 2\frac{q_i \phi_B}{m_i v_B^2}\right)^{1/2}$$

Figure 4.15: Illustration of the effective ion collection area of a sphere (left) and cylinder (right).

4.4.2   Comparison of Numerical and Analytical Predictions

The foundation of the argument that ionospheric aerodynamics is negligible in (Brundin, 1963) revolves around the assertion that $0 < -\phi_B \leq 0.75$ V and therefore the ion collection enhancement term in Eqn. 4.10 (and Eqn. 4.13) is always less than or equal to two (($1 - 2q_e\phi_B/m_i v_B^2) \leq 2$). Brundin, (1963) then argued that the maximum ratio of direct charged to neutral drag is given by,
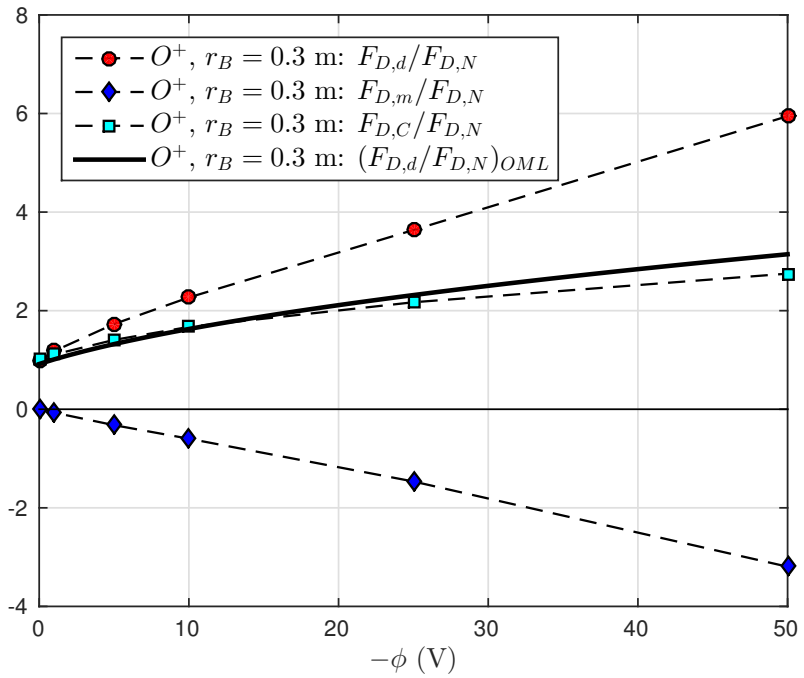
$$(F_{D,d}/F_{D,N})_{\max} = 2\frac{n_{O^+}}{n_O} \tag{4.14}$$

Given an assumed maximum oxygen ion to neutral number density ratio of 0.1 (10% ionisation of the environment), Brundin, (1963) concluded that neglecting direct ionospheric aerodynamics would result in a maximum under-estimation of total drag by 20%. Framed another way, *neglecting ionospheric aerodynamics would result in a maximum over-estimation of neutral number density by* 20% *when based on satellite accelerations*. With advances in atmospheric and aerodynamic models since the 1960s, a 20% error is now significant. For example, Doornbos, Klinkrad, and Visser, (2005) cited a desire to reduce uncertainties in atmospheric models to within 5% to achieve required SSA capabilities in a congested LEO environment.
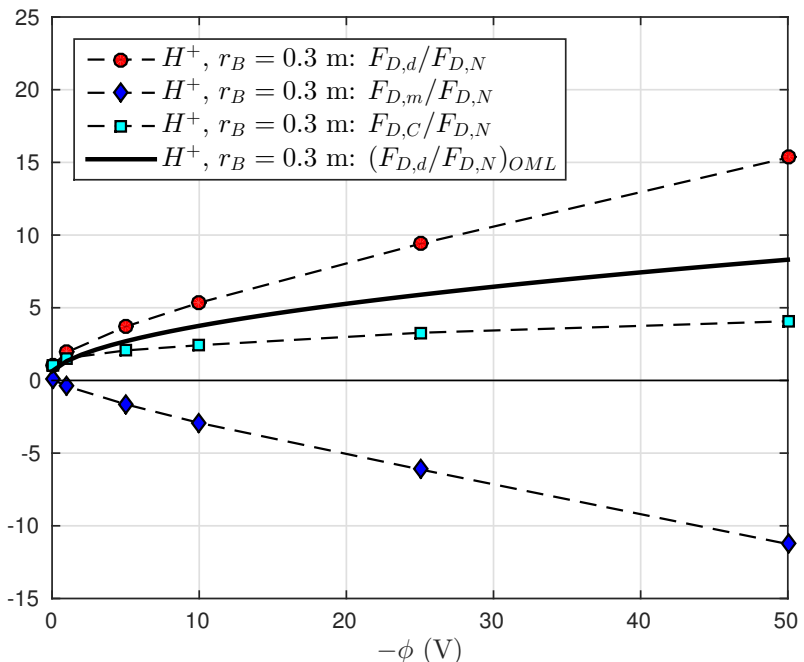
To ascertain the significance of the observations in Section 4.3 to ionospheric aerodynamic predictions, Figures 4.16 and 4.17 plot $F_{D,d}/F_{D,N}$, $F_{D,m}/F_{D,N}$ and $F_{D,C}/F_{D,n}$ against $-\phi_B$ for a 0.3 m cylinder in an O^+ (Cases 1-6) and H^+ (Cases 7-12) ionospheric plasma. Similarly, Figures 4.18 and 4.19 plot $F_{D,c}/F_{D,N}$, $F_{D,m}/F_{D,N}$ and $F_{D,C}/F_{D,N}$ against $-\phi_B$ for a 0.03 m cylinder in an O^+ (Cases 13-18) and H^+ (Cases 19-24) ionospheric plasma. $F_{D,d}/F_{D,N}$ predictions from Eqn. 4.13 are overlaid for comparison, where both analytical and numerical $F_{D,N}$ is for equivalent neutral interactions i.e. $n_i/n_n = m_i/m_n = 1$ i.e trends shown in Figures 4.16 and 4.19 are purely the result of plasma interaction phenomena.

When compared against numerical $F_{D,C}/F_{D,N}$ predictions, Eqn 4.13 under-predicts the contribution of direct charged drag to the total charged drag for all cases. As discussed previously, this under-prediction is a reflection of the additional momentum gained by the ions after accelerating through the plasma sheath. By accounting for the indirect thrust balance to counter the momentum transfer between collected ions and fields, Figures 4.16, 4.16 and 4.19 show remarkably close agreement with Eqn. 4.13. Therefore, by accounting for indirect ion accelerations we conclude that the increase in direct charged drag compared to neutral drag is caused by the enhanced ion collection area.
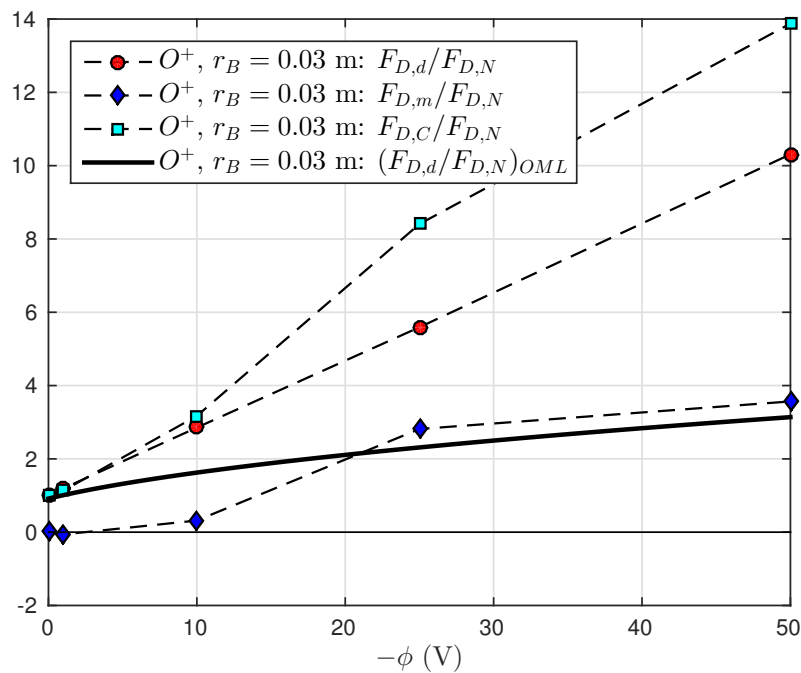
For the 0.3 m O^+ (Cases 1-6) and H^+ (Cases 7-12) flows, the indirect ion acceleration thrust outweighs the direct charged drag contribution. This leads to a charged to neutral drag
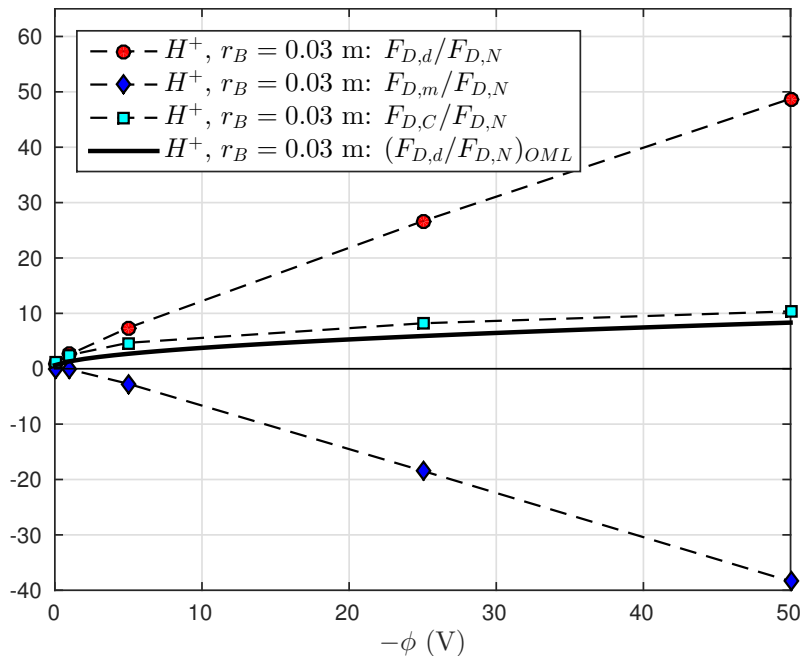
Figure 4.16: Effect of $-\phi_B$ on charged drag predictions for Cases 1-6 for $n_i/n_n = 1$. Drag measurements are from pdFOAM. Interaction quantities: O^+, $r_B = 0.3$ m.

Figure 4.17: Effect of $-\phi_B$ on charged drag predictions for Cases 7-12 for $n_i/n_n = 1$. Drag measurements are from pdFOAM. Interaction quantities: H^+, $r_B = 0.3$ m.

Figure 4.18: Effect of $-\phi_B$ on charged drag predictions for Cases 13-18 for $n_i/n_n = 1$. Drag measurements are from pdFOAM. Interaction quantities: O^+, $r_B = 0.03$ m.

Figure 4.19: Effect of $-\phi_B$ on charged drag predictions for Cases 19-24 for $n_i/n_n = 1$. Drag measurements are from pdFOAM. Interaction quantities: H^+, $r_B = 0.03$ m.

ratio less than that predicted by Eqn. 4.13. For the H^+ flows (Cases 7-12), the contribution of indirect charged drag is greater than the O^+ flows (Cases 1-6). This is consistent with observations of phenomena in Section 4.3. As the relative sheath thickness increases, the contribution of indirect charged aerodynamic forces dominate the aerodynamic interaction. This is particularly evident in the 0.03 m cases seen in Figures 4.18 and 4.19 .

Figures 4.18 and 4.19 plot the variation of charged to neutral drag with $-\phi_B$ for the 0.03 m radius cylinder cases. While both Figures 4.18 and 4.19 exhibit cases where Eqn. 4.13 is under-predicted compared to $F_{D,C}/F_{D,N}$, the trends in indirect charged drag indicate fundamentally different interactions. The trends in Figure 4.19 are largely similar to those seen in the 0.3 m cases, the indirect drag tending to cancel a portion of the direct drag. However, Figure 4.18 shows that there exist conditions where the direct and indirect charged drag contributions both tend to increase the total charged drag. This observation would be consistent with trends observed by (Knechtel and Pitts, 1965) for a small object in a flowing plasma where indirect charged drag forces were attributed to the net increase in total drag. As a consequence, Eqn. 4.13 substantially under-predicts the total charged aerodynamic forces in Figure 4.18. For example, at -50 V $F_{D,C}/F_{D,N}$ is 4.4 times larger than the $F_{D,d}/F_{D,N}$ predicted by Eqn. 4.13; numerical $F_{D,d}/FD, N$ 3.3 times larger than Eqn. 4.13 and $F_{D,m}/F_{D,N}$ causing an additional 37.5% increasing in $F_{D,C}/F_{D,N}$.

4.4.3 Review of Past Conclusions Regarding Ionospheric Aerodynamics

Following a similar line of argument as in (Brundin, 1963), the significance of charged aerodynamics based on the data presented in Figures 4.16-4.19 can be made clearer by considering the n_i/n_n required to maintain a particular $F_{D,C}/F_{D,N}$ at a given ϕ_B.

Consider for example $F_{D,C}/F_{D,N}$ for a 0.3 m cylindrical body with $\phi_B = -10$ in an O^+ and H^+ plasma. When $n_i/n_n = 1$, Figures 4.16 and 4.17 predict an $F_{D,C}/F_{D,N}$ of 2.172 and 3.286 respectively. Table 4.2 lists the n_i/n_n required to maintain particular $F_{D,C}/F_{D,N}$ ratios assuming the -10 V $F_{D,C}/F_{D,N}$ ratios remain constant with ion number density.

Contrary to the assertion in (Brundin, 1963) that $n_i/n_n \leq 0.1$, Section 2.2.1 presented plots demonstrating that n_i/n_n varies throughout the LEO environment and that there exist conditions in LEO where $n_i/n_n \to 1$. To illustrate this, Figure 4.20 plots contoured slices through altitude highlighting regions where $F_{D,C}/F_{D,N}$ would be greater than or equal to 1, 0.5 and 0.1 for a 0.3 m object in O^+ and H^+ dominated plasmas. Here n_i/n_n is calculated as in Section 2.2.1 based on NRLMSISE-00 (Picone et al., 2002) and IRI-2012 (Bilitza et al., 2014) atmospheric models. Conditions are for 4th January 2007 UT 12:00:00 with solar indices $f_{10.7} = 87.7$, $f_{10.7a} = 83.35$ and using the daily magnetic index $a_p = [17.3750, 15.0, 20.0, 15.0, 27.0, 18.125, 21.75]$. Contours for altitudes less than or equal

to 700 km show $F_{D,O^+}/F_{D,O}$, while altitude at or above 900 km show $F_{D,H^+}/F_{D,H}$ to reflect the relative dominance of O^+ and H^+ through altitude.

Figure 4.20 demonstrates that for large objects with moderate surface potentials, ionospheric aerodynamics can become significant compared to neutral in LEO. As the surface potential approaches zero, the significance of ionospheric aerodynamics compared to neutral aerodynamics rapidly decays. Based on trends in $F_{D,C}/F_{D,N}$, ionospheric aerodynamic forces become increasingly important as body scale decreases (and surface potential remains constant). *Therefore we conclude that the conclusions in Brundin, (1963) are valid for low-voltage objects provided that n_i/n_n is small. Further, that there exist a large range of conditions where this does not hold and ionospheric aerodynamic forces may become significant compared to neutral aerodynamics. Following from this, we conclude that for conditions where the surface potential of LEO objects become large, ionospheric aerodynamics forces become comparable to neutral aerodynamics forces.* This is consistent with predictions by Jastrow and Pearse, (1957).

Limitations of this Approach
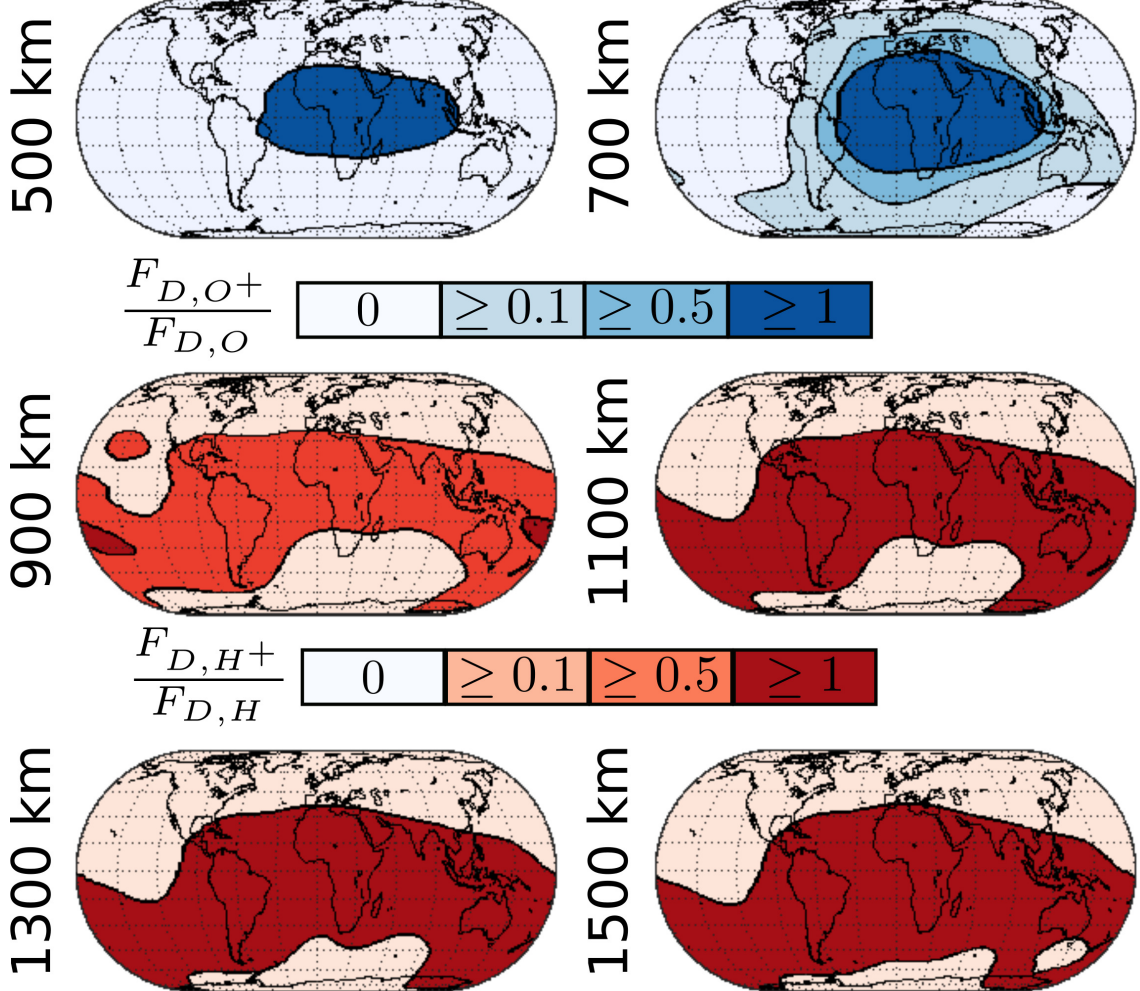
It is important to note however that the above conclusions, while illustrative, are fundamentally limited.

Based on observations in Figure 4.20, it was concluded that conclusions in (Brundin, 1963) regarding the significance of ionospheric aerodynamics compared to neutral aerodynamics are not valid for all conditions in LEO; altitudes as low as 500 km show regions where charged aerodynamic forces approach neutral aerodynamic forces for a 0.3 m cylinder at $-10V$. However, while the line of argument in (Brundin, 1963) was followed to allow a direct assessment of the validity of their conclusions, this line of argument is fundamentally limited. Specifically, *the approach employs an implicit assumption that ionospheric aerodynamic phenomena are not affected by the ion number density, orbital velocity or ion and electron temperature.*

Given the complex and non-linear coupling observed throughout this chapter between plasma-body interaction phenomena, ion mass, body radius and body potential, it is reasonable to assume that there will exist a similar variation with other interaction quantities. Quantities that describe plasma-body interactions include:ion number density (n_i), ion mass (m_i), ion temperature (T_i), ion charge (q_i), electron temperature (T_e), electron number density (n_e), body velocity (v_B), body scale (r_B) and body potential (ϕ_B) (electron mass (m_e) and charge (q_e) being constants). Characterising the variation of charged aerodynamics in LEO given the number of possible combinations of these interaction quantities represents a formidable numerical challenge. This is a similar challenge to that faced

Table 4.2: n_i/n_n required for particular $F_{D,c}/F_{D,n}$ when $F_{D,O^+}/F_{D,O} = 2.172$ and $F_{D,H^+}/F_{D,H} = 3.286$ at $n_i/n_n = 1$.

$F_{D,c}/F_{D,n}$	1	0.5	0.1
n_O^+/n_O	0.46	0.23	0.046
n_H^+/n_H	0.30	0.15	0.03

Figure 4.20: Contoured slices through altitude illustrating regional variation in $F_{D,c}/F_{D,n}$, n_i/n_n calculated using the NRLMSISE-00 (Picone et al., 2002) and IRI-2012 (Bilitza et al., 2014) atmospheric models. Conditions are for 4/1/2007 UT 12:00:00 with solar indices $f_{10.7} = 87.7$, $f_{10.7a} = 83.35$ and using the daily magnetic index $a_p = [17.3750, 15.0, 20.0, 15.0, 27.0, 18.125, 21.75]$.

in fluid dynamics however, where complex, non-linear phenomena are described by a large number of independent quantities.

This challenge is addressed in fluid dynamics by determining dimensionless parameters that describe the scaling of phenomena. These dimensionless parameters are then used as a framework within which to study and provide physical insights into phenomena. This work takes a similar approach. The dimensionless parameters that describe multi-species plasma-body interactions derived in Chapter 5 are used in Chapter 6 as a framework within which to study the influence of plasma-body interaction phenomena on charged aerodynamic forces. Chapter 7 then revisits the questions posed above regarding the significance of charged aerodynamics by applying this framework to establish whether there exist regions in LEO where ionospheric aerodynamic forces become significant compared to neutral aerodynamic forces.

4.5   Summary

The purpose of this chapter was to explore self-consistent plasma-body interaction phenomena that arise from the interaction between a mesothermal plasma and a negatively charged object to identify phenomena significant to ionospheric aerodynamics. By studying the effect of ion mass (m_i), body radius (r_B) and body potential (ϕ_B) on plasma-body interaction phenomena, the limitations of previous ionospheric aerodynamics studies, specifically those based on OML arguments, were clarified. These assumptions are that: (1) sheath thickness does not limit ion collection; (2) ion absorption barriers do not effect ion collection; (3) ion acceleration does not contribute to incident direct charged drag; (4) the momentum transfer of the ions is in the drag direction.

Based on observations of plasma-body interaction phenomena in Section 4.3, the following conclusions were drawn:

1. *Direct charged aerodynamic forces caused by the sheath enhanced ion collection dominates low-voltage plasma-body interactions.*

2. *Kinetic phenomena not accounted for by OML may have an appreciable effect on high-voltage plasma-body interactions e.g. bounded ion jets.*

3. *There exists conditions where indirect charged aerodynamic forces dominate the total charged aerodynamic force experienced by an object.*

4. *Neglecting indirect charged drag will result in the over-prediction of charged aerodynamic forces by not accounting for the indirect ion thrust required to balance the momentum exchanged with accelerated ions.*

5. *The relative sheath thickness plays a significant role in charged aerodynamics, primarily through indirect effects, and therefore any assumptions regarding the structure of the sheath that do not account for the relative sheath thickness will not capture the complexities of charged aerodynamics e.g. OML.*

These observations were further supported in Section 4.4, where the OML based direct charged aerodynamic predictions were unable to predict the trends in $F_{D,C}/F_{D,N}$ with $-\phi_B$ for different cases of ion mass and body radius. For relatively large cylinders ($r_B = 0.3$ m), OML based direct charged aerodynamic predictions over-predicted the numerical total charged aerodynamic predictions, in part reflecting the transfer of momentum into lift directions. For small cylinders ($r_B = 0.03$ m), the sheath thickness was shown not to scale with body radius and as a result the relative thickness of the sheath increased. Two different charged aerodynamic regimes were observed for the small cylinder cases.

The first regime corresponded to a regime where the total charged drag was greater than that predicted by OML theory i.e. indirect thrust forces countering ion accelerations dominated the net indirect charged aerodynamic force. The second regime corresponded to the interactions where the indirect charged drag outweighed the indirect thrust caused by ion accelerations i.e. the net indirect charged aerodynamic force was in the drag direction. As a result, the total charged drag for this second regime was enhanced by indirect charged aerodynamics forces, the indirect charged aerodynamic forces at -50 V in a O^+ flow causing a 37.5% increase in total charged drag.

To summarise, observations here demonstrate that:

1. *The relative thickness of the sheath has a significant effect on charged aerodynamic predictions.*

2. *Bounded ion jets caused by ion absorption barriers in the sheath can have an appreciable and non-linear effect on surface forces.*

3. *The ion acceleration does not contribute to the incident charged drag provided that calculations account for indirect charged drag forces.*

To emphasis the importance of these observations to ionospheric aerodynamics, conclusions regarding the significance of charged aerodynamics to LEO objects in Brundin, (1963) and Jastrow and Pearse, (1957) were re-examined. To achieve this, the ratio of ion to neutral number density (n_i/n_n) required to maintain charged to neutral drag ratios of 1, 0.5 and 0.1 at a given surface potential was considered. By calculating n_i/n_n ratios using the NRLMSISE-00 and IRI-2012 atmospheric models, it was demonstrated that there exist regions as low as 500 km altitude in LEO where a 0.3 m cylindrical object with a surface potential of -10 V would experience an ionospheric aerodynamic force larger than neutral aerodynamic forces.

Chapter 5

Organising the Flow Physics I: Derivation of Scaling Laws for Plasma-Body Interactions

5.1 Introduction

Dimensional analysis allows the reduction of a system defined by a large number of quantities to be expressed as a set of dimensionless parameters that scale system phenomena i.e. *"scaling parameters"*. By understanding the physical relationship between scaling parameters and phenomena, complex highly dimensional problems can be characterised by a significantly reduced number of experiments - whether numerical or experimental. The purpose of this chapter is to determine the set of dimensionless parameters that scale plasma-body interactions.

The scaling of plasmas has been treated by a variety of authors (Beiser and Raab, 1961; Knechtel and Pitts, 1965; Fahleson, 1967; Lam, 1969; Gurevich, Pariiskaya, and Pitaevskii, 1966; Stone, 1981a; Jeong, 2008; Samir, Wright, and Stone, 1983; Choinière and Gilchrist, 2007). Limiting this discussion to geometrically similar objects, the parameters that affect single species plasma interaction phenomena include: ion number density (n_i), ion mass (m_i), ion temperature (T_i), ion charge (q_i), electron temperature (T_e), electron number density (n_e), body velocity (v_B), body scale (r_B) and body potential (ϕ_B) (electron mass (m_e) and charge (q_e) being constants). Beiser and Raab, (1961) applied the Buckingham Pi theorem to the Navier-Stokes and Maxwell equations to determine the hydromagnetic similarity parameters of a dielectric, conducting, viscous medium. Lacina, (1971) approached the same problem from a microscopic perspective, applying the Buckingham Pi theory to the Vlasov-Maxwell system which describes the kinetic motion of ions in a plasma. The generality of the Buckingham Pi theorem is, paradoxically, both powerful and limiting.

The principle drawback to the Buckingham Pi theorem is that without careful selection of repeating variables, the physical role of the dimensionless parameters is unknown. While experimentally this may be acceptable, it is not ideal. An alternative approach is to determine the dimensionless transformation of the set of equations that govern a physical system. This was the approach taken in (Knechtel and Pitts, 1965) and (Stone, 1981a).

Knechtel and Pitts, (1965) attempted to determine the set of parameters that scale LEO plasma-body interactions by considering the dimensionless parameters that describe the linearised Poisson equation. The analysis by Knechtel and Pitts, (1965) did not account for the motion of the ions within the potential field and the subsequent coupling (see also Choinière and Gilchrist, (2007)). Stone, (1981a) accounted for this coupling by considering the electrostatic Vlasov-Maxwell system of equations with a Boltzmann electron fluid and assuming a singly charged, unmagnetised, single species plasma. By introducing the body velocity, potential, and characteristic dimension (e.g. body radius), Stone, (1981a) explicitly incorporated the body disturbance as part of their similarity analysis. As a result, Stone, (1981b) proposed that the dimensionless function Θ may define a dimensionless quantity Q, such that,

$$Q = \Theta \left(\frac{q_i}{q_e}, \frac{v_B}{\sqrt{2k_B T_e / m_i}}, \frac{r_B}{\lambda_{D,e}}, \frac{q_e \phi_B}{k_B T_e} \right) \tag{5.1}$$

The advantage of the approach in Stone, (1981b) is to clearly relate the dimensionless parameters with the governing equations, providing additional physical insight into the nature of the scaling parameters and their role in the system. However, this approach requires knowledge about a system that might be unknown e.g. the governing equations. More importantly, the non-dimensionalisation of governing equations is strongly influenced by assumptions. To demonstrate this, let us consider the assumptions that underlie the general Debye length λ_D (and electron Debye length $\lambda_{D,e}$).

The general Debye length arises from the linearised Poisson equation. Starting with the k species Poisson equation, where each species is described by a Boltzmann distribution,

$$\epsilon_0 \nabla \phi(\mathbf{x}) = - \sum_{k}^{K} q_k n_{k,\infty} \exp \left[\frac{q_k \phi(\mathbf{x})}{k_B T_k} \right] \tag{5.2}$$

The linearised Poisson's equation is obtained by applying a Taylor expansion about the exponential term in Eqn. 5.2 under the assumption that the disturbance energy is much less than the surrounding ion thermal energy ($q_k \phi(\mathbf{x}) \ll k_B T_k$),

$$\exp \left[\frac{q_k \phi(\mathbf{x})}{k_B T_k} \right] \approx 1 - \frac{q_k \phi(\mathbf{x})}{k_B T_k} \tag{5.3}$$

Applying this expansion to Eqn. 5.2, Eqn. 5.2 can be expressed as,

$$
\epsilon_0 \nabla \phi\left(\mathbf{x}\right) - \left(\sum_k^K \frac{n_{k,\infty} q_k^2}{k_B T_k}\right) \phi\left(\mathbf{x}\right) = - \overbrace{\sum_k^K \cancel{q_k n_{k,\infty}}}^{\text{quasi-neutral freestream}}{}^{0}
$$

$$
\nabla \phi\left(\mathbf{x}\right) - \lambda_D^{-2} \phi\left(\mathbf{x}\right) = 0
$$
(5.4)

where $n_{k,\infty}$ and Z_k are the reference density and charge ratio (q_k/q_e) of the kth charged species, and λ_D is the general Debye length,

$$
\lambda_D = \sqrt{\frac{\epsilon_0 k_B / q_e^2}{n_e/T_e + \sum_k^K Z_k^2 n_k / T_k}}
$$
(5.5)

The electron Debye length is then obtained under the additional restriction that $T_e \gg T_i$ such that,

$$
\lambda_{D,e} = \sqrt{\frac{\epsilon_0 k_B T_e}{q_e^2 n_e}}, \quad T_e \gg T_i
$$
(5.6)

Hence, as mentioned in Section 2.3.5, any scaling parameters that non-dimensionalise length scales using λ_D (or $\lambda_{D,e}$) restrict the applicability of the scaling parameters to low voltage systems. To be consistent, scaling parameters must all apply the same assumptions.

For example, scaling parameters that employ the electron Debye length inherently apply both the high-temperature (weakly-coupled) and cold ion assumptions and are only valid for situations these assumptions apply. The ion acoustic wave speed of species k ($v_{k,s}$) is commonly used for non-dimensionalisation of velocity terms (also seen in Section 2.3.5) and can be written as (Burgess and Scholer, 2015),

$$
v_{k,s} = \sqrt{\frac{k_B \left(\gamma_e T_e + \sum_k^K \gamma_k Z_k T_k\right)}{m_k}}, \quad \gamma_k = 1 + \frac{2}{n}
$$
(5.7)

where γ_k and γ_e are the adiabatic indices of the kth ion species and electrons respectively. γ_e is generally taken as 1 by assuming an isotropic electron temperature. γ_k is defined by the ion degrees of freedom n, where degrees of freedom refers to the ability of a real gas to transfer thermal energy into higher rotational and vibrational modes. In a collisionless plasma, $n = 1$ and $\gamma_k = 3$ (Burgess and Scholer, 2015).

The ion acoustic Mach number is then the ratio of a disturbance velocity (either flow or body velocity) with respect to the ion acoustic wave speed of species k, i.e.

$$M_i = \frac{v_{k,B}}{v_{k,s}} \tag{5.8}$$

For a system described by the Debye length $\lambda_{D,e}$, the ion terms must be dropped to remain consistent e.g.

$$M_i = \frac{v_B}{v_s} = \frac{v_B}{\sqrt{k_B T_e/m_i}}, \quad T_e \gg T_i \tag{5.9}$$

The ion acoustic Mach number M_i should not be confused with the ion thermal speed ratio (S_i),

$$S_i = \frac{v_B}{v_{t,i}} = \frac{v_B}{\sqrt{2k_B T_i/m_i}} \tag{5.10}$$

where $v_{t,i}$ is the ion thermal velocity, and the factor of 2 from kinetic theory reflects the most probable thermal velocity of a gas in three dimensions. This appears to be the case in Eqn. 5.1 for the $v_B/\sqrt{2k_B T_e/m_i}$ term.

One of the main consequences of our incomplete understanding of scaling in plasmas is the lack of a single set of parameters capable of predicting the shielding of both high and low voltage disturbances. To illustrate this point, Eqn. 5.4 suggests that the shielding of disturbances is purely dependent on the general Debye length λ_D, which is independent of $\phi_{(0)}$. However, it is well established that plasma sheaths scale with surface potential (Beiser and Raab, 1961; Laframboise and Parker, 1973; Samir, Wright, and Stone, 1983; Whipple, 1981; Choinière and Gilchrist, 2007). It is no surprise then that, as both McMahon, Xu, and Laframboise, (2005), and Choinière and Gilchrist, (2007) note, relationships for plasma-interaction phenomena established based on previous scaling parameters break down for large surface potentials ϕ_B.

One of the contributions of the present work therefore, and a necessary step in organising and understanding the essential flow physics of LEO plasma-body interactions, is to determine the link between high and low voltage sheath thickness through a general set of scaling parameters. This chapter is laid out as follows: Section 5.2 begins by determining the dimensionless parameters that govern the multi-species Vlasov-Maxwell system of equations and compares these parameters against those predicted by the Buckingham Pi theorem. Section 5.3 then discusses the physical implications of the identified scaling parameters based on their role in the governing equations. Some of these implications are explored in Section 5.5, where the ability of the scaling parameters to predict self-similar transformations is demonstrated.

5.2 Derivation of Scaling Laws

5.2.1 Dimensionless Vlasov-Maxwell Equations

Here we return to the phase-space distribution function f_k introduced in Chapter 2, the evolution of which is described by the Boltzmann equation (Boltzmann, 1872),

$$\frac{\partial f_k}{\partial t} + \mathbf{c}_k \cdot \nabla_x f_k + \frac{\mathbf{F}_\alpha}{m_k} \cdot \nabla_c f_k = \left(\frac{\partial f_k}{\partial t}\right)_{\text{coll}} \tag{5.11}$$

where the Lorentz force $\mathbf{F}_k$, describes the interaction of charged species through their mutual electric ($\mathbf{E}$) and magnetic ($\mathbf{B}$) fields (Fehske, Schneider, and Weibe, 2008),

$$\mathbf{F}_k = q_k \left(\mathbf{E}(\mathbf{x}, t) + \mathbf{c}_k \times \mathbf{B}_k(\mathbf{x}, t)\right) \tag{5.12}$$

For an electrostatic, collisionless ($(\partial f/\partial t)_{\text{coll}} = 0$) interaction, Maxwell's equations are greatly simplified; the description of $\mathbf{E}$ reduces to Poisson's equations for electrostatic field potential (ϕ) (Birdsall and Langdon, 1991),

$$\mathbf{E} = -\nabla\phi, \qquad \epsilon_0 \nabla^2 \phi = -\rho_c(\mathbf{x}) \tag{5.13}$$

where the space-charge density ($\rho_c(\mathbf{x})$) of a plasma with K ion species is given by (Birdsall and Langdon, 1991),

$$\rho(\mathbf{x}) = \left(\sum_k^K q_k n_k\right) - q_e n_e, \qquad n_k = \int f_k d\mathbf{c} \tag{5.14}$$

and n_e is described by a Boltzmann electron fluid and reference electron number density $n_{e,(0)}$,

$$n_e = n_{e,(0)} \exp\left[\frac{q_e \phi(\mathbf{x}) - \phi_\infty}{k_B T_e}\right] \tag{5.15}$$

Defining reference electron number density $n_{e,(0)}$ with respect to a quasi-neutral freestream ($\phi_\infty = 0$), $n_{e,\infty}$ can be written as,

$$n_{e,\infty} = \frac{1}{q_e} \sum_k^K q_k n_{k,\infty} = \sum_k^K Z_k n_{k,\infty} \tag{5.16}$$

Substituting Eqn. 5.14, 5.15, and 5.16 into Eqn. 5.13, the electrostatic Vlasov-Maxwell equations from Chapter 2 are generalised to describe the distribution of a K-species plasma,

$$\frac{\partial f_k}{\partial t} + \mathbf{c}_k \cdot \nabla_x f_k - \frac{q_k}{m_k} \nabla_x \phi \cdot \nabla_c f_k = 0 \tag{5.17}$$

$$\nabla^2 \phi = -\frac{q_e}{\epsilon_0} \frac{q_k}{q_e} \sum_k^K \left(n_k - n_{k,\infty} \exp\left[\frac{q_e \phi(\mathbf{x})}{k_B T_e} \right] \right) \tag{5.18}$$

To express Eqns. 5.17 and 5.18 in dimensionless form, we now introduce the following transformations:

$$
\begin{aligned}
\mathbf{x} &= r_{(0)}\mathbf{X}, & t &= \tau/\omega_{(0)}, & \mathbf{c}_k &= v_{k,(0)}\mathbf{u_k} \\
f_k &= n_{k,\infty}F_k, & \phi &= \phi_{(0)}\Phi, & q_k &= q_e Z_k \\
n_k &= n_{k,\infty}N_k, & \nabla_x &= \hat{\nabla}_X/r_{(0)}, & \nabla_c &= \hat{\nabla}_u/v_{k,(0)}
\end{aligned}
\tag{5.19}
$$

$\mathbf{X}$, τ, $\mathbf{u}$, F, Φ, Z, and $N_{i/e}$ are dimensionless parameters, and ∇_X and ∇_u are the dimensionless gradient operators in physical and velocity space respectively. Note that the characteristic disturbance $\phi_{(0)}$, frequency $\omega_{(0)}$, velocity $v_{k,(0)}$ and length scale $r_{(0)}$ remain arbitrary, while number density and particle distribution are tied to freestream conditions by the quasi-neutral freestream assumption employed to eliminate $n_{e,\infty}$ by expressing it as a function of $n_{k,\infty}$ in Eqn. 5.16.

Substituting the transformations in Eqn. 5.19 into Eqns. 5.17 and 5.18 gives,

$$\left(\frac{\omega_{(0)} r_{(0)}}{v_{k,(0)}} \right) \frac{\partial F_k}{\partial \tau} + \mathbf{u}_k \cdot \hat{\nabla}_X F_k - Z_k \left(\frac{q_e \phi_{(0)}}{m_k v_{k,(0)}^2} \right) \hat{\nabla}_X \Phi \cdot \hat{\nabla}_u F_k = 0 \tag{5.20}$$

$$\hat{\nabla}_X^2 \Phi = \sum_k^K -Z_k \frac{r_{(0)}^2 q_e n_{k,\infty}}{\epsilon_0 \phi_{(0)}} \left(N_k - \exp\left[\left(\frac{q_e \phi_{(0)}}{k_B T_e} \right) \Phi \right] \right) \tag{5.21}$$

Here we shall separate $v_{k,(0)}$ into a drift $(v_{k,(0)})$ and thermal $(v_{t,k,(0)})$ component,

$$v_{k,(0)} = v_{d,k,(0)} + v_{t,k,(0)} \tag{5.22}$$

Physically the drift component describes the relative streaming velocity between the plasma and disturbance i.e. $v_{d,k,(0)} = v_{d,k,\infty} = v_{d,k,B}$. For compactness, $v_{d,k,B}$ shall be written as $v_{k,B}$ (the relative velocity between ion species k and body). The thermal component $v_{t,k,(0)}$ on the other hand is purely a property of the plasma. As the drift component was linked to a freestream quantity, the thermal component is taken to be described by the freestream ion thermal velocity,

$$v_{t,k,\infty} = \sqrt{\frac{2k_B T_{k,\infty}}{m_k}} \tag{5.23}$$

Again, for compactness, the ion drift ratio of the kth ion species shall be written as,

$$S_k = \frac{v_{k,B}}{v_{t,k,\infty}} \tag{5.24}$$

As a result, the drift and thermal effects can be separated in Eqn. 5.20 such that,

$$\left(\frac{\omega_{(0)}r_{(0)}}{v_{k,B}}\right)\frac{\partial F_k}{\partial \tau} + \left(1 + S_k^{-1}\right)\mathbf{u}_k \cdot \hat{\nabla}_X F_k$$
$$- Z_k\left(\frac{q_e\phi_{(0)}}{m_k v_{k,B}^2}\right)\left(1 + S_k^{-1}\right)^{-1}\hat{\nabla}_X\Phi \cdot \hat{\nabla}_u F_k = 0 \tag{5.25}$$

Note that ion thermal effects have been linked with ion diffusion and deflection terms by multiplying through by $\left(1 + S_k^{-1}\right)$. There is some ambiguity in this choice. The role of this term is investigated further in Section 5.3.2.

From inspection, there are five dimensionless parameters that govern the behaviour of Eqns. 5.25 and 5.21. These are,

$$\alpha_k = -Z_k\left(\frac{q_e\phi_{(0)}}{m_k v_{k,B}^2}\right), \qquad\qquad \mu_e = \left(\frac{q_e\phi_{(0)}}{k_B T_{e,\infty}}\right),$$
$$\xi_k = -Z_k\left(\frac{r_{(0)}^2 n_{k,\infty} q_e}{\epsilon_0\phi_{(0)}}\right) \qquad\qquad \Omega_k = \left(\frac{\omega_{(0)}r_{(0)}}{v_{k,B}}\right) \tag{5.26}$$
$$S_k = v_{k,B}/v_{t,k,\infty} = v_{k,B}/\sqrt{2k_B T_{k,\infty}/m_k}$$

Substituting these parameters into Eqn. 5.21 and 5.25 gives,

$$\Omega_k\frac{\partial F_k}{\partial \tau} + \left(1 + S_k^{-1}\right)\mathbf{u}_k \cdot \hat{\nabla}_X F_k + \alpha_k\left(1 + S_k^{-1}\right)^{-1}\hat{\nabla}_X\Phi \cdot \hat{\nabla}_u F_k = 0 \tag{5.27}$$

$$\hat{\nabla}_X^2\Phi = \sum_k^K \xi_k\left(N_k - \exp\left[\mu_e\Phi\right]\right) \tag{5.28}$$

Hence, the $4 + 5K$ quantities (each ion species introducing ion properties m_k, q_k, $T_{k,\infty}$, $n_{k,\infty}$ and $v_{k,B}$) describing plasma-body interactions have reduced to $1 + 4K$ dimensionless parameters (each ion species described by its own α_k, ξ_k, S_k and Ω_k).

The relative effect of each species on Φ can be made more explicit by introducing the dimensionless parameters χ and β_k,

$$\chi = \left(\sum_k^K \xi_k\right)^{1/2} = r_B\left(-\frac{\epsilon_0\phi_{(0)}}{q_e\sum_k^K Z_k n_{k,\infty}}\right)^{-1/2}, \quad \beta_k = \frac{\xi_k}{\chi^2} = \left(\frac{Z_k n_{k,\infty}}{\sum_k^K Z_k n_{k,\infty}}\right) \tag{5.29}$$

Eqn. 5.28 can then be re-written as,

$$
\begin{aligned}
\hat{\nabla}_X^2 \Phi &= (\xi_1 + \xi_2 + ... + \xi_K) \left(\frac{\xi_1}{\xi_1 + \xi_2 + ... + \xi_K} N_1 + \frac{\xi_2}{\xi_1 + \xi_2 + ... + \xi_K} N_2 \right. \\
&\quad \left. +... + \frac{\xi_K}{\xi_1 + \xi_2 + ... + \xi_K} N_K - \exp\left[\mu_e \Phi\right] \right) \\
&= \sum_k^K \xi_k \left(\sum_k^K \left(\frac{\xi_k N_k}{\sum_k^K \xi_k} \right) - \exp\left[\mu_e \Phi\right] \right) \\
&= \chi^2 \left(\sum_k^K (\beta_k N_k) - \exp\left[\mu_e \Phi\right] \right)
\end{aligned}
\tag{5.30}
$$

The physical significance of these dimensionless parameters and the advantage of the $\chi - \beta_k$ form is discussed in Section 5.3.

To summarise:

Dimensionless Parameters

$$
\begin{aligned}
\alpha_k &= -Z_k \left(\frac{q_e \phi_{(0)}}{m_k v_{k,B}^2} \right), & \mu_e &= \left(\frac{q_e \phi_{(0)}}{k_B T_{e,\infty}} \right) \\
\chi &= r_{(0)} \left(-\frac{\epsilon_0 \phi_{(0)}}{q_e \sum_k^K Z_k n_{k,\infty}} \right)^{-1/2}, & \Omega_k &= \left(\frac{\omega_{(0)} r_{(0)}}{v_{k,B}} \right) \\
S_k &= \frac{v_{k,B}}{\sqrt{2 k_B T_{k,\infty}/m_k}}, & \beta_k &= \left(\frac{Z_k n_{k,\infty}}{\sum_k^K Z_k n_{k,\infty}} \right)
\end{aligned}
\tag{5.31}
$$

Governing Equations

$$
\begin{aligned}
\Omega_k \frac{\partial F_k}{\partial \tau} + \left(1 + S_k^{-1}\right) \mathbf{u}_k \cdot \hat{\nabla}_X F_k + \alpha_k \left(1 + S_k^{-1}\right)^{-1} \hat{\nabla}_X \Phi \cdot \hat{\nabla}_u F_k &= 0 \\
\hat{\nabla}_X^2 \Phi &= \chi^2 \left(\sum_k^K (\beta_k N_k) - \exp\left[\mu_e \Phi\right] \right)
\end{aligned}
\tag{5.32}
$$

5.2.2 Buckingham Pi Analysis

The above section derived $1+4K$ independent dimensionless parameters ($2+4K$ dependent parameters in the $\chi - \beta$ form) that govern the Vlasov-Maxwell system of equations that describes plasma-body interactions defined by $7 + 5K$ quantities (including constants k_B, ϵ_0 and q_e) with 5 independent dimensions. According to the Buckingham Pi theorem however, a system described by n quantities with m independent dimensions is described by a *minimum* of $m-n$ dimensionless parameters (Barenblatt, 1996) - two more parameters than indicated in Eqn. 5.26. This raises the question, *are there additional dimensionless groups not accounted for in Eqn. 5.26*? This section applies the Buckingham Pi theorem to address this question.

The general procedure of the Buckingham Pi theorem is simple: (1) select m repeating or *"independent"* quantities with independent dimensions. (2) express the remaining *"dependent"* quantities as a product of the independent quantities. (3) take the ratio of dependent and independent variables. These ratios are Pi-groups (Π), the set of which describes the dimensionless function Θ. We refer the reader to Barenblatt, (1996) for a comprehensive discussion of the Buckingham Pi theorem and its application.

From inspection, Eqns. 5.18 and 5.25 are described by the quantities $r_{(0)}$, $n_{k,\infty}$, T_e, T_k, ω, $v_{k,B}$, q_k, q_e, m_k, $\phi_{(0)}$, k_B and ϵ_0. For simplicity let us consider a two ion species (K=2) plasma, with species x and y. Table 5.1 outlines these quantities and their dimensions.

Applying the Buckingham Pi theorem (Barenblatt, 1996), the independent quantities listed in Table 5.1 result in the following dimensionless parameters:

$$\Pi_1 = n_{x,\infty}r_{(0)}^3 \qquad \Pi_2 = n_{y,\infty}r_{(0)}^3 \qquad \Pi_3 = m_x/m_y \quad \Pi_4 = q_x/q_e$$

$$\Pi_5 = q_y/q_e \qquad \Pi_6 = \omega r_{(0)}/v_{x,B} \quad \Pi_7 = \frac{q_e\phi_{(0)}}{m_x v_{x,B}^2} \quad \Pi_8 = \frac{m_x v_{x,B}^2}{k_B T_e} \tag{5.33}$$

$$\Pi_9 = \frac{q_e^2}{r_{(0)}m_x v_{(0)}^2 \epsilon_0} \quad \Pi_{10} = T_e/T_x \qquad \Pi_{11} = T_e/T_y \quad \Pi_{12} = v_{x,B}/v_{y,B}$$

Substituting Eqn. 5.33 into Eqns. 5.20 and 5.21 gives,

$$\Pi_6 \frac{\partial F_x}{\partial t} + \left(1 + (\Pi_8\Pi_{10})^{-1/2}\right)\mathbf{u}_x \cdot \hat{\nabla}_X F_x$$
$$- \Pi_4\Pi_7 \left(1 + (\Pi_8\Pi_{10})^{-1/2}\right)^{-1}\hat{\nabla}_X\Phi \cdot \hat{\nabla}_u F_x = 0$$
$$\Pi_6\Pi_{12}\frac{\partial F_y}{\partial t} + \left(1 + (\Pi_5\Pi_8\Pi_{11})^{-1/2}\right)\mathbf{u}_y \cdot \hat{\nabla}_X F_y \tag{5.34}$$
$$- \Pi_3\Pi_5\Pi_7 \left(1 + (\Pi_5\Pi_8\Pi_{11})^{-1/2}\right)^{-1}\hat{\nabla}_X\Phi \cdot \hat{\nabla}_u F_i = 0$$

Table 5.1: Set of independent and dependent quantities that describe LEO plasma-body interactions.

Independant Quantities	Symbol	Dimensions
Disturbance Length	$r_{(0)}$	$[L]$
Ion Mass x	m_x	$[M]$
Electron Temperature	T_e	$[T]$
Disturbance Velocity x	$v_{x,B}$	$[L][t]^{-1}$
Electron Charge	q_e	$[A][t]$
Dependant Quantities		
Freestream Number Density x	$n_{x,\infty}$	$[L]^{-3}$
Freestream Number Density y	$n_{y,\infty}$	$[L]^{-3}$
Ion Mass y	m_y	$[M]$
Ion Charge x	q_x	$[A][t]$
Ion Charge y	q_y	$[A][t]$
Disturbance Frequency	ω	$[t]^{-1}$
Disturbance Potential	$\phi_{(0)}$	$[M][L]^2[t]^{-3}[A]^{-1}$
Boltzmann Constant	k_B	$[M][L]^2[t]^{-2}[T]^{-1}$
Permittivity of Freespace	ϵ_0	$M^{-1}L^{-3}[t]^4[A]^2$
Ion Temperature x	T_x	$[T]$
Ion Temperature y	T_y	$[T]$
Disturbance Velocity y	$v_{y,B}$	$[L][t]^{-1}$

$$\hat{\nabla}_X^2 \Phi = - \Pi_1\Pi_4\Pi_7^{-1}\Pi_9 \left(N_x - \exp\left[\Pi_7\Pi_8\Phi\right]\right)$$
$$- \Pi_2\Pi_5\Pi_7^{-1}\Pi_9 \left(N_y - \exp\left[\Pi_7\Pi_8\Phi\right]\right) \tag{5.35}$$

From inspection, the relationship between Eqn. 5.33 and the parameters in Eqn 5.26 is,

$$\begin{aligned}
&\alpha_x = -\Pi_3\Pi_4 & &\alpha_y = -\Pi_3\Pi_4 & &\xi_x = -\Pi_1\Pi_4\Pi_7^{-1}\Pi_9 \\
&\xi_y = -\Pi_2\Pi_5\Pi_7^{-1}\Pi_9 & &S_x = (\Pi_8\Pi_{10})^{1/2} & &S_y = (\Pi_5\Pi_8\Pi_{11})^{1/2} \\
&\Omega_x = \Pi_6 & &\Omega_y = \Pi_6\Pi_{12} & &\mu_e = \Pi_4\Pi_5
\end{aligned} \tag{5.36}$$

In other words, each set of Π-group that scale a particular phenomena can be grouped as a single scaling parameter. Provided that the full set of Π-groups is represented in the set of scaling parameters, the Buckingham Pi theorem is satisfied. Hence, the results from the previous section are recovered; the $1+4K$ dimensionless parameters identified in Eqn. 5.26 contain the complete set of Π-groups. Here, the reduction in scaling parameter beyond that predicted by Buckingham Pi theorem is possible because several Π groups scale the same term. Another advantage of knowing the relationship between scaling parameters and governing equations is that further physical insights into their nature can be made that cannot be identified by Π-groups alone.

5.3 Physical Interpretation of Scaling Parameters

In Section 5.2, non-dimensionalisation of the K species Vlasov-Maxwell system of equations resulted in the identification of $1 + 4K$ independent dimensionless parameters and $2 + 4K$ dimensionless parameters in the $\chi - \beta_k$ form - the $\chi - \beta_k$ form is used from here on in this work. A subsequent analysis of the system using the Buckingham Pi approach showed that these parameters constitute a complete set of Π-groups and therefore represent physically relevant scaling laws. We now consider the nature and role of these scaling parameters in plasma-body interactions based on Eqns. 5.27 and 5.30.

5.3.1 α_k: Ion Deflection Parameter

Physically, α_k is the ratio of disturbance potential energy (P.E.) to kinetic energy (K.E).

$$\alpha_k = -\frac{1}{2}\frac{2Z_k q_e \phi_{(0)}}{m_k v_{(0)}^2} = \frac{1}{2}\frac{P.E.}{K.E.} \tag{5.37}$$

The role of α_k in Eqn. 5.32 is to scale the deflection of ions by electrical disturbances i.e. $\nabla\Phi$. The relative sign between Z_k and $\phi_{(0)}$ controls the direction of ion deflection. For example, positive ions will be deflected toward a negative disturbance ($\phi_{(0)} < 0$), following the potential gradient $\nabla\Phi$. Conversely, negative ions will be deflected away from positive disturbances, impeded by $-\nabla\Phi$. Similarly the magnitude of the deflection is related to $|\alpha_k|$. As $|\alpha_k| \to 0$, the ion kinetic energy dominates the motion of the ions, decoupling their motion from the electric field. In the converse limit, when $|\alpha_k| \to \infty$, the motion of the ions becomes dominated by their potential energy. In essence, α_k describes the deflection of ions by field effects, and hence, it is called here the *"ion deflection parameter"*.

With regard to the prior scaling relationships identified previously, the single species form of α_k was also identified by (Knechtel and Pitts, 1965), who included the factor of 2 for the kinetic energy component. While (Knechtel and Pitts, 1965) limited $\phi_{(0)}$ to the body potential ϕ_B, as we shall show in Section 5.4, this is not necessary. α_k also appears in various expressions throughout the literature. For example, in the OML impact parameter b_{OML},

$$b_{OML} = r_B \left(1 - \frac{2q_e \phi_B}{m_i v_\infty^2}\right)^{1/2} = r_B \left(1 - 2\alpha_k\right)^{1/2} \tag{5.38}$$

as well as in dusty plasma aerodynamic literature, such as expressions in (Hutchinson, 2006), A more comprehensive investigation of α_k, its influence on plasma-interaction phenomena and its appearance in prior work is found in Chapter 6.

5.3.2 S_k: Ion Thermal Ratio

By splitting $v_{k,(0)}$ into a drift $v_{d,k,(O)}$ and thermal component $v_{t,k,(0)}$, the effect of ion thermal energy on Eqn. 5.27 becomes explicit. S_k is the ratio of these velocity components,
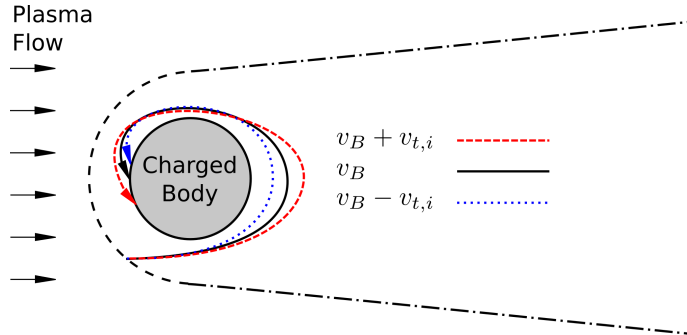
$$S_k = \frac{v_{d,k,(0)}}{v_{t,k,(0)}} = \frac{v_{k,B}}{\sqrt{2k_B T_k/m_k}} \tag{5.39}$$

S_k is a fairly standard non-dimensionalisation of ion drift (streaming) velocity and is generally referred to as the *"ion thermal ratio"* (Gurevich, Pitaevskii, and Smirnova, 1970). Hence, we shall follow this nomenclature.

In the hyper-thermal limit where the drift velocity is much larger than the thermal velocity ($v_{k,B} \gg v_{t,k,\infty}$ or $S_k \to 0$), the evolution of the particle distribution F_k becomes decoupled from thermal effects. In the converse limit, as the thermal velocity becomes large ($S_i \gg 1$) the diffusion term in Eqn. 5.27 is enhanced by the ion temperature and the deflection of ions by field effects is dampened. To illustrate this, diffusion and deflection terms are labelled in Eqn. 5.40 As with the ion deflection parameter α_k, if $S_k \to 0$ (thermal velocity dominates over drift velocity) and the ion thermal energy is much greater than the disturbance energy ($m_k v_{t,k,\infty}/Z_k q_e \gg \phi_{(0)}$), then ion motion is decoupled from field effects and the system becomes thermally dominated.

$$\Omega_k \frac{\partial F_k}{\partial \tau} + \underbrace{\left(1 + S_k^{-1}\right)}_{\text{ion diffusion term}} \mathbf{u}_k \cdot \hat{\nabla}_X F_k + \overbrace{\alpha_k \left(1 + S_k^{-1}\right)^{-1} \hat{\nabla}_X \Phi \cdot \hat{\nabla}_u F_k}^{\text{ion deflection term}} = 0 \tag{5.40}$$

In the context of a mesothermal flow, such as that found in LEO, thermally dominated interactions are unlikely for O^+ flows ($v_{O^+,B} \gg v_{O^+,t,\infty}$). As altitude increases and H^+ ions dominate the flow, $S_{H^+} \to 1$ and ion thermal effects may become significant. As the ion thermal ratio approaches unity ($S_k \to 1$), Eqn. 5.40 predicts two effects. The first is to cause a small increase in the resistance of ions to field deflections compared to the drift velocity. Depending on the magnitude of S_k, this effect may be neglected. The second, and more important effect, is the increase of thermal ion diffusion which is *independent* of field effects. In effect, S_k will tend to diffuse mesothermal plasma phenomena. Figure 5.1 provides an illustrative example of the physical basis for this conclusion. The black solid line represents the path followed by an ion at a representative drift velocity, the dashed red and blue lines represent the paths followed by ions which have entered the sheath with velocities greater than and less than the drift velocity by the ion thermal velocity, respectively (the ion thermal velocity being a uniform velocity distribution).

Figure 5.1: Illustration of the effect of T_i on plasma phenomena.

5.3.3 χ: General Shielding Ratio

By expressing the governing equations in the $\chi - \beta$ form, the dimensionless parameters that govern plasma body interactions was increased from 1+4K to 2+4K. The reason for this substitution was to express Eqn. 5.40 in a form that can be directly related to prior shielding expression. χ is written as,

$$\chi = r_B \left(-\frac{\epsilon_0 \phi_{(0)}}{q_e \sum_k^K Z_k n_{k,\infty}} \right)^{-1/2} \tag{5.41}$$

Let us now define the parameter λ_ϕ,

$$\lambda_\phi = \sqrt{-\frac{\epsilon_0 \phi_{(0)}}{q_e \sum_k^K Z_k n_{k,\infty}}} \tag{5.42}$$

Eqn. 5.41 can now be written in the form,

$$\chi = \frac{r_B}{\lambda_\phi} \tag{5.43}$$

Therefore, χ appears functionally similar to prior expressions for the scaling of sheath thickness in terms of λ_D seen in Table 2.1 i.e. r_B/λ_D. Let us consider the case where the potential energy of the disturbances $\phi_{(0)}$ equals the thermal energy of the freestream plasma e.g. $\phi_{(0)} = k_B \left(T_e + \sum_k^K Z_k^{-1} T_k \right) / q_e$. λ_ϕ then becomes,

$$
\begin{aligned}
\lambda_\phi &= \left(\frac{\epsilon_0 k_B / q_e}{\sum_k^K Z_k n_{k,\infty}/T_e + \sum_k^K Z_k^2 n_{k,\infty}/T_k} \right)^{1/2} \\
&= \left(\frac{\epsilon_0 k_B / q_e^2}{n_e/T_e + \sum_k^K \gamma_k Z_k^2 n_k/T_k} \right)^{1/2} = \lambda_D, \qquad q_e n_e = \sum_k^K q_e Z_k n_k
\end{aligned}
\tag{5.44}
$$

In other words, within the high-temperature (weak-coupling) assumption used in the linearisation of Poisson's equation, $\lambda_\phi = \lambda_D$. Similarly, under the additional cold ion assumption, $\lambda_\phi = \lambda_{D,e}$. Hence, the scaling relationships for shielding in low voltage plasma-interactions recovered from λ_ϕ.

Based on the role of χ in Eqn. 5.40, χ (and r_B/λ_D) describes shielding of electrical disturbances. As the body size becomes large compared to λ_ϕ, $\nabla^2\Phi \to \infty$ and the distance that electrical disturbances travel approaches zero i.e. the electric field of space-charge disturbances are strongly shielded. In the converse limit, as $r_{(0)}/\lambda_\phi \to 0$, $\nabla^2\Phi \to 0$ and the disturbance is described by Laplace's equation i.e. electrical disturbances move toward infinity. Unlike r_B/λ_D, χ captures the influence of the disturbance's energy on the shielding of the disturbance i.e. it is coupled relationship. To demonstrate this, let us now consider high-voltage (space-charge limited) sheaths.

Applying the Child-Langmuir law to a high-voltage cathode, the space-charge limited ion current (I_i) between two charge infinite flat plates separated by distance d is calculated as (Benilov, 2008),

$$I_i = \left(\frac{32 q_e \epsilon_0^2 \phi_B^3}{81 m_i d^4} \right) \tag{5.45}$$

In the typical application of Eqn. 5.45, the voltage and distance between electrodes is known, and the aim is to calculate the current density that can flow when the system is space-charge limited (Benilov, 2008). When considering a high-voltage near-cathode sheath in a plasma discharge, d represents the ion sheath thickness d_{sh}. In this case, I_i is a result of the plasma-body interaction, and the voltage of the body is known. Eqn. 5.45 can then be used to solve for d_{sh} given some I_i. Benilov, (2008) demonstrated that by introducing the characteristic ion density in the sheath $n_{i,S} = I_i/q_i \sqrt{q_e \phi_B/m_i}$ and assuming all electrons are repelled by the sheath ($n_e = 0$), I_i can be eliminated from Eqn. 5.45, such that,

$$\frac{r_{i,S}}{r_B} = \frac{2^{5/4}}{3} \frac{1}{r_B} \sqrt{\frac{\epsilon_0 \phi_B}{q_i n_i}} = \frac{2^{5/4}}{3} \frac{\lambda_\phi}{r_B} = \frac{2^{5/4}}{3} \chi^{-1} \tag{5.46}$$

In other words, *the Child-Langmuir law applied to high-voltage cathodes predicts an inverse dependence of χ on d_{sh} (and the proportionality of λ_ϕ).* Therefore, λ_ϕ describes the generalised shielding of electrical disturbances in a plasma, becoming the general Debye length in the high-temperature (weak-coupled) limit and describing the Child-Langmuir law applied to high-voltage cathodes. Hence, we refer to χ as the *"general shielding ratio"*, λ_ϕ being the *"general shielding length"*.

5.3.4 β_k: Ion Coupling Parameter

The influence of β_k becomes clearer by re-writing it in terms of the charge density of species k ($\rho_{c,k}$),

$$\beta_k = \left(\frac{Z_k n_{k,\infty}}{\sum_k^K Z_k n_{k,\infty}} \right) = \frac{\rho_{c,k}}{\sum_k^K \rho_{c,k}} \tag{5.47}$$

Hence, β_k describes the relative contribution of ion species k to electrical disturbances through its contribution to the total ion space-charge density. As $\beta_k \to 0$, the contribution of the k ion species goes to zero and Φ is governed by the remaining species. In essence, β_k describes the relative coupling of ions species k with electrical disturbances and, hence, we call it the *"ion coupling parameter"*.

5.3.5 μ_e: Electron Energy Coefficient

μ_e is a common non-dimensionalisation of potential energy against electron thermal energy (Knechtel and Pitts, 1965; Whipple, 1981; Stone, 1981a; Godd and Laframboise, 1983). Based on Eqn. 5.32, the role of μ_e is to dampen or enhance the ability of the electron distribution to respond to electrical disturbances caused by the ion distribution. The disturbance caused by a localised abundance of ions ($\phi_{(0)} > 0$) attracts electrons and causes an increase in N_e scaled by μ_e as described by the dimensionless Boltzmann electron fluid,

$$N_e = \exp\left[\mu_e \Phi\right] \tag{5.48}$$

The converse is also true, a localised depletion of ions ($\phi_{(0)} < 0$) dampens the ability of electrons to populate this area. The degree of enhancement or damping is then described by the relative energy of the electrons compared to the disturbance energy. In essence, μ_e describes the relative energy between a disturbance and the Boltzmann electron fluid and we refer to it as the *"electron energy coefficient"*.

5.3.6 Ω_k: Ion Temporal Parameter

Ω describes the transit time of a disturbance relative to its frequency $\omega_{(0)}$. Without knowing the nature of the characteristic frequency $\omega_{(0)}$, Ω cannot be used as a scaling parameter. Nevertheless, the effect of Ω is to scale any temporal fluctuations in F_k. It implies that if temporal effects are to be scaled, then the scaling of any frequency effects must preserve the transit time of an ion across the disturbance (Stone, 1981a). Conversely, in the steady-state limit, Ω can be neglected. Stone, (1981a) also identified this parameter and referred to it as the *"temporal parameter"* Ω, hence we follow their nomenclature.

5.4   Example Application of Scaling Parameters: Ion Acoustic Waves

The reason for not specifying a particular location (such as a body) for $\phi_{(0)}$ and $r_{(0)}$ in the above discussion is to emphasize the generality of the derivations. To demonstrate the utility of the identified scaling parameters to plasma phenomena in general, we shall consider the parameters that describe the edge of an ion acoustic wave (i.e. the rarefaction wave edge (r)).

The disturbance energy at the wave edge will be proportional to the surrounding thermal energy of the plasma. To start, let us assume that,

$$\phi_{(r)} = \frac{k_B}{q_e} \left(T_e + \sum_k^K \gamma_k Z_k^{-1} T_k \right) \tag{5.49}$$

where the ion adiabatic index γ_k has been included for completeness.

The ion deflection parameter α_k then becomes,

$$\alpha_k = \frac{k_B \left(T_e + \sum_k^K \gamma_k Z_k^{-1} T_k \right)}{m_k v_{k,B}^2} = M_k^{-2} \tag{5.50}$$

and the general shielding ratio at (r) becomes,

$$\chi = r_{(r)} \left(\frac{\epsilon_0 k_B / q_e}{\sum_k^K Z_k n_{k,\infty}/T_e + \sum_k^K Z_k^2 n_{k,\infty}/T_k} \right)^{-1/2} = \frac{r_{(r)}}{\lambda_D} = \frac{\lambda_D}{\lambda_D} = 1 \tag{5.51}$$

Note that $r_{(0)}$ has been taken at the rarefaction wave edge to be consistent. Based on the definition of λ_D as the shielding length in a plasma, it is reasonable to assume that the characteristic disturbance length at the wave edge is equal to the shielding length i.e. $r_{(r)} = \lambda_D$). Therefore, the general shielding ratio becomes $\chi = 1$. Similarly, substituting $\phi_{(r)}$ into μ_e and $r_{(r)}$ in Ω_k and letting $\omega_{(r)}$ equal the electron plasma frequency ω_{pe} gives,

$$\Omega_k = \frac{\omega_{pe} \lambda_D}{v_{k,B}}, \quad \mu_e = 1 + \sum_k^K \frac{\gamma_k Z_k T_k}{T_e} \tag{5.52}$$

Taking advantage of the steady-state (electrostatic) nature of the wave edge ($\partial F_k / \partial \tau = 0$) Ω_k can be dropped. Substituting the above parameters into Eqn 5.32 gives,

$$
\left(1 + S_k^{-1}\right) \quad \mathbf{u}_k \cdot \hat{\nabla}_X F_k \tag{5.53}
$$
$$
+ M_i^{-2} \left(1 + S_k^{-1}\right)^{-1} \hat{\nabla}_X \Phi \cdot \hat{\nabla}_u F_k = 0
$$
$$
\hat{\nabla}_X^2 \Phi = \quad \sum_k^K \left(\beta_k N_k\right) - \exp\left[\left(1 + \sum_k^K \frac{\gamma_k Z_k T_k}{T_e}\right) \Phi\right]
$$
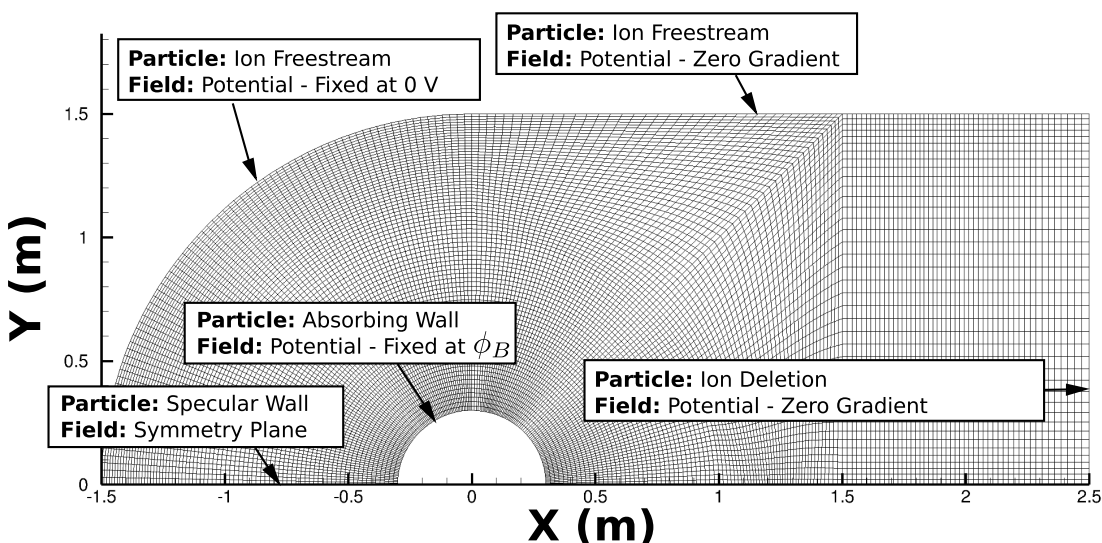
Eqn. 5.53 implies that the deflection of ions at the wave edge is scaled by the ion acoustic Mach number and ion thermal ratio. As discussed in Section 5.3.2, the ion thermal velocity tends to suppress ion deflections as $v_{t,k} > v_{k,B}$, while enhancing the diffusion of ions independent of the wave deflections. Meanwhile, the ratio of ion temperature to electron temperature enhances the dimensionless potential exponent in the Boltzmann electron distribution i.e. for $\Phi < 0$, the ion temperature tends to impede the ability of ions to penetrate the disturbance, for $\Phi > 0$, it enhances it. In the limit that $T_e \gg T_i$ and $v_{k,B} \gg v_{k,B}$, Eqn. 5.53 implies that the wave edge is purely defined by the ion acoustic Mach number in a single species plasma. This is consistent with prior observations (Stone, 1981a; Wang, 1991; Wang and Hastings, 1992b; McMahon, Xu, and Laframboise, 2005; Choinière and Gilchrist, 2007). The above application of the scaling parameters provides a consistent theoretical basis to support these observations.

5.5   Self-Similarity of Plasma-Body Interactions

A consequence of the Buckingham Pi theorem is that two systems will be identical in dimensionless space if the product of dimensioned quantities within the Π-groups causes the two systems to have an identical and complete set of Π-groups values. This is known as *"self-similarity"*, where two systems with different system quantities experience an identical interaction because phenomena in each system, described by the scaling parameters, are identical. If flow physics is preserved then the flow structures that lead to, for example, charged aerodynamic forces, must also be preserved. The purpose of this section is to develop confidence in the identified scaling parameters as a means to organise and scale plasma-body interactions by demonstrating the ability of the scaling parameters to predict self-similar flow transformations.

5.5.1   Self-Similar Transformation Methodology

Four self-similarity transformations are demonstrated: three single species transformations matching dissimilar ion species, body size, and body potential respectively; and a multi-species transformation matching the interaction of plasma mixtures with dissimilar ion charges. The general approach in each transformation is to consider two reference interactions R_1 and R_2 that differ in some aspect e.g. ion species. The self-similarity transformation required to make the R_2 match R_1 is then denoted as $S_{2\to1}$.

Figure 5.2: Simulation topology with particle and field boundary conditions. Every tenth node shown for clarity.

Numerical setup was identical to Chapter 4, and super-particle density was varied with number density to maintain a minimum of 1 million particles at initialisation. Figure 5.2 illustrates the computational setup for cylinder simulations (setup is identical for the flat plate case in Section 5.5.4). Flow is from left to right, particle and field boundary conditions are listed, and every tenth node is shown for clarity. The simulation time step is 5×10^{-8} s for cases where $v_B \leq 10$ km/s and 1×10^{-9} s for those at different velocities greater than 10 km/s. Reference plasma conditions (R_1) are taken from Hastings, (1995) representing the mean ionospheric conditions experienced by the EOS satellite during a period of mean sunspot activity.

5.5.2 Transformation 1: Ion Mass

Consider two identical single species plasma-body interactions with ion mass $m_{(R_1)}$ and $m_{(R_2)}$ where $m_{(R1)} \neq m_{(R_2)}$. The self-similarity of different ion species requires the scaling of only α_k, the remaining scaling parameters being independent of m_k (except for S_k as will be discussed in Section 5.5.4). One application of this scaling transformation is in experimental facilities e.g. the study of O^+ LEO plasma-body interactions using an Ar ion source. An available experimental parameter is the flow velocity v_B. By scaling $v_{B,(R_2)}$, the ion deflection parameters $\alpha_{(R_1)}$ and $\alpha_{(S_{2\to1})}$ are similar when,
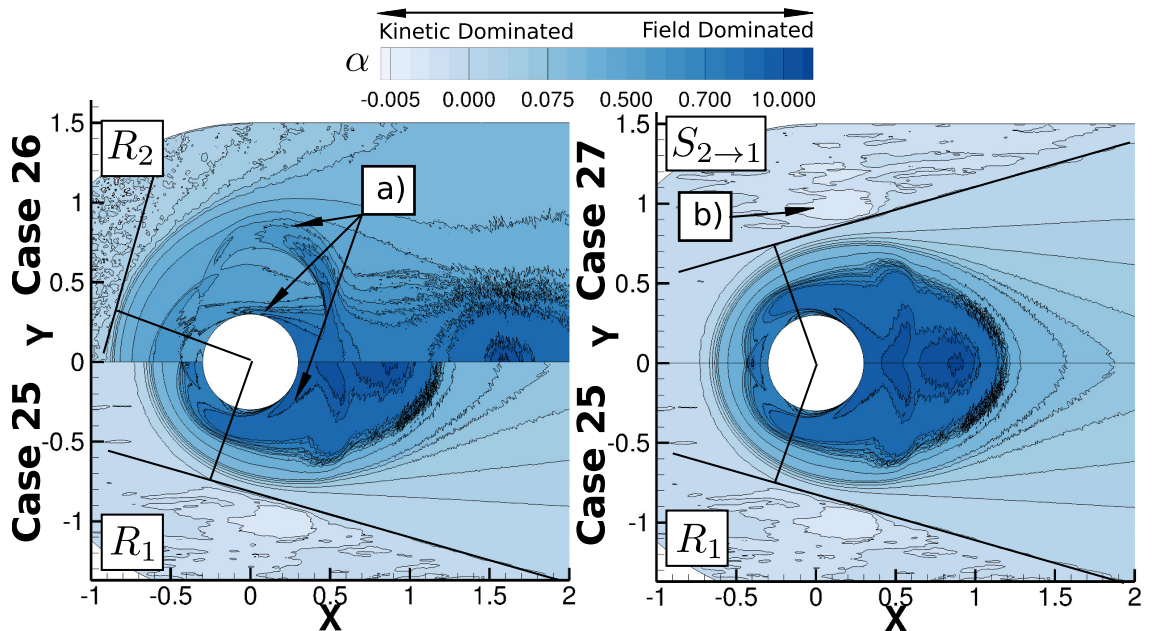
$$v_{B,(S_{2\to1})} = \left(m_{(R_1)}/m_{(R_2)}\right)^{1/2} v_{B,(R_1)} \tag{5.54}$$

From an ionospheric aerodynamic context, this transformation implies that there exist conditions where O^+ and H^+ dominated flows are similar for a given orbital velocity. Among other parameters, Chapter 4 examined the effect of ion mass on plasma-body interactions. In comparing the flow of O^+ and H^+ flows over a 0.3 m cylinder with a surface potential of -50 V compared to the freestream plasma, it was argued based on OM theory that drastic changes in sheath structure were primarily a reflection of the ratio of potential to kinetic energy, or as demonstrated in this chapter, α. These cases are reproduced in Figure 5.3 (top), which compares the flow of an O^+ (Case 25) and H^+ (Case 26) plasma over a 0.3 m cylinder with a surface potential of -50 V compared to the freestream plasma. In line with the physical description of α_k, Case 26 is dominated by field effects, reflected by the sheath expansion and the capture of ions that escape the sheath in Case 25 (a reflection of the larger kinetic energy).

Figure 5.3 (bottom) compares the scaled flow $S_{2\to1}$ (Case 27) against the reference flow R_1 (Case 25). Table 5.2 lists the interaction quantities for Cases 25-27. The bold values in Table 5.2 highlight the link between interaction quantities and scaling parameters. Excellent qualitative agreement is shown between Case 25 and 27: the sheath compression, wake elongation, rarefaction wave angle and collection of unbounded and bounded ion jets of the O^+ case all reproduced by the H^+ case. Hence, by balancing the ratio of body potential energy and incident ion kinetic energy, the flow physics of R_1 is preserved in $S_{2\to1}$, supporting the assertion that α_k describes the deflection of ions by field effects.

Table 5.2: Interaction parameters for self-similar scaling of ion mass example. Bold numbers highlight the effect of scaled parameters on dimensionless parameters. Ion thermal effects are not scaled.

Case	$\phi_{(B)}$ (V)	$r_{(B)}$ (m)	$v_{(B)}$ (km/s)	m ($10^{-27}kg$)	n_∞ ($10^{10}m^{-3}$)	T_e (K)
25 (R_1)	-50	0.3	7.5	26.55	4	1997
26 (R_2)	-50	0.3	7.5	**1.67**	4	1997
27 ($S_{2\to1}$)	-50	0.3	**29.9**	**1.67**	4	1997

	α_k	χ	μ_e
25 (R_1)	5.364	1.1414	-290.5
26 (R_2)	**85.2785**	1.1414	-290.5
27 ($S_{2\to1}$)	**5.364**	1.1414	-290.5

Figure 5.3: Self-similar transformation of O^+ (R_1) and H^+ flows (R_2). The scaled H^+ ($S_{2\to1}$) has flow velocity is $v_{(S_{2\to1})} = 4v_{(R_1)}$. Full flow conditions are listed in Table 5.2 case 25-27. Rarefaction angle measures are overlaid to aid comparison of fields. a) bounded ion jets, b) ion pseudo-wave

5.5.3 Transformation 2: Body Scale

Consider for example two identical plasma flows about a body $r_{B,(R_1)}$ and $r_{B,(R_2)}$ where $r_{B,(R_1)} \neq r_{B,(R_2)}$. By scaling $n_{(R_1)}$ to $n_{\infty,(S_2 \to 1)}$, the physics scaled by the general shielding ratio χ will be preserved when,

$$n_{\infty,(S_2 \to 1)} = \left(\frac{r_{B,(R_1)}}{r_{B,(R_2)}} \right)^2 n_{\infty,(R_1)} \tag{5.55}$$

Note that $T_{e,(R_2)}$ or $\phi_{B,(R_2)}$ could also have been scaled in this interaction. The drawback of these variables is that T_e scales both χ and μ_e, while $\phi_{(0)}$ scales χ, α and μ_e; the latter is demonstrated in Section 5.5.4.
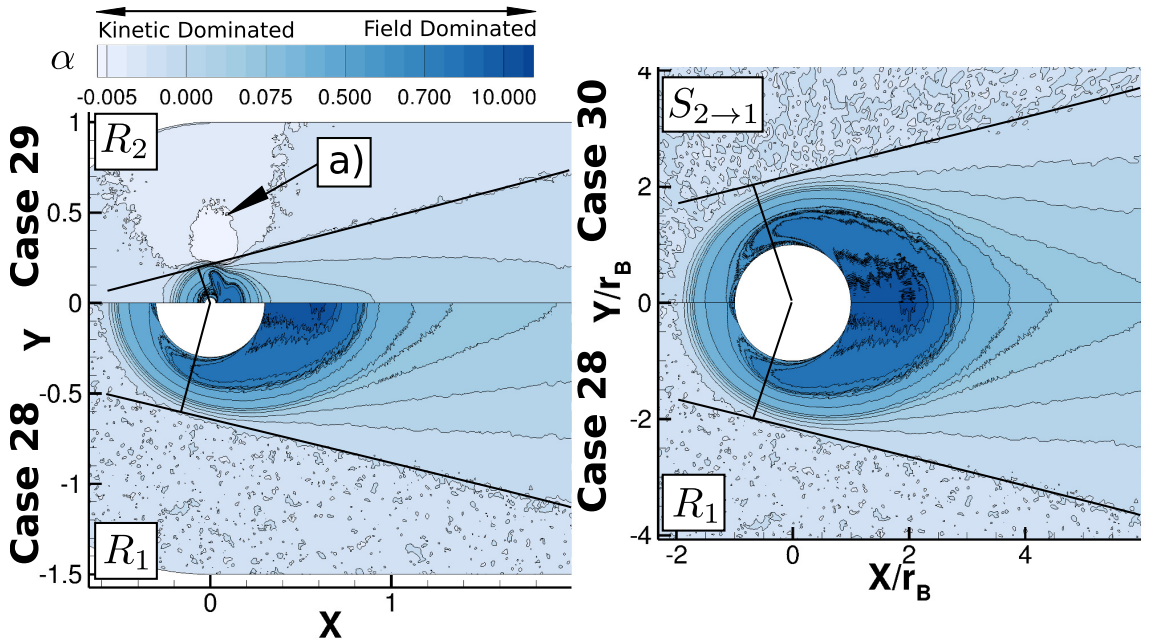
Figure 5.4 (top) compares the interaction of an O^+ plasma with two cylinders with radii 0.3 m (Case 28) and 0.03 m (Case 29) at $-25V$. Again the general features of mesothermal plasma body interactions have been reproduced. As predicted in Section 5.4, r_B has little effect on the rarefaction angle, the measured rarefaction angle in Case 28 and Case 29 being $13.4^o \pm 2^o$ and 14.5 ± 2° respectively. Again, this compares well with a predicted θ_r of 14.3.

As discussed in Section 5.3, the commonly used shielding ratio $r_B/\lambda_{D,e}$ does not accurately predict sheath thickness near high-voltage objects (fundamentally limited by $q_e\phi_B \ll k_B T_e$ and $T_e > T_i$ assumptions). The electron Debye length in Case 28 and 29 is 1.54 cm, compared to a predicted general shielding length of 18.58 cm. Comparing this with Figure 5.4 (top) and taking the sheath edge where $\alpha = 0.1$, the sheath thickness in Case 28 and Case 29 is 19.5 ± 1 cm and 18 ± 1 cm, agreeing well with λ_ϕ. While the relationship between sheath thickness and λ_ϕ is thoroughly explored in Chapter 6, Figure 5.4 (top) clearly demonstrates that the fore-body sheath thickness is much larger than 1.54 cm, much closer to 18.58 cm in both cases.

Figure 5.4 (bottom) further supports our assertion that λ_ϕ describes the shielding of an object at an arbitrary surface potential, showing the reference flow R_1 (Case 28) compared against the scaled flow $S_{2 \to 1}$ (Case 30) (with a 10^2 increase ion number density) in dimensionless space r_B/λ_ϕ. Table 5.3 lists the interaction quantities for Cases 28-30. The bold values in Table 5.3 highlight the link between interaction quantities and scaling parameters. Figure 5.4 demonstrates the scaling of sheath structure in dimensionless space, the increase in number density causing a reduction in sheath thickness in Case 30 to match Case 28. Overall, the scaling parameter χ was been demonstrated to successfully preserve self-similarity in this transformation. It is worth noting that the number density transformation is implied by both λ_ϕ and λ_D. To demonstrate that λ_ϕ is correct requires a scaling transformation of λ_ϕ not implied by λ_D e.g. the body potential ϕ_B.

Table 5.3: Interaction parameters for self-similar scaling of body scale example. Bold numbers highlight the effect of scaled parameters on dimensionless parameters. Ion thermal effects are not scaled.

Case	$\phi_{(B)}$ (V)	$r_{(B)}$ (m)	$v_{(B)}$ (km/s)	m $(10^{-27}kg)$	n_∞ $(10^{10}m^{-3})$	T_e (K)
28 (R_1)	-25	0.3	7.5	26.55	4	1997
29 (R_2)	-25	**0.03**	7.5	26.55	4	1997
30 ($S_{2\to1}$)	-25	**0.03**	7.5	26.55	**400**	1997

	α_k	χ	μ_e
28 (R_1)	2.682	1.6142	-145.27
29 (R_2)	2.682	**0.1614**	-145.27
30 ($S_{2\to1}$)	2.682	**1.6142**	-145.27

Figure 5.4: Self-similar transformation of 0.3 m radius cylinder (R_1) and 0.03 m radius cylinder (R_2). The scaled ion number density in of the 0.03 m cylinder in $S_{2\to1}$ is $n_{(S_{2\to1})} = 10n_{(R_1)}$. Full flow conditions are listed in Table 5.3 case 28-30. Rarefaction angle measures are overlaid to aid comparison of fields. a) Ion pseudo-wave.

5.5.4 Transformation 3: Body Potential

A key limitation of previous scaling parameters is their limitation to low voltage objects, whether explicit or implicitly through the use of λ_D. This section demonstrates the ability of the scaling parameters to predict the self-similar scaling transformation of two high-voltage objects, R_1 and R_2. To preserve the flow physics of the R_1 requires scaling of α_k, χ and μ_e. This can be achieved, for example, by scaling v_B, $n_{i,\infty}$ and T_e such that,

$$
\begin{aligned}
v_{B,(S_{2\to1})} &= \left(\phi_{B,(R_2)}/\phi_{B,(R_1)}\right)^{1/2} v_{B,(R_1)} \\
n_{\infty,(S_{2\to1})} &= (\phi_{B,(R_2)}/\phi_{B,(R_1)})n_{\infty,(R_1)} \\
T_{e,(S_{2\to1})} &= (\phi_{B,(R_2)}/\phi_{B,(R_1)})T_{e,(R_1)}
\end{aligned}
\tag{5.56}
$$

These transformations are important as they apply a combination of transformations not predicted by past scaling relationships as outlined in Section 2.3.5. Further, the scaling parameters are not limited to cylindrical geometries but rather geometrically similar objects. This section considers the scaling of a thin flat plate to demonstrate the applicability of the scaling parameters to different geometries.
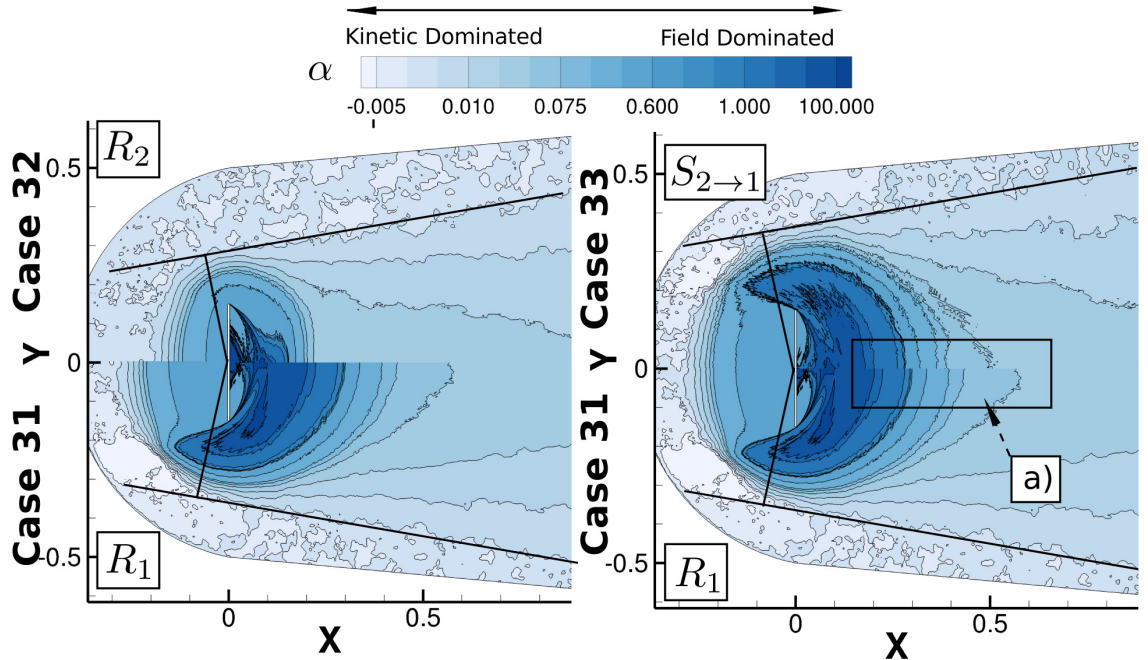
Figure 5.5 (top) compares the interaction of a thin 0.3 m wide flat plate at -25 V (Case 31) and -10 V (Case 32). Unlike the previous two similarity examples, it is difficult to decouple the physical influence of α_k, χ and μ_e on flow phenomena between Case 31 and 32. The net effect of increasingly negative ϕ_B from Case 32 to Case 31 appears as an expansion of the sheath and the field dominated region in the wake. This is consistent with above observations of α_k and χ. An important point to note is the similar rarefaction wave angle, θ_r being independent of ϕ_B as predicted in Section 5.4.

Figure 5.5 (bottom) compares the interaction of the reference flow R_1 (Case 31) with the scaled flow $S_{2\to1}$ (Case 33). Table 5.4 lists the interaction quantities for Cases 31-33. The bold values in Table 5.4 highlight the link between interaction quantities and scaling parameters. The flow velocity, ion number density and electron temperature all reduced in Case 33 to match α_k, χ and μ_e in Case 31. Figure 5.5 (bottom) demonstrates that the scaling parameters, again, correctly preserve self-similarity. Note however that while the majority of the structures in Case 31 are reproduced in Case 33, there exists a region of disagreement in the wake region a). An explanation for this disagreement is that relative influence ion thermal effects has not been scaled.

The transformation of α_k caused a reduction in velocity from 7.5 km/s to 4.73 km/s, S_i reducing from 5.9 to 3.74. In other words, the contribution of thermal effects to ion deflections almost doubles between Case 33 and Case 31. The similarity transformation presented in the next section demonstrates that this region of dissimilarity is indeed caused by ion thermal effects.

Table 5.4: Interaction parameters for self-similar scaling of body scale example. Bold numbers highlight the effect of scaled parameters on dimensionless parameters. Ion thermal effects are not scaled.

Case	$\phi_{(B)}$ (V)	$r_{(B)}$ (m)	$v_{(B)}$ (km/s)	m $(10^{-27}kg)$	n_∞ $(10^{10}m^{-3})$	T_e (K)
31 (R_1)	-25	0.3	7.5	26.55	4	1997
32 (R_2)	**-10**	0.3	7.5	26.55	4	1997
33 $(S_{2\to1})$	**-10**	0.3	**4.73**	26.55	**1.6**	**798.8**

Case	α_k	χ	μ_e
31 (R_1)	2.682	1.6142	-145.27
32 (R_2)	**1.0728**	**2.5524**	**-58.1097**
33 $(S_{2\to1})$	**2.6973**	**1.6142**	**-145.27**

Figure 5.5: Self-similar transformation of -25 V cylinder (R_1) and -10 V cylinder (R_2). Parameters in the scaled case $(S_{2\to1})$ $v_{(S_{2\to1})} = \sqrt{0.4}v_{(R_1)}$, $n_{(S_{2\to1})} = 0.4n_{(R_1)}$ and $T_{e,(S_{2\to1})} = 0.4T_{e,(R_1)}$. Full flow conditions are listed in Table 5.4 case 31-33. Rarefaction angle measures are overlaid to aid comparison of fields. a) Region of dis-similarity.

5.5.5   Transformation 4: Multi-Species Ion Charge

Past work has focused on the scaling of singly charged ions in a single ion species plasma. The scaling parameters presented in this work suggest that there exist transformations such that the interaction of multi-species plasmas with dissimilar ion charges can be made similar. This section demonstrates that this is the case.

Consider a plasma composed of a heavy ion species x and a light ion species y, where $Z_{y,(R_2)}$ is the test variable. R_1 and R_2 are similar when,

$$
\begin{aligned}
n_{x,\infty,(S_2\to 1)} &= (Z_{y,(R_2)}/Z_{x,(R_2)})n_{x,\infty,(R_1)} \\
\phi_{B,(S_2\to 1)} &= (Z_{y,(R_2)}/Z_{x,(R_2)})\phi_{B,(R_1)} \\
m_{y,(S_2\to 1)} &= (Z_{y,(R_2)}/Z_{x,(R_2)})m_{y,(R_1)} \\
T_{e,(S_2\to 1)} &= (\phi_{B,(S_2\to 1)}/\phi_{B,(R_1)})T_{e,(R_1)} \\
v_{y,\infty,(S_2\to 1)} &= \left(\phi_{B,(S_2\to 1)}/\phi_{B,(R_1)}\right)^{1/2}v_{y,\infty,(S_2\to 1)} \\
v_{x,\infty,(S_2\to 1)} &= \left(\phi_{B,(S_2\to 1)}/\phi_{B,(R_1)}\right)^{1/2}v_{x,\infty,(S_2\to 1)}
\end{aligned}
\tag{5.57}
$$

The first three transformations capture the scaling required by $Z_{y,(R_2)}$, while the second three correct for the secondary scaling of phenomena caused by scaling of $\phi_{B,(S_2\to 1)}$. As discussed in Section 5.3.2 however, the scaling of $v_{k,B}$ or m_k will affect S_k, scaling ion thermal effects. Provided that the system is mesothermal, the system phenomena should be insensitive to ion thermal effects. *Care must be taken when scaling mesothermal phenomena as ion thermal effects may become significant as a consequence of a reduced mass or drift velocity.*

To account for ion thermal effects in the above multi-species example would require the additional transformations,

$$
\begin{aligned}
T_{x,(S_2\to 1)} &= \left(v_{x,\infty,(S_2\to 1)}/v_{x,\infty,(R_1)}\right)^2 T_{x,(R_1)} \\
T_{y,(S_2\to 1)} &= \left(\frac{m_{y,(S_2\to 1)}}{m_{y,(R_1)}}\right)\left(\frac{v_{y,\infty,(S_2\to 1)}}{v_{y,\infty,(R_1)}}\right)^2 T_{y,(R_1)}
\end{aligned}
\tag{5.58}
$$

The temperature of species x requires scaling to account for changes in $v_{x,(S)}$, the temperature of species y requires scaling to account for scaling of both $m_{y,(S)}$ and $v_{y,(S)}$.

Figure 5.6 (top) compares the relative contribution of species x and y in an $O^+ - H^+$ plasma (Case 34) and $O^+ - H^{++}$ (Case 35) interacting with a -25 V 0.3 m radius cylinder ($O^+ = x$, $H^+ = H^{++} = y$. Figure 5.6 (top) illustrates how, by doubling its charge, the y ion species dominates the rarefaction wave, causing the rarefaction angle to increase. Other flow features in Cases 34 and 35 include a light species dominated wake-core and heavy species dominated sheath structure. These features appear to be a reflection of
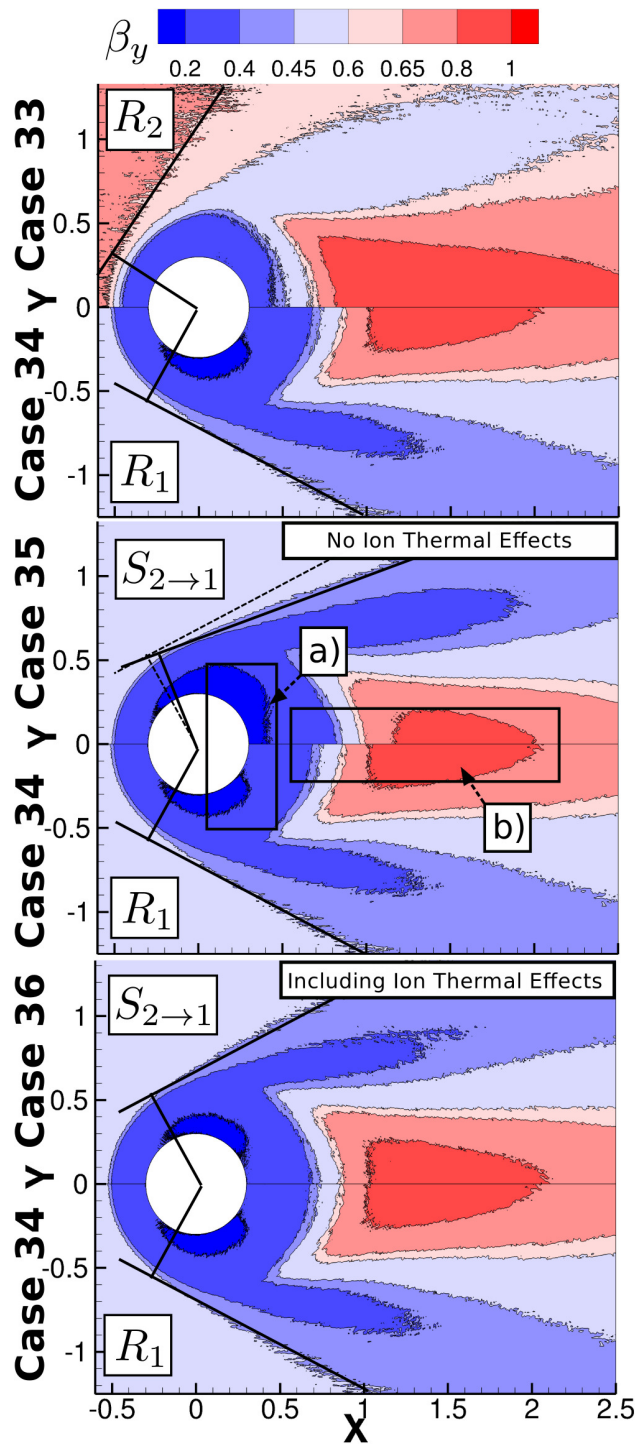
Table 5.5: Two species self-similarity example with dissimilar ion charges and including ion thermal effects. Bold numbers highlight the effect of scaled parameters on dimensionless parameters.

Case #	34		35		36		37	
	$(R_1)_x$	$(R_1)_y$	$(R_2)_x$	$(R_2)_y$	$(S_{2\to1})_x$	$(S_{2\to1})_y$	$(S_{2\to1})_x$	$(S_{2\to1})_y$
$\phi_{(B)}$ (V)	-25	-25	-25	-25	**-50**	**-50**	**-50**	**-50**
$r_{(B)}$ (m)	0.3	0.3	0.3	0.3	0.3	0.3	0.3	0.3
$v_{(B)}$ (km/s)	7.5	7.5	7.5	7.5	**10.6**	**10.6**	**10.6**	**10.6**
m $(10^{-27}kg)$	26.55	1.67	26.55	1.67	26.55	**3.34**	26.55	**3.34**
Z_x	1	1	1	**2**	1	**2**	1	**2**
n_∞ $(10^{10}m^{-3})$	4	4	4	4	**8**	4	**8**	4
T_e (K)	1997	1997	1997	1997	**3994**	**3994**	**3994**	**3994**
T_i (K)	1537	1537	1537	1537	1537	1537	**3074**	**6124**
α	2.682	42.63	2.682	**85.2785**	**2.6854**	**42.6924**	**2.6854**	**42.6924**
χ	2.2828	2.2828	**2.7959**	**2.7959**	**2.2828**	**2.2828**	**2.2828**	**2.2828**
β	0.5	0.5	**0.33**	**0.66**	**0.5**	**0.5**	**0.5**	**0.5**
μ_e	-145.5	-145.5	-145.5	-145.5	**-145.5**	**-145.5**	**-145.5**	**-172.5**
S_k	5.932	1.488	5.932	1.488	**8.385**	**2.974**	**5.932**	**1.488**

ion mobility; the light ions accelerated through the sheath faster than the heavier ions, the resulting ion gradient making the near-body region appear to be dominated by heavy species.

Figure 5.6 (middle) then compares the reference case R_1 (Case 34) against the scaled case $S_{2\to1}$ without accounting for ion thermal effects (Case 36). While a majority of flow features have been matched, dissimilarities in wake structure similar to those observed in Figure 5.5 can be seen at both a) and b). Further, the rarefaction wave angle of Case 36 is suppressed (smaller) compared to the reference case (Case 34); the rarefaction wave angle in Case 10 is super-imposed on Case 12 as a dotted line to illustrate this point. Figure 5.6 (bottom) demonstrates that ion thermal effects cause these discrepancies.

In scaling $m_{y,(S_{2\to1})}$, $v_{x,B,(S_{2\to1})}$ and $v_{y,B,(S_{2\to1})}$, S_x increased from 5.933 to 8.385 and S_y from 1.488 to 2.974 in Case 36 compared to Case 34. In other words, the net contribution of ion thermal effects *decreased* in Case 36 compared to Case 34. As a result, there was less thermal resistance to the expansion of the ion acoustic Mach wave, resulting in the larger rarefaction wave angle seen in Case 33 in Figure 5.6. By scaling ion thermal effects in Case 37 to match Case 34, Figure 5.6 confirms both the ability of the scaling parameters to predict the self-similarity of multi-species plasmas. This is the first demonstration of that it is possible to scale multi-species plasma interaction phenomena with dis-similarly charged ion species using PIC simulations. Furthermore, this section demonstrates that ion thermal effects can have an appreciable effect on mesothermal flow structures.

Figure 5.6: Self-similar transformation of multi-species plasma composed of heavy x and light y ion species interacting with cylinder -25 V cylinder. Contours are of β_y, blue regions dominated by x, red regions dominated by y. Full flow conditions are listed in Table 5.5. Rarefaction angle measures are overlaid to aid comparison of fields. Labelled features include: a) x dissimilarity, b) y dissimilarity.

5.6 Multi-Species Plasma-Body Interaction Phenomena: Necessary for Ionospheric Aerodynamics?

From an ionospheric aerodynamics perspective, the identification of the multi-species ion coupling parameter β_k makes it possible to answer one question not addressed in the prior literature. *Are multi-species effects significant to ionospheric aerodynamics in LEO?* To address this question, we consider the role of the ion coupling parameter β_k in the governing equations.
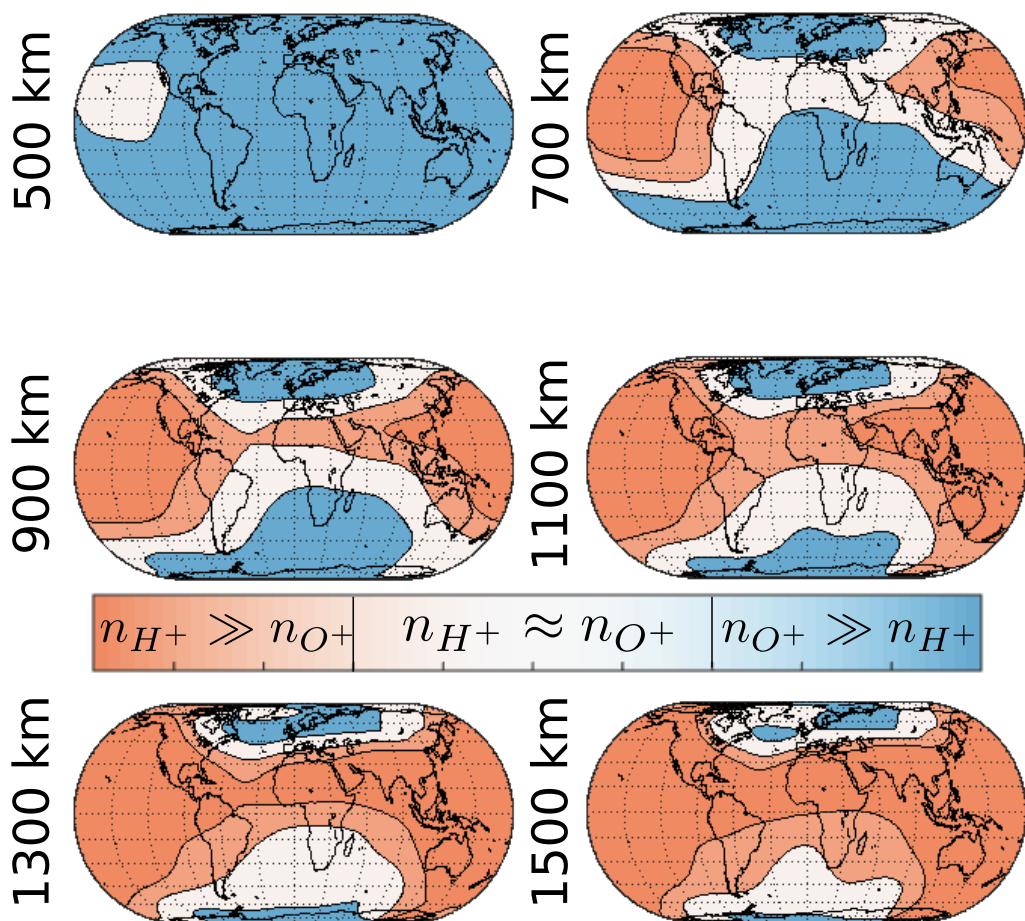
The ion coupling parameter β_k suggests that when $n_{O^+} \gg n_{H^+}$, the effect of H^+ ions to plasma phenomena can be neglected and *vice versa*. In other words, multi-species phenomena are only significant when $\beta_k \approx 1$. To illustrate regions in LEO where multi-species phenomena occur, Figure 5.7 plots the regional variation of β_{O^+} through altitude; red regions reflecting H^+ dominated interactions, blue regions reflecting O^+ dominated regions. Figure 5.7 is based on the same IRI-2012 data presented in Section 2.2.1.

Based on Figure 5.7, below 700 km the contribution from H^+ ions can be largely neglected. Similarly, above 900 km the effect of O^+ ions can be neglected, and multi-species simulations are required only in select regions primarily between 700 km and 900 km altitude and near the poles above 900 km altitude. In general however, Figure 5.7 suggests that single species phenomena will dominate the majority of ionospheric aerodynamic interactions in LEO. This work will therefore focus on the characterising the effect of single species plasma-body interaction phenomena on the motion of LEO objects.

5.7 Summary

The complex, non-linear relationship between interaction quantities and plasma-body interaction phenomena was identified as a key challenge to the study of ionospheric aerodynamics at the end of the previous chapter. To address this challenge, the set of dimensionless parameters that scale plasma-body interactions were derived here.

Based on the unmagnetised Vlasov-Maxwell equations and validated against the Buckingham Pi theorem, the $7 + 5K$ quantities (including constants) that define K species plasma-body interactions (including constants) were expressed as $1 + 4K$ independent dimensionless parameters (or $2 + 4K$ dimensionless parameters in the χ, β_k form). The reason for expressing ξ_k as χ and β_k became clear when considering a disturbance with potential energy equal to the surrounding thermal energy of the plasma. Introducing the new general shielding length scale λ_ϕ, Section 5.3.3 demonstrated that the general shielding length λ_ϕ becomes the general Debye length λ_D in the limit that the potential energy

Figure 5.7: Regional variation of ion dominance through altitude calculated using the IRI-2012 (Bilitza et al., 2014) atmospheric model. Parameters are as outlined in Section 2.2.1.

of the disturbance is on the order of the thermal energy of the surrounding plasma (and becomes the electron Debye length with an additional cold ion restriction). In essence, the general shielding length λ_ϕ provides a consistent link between the shielding of low and high-voltage plasma phenomena.

The validity of the scaling parameters was demonstrated in Section 5.5 by successfully predicting the self-similar transformations required to preserve the flow physics between two plasma-body interactions with dis-similar flow and body quantities. While this sort of analysis is typical in fluid mechanics, to date this is the first demonstration of self-similarity transformations of plasma-body interactions using a PIC code. Limitations of previous scaling parameters identified in Chapter 2, in particular the implicit high-temperature (weakly-coupled) assumption, are addressed by the presented scaling parameters. Furthermore the final multi-species similarity transformation is the *first demonstration of self-similarity between two multi-species plasmas with dis-similarly charged ions including ion thermal effects in a mesothermal plasma.*

Framed in terms of the research questions posed at the beginning of this work, this chapter has established the dimensionless parameters that describe LEO plasma-body interactions and therefore charged aerodynamics. More than that however, the above scaling parameters represent a powerful tool for studying both plasma phenomena and the phenomena resulting from plasma-body interactions, ionospheric aerodynamics being a subset of plasma phenomena described within the phase-space described by the scaling parameters.

Summary of Scaling Parameters

$$
\begin{aligned}
\text{Ion Deflection Parameter} \quad \alpha_k &= -Z_k \left(\frac{q_e \phi_{(0)}}{m_k v_{k,B}^2} \right), \\[2ex]
\text{Electron Energy Coefficient} \quad \mu_e &= \left(\frac{q_e \phi_{(0)}}{k_B T_{e,\infty}} \right), \\[2ex]
\text{General Body Shielding Ratio} \quad \chi &= \frac{r_{(0)}}{\lambda_\phi}, \\[2ex]
\text{Ion Temporal Parameter} \quad \Omega_k &= \left(\frac{\omega_{(0)} r_{(0)}}{v_{k,B}} \right), \\[2ex]
\text{Ion Thermal Ratio} \quad S_k &= \frac{v_{k,B}}{\sqrt{2 k_B T_{k,\infty}/m_k}}, \\[2ex]
\text{Ion Coupling Parameter} \quad \beta_k &= \left(\frac{Z_k n_{k,\infty}}{\sum_k^K Z_k n_{k,\infty}} \right)
\end{aligned}
\tag{5.59}
$$

$$
\text{General Shielding Length} \quad \lambda_\phi = \left(-\frac{\epsilon_0 \phi_{(0)}}{q_e \sum_k^K Z_k n_{k,\infty}} \right)^{1/2} \quad [m] \tag{5.60}
$$

Chapter 6

Organising the Flow Physics II: Mapping Interaction Phenomena

6.1 Introduction

Physical systems often exhibit limiting (asymptotic) behaviours, and plasma-body interactions are no exception. Among observations of plasma interaction phenomena in Chapter 4, several limiting behaviours were observed: For example,

1. As the sheath thickness becomes small compared to the body (thin sheath), direct charged aerodynamic forces dominate the total charged aerodynamic forces.

2. As the sheath thickness becomes large compared to the body (thick sheath), indirect charged aerodynamic forces dominate the total charged aerodynamic forces.

3. As the potential energy of the body becomes very large compared to the ion kinetic energy (field dominated), indirect charged aerodynamic forces dominate the total charged aerodynamic force and direct charged aerodynamic forces plateau.

4. As the ion kinetic energy becomes much larger than the potential energy of the body (kinetic dominated), direct charged aerodynamic forces dominate the total charged aerodynamic forces and are primarily caused by fore-body ion collection.

Complex coupling effects were also observed where direct and indirect charged aerodynamic forces were seen to either compete with or enhance total charged aerodynamic forces depending on the combination of interaction quantities. Based on these observations, key phenomena that affect charged aerodynamics appear to be related to the relative thickness of the sheath compared to the body (collective phenomena) and the orbits taken by the ions through the structure of the sheath surrounding the body (kinetic phenomena). Chapter 4 was limited however, in that the relationship between plasma phenomena and the interactions quantities r_B, ϕ_B and m_i, could not be separated.

Chapter 5 addressed this challenge by demonstrating that $2+4K$ scaling parameters (or $1 + 4K$ independent parameters) completely describe multi-species plasma-body interactions in LEO. By inspecting the role of these scaling parameters in the governing equations, Chapter 5 argued that: (1) multi-species coupling effects are negligible for a majority of LEO conditions; (2) the steady-state nature of the observed interactions suggests the temporal parameter Ω does not influence charged aerodynamics calculations; and (3) in the mesothermal limit ion thermal effects tend to diffuse plasma interaction phenomena but not govern them. These conclusions justified the further reduction of scaling parameters that influence charged aerodynamics in LEO to the ion deflection parameter α_k, general shielding ratio χ and electron energy coefficient μ_e. In other words, plasma interaction phenomena that influence ionospheric aerodynamics forces can be mapped to the three dimensional phase-space $\mathcal{P}(\alpha, \chi, \mu_e)$ - each point within $\mathcal{P}$ corresponding to a unique physical interaction. $\mathcal{P}(\alpha, \chi, \mu_e)$ is referred to as the *"Plasma Interaction Phase-space"* (PIP) in this work.

The purpose of this chapter is to map out the relationship between the flow physics, charged aerodynamic forces and points within $\mathcal{P}(\alpha_k, \chi, \mu_e)$ to develop a framework within which to understand ionospheric aerodynamics. Section 6.2 begins by outlining the methodology used in this chapter. Section 6.3 then explores the relationship between collective phenomena and $\mathcal{P}(\alpha, \chi, \mu_e)$. These relationships are then developed further in Section 6.4 by studying kinetic phenomena in $\mathcal{P}(\alpha, \chi, \mu_e)$. Based on the relationships observed in these sections, Section 6.5 identifies the link between charged aerodynamic forces and plasma interaction phenomena.

6.2   Methodology

The methodology taken in this chapter is to vary a single scaling parameter about a reference condition and measure the resulting variation of collective and kinetic phenomena. The subsequent influence of these phenomena on local charged aerodynamic force distributions is used to develop a phenomenological map of charged aerodynamics within $\mathcal{P}(\alpha_k, \chi, \mu_e)$.

Figure 6.1 illustrates the region mapped out in $\mathcal{P}(\alpha_k, \chi, \mu_e)$ by Cases 38-66. Table 6.1 lists interaction quantities and scaling parameters for Cases 38-66. The numerical setup of the simulations is identical to that used in Chapter 4. Cases 38 to 43 investigate the scaling of the single species ion deflection parameter α_k. Cases 44 to 49 investigate the scaling of the general shielding ratio χ. Cases 50 to 55 investigate the scaling of the electron energy coefficient μ_e. Cases 56 to 62 and Cases 63 to 67 investigate the coupling between the α_k, χ and μ_e by measuring trends in α_k and χ about a different point in $\mathcal{P}$. The reason μ_e is not

investigated at this second point is discussed later. Measurement approaches specific to collective and kinetic phenomena are outlined in Section 6.3 and Section 6.4 respectively. All gas-surface interactions considered are for a neutralising, diffusely reflecting surface with complete thermal accommodation to a 500 K wall. Indirect charged aerodynamic forces are calculated from the Maxwell stress tensor calculated at the body's surface.
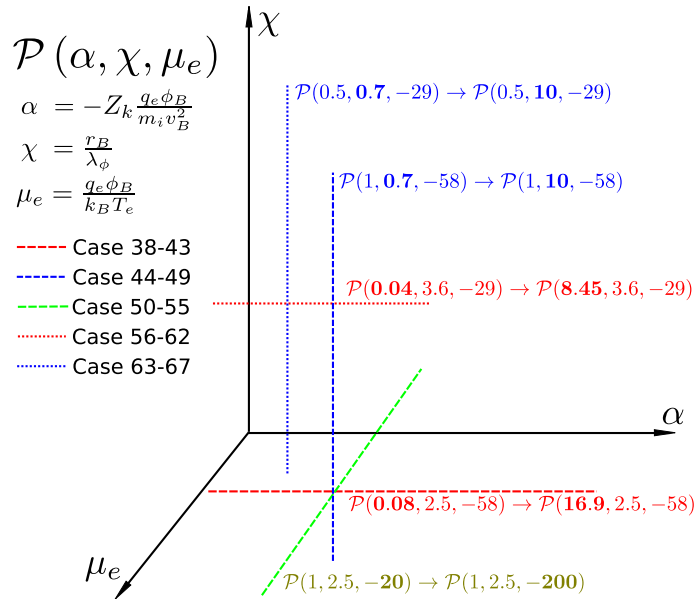
6.2.1 A Note on Collective and Kinetic Phenomena

This work makes an important distinction between collective and kinetic phenomena.

Collective phenomena: refer to plasma interactions phenomena caused by the response of the plasma to the disturbance generated by the body e.g. the structure of the plasma sheath and the rarefaction wave.

Kinetic phenomena: refer to features caused by the trajectories (orbits) of ions through this disturbance e.g. bounded ion jets and ion pseudo-waves.

Collective and kinetic phenomena are intrinsically related; the steady-state solution of the electrical disturbance caused by the body accounting for the space-charge effects of both collective and kinetic phenomena. This distinction helps differentiate indirect and direct charged aerodynamics mechanisms.

Figure 6.1: Illustration of space within $\mathcal{P}(\alpha, \chi, \mu_e)$ mapped out by Cases 38-66. Red lines show variations in the ion deflection parameter α, blues lines show variations in the general shielding ratio χ, green lines show variations in the electron energy coefficient μ_e.

Table 6.1: Interaction quantities and scaling parameters used for investigating the collective and kinetic plasma interaction phenomena in the plasma interaction phase-space $\mathcal{P}(\alpha, \chi, \mu_e)$. Reference conditions are from Hastings, (1995) corresponding to the mean conditions experienced the EOS satellite during a period of mean sunspot activity. Bold numbers highlight scaled parameters.
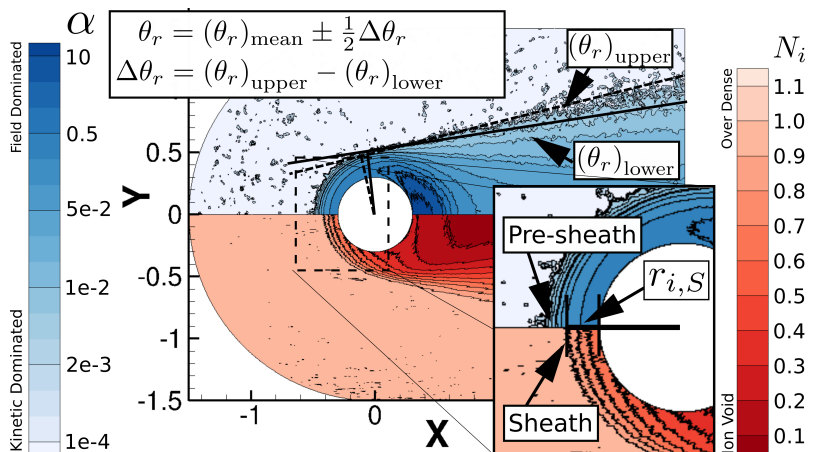
Reference Conditions					
v_B (m/s)	n_i (m^{-3})	n_e (m^{-3})	T_i (K)	T_e (K)	r_B (m)
7500	4×10^{10}	4×10^{10}	1531	1997	0.3

#	$\phi_B = -10$ V			#	$\phi_B = -5$ V		
	v_B (m/s)	α	χ	μ		v_B (m/s)	α	χ	μ
38	26765	**0.084**	2.55	-58.13	56	26765	**0.042**	3.6	-29.06
39	11969	**0.42**	2.55	-58.13	57	11969	**0.201**	3.6	-29.06
40	7500	**1.072**	2.55	-58.13	59	8463	**0.421**	3.6	-29.06
41	3778	**4.227**	2.55	-58.13	60	5984	**0.842**	3.6	-29.06
42	2676	**8.426**	2.55	-58.13	61	2676	**4.213**	3.6	-29.06
43	1889	**16.90**	2.55	-58.13	62	1889	**8.4512**	3.6	-29.06
	n_∞ (m^{-3})					n_∞ (m^{-3})			
44	3.07e9	1.072	**0.7**	-58.13	63	1.535e9	0.536	**0.7**	-29.06
45	6.14e9	1.072	**1**	-58.13	64	3.07e9	0.536	**1**	-29.06
46	3.07e10	1.072	**2.23**	-58.13	65	6.14e9	0.536	**1.41**	-29.06
47	1.535e11	1.072	**5**	-58.13	66	3.07e10	0.536	**3.61**	-29.06
48	3.07e11	1.072	**7.07**	-58.13	67	3.07e11	0.536	**10**	-29.06
49	6.14e11	1.072	**10**	-58.13					
	T_e (K)								
50	5802.3	1.072	2.55	**-20**					
51	2901.2	1.072	2.55	**-40**					
52	1934.1	1.072	2.55	**-60**					
53	1450.6	1.072	2.55	**-80**					
54	1160.5	1.072	2.55	**-100**					
55	580.2	1.072	2.55	**-200**					

6.3 Organising Collective Phenomena within the Plasma Interaction Phase-Space

This section organises collective interaction phenomena within $\mathcal{P}\left(\alpha_k, \chi, \mu_e\right)$. In particular, it focuses on characterising the leading edge of the electrostatic disturbance generated by the motion of a charged object through a single species plasma i.e. *"disturbance envelope"*. This work defines the disturbance envelope in terms of the leading edge of the fore-body ion sheath thickness $r_{i,S}$ and rarefaction wave angle θ_r. Figure 6.2 illustrates the physical meaning of $r_{i,S}$ and θ_r.

Various methods have been proposed for locating the sheath edge (Heatley, 1937; Kiel, 1968; Riemann, 1991; McMahon, Xu, and Laframboise, 2005; Choinière and Gilchrist, 2007). One approach is to define the sheath edge in terms of the local disturbance potential $\phi(\mathbf{x})$ to reflect the breakdown in quasi-neutrality near the body (Heatley, 1937; Kiel, 1968). Another approach is to defined the ion sheath thickness directly in terms of the quasi-neutrality breakdown e.g. $N_i(\mathbf{x}) - N_e(\mathbf{x})$, where $N_i(\mathbf{x})$ and $N_e(\mathbf{x})$ are the dimensionless ion and electron distributions (McMahon, Xu, and Laframboise, 2005; Choinière and Gilchrist, 2007). This work takes the latter approach.

Here, $r_{i,S}$ and $r_{e,S}$ are defined as departures from the freestream number density, where the electron sheath $r_{e,S}$ describes the onset of the disturbance caused by the body (pre-sheath), while the ion sheath $r_{i,S}$ describes the region where ion disturbances become significant (sheath). This distinction is illustrated in the cut-out in Figure 6.2. The effect of numerical noise on measurement is also shown in Figure 6.2, where the uncertainty measuring the rarefaction angle is shown by $(\theta_r)_{\text{upper}}$ and $(\theta_r)_{\text{lower}}$.

Figure 6.2: Illustration of the ion sheath thickness $r_{i,S}$, rarefaction wave angle θ_r and the effect of noise on measurements. Flowfields shown corresponds to Case 40, the α flowfield shown top, N_i shown at the bottom.

6.3.1   Overview of Collective Phenomena
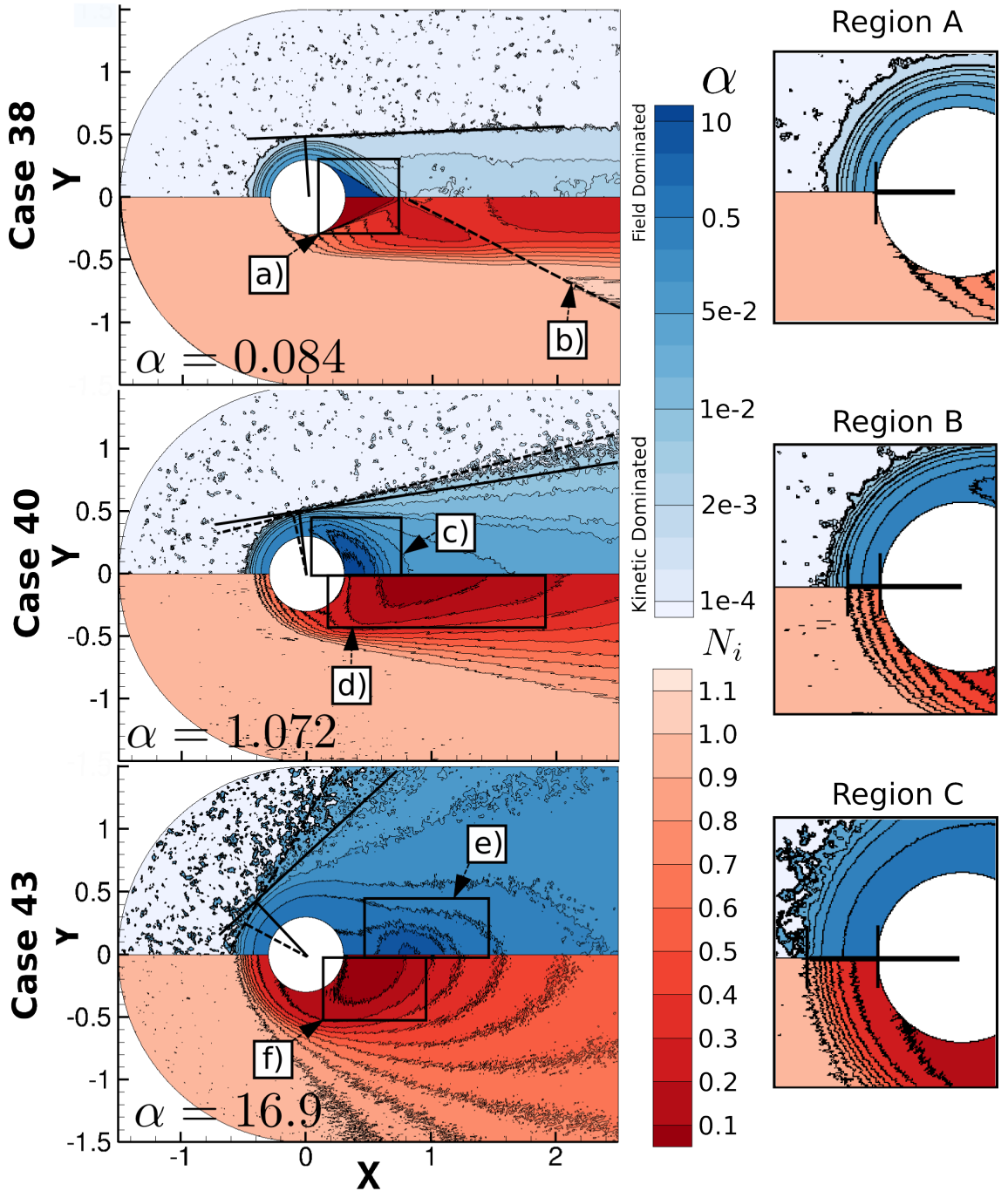
Effect of Ion Deflection Parameter on Collective Phenomena

To investigate the qualitative effects of the ion deflection parameter α_k on plasma interaction phenomena, Figure 6.3 plots Case 38, 40 and 43 flowfields with contours of α_k (top) and N_i (bottom). Upper and lower bounds of θ_r are indicated in Figure 6.3, while enlarged fore-body cut-outs (Region A, B and C) illustrate the effect of α on $r_{i,S}$. Two regimes are shown in Figure 6.3, flows dominated by ion kinetic energy (top) and field dominated flows (bottom), the middle the intermediate case where kinetic and field effects are balanced.

Ion Kinetic Dominated Flow: Figure 6.3 (top) corresponds to a flow where the ion kinetic energy is much larger than the body potential energy ($\alpha \ll 1$, Case 38). The sheath structure and rarefaction angle seen in Figure 6.3 reflect this; the fore-body ion sheath no longer evident (fore-body ions are not accelerated by the fore-body sheath) and the rarefaction wave angle θ_r is approaching zero (ion rarefaction wave does not expand into the freestream). Two features unique to kinetic dominated flows are labelled. The first corresponds to the ion void at a), the sheath unable to deflect ions into this region. The second corresponds to the ion pseudo-wave labelled at b), ion pseudo-waves at this angle usually concealed by the rarefaction wave.

Intermediate Kinetic/Field Coupling: Figure 6.3 (middle) corresponds to a flow where the ion kinetic energy is approximately the same as body's potential energy ($\alpha \approx 1$, Case 40). Compared to the kinetic dominated case, the potential disturbance caused by the ion void is able to travel outward into the plasma and the rarefaction angle is no longer zero. The ion void region in the kinetic dominated region is also no longer evident, instead a higher density region indicated at d) is seen in the immediate wake of the body compared to further back in the wake. As will be shown in Section 6.4, the presence of this region is indicative of bounded ion jets.

Field Dominated Flow: Figure 6.3 (bottom) then shows the opposite extreme compared to that seen in Figure 6.3 (top) where the body potential energy is much larger than the ion kinetic energy ($\alpha \gg 1$, Case 43). Here, the decrease in relative ion kinetic energy enhances the susceptibility of the ions deflections by potential disturbances, hence the rarefaction wave angle has increased further in Figure 6.3 (bottom) compared to 6.3 (middle) and the ion sheath has expanded further into the flow. This is consistent with observations in Chapter 4 and prior observations that studied the influence of ion drift (streaming) velocity on sheath structure (Stone, 1981a; McMahon, Xu, and Laframboise, 2005; Choinière and Gilchrist, 2007).

Figure 6.3: Effect of α on plasma-interaction phenomena. Contours show variations in α (top) and N_i (bottom). θ_r lines show upper (dashed line) and lower (solid line) measurement bounds. Region A, B and C show cutouts with $r_{i,S}$ measures. Labelled features include: a) kinetic dominated ion void, b) kinetic dominated pseudo-wave, c) bounded ion jet, d) separation of ion void from the wake surface, e) separation of the kinetic dominated region into the wake and f) widening of ion void structure.
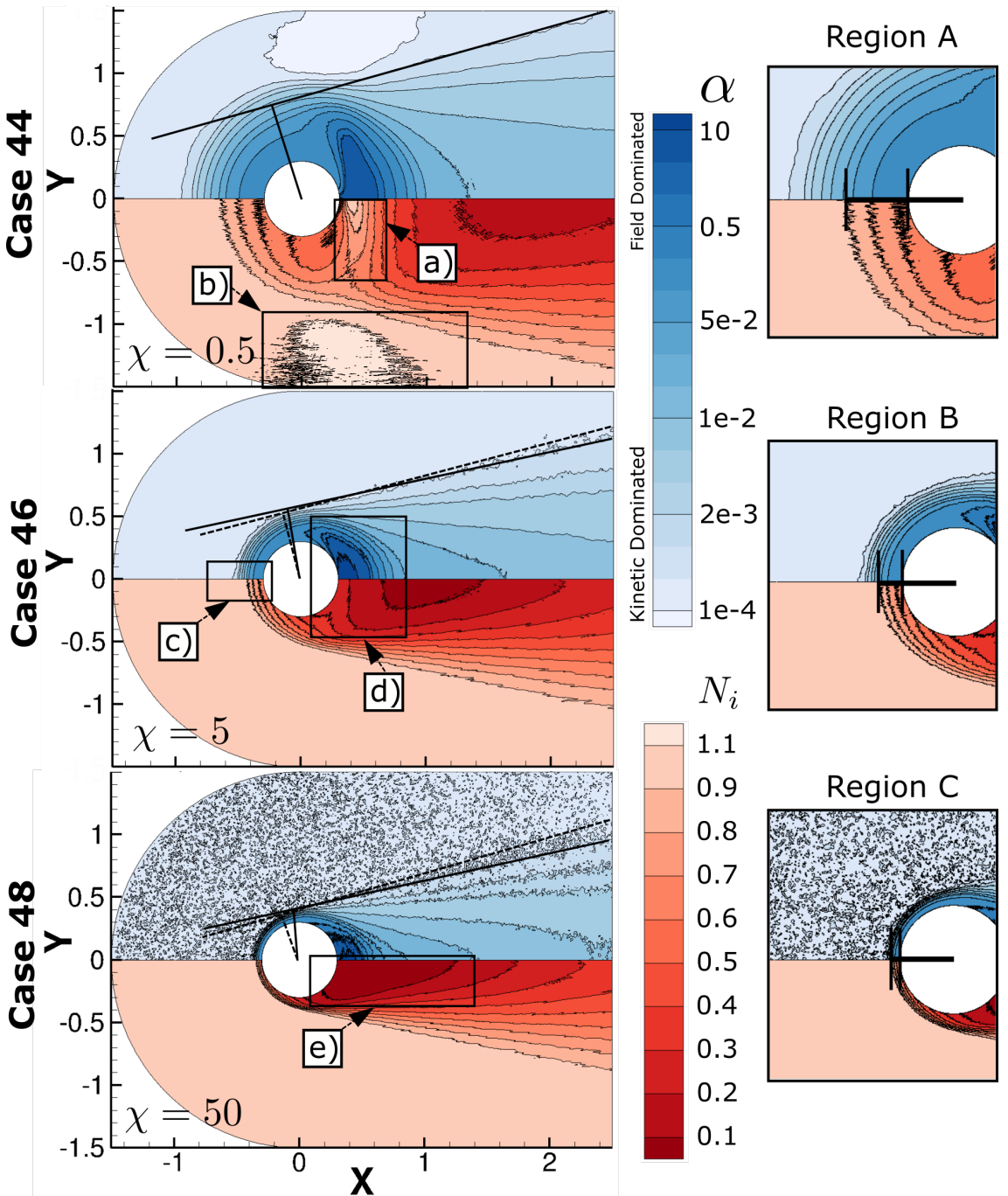
Effect of General Shielding Ratio on Collective Phenomena

Figure 6.4 presents a similar set of plots to those in Figure 6.3 investigating the effect of χ on interaction phenomena. Figure 6.4 shows an inverse relationship between χ and $r_{i,S}$ (or proportionally with λ_ϕ). Hence, the assertion in Chapter 5 that the physical nature of λ_ϕ is to describe the shielding of plasma-body interactions appears correct (χ representing the relative thickness of the sheath). Two limiting behaviours are shown in Figure 6.4 corresponding to weakly shielded interactions (top) and strongly shielded interactions (bottom), the middle case corresponding to a shielding regime within these limits (intermediate shielding).

Weak Shielding: Figure 6.4 (top) shows the case where the body radius r_B is half the general shielding length λ_ϕ ($\chi < 1$, Case 44). Framed another way, if the role of λ_ϕ is to describe the thickness of the sheath, then the sheath in Figure 6.4 (top) should be larger than the body (thick sheath). As seen in Figure 6.4 (top), this is case. Two important features flow features are labelled at a) and b). a) appears as a localised over-dense region in the wake. As will be seen in Section 6.4, this peak is directly related to the ion pseudo-wave structure highlighted at b) as an over-dense region orthogonal to the flow.

Intermediate Shielding: Figure 6.4 (middle) shows the case where λ_ϕ is smaller than the body ($\chi > 1$, Case 46). Again this is reflected in the sheath thickness. Note the absence of the ion peak and ion pseudo-wave in Figure 6.4 (middle). Instead, a detached ion void region suggests the presence of bounded ion jets i.e. the reduction in sheath thickness has caused the unbounded ion deflections to become bounded. This suggests that both the relative thickness of the sheath and the ratio of ion kinetic energy to body potential influence the critical impact parameter i.e. χ and α_k influence the formation of potential barriers that deflect ions onto unbounded orbits.

Strong Shielding: Figure 6.4 (bottom) shows the case where λ_ϕ becomes small compared to the body radius r_B ($\chi \gg 1$, Case 48) i.e. a thin-sheath. The ion void region in the wake of the body in Figure 6.4 (middle) is now attached to the rear of the body in Figure 6.4 (bottom). Physically this reflects the absence of bounded ion jets. Note also that the rarefaction wave angle θ_r appears largely independent of the general shielding ratio χ in Figure 6.4.
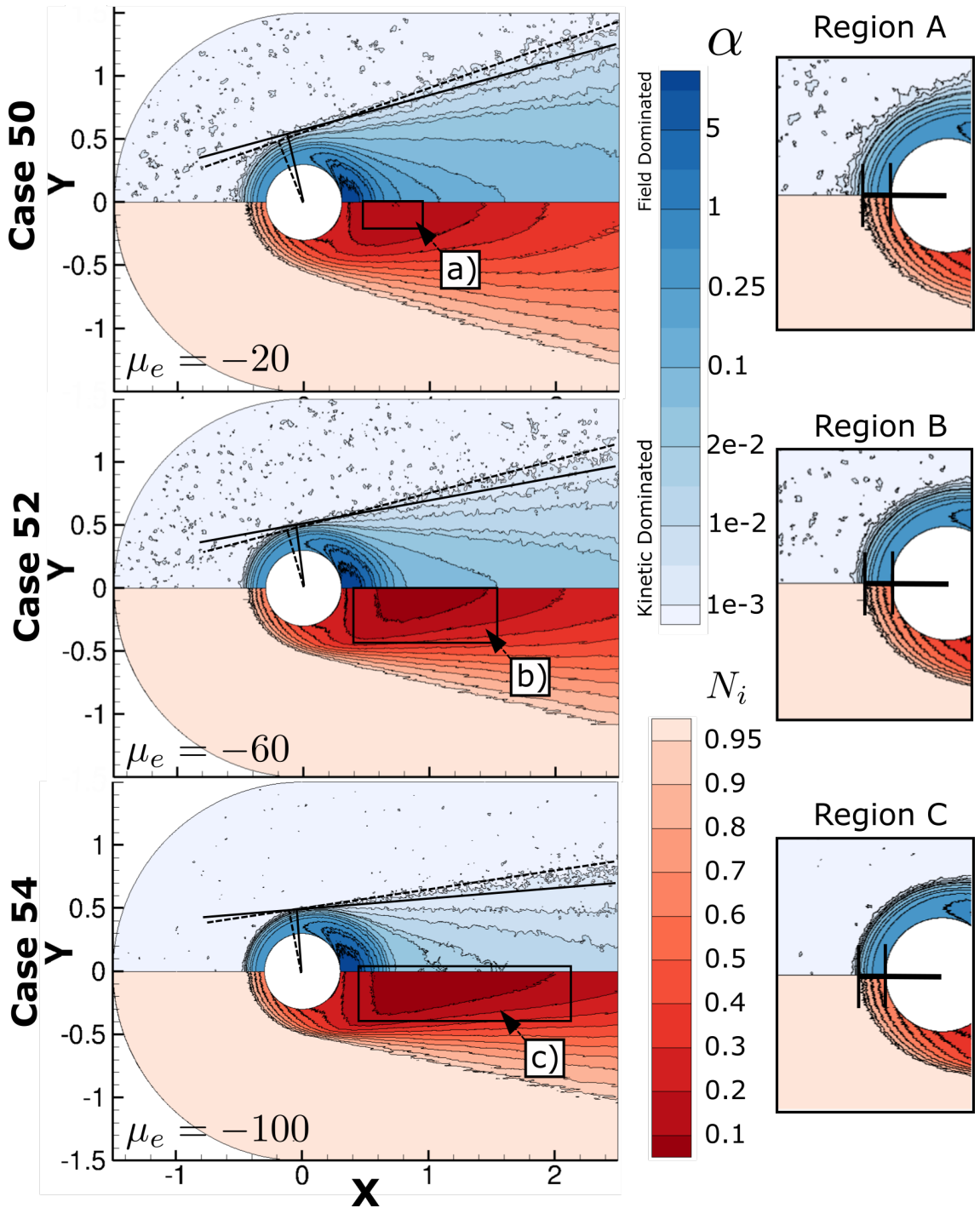
Figure 6.4: Effect of the general shielding ratio χ on plasma-interaction phenomena. Contours show variations in α_k (top) and N_i (bottom). θ_r lines show upper (dashed lines) and lower (solid lines) measurement bounds. Region A, B and C show cut-outs with $r_{i,S}$ measures. Labelled features include: a) near-wake ion density peak, b) ion pseudo-wave, c) difference between $r_{i,S}$ and $r_{e,S}$, d) bounded ion jet and e) re-attachment of ion void.

Effect of Electron Energy Coefficient on Collective Phenomena

Unlike the ion deflection parameter α_k and the general shielding ratio χ, the electron energy coefficient μ_e has little effect on near-body flow structures. This is reflected in Figure 6.5, which presents a similar plot to Figure 6.3 and Figure 6.4, but investigates the effect of μ_e on flow physics.

The cut-out regions illustrate that $r_{i,S}$ is largely invariant with μ_e. The primary effect of μ_e appears to be on θ_r (discussed in detail the following section). A consequence of the influence of μ_e on the rarefaction wave angle θ_r is that μ_e effects the elongation of the ion void region ($N_i = 0.1$ contour). Physically this appears to be a reflection of the ability of the electrons to populate negatively charged regions and in turn, promote the deflection of ions into these areas.

Figure 6.5: Effect of μ_e on plasma-interaction phenomena. Contours show variations in α (top) and N_i (bottom). θ_r lines show upper (dashed lines) and lower (solid lines) measurement bounds. Region A, B and C show cut-outs with $r_{i,S}$ measures. Labelled features a), b) and c) indicate the elongation of the $N_i = 0.1$ contour with μ_e.

6.3.2 Behaviour of the Rarefaction Wave Angle in $\mathcal{P}\left(\alpha, \chi, \mu_e\right)$

Predicted Relationship

As has been discussed previously, the expansion of ions into the wake region of a mesothermal body is dictated by the ion acoustic Mach number M_i, which describes the speed at which an electrical disturbance may travel through a plasma as a result of longitudinal unmagnetised ion oscillations i.e. electrostatic ion wave speed. The ion acoustic Mach number is given by (Burgess and Scholer, 2015),

$$M_i = v_B / \sqrt{k_B(T_e + \gamma_i T_i)/m_i}, \quad \gamma_i = 1 + 2/n \tag{6.1}$$

$\gamma_i = 3$ ($n = 1$) in a collisionless plasma (Burgess and Scholer, 2015).

In the frame of the body, the disturbance caused by the body travels outwards at M_i. As a result, the outer edge of the rarefaction wave can defined as (Samir, Wright, and Stone, 1983),

$$\theta_r = \sin\left[M_i^{-1}\right] \tag{6.2}$$

Recall in Section 5.4 however, that an analysis of the wave edge allowing for ion thermal effects allowed the electrostatic Vlasov equation to be expressed as,
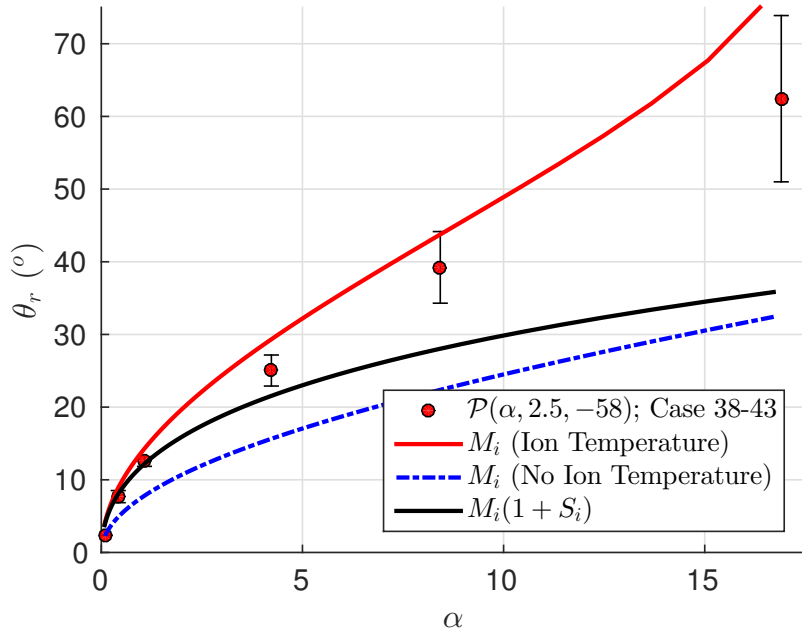
$$\mathbf{u}_k \cdot \hat{\nabla}_X F_k + M_i^{-2} \left(1 + S_i^{-1}\right)^{-2} \hat{\nabla}_X \Phi \cdot \hat{\nabla}_u F_k = 0 \tag{6.3}$$

As S_i becomes large (ion thermal effects become small), Eqn. 6.3 implies that ion deflections are governed by M_i which is consistent with Eqn. 6.2. Away from this limit however, Eqn. 6.3 suggests that both S_i and M_i will influence ion deflections and therefore the rarefaction wave angle. Assuming a similar relationship between the $1 + S_i^{-1}$ term as with M_i based on Eqn. 6.3, Eqn. 6.2 can be written as,
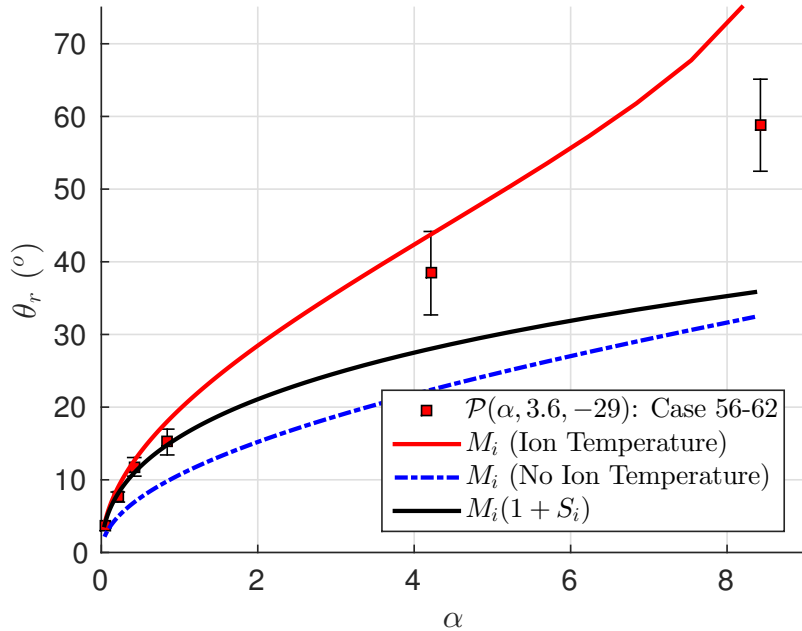
$$\theta_r = \sin\left[M_i^{-1}\left(1 + S_i^{-1}\right)\right] \tag{6.4}$$

For the case where the electron temperature is much larger than the ion temperature ($T_e \gg T_i$) and the ion thermal ratio S_i is non-negligible, Eqn. 6.4 can be expressed as a function of the scaling parameters such that,

$$\theta_r = \sin\left[Z_i^{-1}\alpha^{1/2}\mu_e^{-1/2}\left(1 + S_i^{-1}\right)\right] \tag{6.5}$$

Figure 6.6: Predicted dependence of rarefaction wave angle θ_r on the ion deflection parameter α compared against simulated trends in $\mathcal{P}(\alpha, 2.5, -58)$ (Cases 38-43).

Figure 6.7: Predicted dependence of rarefaction wave angle θ_r on the ion deflection parameter α compared against simulated trends in $\mathcal{P}(\alpha, 3.6, -29)$ (Cases 56-62).

Observed Relationship

To test this prediction, Figures 6.6 and 6.7 compare the variation of θ_r against the ion deflection parameter α_k spanning kinetic dominated and field dominated flow regimes at two points in the PIP, $\mathcal{P}(0 \leq \alpha \leq 17, 2.55, -58)$ (Cases 38-43) and $\mathcal{P}(0 \leq \alpha \leq 17, 3.6, -29)$ (Cases 56-62) - the latter set of cases having a thinner sheath. In a similar fashion, Figure 6.8 plots the variation of θ_r with the general shielding ratio χ, and Figure 6.9 plots the variation of θ_r with the electron energy coefficient μ_e.
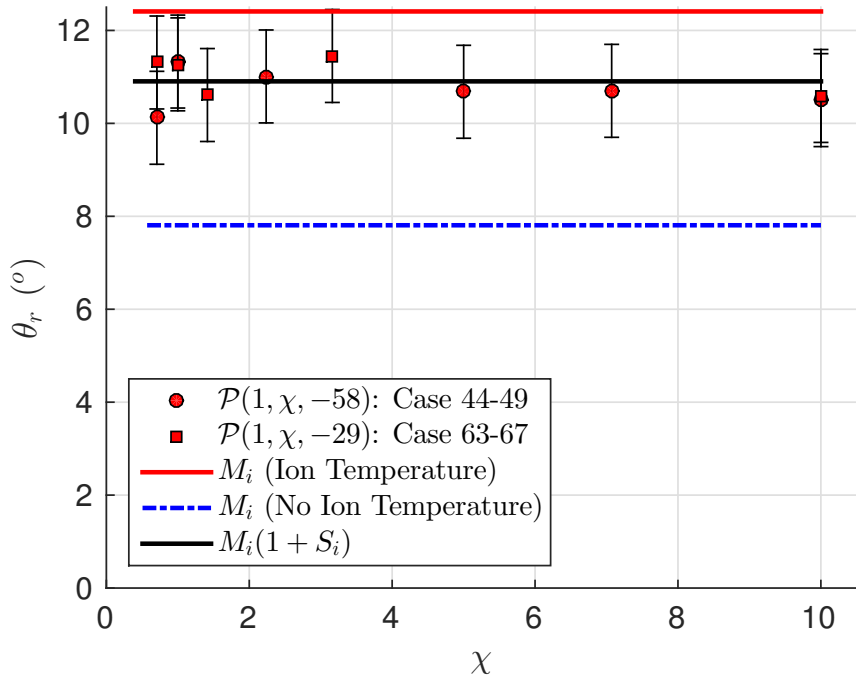
Three theoretical lines are included in these figures; the blue line corresponds to Eqn 6.7 where $S_i \to 0$, the red lines corresponds to Eqn. 6.7 which includes T_i and the black line corresponds to Eqn. 6.8 and includes both T_i and S_i terms,

$$(\theta_r)_{\text{red}} = \sin\left[\frac{1}{v_B}\sqrt{\frac{k_B\,(T_e + 3T_i)}{m_i}}\right] \tag{6.6}$$
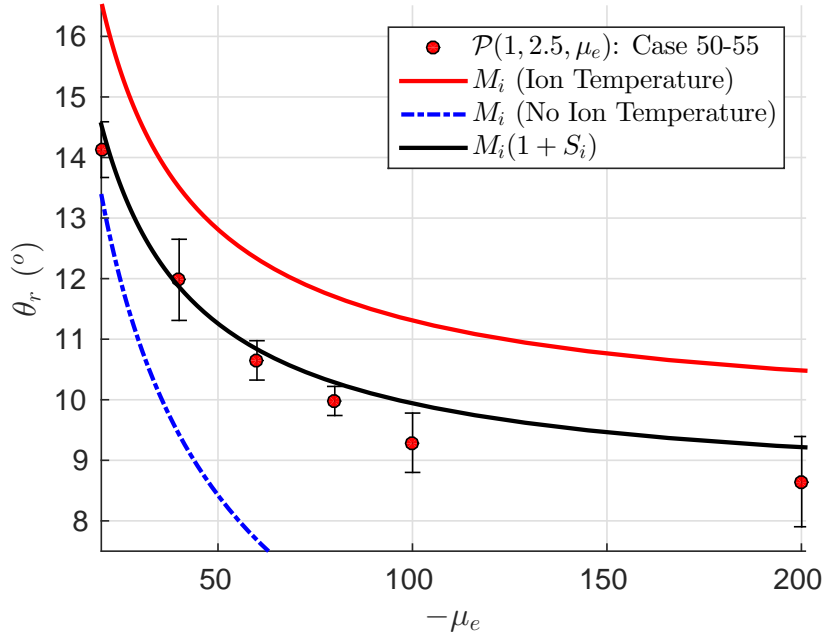
$$(\theta_r)_{\text{blue}} = \sin\left[\frac{1}{v_B}\sqrt{\frac{k_B T_e}{m_i}}\right] \tag{6.7}$$

$$(\theta_r)_{\text{black}} = \sin\left[\frac{1}{v_B}\sqrt{\frac{k_B\,(T_e + 3T_i)}{m_i}}\left(1 + \sqrt{\frac{2k_B T_i}{m_i}}\right)\right] \tag{6.8}$$

Figures 6.6 and 6.7 show that for low values of $\alpha_k < 1$, the inclusion of the ion thermal term provides an excellent prediction of θ_r. For high values of α_k corresponding to low flow velocities, none of the above equations correctly capture the simulated rarefaction angles observations. The departure from Eqn. 6.8 may more accurately reflect a breakdown of the mesothermal assumption as the flow velocity v_B has been scaled to increase α_k but S_i was not been held constant to scale the ion temperature effects i.e. Cases 38-43, and Cases 56-62 correspond to scaling of both α_k and S_i. This breakdown is reflected in the increase in measurement uncertainty, high-temperature tails of the particle distribution approach $S_i = 1$. Similar behaviour was seen in Chapter 4 where H^+ were only marginally mesothermal. As will be shown however, the rarefaction wave angle does not have a strong influence on charged aerodynamic forces, and therefore the assumption that ion thermal effects may be neglected in Chapter 5 remains valid.

Figure 6.8: Predicted dependence of rarefaction wave angle θ_r on the general shielding ratio χ compared against simulated trends in $\mathcal{P}(1, \chi, -58)$ (Cases 44-49) and $\mathcal{P}(0.5, \chi, -29)$ (Cases 63-67).

Figure 6.9: Predicted dependence of rarefaction wave angle θ_r on the electron energy coefficient μ_e compared against simulated trends in $\mathcal{P}(1, 2.5, \mu_e)$ (Cases 50-55).

6.3.3   Behaviour of the Ion Sheath Thickness in $\mathcal{P}\left(\alpha, \chi, \mu_e\right)$

Predicted Relationship

Given the similarities between the general shielding length λ_ϕ and the general Debye length λ_D and the Child-Langmuir law, the role of λ_ϕ was predicted to describe the electrostatic shielding of disturbances with potential energy ϕ in Chapter 5. As the ratio of body dimension r_B with λ_ϕ, χ then describes the dimensionless sheath thickness. However, as Section 6.3.1 showed in Figure 6.3, α_k also influences sheath thickness in a mesothermal flow, compressing the fore-body sheath has system becomes increasingly kinetic dominated.

To provide a physical basis for this compression, consider that functionally the plasma sheath's role is to enhance/retard ion/electron currents such that $I_i = I_e$ - the resultant electrical shielding a by-product of the governing equations. In a stationary plasma where $q_e \phi_B \ll k_B T_e$, the sheath thickness $r_{i,S}$ is defined by λ_D (Godd and Laframboise, 1983). As shown above, when this assumption breaks down, and the Child-Langmuir law provides a more accurate prediction of $r_{i,S}$, the sheath thickness is proportional to λ_ϕ. In a mesothermal plasma, neither $\lambda_{D,e}$, λ_D or λ_ϕ adequately describe the sheath thickness. The directed ion velocity provides an increased fore-body ion current while decreasing the flow on the side and rear of the body. To compensate for this non-uniform ion collection, the sheath must expand at a non-uniform rate about the body to capture ions. Therefore, the sheath should depend on both α and χ.

Based on the above discussions and observations in Chapter 4 where the sheath thickness was observed to be related to both ion mass and body potential, the ion sheath thickness $r_{i,S}$ is predicted to vary proportionally to the ion deflection parameter α and inversely proportionally to the general shielding ratio χ such that,

$$\frac{r_{i,S}}{r_B} = \alpha^a \chi^{-b} \tag{6.9}$$

where a, b are fitting coefficients.

This prediction is also consistent with numerical observations from McMahon, Xu, and Laframboise, (2005) and Choinière and Gilchrist, (2007), who studied the plasma sheath surrounding high-voltage cylinders, and the experimental observations in Stone, (1981a).
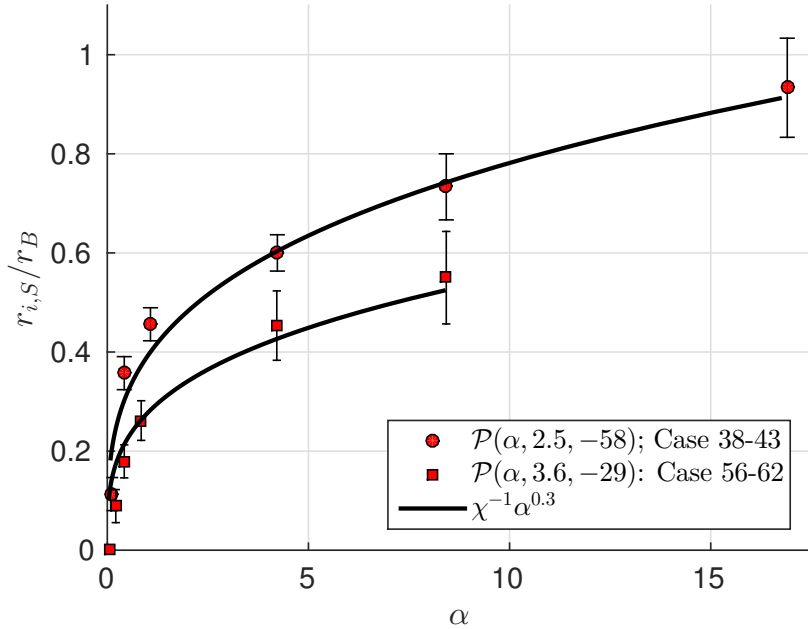
Observed Relationship

To test the predicted relationship between ion sheath thickness $r_{i,S}$ and Eqn. 6.9, Figures 6.10, 6.11 and 6.12 plot the variation of $r_{i,S}/r_B$ with α_k, χ and μ_e for Cases 38-67. Based on
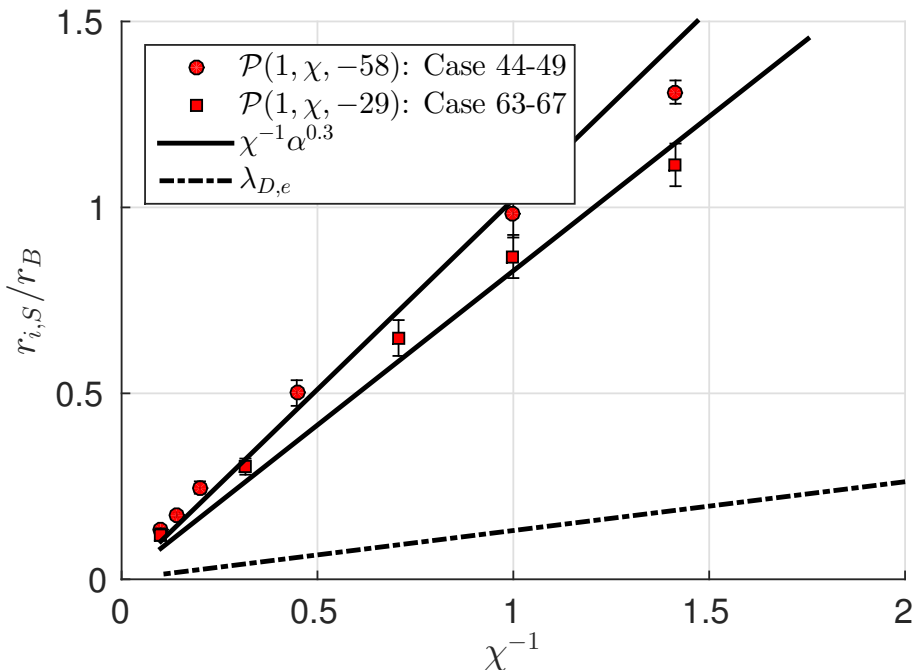
the data presented in Figures 6.10-6.12, the fitting coefficients in Eqn. 6.9 were determined to be $a \approx 0.3$ and $b = -1$ over the α range $0 < \alpha < 17$ for χ, μ_e pairs $2.5 - 58$ and $3.6, -29$.

Eqn. 6.9 overlaid on α_k and χ data in Figures 6.10 and 6.11 shows excellent agreement. This agreement degrades as $\alpha \to 1$ as illustrated in Figure 6.12, where $r_{i,S}/r_B$ is under-predicted by Eqn. 6.9. Figure 6.12 also shows a weak dependence of $r_{i,S}/r_B$ on μ_e when $q_e\phi_B \ll T_e$ (high-temperature limit), where the electron Debye length $\lambda_{D,e}$ appears to effect sheath thickness. $\lambda_{D,e}$ substantially under-predicts $r_{i,S}$ for all cases.
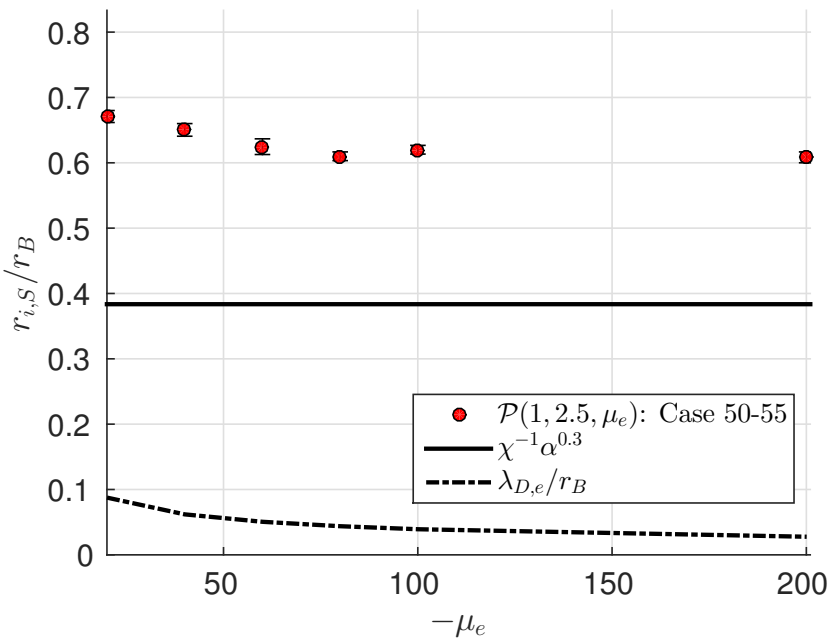
Based on the observations in Figures 6.10-6.12 and those made prior to this in Chapter 5, this work concludes the general shielding length λ_ϕ (and general shielding ratio χ) describes the electrostatic shielding disturbances with potential energy ϕ. This is a significant result as λ_ϕ represents a link between high and low voltage shielding phenomena apparently absent in the literature. Figures 6.10-6.12 also confirm the role of the ion deflection parameter α_k in the fore-body compression of the sheath structure in a mesothermal plasma.

Figure 6.10: Comparison between predicted dependence of $r_{i,S}$ on α with simulated measurements. Fit between Cases 38-43 and Eqn. 6.9: $R^2 = 0.972$. Fit between Cases 56-62 and Eqn. 6.9: $R^2 = 0.9319$.

Figure 6.11: Comparison between predicted dependence of $r_{i,S}$ on χ with simulated measurements. Fit between Cases 44-49 and Eqn. 6.9: $R^2 = 0.9789$. Fit between Cases 63-67 and Eqn. 6.9: $R^2 = 0.9819$.
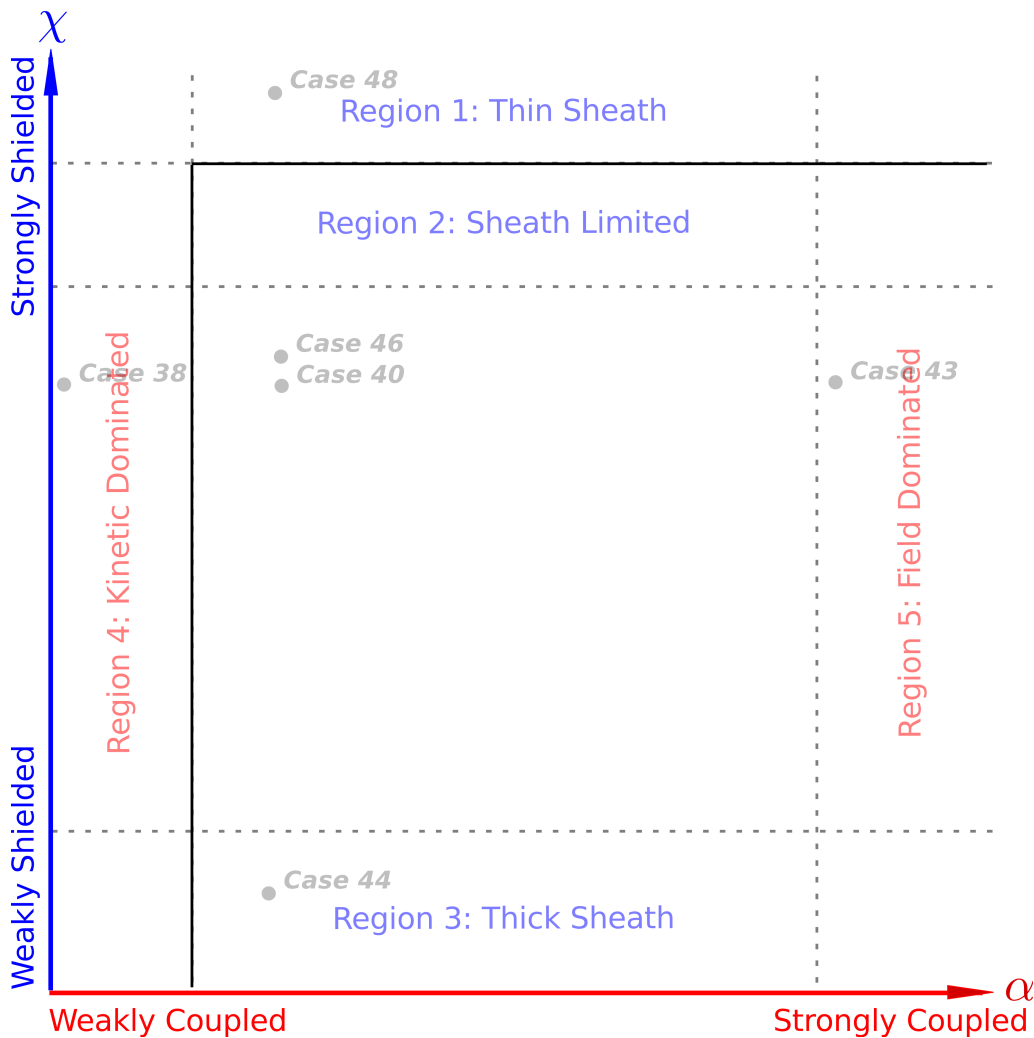
Figure 6.12: Comparison between predicted dependence of $r_{i,S}$ on μ_e with simulated measurements for Cases 50-55.

6.3.4 Summary of Collective Phenomena Observations

This section organised collective plasma interaction phenomena within $\mathcal{P}(\alpha, \chi, \mu_e)$, each point in mapping to a unique flow interaction. In particular, this section focused on identifying the relationship between the leading edge of the disturbance envelope generated by the motion of a charged 2D cylinder through a plasma. This disturbance envelope was defined here by the ion sheath thickness $r_{i,S}$ and rarefaction wave edge θ_r. Based on general observations of collective phenomena in Section 6.3.1 and specific observations of the relationship between $r_{i,S}$, θ_r and the scaling parameters in Section 6.3.2 and Section 6.3.3, the observed limiting behaviours are:

1. $\chi \gg 1$: *the sheath thickness becomes vanishingly small, and the flow approaching that of a neutral flow.*

2. $\chi > 1$: *the sheath thickness becomes thin compared to the body (strongly shielded). There is no evidence of bounded ion jets.*

3. $\chi < 1$: *the sheath thickness becomes thick compared to the body (weakly shielded). An over-dense ion peak forms in the wake and appears related to the ion pseudo-wave (this is investigated in the following section).*

4. $\alpha \ll 1$: *the fore-body ion sheath is not evident. The wake sheath structure was dominated by ion kinetic energy (kinetic dominated).*

5. $\alpha \gg 1$: *the fore-body sheath thickness becomes large, and the wake sheath structure becomes elongated (field dominated).*

These observations are illustrated in the plasma interaction phase-space $\mathcal{P}(\alpha, \chi)$ in Figure 6.13. The influence of electron energy coefficient μ_e is not shown as this work shall focus on characterising phenomena that influence charged aerodynamic forces. The electron energy coefficient primarily influences the rarefaction wave angle. As will be demonstrated, the rarefaction wave angle has a negligible affect on charged aerodynamic forces.
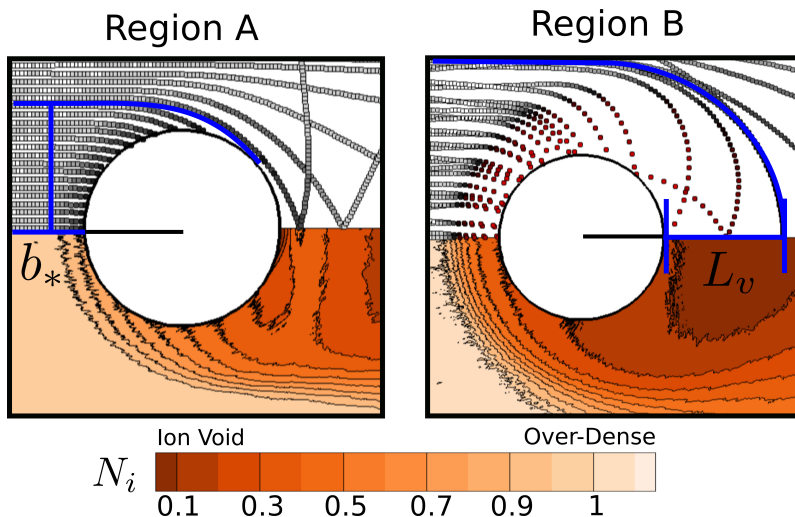
Figure 6.13: The limiting behaviour of collective phenomena observations in the plasma interaction phase-space $\mathcal{P}(\alpha_k, \chi)$. Red quantities refer to regions governed by the ion deflection parameter α_k. Blue regions refer to regions governed by the general shielding ratio χ.

6.4 Organising Kinetic Phenomena within the Plasma Interaction Phase-Space

This section focuses on organising kinetic plasma interaction phenomena within the PIP defined $\mathcal{P}(\alpha, \chi)$. In particular, this section focuses on characterising the ion absorption barrier shape which is responsible for both the bounded ion jet and ion pseudo-wave phenomenon.

Unlike the OM ion absorption barrier, which is symmetric in nature, the ion absorption barrier in mesothermal flows is elongated to reflect the structure of the sheath. As a result, this work uses two length measurements to capture the shape of the ion absorption barrier; the critical impact parameter b_* used to define the OM ion absorption barrier, and the wake velocity saddle point location L_v. Example measurements b_* and L_v measurements are illustrated in Figure 6.14. Physically, b_* capture corresponds to the effective ion collection enhancement caused by the sheath, while L_v represents the maximum distance behind the body an ion may be deflected through the wake axis and still be absorbed by the body.

To aid the investigation of particle kinetics, particle traces are included in this section. These particle traces are obtained by holding the steady-state potential fields constant and tracking the motion of particles through these fields. Traces shown correspond to particles with drift velocity v_B, the effect of particle thermalisation is not shown in these plots but is accounted for in the associated dimensionless ion density flowfields. The purpose of the traces being to provide a clear illustration of particle kinetics, whereas thermal effects introduce unnecessary visual complexities.

Figure 6.14: Illustration of critical impact parameter b_* (Region A) and wake velocity saddle point L_v (Region B) shown in blue.

6.4.1   Overview of Kinetic Phenomena
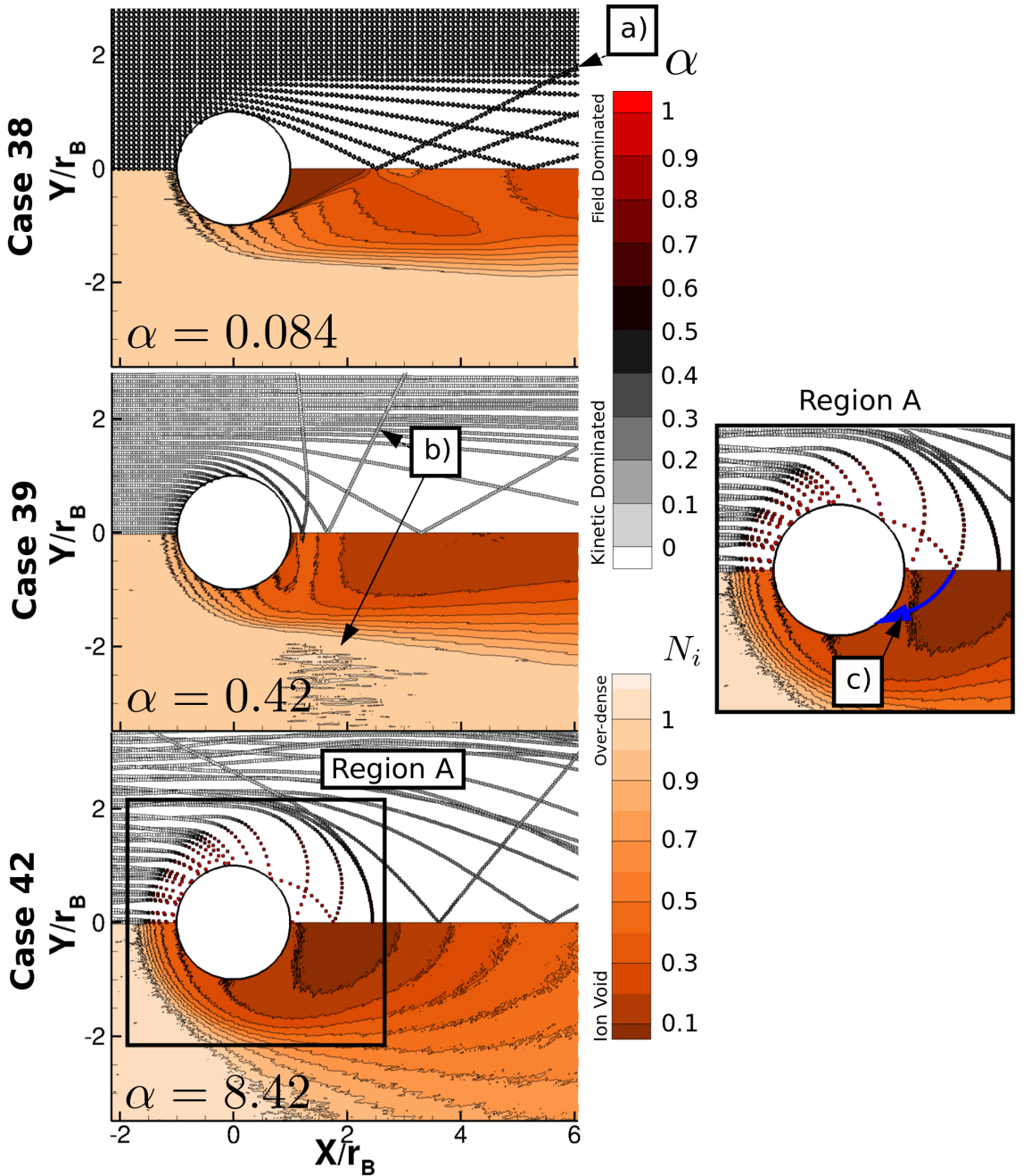
Effect of Ion Deflection Parameter on Kinetic Phenomena

To investigate the qualitative effects of the ion deflection parameter α_k on plasma interaction phenomena, Figure 6.3 plots kinetic (top), transitional (middle) and field dominated (bottom) flowfields in each frame corresponding to particle traces coloured by α (top) and dimensionless ion density N_i (bottom).

Ion Kinetic Dominated Flow: Figure 6.15 (top) confirms the assertion in Section 6.3.1 that the ion void region in the immediate wake of a cylinder in a kinetic dominated flow ($\alpha \ll 1$) is caused by the inability of the flow to deflect ions into orbits about the body (no ion velocity saddle point exists). The nature of the ion pseudo-wave at the outlet of the simulation is shown at a), ion beams deflected across the wake creating a small over-dense region in the far-wake.

Intermediate Kinetic/Field Coupling: Following from the kinetic dominated case in Figure 6.15 (top), the ion pseudo-wave phenomena is clearer in intermediate case. Here the reduction in ion kinetic energy (or increase in body potential energy) allows ions to be deflected through greater angles. This has two effects. First, the effective ion collection area has increased when compared to kinetic dominated flow. Second, a wake velocity saddle point now exists, illustrated by the unbounded ion trajectories ejected from the sheath perpendicular to the flow direction. These unbounded ion trajectories being the underlying physical process causing the ion pseudo-waves.

Field Dominated Flow: As the potential energy of the body dominates the ion kinetic energy ($\alpha \gg 1$), the ion absorption barrier appears to have elongated in Figure 6.15 (bottom). This elongation is reflected by the increase in the wake velocity saddle point location, shown in Figure 6.15 (bottom) by ion trajectory ejected forward into the flow. The most important feature is highlighted in Region A, a bounded ion trajectory impacting the rear surface of the cylinder c). This ion trajectory is responsible for the direct ion thrust seen previously in Chapter 4 and is discussed further in Section 6.5.

Figure 6.15: Effect of α on ion trajectories. Particle traces (top) are compared again N_i (bottom) distributions. Region A and B highlight b_* and L_v respectively. Labelled features include: a) kinetic dominated ion pseudo-wave, b) increased pseudo-wave speed with increasing α, c) bounded ion trajectory.
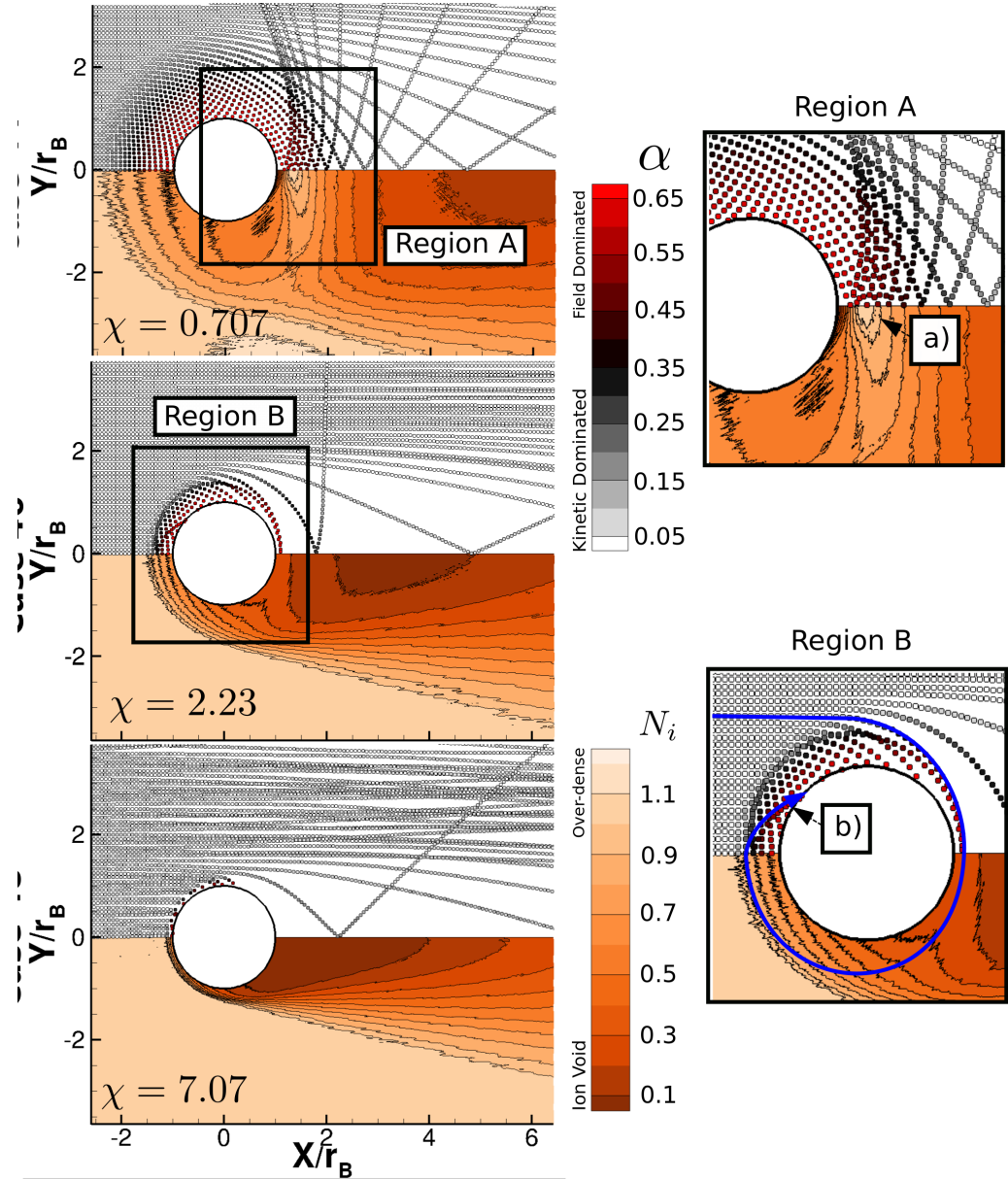
Effect of Body Shielding Ratio on Kinetic Phenomena

Figure 6.16 presents a similar set of plots to those in Figure 6.15 but investigates the effect of χ. As in Section 6.3.1, two limiting behaviours can be seen in Figure 6.16. These behaviours correspond to weakly shielded ($\chi < 1$) and strongly shielded ($\chi > 1$) interactions. Figure 6.16 clarifies the kinetic nature of several observations in Section 6.3.1.

Weak Shielding: An important feature observed in the weakly shielded case in Section 6.3.1 was the ion peak (over-dense region) in the wake flow. Figure 6.16 (top) illustrates that this ion peak is caused by the concentration of unbounded ion deflections into the wake region. Further, Figure 6.16 (top) demonstrates how these unbounded ion trajectories generate the ion pseudo-wave phenomenon discussed previously. Less evident from Figure 6.16 is that this feature is indicative of orbital motion limited ion collection (OML). This is investigated further in the following sections.

Intermediate Shielding: As the sheath thickness decreases in Figure 6.16 (middle) compared to Figure 6.16 (top) ion collection becomes sheath limited. As a consequence bounded ion trajectories, such as that highlighted in Figure 6.16 Region B, form. Here, the ion at b) is deflected through the near-wake into an orbit that travels around the body where it then connects with the fore-body surface (much like the bounded ion jet seen previously in Chapter 4).

Strong Shielding: For the strongly shielded case ($\chi > 1$, Case 48), the thin sheath means the effective ion collection is small. Another feature is the absence of bounded ion jets, consistent with observations regarding the attachment of the ion void contour in Figure 6.16 compared to intermediate shielding case in Figure 6.16 (middle) in Section 6.3.1.

Figure 6.16: Effect of χ on ion trajectories. Particle traces (top) are compared again N_i (bottom) distributions. Region A and B highlight a) the particle nature of the near-wake axial ion density peak b) bounded ion trajectory connecting to fore-body.

6.4.2   Behaviour of the Critical Impact Parameter in $\mathcal{P}(\alpha, \chi)$

Predicted Relationship

Chapter 4 introduced the OML impact parameter b_{OML} in an attempt to estimate the significance of direct charged aerodynamics to LEO objects. b_{OML} can be written as,
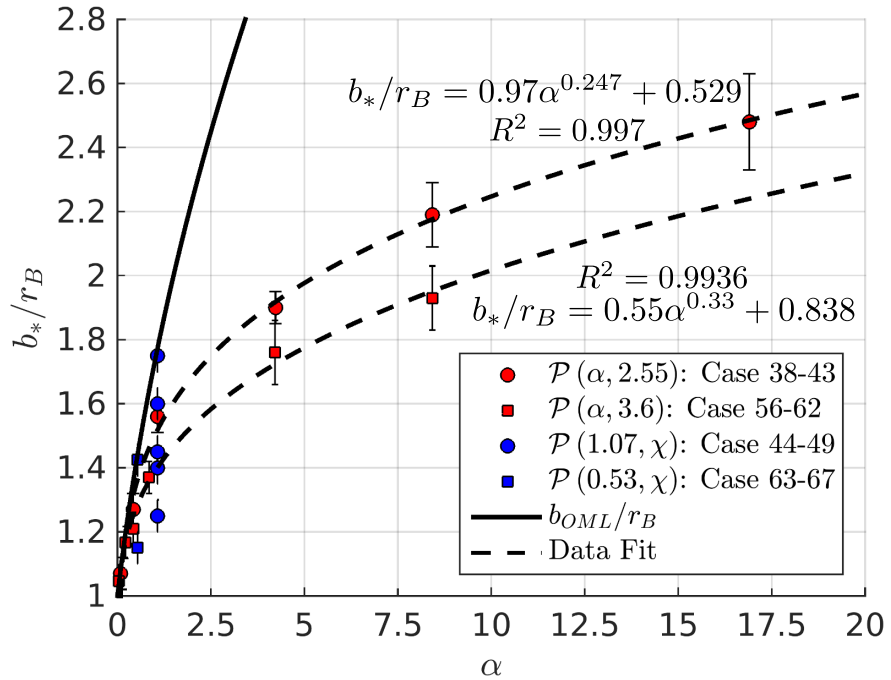
$$b_{\mathrm{OML}}/r_B = (1 + 2\alpha)^{1/2} \qquad\qquad (6.10)$$

Comparisons of theoretical and numerical direct charged drag $F_{D,d}$ measurements found in Chapter 4 showed that the OML approach consistently under-predicted $F_{D,d}$ but that this under-prediction was largely accounted for by considering indirect charged aerodynamic forces, which accounted for the force increased caused by ion accelerations. As a result, it was concluded that the increase in direct charged aerodynamic forces was largely a reflection of an enhanced ion collection area and therefore b_*. The following observations support this conclusion.
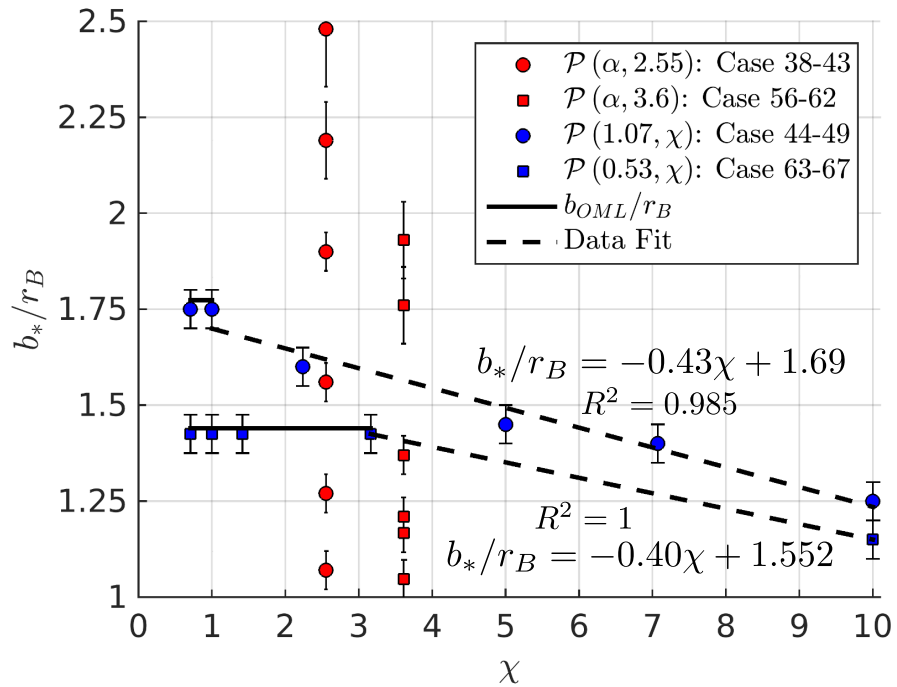
Observed Relationship

Figure 6.17 plots the variation of the dimensionless critical impact parameter b_*/r_B measured from simulations with the ion deflection parameter α_k and overlaid with b_{OML}. Similarly, Figure 6.18 plots the variation of b_*/r_B with the general shielding parameter χ. Lines of best fit have been included in Figure 6.17 to highlight the power law relationship between α and b_*, while lines of best fit in Figure 6.18 highlight the linear relationship of b_* with χ - points corresponding to b_{OML} were not included, hence, the fit between two points in Figure 6.18. Given the coupled nature of α_k and χ with $r_{i,S}$ observed in Section 6.3.3, cases that vary both α_k and χ have been included on both plots.

A key feature evident in both Figures 6.17 and 6.18 is that as the sheath becomes large (χ becomes small), the value of the critical impact parameter plateaus and this limiting value in ion current collection corresponds to b_{OML}. Consistent with Eqn. 6.10, this plateau is purely dependent on α_k. Therefore, this work concludes that α_k describes the upper limit of ion collection and that this corresponds to the Orbital Limited Motion (OML) limit. As the sheath thickness decreases however, the trend of b_* with α_k rapidly decreases. In the limit that the sheath thickness becomes thin ($\chi \gg 1$), b_* approaches the body radius, and ion collection is sheath-limited. A similar trend can also be seen in kinetic dominated flows where the effective ion collection area approaches the body radius ($b_* \to r_B$) to reflect the resistance of ions to field effects and the compression of the fore-body sheath.
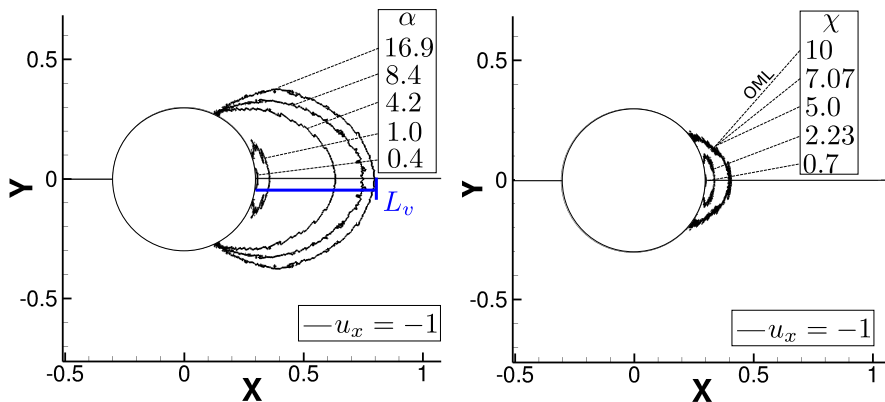
Figure 6.17: Effect of α on b_*. Equations of best fit are labelled

Figure 6.18: Effect of χ on b_*. Equations of best fit are labelled.

6.4.3   Behaviour of the Wake Velocity Saddle Point in $\mathcal{P}(\alpha, \chi)$
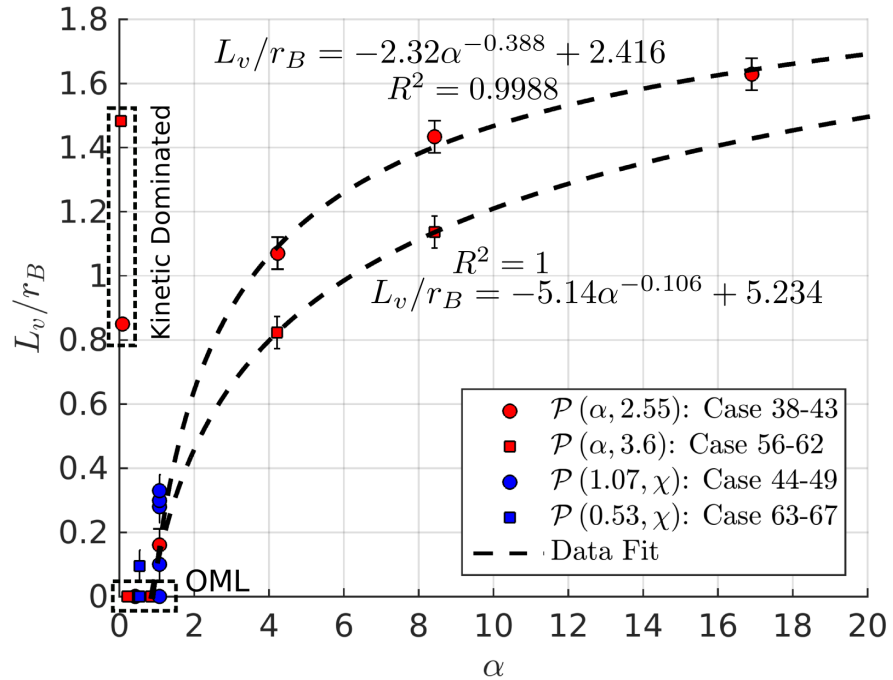
To quantify the elongation of the wake sheath a logical feature to inspect is the point at which ions are deflected back toward the body ($u_x < 0$). Figure 6.14 showed particle traces to illustrate the meaning of the wake velocity saddle point L_v. Figure 6.19 supplements this discussion with contour plots of $u_x = -1$ m/s for $\mathcal{P}(\alpha, 2.5)$ (Cases 38-43) (left) and $\mathcal{P}(1, \chi)$ (Cases 44-49) (right).
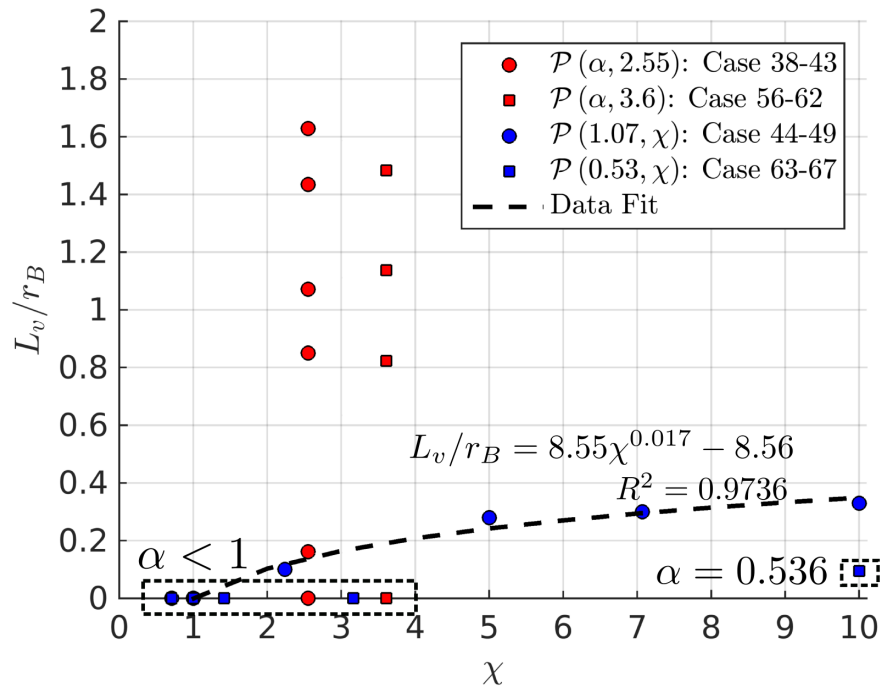
Figure 6.19: $u_x = -1$ contours for $\mathcal{P}(\alpha, 2.5)$ (Cases 38-43) (left) and $\mathcal{P}(1, \chi)$ (Cases 44-49) (right). No velocity inflection is seen in $\mathcal{P}(0.08, 2.5)$ (Case 38) and is therefore not shown.

Figure 6.19 illustrates the strong dependency of L_v on the ion deflection parameter α and its asymptotic behaviour with χ. As seen in the previous section, this asymptotic behaviour corresponds to OML ion collection. These behaviours are shown in Figures 6.20 and 6.21, which plot the variation of L_v with α and χ respectively. Again, a power law type dependence of L_v on α can be seen for $\alpha > 1$ - data points with $\alpha \leq 1$ were not included in the fit. For a majority of cases studied, when the kinetic energy of the incoming ions is greater than the electrostatic energy of the body there is no velocity inflection point in the wake of the body - the exception being the strongly shielded, weakly coupled case at $\mathcal{P}(0.536, 10)$ (Case 67). The flow then takes on one of two distinctive patterns.

The first is the ion kinetic dominated case seen in $\mathcal{P}(0.08, 2.55)$ (Case 38) of Figure 6.15, where ions are unable to fill the void immediately behind the body i.e. ion orbits are hyperbolic. The second is that seen in Figure 6.16, $\mathcal{P}(1.0, 0.7)$ (Case 44). These cases are characterised by dense ion pseudo-waves, where ions are deflected through the near-wake of the body on unbounded trajectories. For $\alpha > 1$, all cases exhibit a velocity inflection ($L_v > 0$) i.e. ions are deflected back toward the body.

Figure 6.20: Effect of α on L_1. Equations of best fit are labelled.
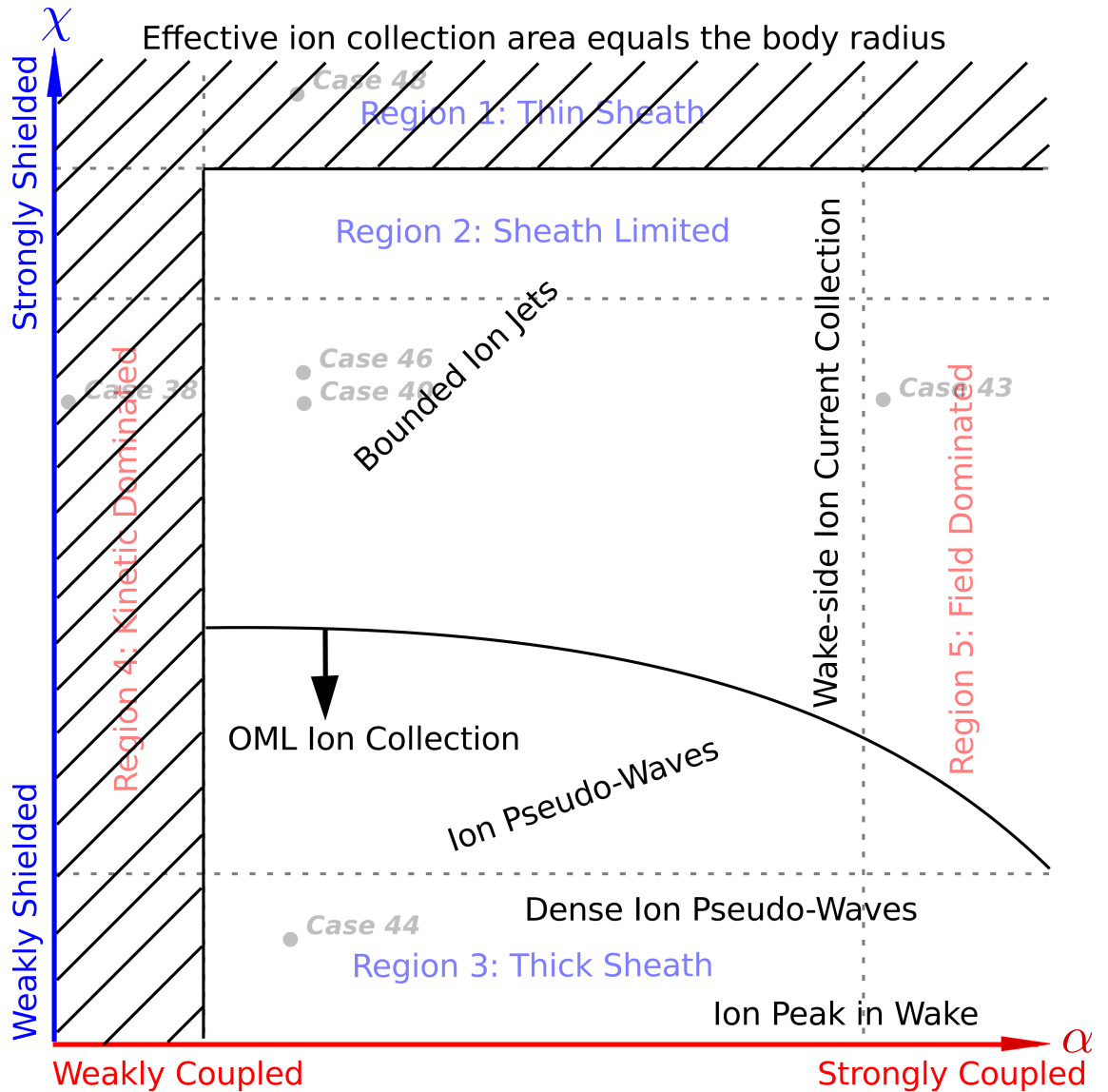
Figure 6.21: Effect of χ on L_1. Equations of best fit are labelled.

6.4.4   Summary of Kinetic Phenomena Observations

This section organised kinetic plasma interaction phenomena within $\mathcal{P}(\alpha, \chi)$. In particular, this section focused on characterising the shape of the ion absorption barrier defined by the critical impact parameter b_* and the wake velocity saddle point L_v. Based on general observations of kinetic phenomena in Section 6.4 and specific observations of the relationship between the critical impact parameter b_*, wake velocity saddle point L_v and the scaling parameters, the following conclusions were drawn:

1. *When the sheath thickness becomes larger than b_{OML} ($\chi > b_{OML}/r_B$), ion collection becomes Orbital Motion Limited (OML).*

2. *When the sheath thickness becomes much larger than b_{OML} ($\chi \gg b_{OML}/r_B$), an axial ion peak and dense ion pseudo-wave form.*

3. *When the sheath thickness becomes smaller than b_{OML} ($\chi < b_{OML}/r_B$), bounded ion jets form.*

4. *As ion kinetic energy decreases relative to the body potential energy ($\alpha > 1$), the elongation of the ion absorption barrier increases.*

5. *In the limit that $\chi \gg 1$ (thin sheath), the effective ion collection area approaches the body radius ($b_* \approx r_B$).*

6. *In the limit that $\alpha \ll 1$ (kinetic dominated), the effective ion collection area approaches the body radius ($b_* \approx r_B$).*

These observations are illustrated in the plasma interaction phase-space $\mathcal{P}(\alpha, \chi)$ in Figure 6.22. Given the physical map of plasma interaction phenomena in $\mathcal{P}(\alpha, \chi)$, the remaining step is to link these phenomena to charged aerodynamics.

Figure 6.22: Observations of kinetic phenomena super-imposed on the plasma interaction phase-space $\mathcal{P}(\alpha, \chi)$. Lines and location of labels are illustrative.

6.5 Charged Aerodynamics and Interaction Phenomena

This sections links observed interaction phenomena to charged aerodynamic forces in $\mathcal{P}(\alpha, \chi)$. Section 6.5.1 begins by re-iterating the physical nature of indirect charged aerodynamics. Section 6.5.2 then briefly demonstrates that the influence of the electron energy coefficient μ_e is indeed negligible. Sections 6.5.3 and 6.5.4 then consider the influence of phenomena governed by the ion deflection parameter α and the general shielding ratio χ on charged aerodynamic forces.

6.5.1 Indirect Charged Aerodynamics: A Refresher
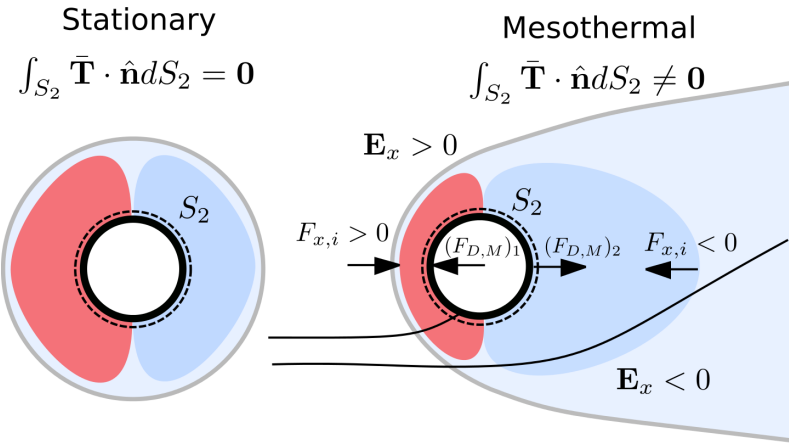
Indirect charged aerodynamic forces represent the momentum exchanged between ion and body required to increase (decrease) the ion (electron) current such that the surface charge on the body reaches a dynamic equilibrium with the surrounding plasma. A physical consequence of this acceleration is the plasma sheath; the intrinsic shielding of disturbances both *within the plasma* and the shielding of external disturbances *by the plasma* resulting in the self-consistent sheath structure observed in simulations presented throughout this work. Section 2.2.3 applied the control surface approach in Allen, (2007) to show that the charged aerodynamic force vector $\mathbf{F}_C$ can be written as,

$$\mathbf{F}_C = -\underbrace{\int_{S_2} n_i m_i \left(\mathbf{v} \cdot \hat{\mathbf{n}}\right) \mathbf{v} dS}_{\text{direct force}} - \int_{S_2} p_e \hat{\mathbf{n}} dS \overset{0}{\nearrow} + \underbrace{\int_{S_2} \bar{\mathbf{T}} \cdot \hat{\mathbf{n}} dS}_{\text{indirect force}} \tag{6.11}$$

where $\bar{\mathbf{T}}$ is the Maxwell stress tensor that describes the flux of momentum in electric and magnetic fields through a surface S_2.

Physically, the Maxwell stress represents the force accelerating ions (and electrons) through electric and magnetic fields. In a stationary plasma, the plasma sheath surrounding an object is symmetric. At steady-state, the ions experience an electrostatic acceleration that is transferred through the self-consistent sheath structure to the body where it is felt as an electrostatic pressure and shear (Newton's third law). Given the symmetric nature of stationary plasma sheaths, the surface integral of this electrostatic force (Maxwell stress) $\mathbf{F}_m$ is zero. The sheath structure surrounding a mesothermal plasma-body interactions is not symmetric.

Figure 6.23 illustrates the physical difference between stationary and mesothermal sheath structures and the relationship between ions that experience a force $F_{x,i}$, and the indirect thrust $(F_{T,m})$ and drag $(F_{D,m})$ forces experienced by the body. As has been shown, the sheath structure in a mesothermal flow is elongated by the directed ion velocity. While
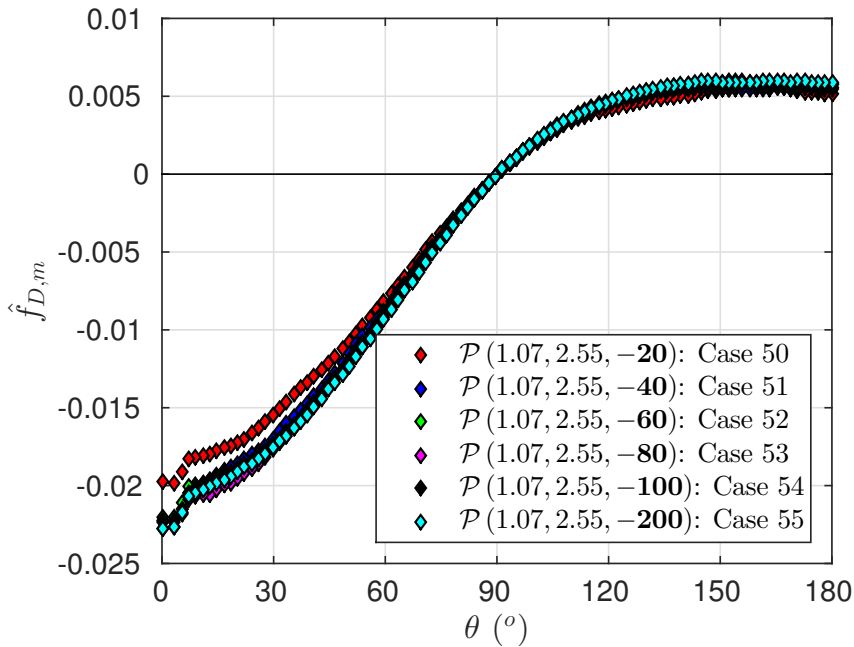
Figure 6.23: Illustration of the linked between collective phenomena and indirect charged aerodynamics through the maxwell stress.

ions are still accelerated through the fore-body sheath, the hyperthermal nature of the ion flow means that the wake sheath tends to exert a deceleration force on the ions. As with the force accelerating ions, this deceleration force is transferred through electric fields and felt as a force on the body surface. In words, indirect charged aerodynamic forces can be represented by a local surface force that reflects the structure of the local fields setup by the surrounding plasma. These fields, in turn, account for the momentum gained and lost by accelerated and scattered ions.
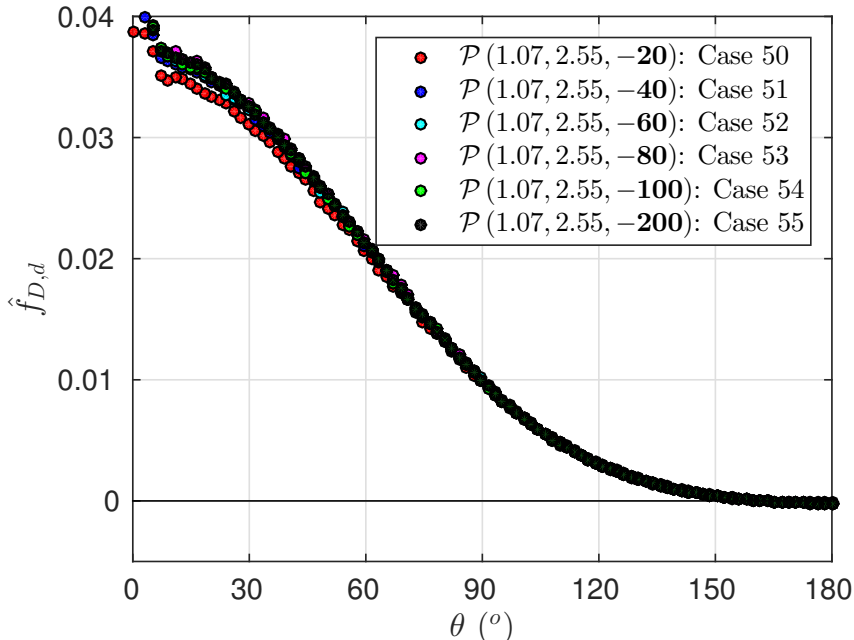
6.5.2 The Electron Energy Coefficient and Charged Aerodynamics

The electron energy coefficient μ_e describes the ability of electrons to penetrate electrical disturbances. The primary influence of the μ_e was on the rarefaction wave angle θ_r. To support this argument, Figures 6.24 and 6.25 plot the variation of normalised indirect $\hat{f}_{D,m}$ and direct $\hat{f}_{D,c}$ charged drag about the cylinder surface (θ) for different values of μ_e. Figure 6.26 plots the variation of the normalised total drag force $\hat{f}_{D,C}$ with μ_e. Normalisation is by total charged drag $F_{D,C}$.
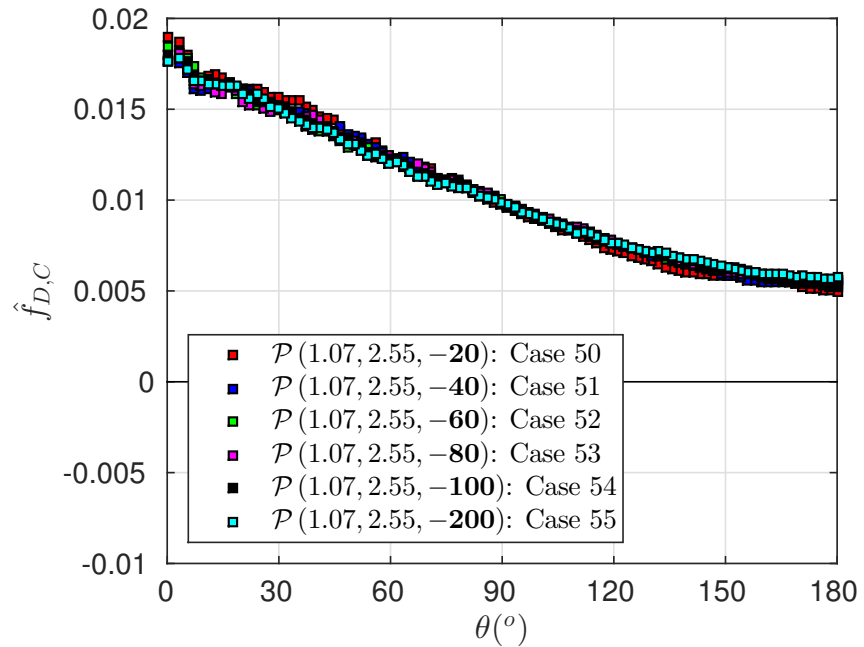
Figures 6.24 and 6.25 demonstrate that, with the exception of the $\mu_e = -20$ case, the distribution of normalised indirect and direct charged aerodynamic forces is not influenced by the electron energy coefficient μ_e. At $\mu_e = -20$, Figure 6.24 shows a small reduction in the relative contribution of both fore-body indirect and direct charged aerodynamic forces in the $\mu_e = -20$ case. Figure 6.26 demonstrates that the net change in indirect and direct charged aerodynamic forces do not affect the total charged drag distribution compared to the other cases and therefore the electron energy coefficient and by extension, rarefaction wave angle, does not influence charged aerodynamics.

Figure 6.24: Influence of phenomena governed by the electron energy coefficient μ_e on the normalised indirect charged aerodynamic force distribution $\hat{f}_{D,m} = f_{D,m}/F_{D,C}$.

Figure 6.25: Influence of phenomena governed by the electron energy coefficient μ_e on the normalised direct charged aerodynamic force distribution $\hat{f}_{D,d} = f_{D,d}/F_{D,C}$.

Figure 6.26: Influence of phenomena governed by the electron energy coefficient μ_e on the normalised total charged aerodynamic force distribution $\hat{f}_{D,C} = f_{D,C}/F_{D,C}$.

6.5.3   The Ion Deflection Parameter and Charged Aerodynamics
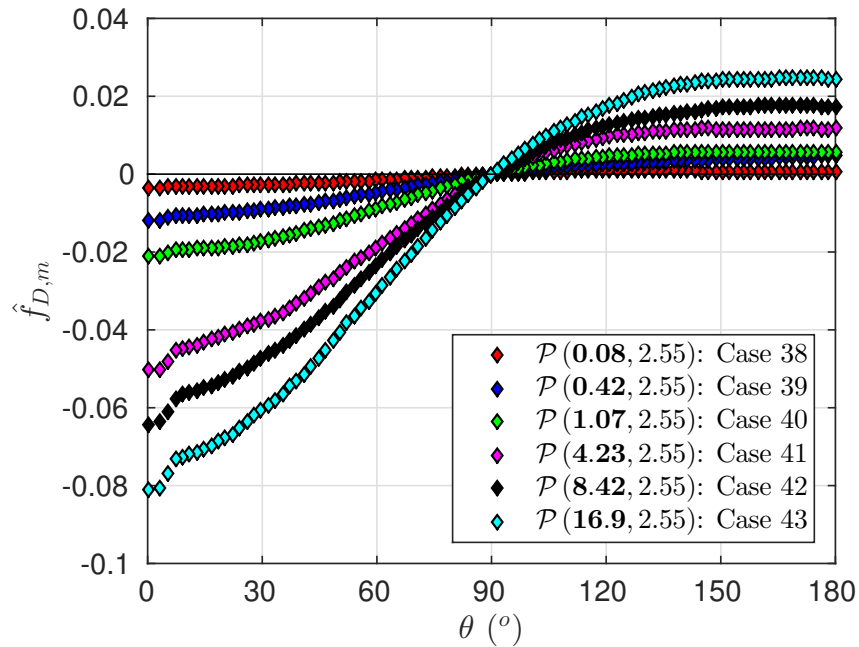
The ion deflection parameter α_k describes the ratio of ion kinetic energy to the potential energy of the body. Section 6.3.1 demonstrated that α_k scales the plasma sheath thickness, an increase in direct ion kinetic energy "compressing" the fore-body sheath. Section 6.4 demonstrated that α_k governs the critical impact parameter b_*, which physically describes the maximum distance from the flow axes within which an ion with a particular velocity can enter the body's sheath and be collected by the body. Section 6.4 also demonstrated that α_k governs the elongation of the wake sheath. Based on these observations, interactions where $\alpha_k \gg 1$ were mapped within the plasma interaction phase-space $\mathcal{P}(\alpha_k, \chi)$ as *"field dominated"* and $\alpha_k \ll 1$ as *"kinetic dominated"*.

To link the observed phenomena influenced by the ion deflection parameter α_k to indirect $(f_{D,m})$ and direct $(f_{D,d})$ charged aerodynamic surface forces, Figures 6.27 and 6.28 plot the distribution of normalised indirect $(\hat{f}_{D,m})$ and direct $(\hat{f}_{D,d})$ charged drag force about the cylinder surface with θ for different values of α_k. To emphasise the relative contribution of indirect and direct charged drag forces, Figure 6.29 plots the variation of the normalised total drag force $\hat{f}_{D,C}$ with α_k. Normalisation is by total charged drag $F_{D,C}$.
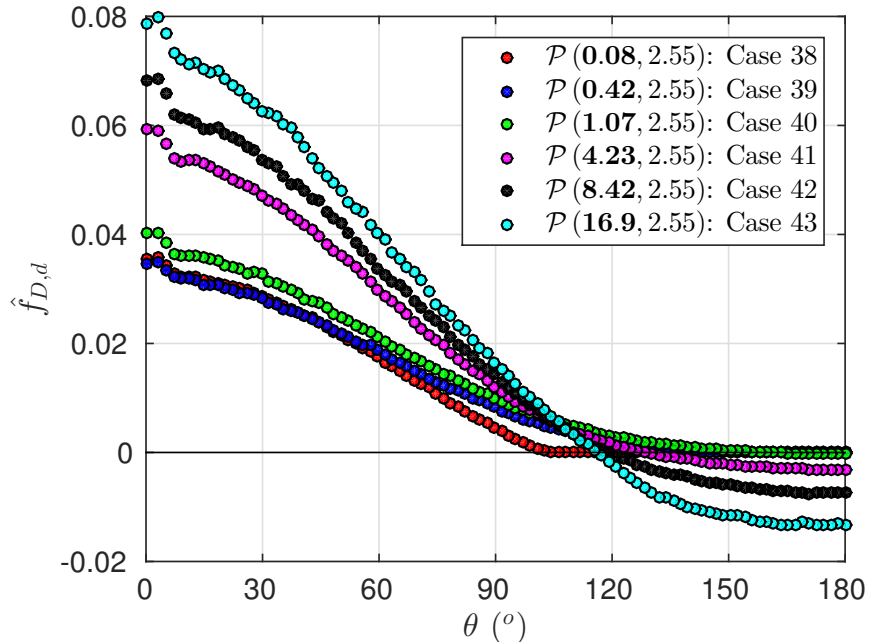
Fore-Body ($\theta \leq 90^o$):   For kinetic dominated flows ($\alpha \ll 1$), direct charged aerodynamic forces are ram dominated and comprise the majority of the total charged drag force as seen in Figure 6.29. This interaction reflects the small sheath thickness combined with the large ion velocity i.e. ions have a short residence time in the sheath and are not accelerated (negligible indirect thrust force). Similarly, the large ion kinetic energy means that the wake sheath does not slow ions, and therefore the indirect scattering force is negligible.

As the relative ion kinetic energy decreases ($\alpha > 1$), the sheath thickness increases and ions are more susceptible to deflection by fields e.g. the plasma sheath. The physical manifestation of this changing balance of kinetic and potential energy on the fore-body is an increased indirect thrust force to counter the increased ion acceleration.
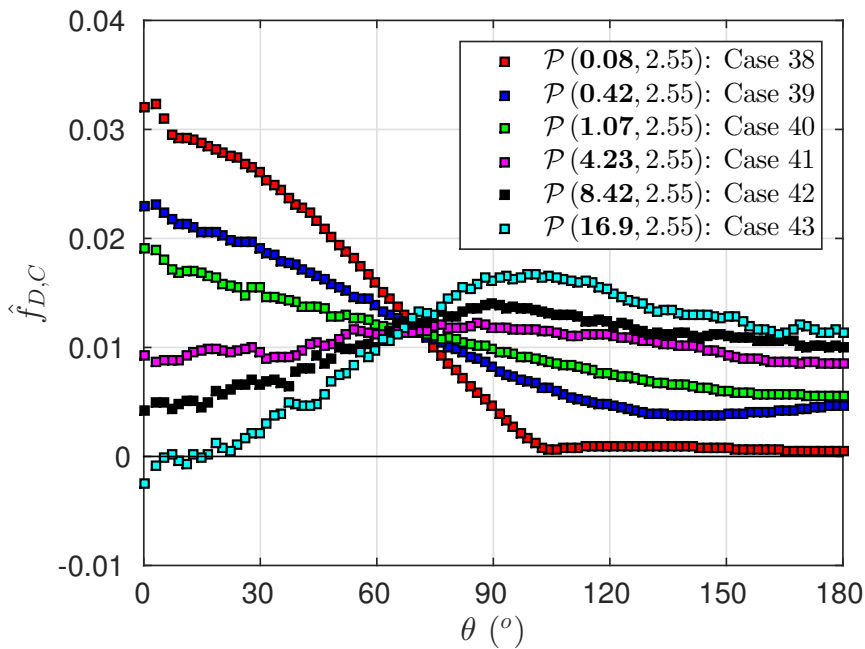
As α continues to increase, ion collection (direct charged aerodynamics) becomes orbital motion limited (OML) provided the sheath is thicker than b_{OML}. As a consequence, the net contribution of fore-body direct charged drag remains constant. However, the indirect charged aerodynamic force is unbounded (continues to increase with α). As a result, the indirect thrust continues to increase to reflect the ions accelerated but not collected by the body. As α increases, this indirect thrust outweighs the direct drag caused by the OML ion collection i.e. the system becomes dominated by indirect charged aerodynamic forces.
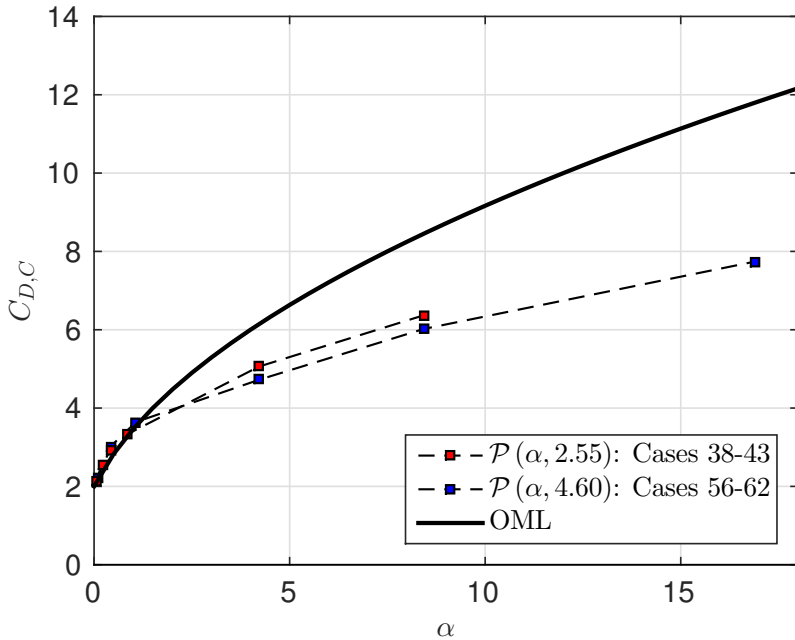
Figure 6.27: Influence of phenomena governed by the ion deflection parameter α on the normalised indirect charged aerodynamic force distribution $\hat{f}_{D,m} = f_{D,m}/F_{D,C}$.

Figure 6.28: Influence of phenomena governed by the ion deflection parameter α on the normalised direct charged aerodynamic force distribution $\hat{f}_{D,d} = f_{D,d}/F_{D,C}$.

Figure 6.29: Influence of phenomena governed by the ion deflection parameter α on the normalised total charged aerodynamic force distribution $\hat{f}_{D,C} = f_{D,C}/F_{D,C}$.

Figure 6.30: Comparison of the effect of χ on $\hat{C}_{D,c}$ Cases 56-62 and Cases 38-43.

Wake Surface $(\theta > 90^o)$: As the relative kinetic energy of the ions decreases compared to the potential energy of the body, ions were observed to be deflected through increasing large angles through the wake, the result being the increasing density of the ion pseudo-waves and the axial ion peak in the wake.

The effect of the elongated wake sheath associated with the ion deflection parameter α_k is a reflection of this where ions are deflected through angles greater than 90° with respect to the flow corresponding to a turning point in u_x. As the flow becomes increasing dominated by field effects, the increasingly deflection of ions manifests itself as an increasing indirect drag and direct thrust force as seen in Figures 6.27 and 6.28 respectively.

As shown in Figure 6.29, the indirect drag on the wake surface of the cylinder dominates the total charged aerodynamic force. This indirect force includes the indirect force exerted by the unbounded ion jets that form the ion pseudo-waves which also represent the increase in fore-body indirect thrust i.e. unbounded ion jets are accelerated past the body and deflected through large angles such that their net contribution is a drag.

Net Effect: Overall, the effect of the ion deflection parameter α_k is to describe kinetic dominated flow regimes characterised by ram dominated direct charged aerodynamic forces, and field dominated flows where indirect charged aerodynamic forces dominate and ion collection becomes orbital motion limited (OML). The relative size of the sheath will influence whether a system exhibits OML or sheath-limited ion collection.
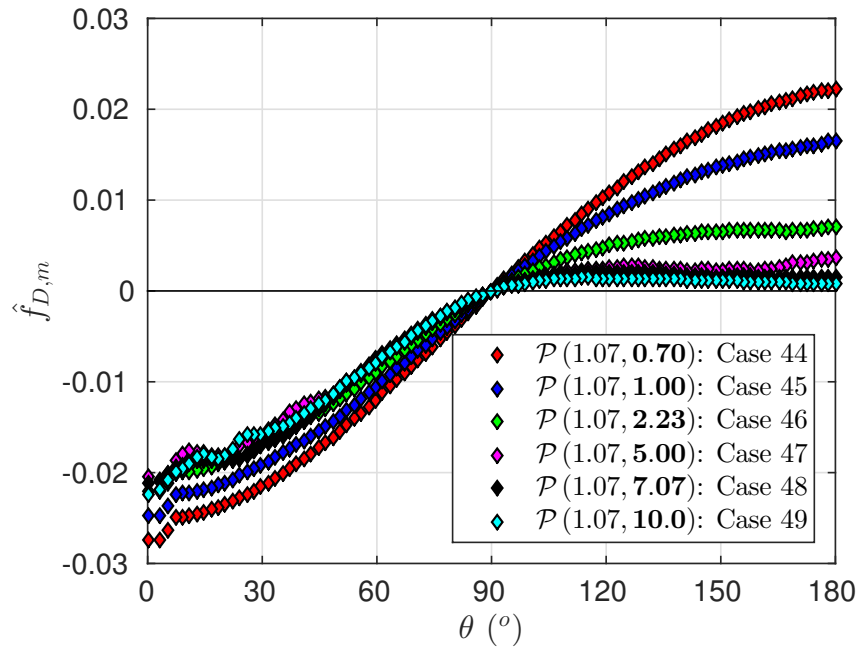
To emphasise these conclusions, Figure 6.30 plots the variation in the total charged drag coefficient $C_{D,C}$ with α_k and compares measured trends with the OML direct charged drag coefficient $C_{D,d}$. Figure 6.30 confirms the previous conclusions in Chapter 4 that OML direct charged aerodynamic predictions over-predict the total charged aerodynamic force on a body for large α_k. For low values of α_k where indirect charged aerodynamic forces are small and the charged aerodynamics is dominated by direct ram ion collection, OML provides a good approximation of $C_{D,C}$. This is not true for cases where indirect charged aerodynamic forces are large e.g. thick sheaths.

6.5.4   The General Shielding Ratio and Charged Aerodynamics
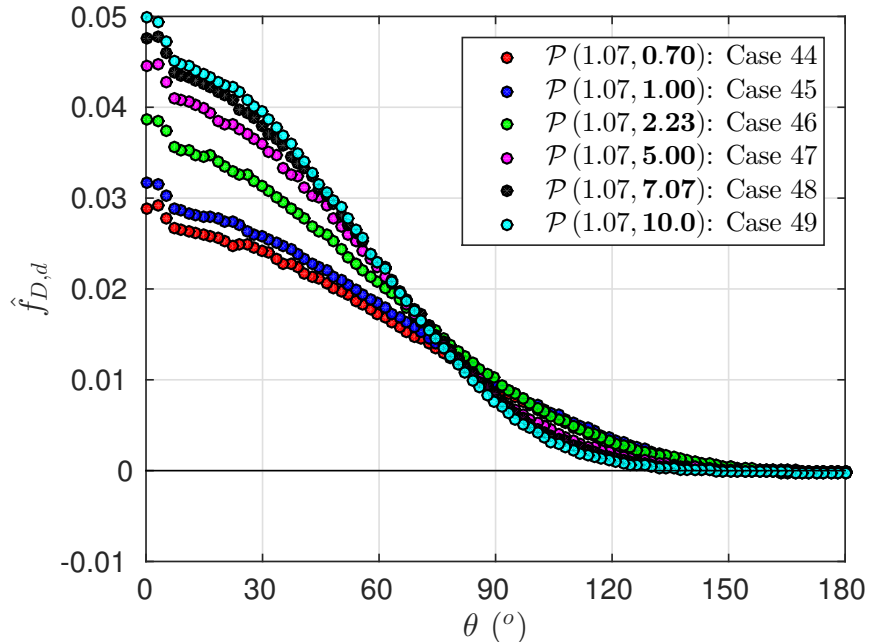
The general shielding ratio χ describes the relative thickness of the plasma sheath with the body. Based on observations in Section 6.3.1 and Section 6.4, interactions were mapped within the plasma interaction phase-space $\mathcal{P}(\alpha, \chi)$ as *"strongly shielded"* ($\chi > 1$) and *"weakly shielded"* ($\chi \ll 1$). The strongly shielded regime was then further grouped into *"sheath-limited"* flows, where the sheath thickness was less than the OML ion collection parameter b_{OML}, and *"thin-sheath"* flows, where the sheath thickness became very small ($\chi \gg 1$) and the effective ion collection area approaches the body size r_B.

To link the observed phenomena influenced by the general shielding ratio χ to indirect ($f_{D,m}$) and direct ($f_{D,d}$) charged aerodynamic surface forces, Figures 6.31 and 6.32 plot the distribution of normalised indirect ($\hat{f}_{D,m}$) and direct ($\hat{f}_{D,d}$) charged drag force about the cylinder surface with θ for different values of χ. To emphasis the relative contribution of indirect and direct charged drag forces, Figure 6.33 plots the variation of the normalised total drag force $\hat{f}_{D,C}$ with χ. Normalisation is by total charged drag $F_{D,C}$.
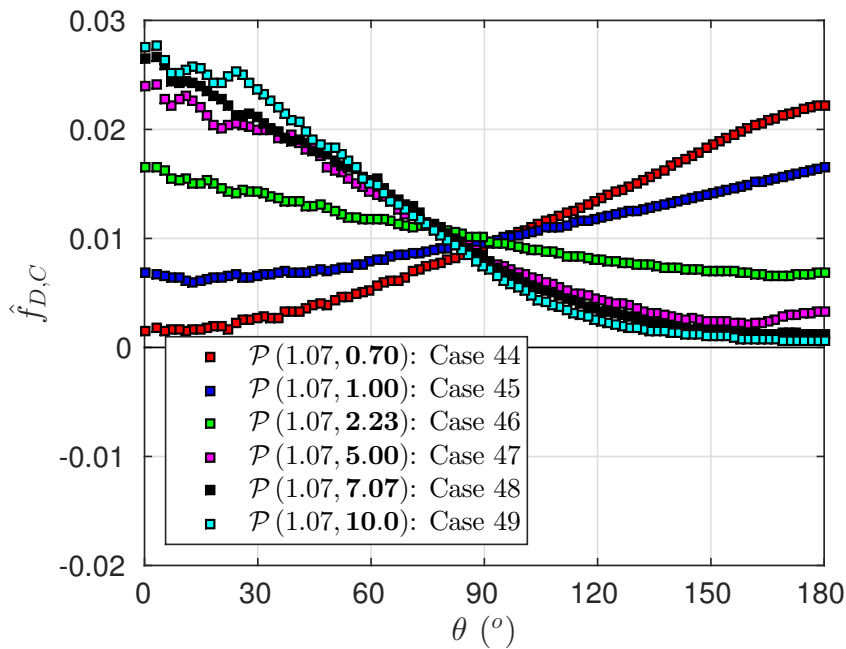
Fore-Body ($\theta \leq 90^o$): Strongly shielded flows, where the sheath thickness has become small, are dominated by direct charged drag forces on the ram surface of the cylinder as seen in Figures 6.31 and 6.32. As the thickness of the sheath increases (χ becomes small), the relative contribution of the direct charged drag on the fore-body compared to the indirect charged thrust decreases. Unlike in the field dominated case, the indirect thrust does not exhibit the same drastic increase with increasing sheath thickness. Physically, this is a reflection of the constant ion kinetic energy, the increase in sheath thickness marginally increasing the residence time of the ion in the sheath but does not significantly affect their net acceleration. As a result, the increase in ion acceleration and therefore indirect charge thrust does not significantly increase with decreasing χ. However, the indirect drag in the wake does increase.
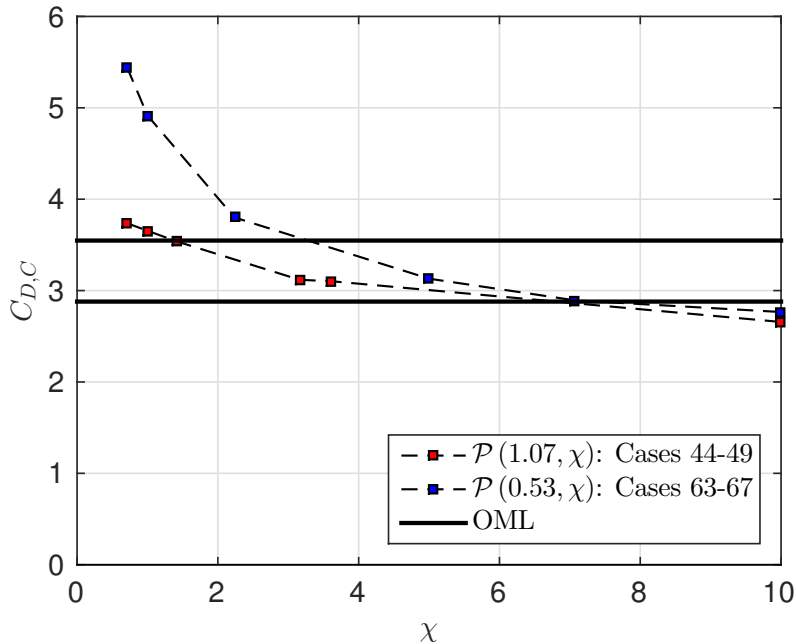
Figure 6.31: Influence of phenomena governed by the general shielding ratio χ on the normalised indirect charged aerodynamic force distribution $\hat{f}_{D,m} = f_{D,m}/F_{D,C}$.

Figure 6.32: Influence of phenomena governed by the general shielding ratio χ on the normalised direct charged aerodynamic force distribution $\hat{f}_{D,d} = f_{D,d}/F_{D,C}$.

Figure 6.33: Influence of phenomena governed by the general shielding ratio χ on the normalised total charged aerodynamic force distribution $\hat{f}_{D,C} = f_{D,C}/F_{D,C}$.

Figure 6.34: Comparison of the effect of χ on $\hat{C}_{D,c}$ Cases 63-67 and Cases 44-49.

Wake Surface ($\theta > 90^o$): The principle effect of increasing sheath thickness is to increase the indirect charged drag contribution. As the sheath thickness increases past the OML ion collection limit, direct charged aerodynamic forces become bounded given a constant α_k. The proportion of ions that enter unbounded orbits and contribute to ion pseudo-waves however increases with the sheath thickness. Further, as the sheath becomes increasingly thick, these ions enter the sheath such that they are not accelerated past the body (do not contribute to indirect thrust forces) but are instead deflected through large angles in the wake (the angle limited by α). Hence, the indirect drag force on the wake surface of the cylinder appears unbounded with χ as illustrated in Figure 6.31. It should be noted that indirect drag forces may become bounded for values of χ larger than those considered here.

Net Effect: The net effect of the general shielding parameter χ is to describe an interaction as dominated by direct charged aerodynamic forces ($\chi > 1$) or indirect charged aerodynamics forces ($\chi < 1$). This is emphasised in Figure 6.33. For large values of χ, total charged aerodynamic forces are ram dominated in Figure 6.33 and correspond to the direct charged aerodynamic forces. As χ becomes small, the influence of direct charged aerodynamic forces on the ram surface decays and the indirect drag on the wake becomes dominant. In the former case, the net drag asymptotes to a common value while in the latter case, net drag increases unbounded. To illustrate this, Figure 6.34 plots the variation of the total drag coefficient $C_{D,C}$ with χ where the OML $C_{D,d}$ is included to emphasise its inability to capture the variations in drag caused by the relative sheath thickness.
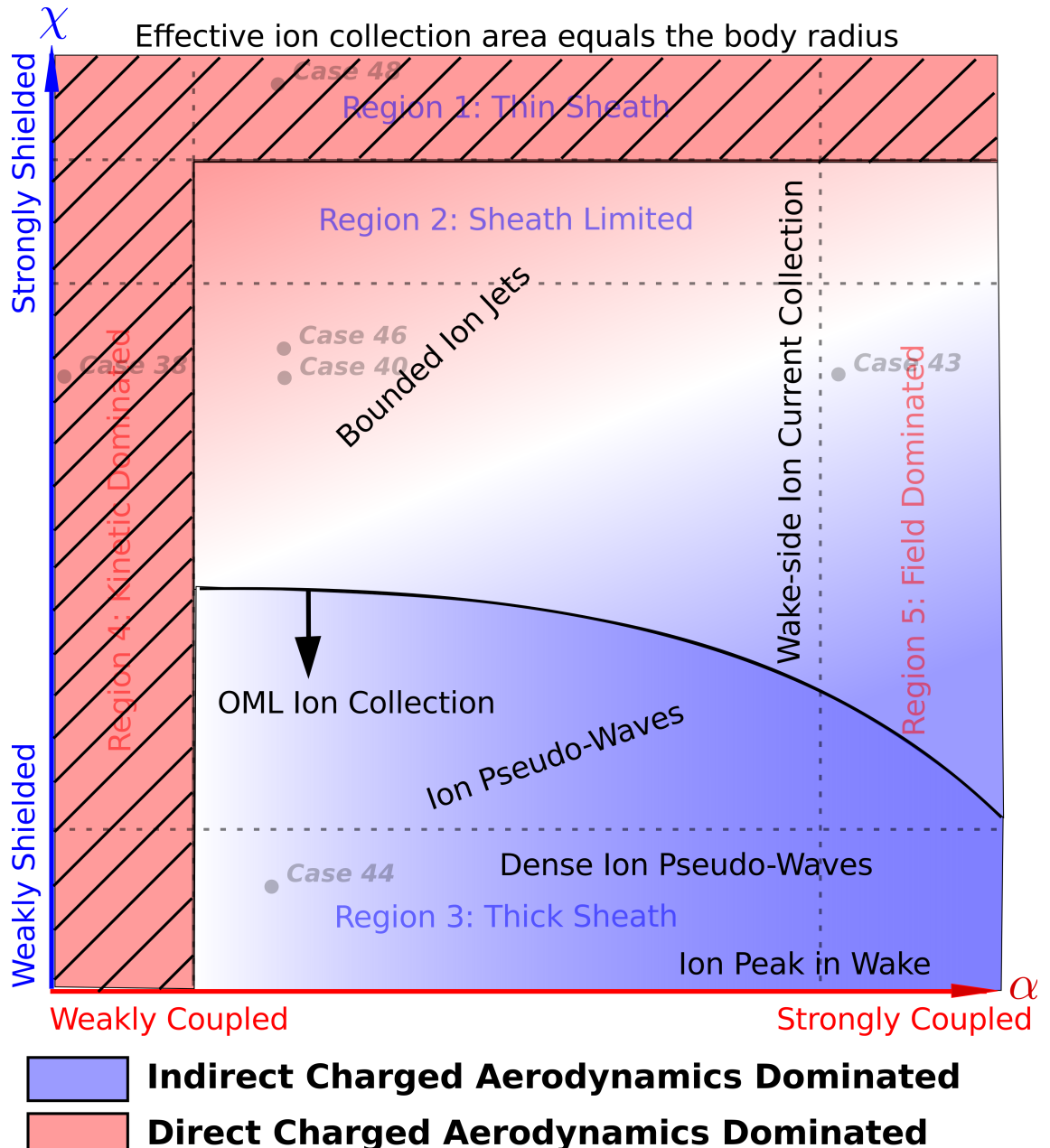
6.6   Summary

The purpose of this chapter was to capture and organise (both qualitatively and quantitatively) the key physical phenomena that influence charged aerodynamics . To achieve this, the relationship between the ion deflection parameter α_k, general shielding ratio χ and the electron energy coefficient μ_e that form the plasma interaction phase-space $\mathcal{P}\left(\alpha_k, \chi, \mu_e\right)$ was explored. Given that each point within $\mathcal{P}\left(\alpha_k, \chi, \mu_e\right)$ maps to a unique plasma interaction, by exploring the variation of collective and kinetic phenomena caused by scaling each of the parameters new physical insights into the nature plasma interaction phenomena were drawn. These insights include:

1. The ion rarefaction wave angle θ_r was shown to be proportional to the ion deflection parameter α_k and the ion thermal ratio S_i, inversely proportional to the electron energy coefficient μ_e and independent of the general shielding ratio χ. *A modification to the theoretical rarefaction wave angle to include S_i was made.*

2. *Based on observations of μ_e, the ion rarefaction wave was shown to not influence charged aerodynamics.*

3. *The electrostatic shielding of both high and low-voltage disturbances is described by the general shielding ratio χ.*

4. *When the sheath thickness is larger than the Orbital Motion Limited (OML) critical impact parameter b_{OML}, ion collection is well described by OML.*

5. *When the sheath thickness limits ion collection, bounded ion jets were observed to form, the extent of the ion jets described by α_k.*

6. *When the sheath becomes much thicker than b_{OML}, an axial ion peak formed by dense unbounded ion jets that form a strong ion pseudo-wave were observed.*

Drawing upon these observations, physical phenomena were mapped within $\mathcal{P}\left(\alpha_k, \chi\right)$. By understanding the physics underpinning these phenomena, their influence on indirect and direct charged aerodynamic forces was established. This link between charged aerodynamics and plasma interaction phenomena is summarised in Figure 6.35 In other words, the relationship between plasma interaction phenomena and charged aerodynamics have the following behaviours:

1. *For strongly shielded ($\chi \gg 1$) or kinetic dominated ($\alpha_k \ll 1$) flows, direct charged aerodynamic forces dominate the total charged aerodynamic forces and asymptote to a constant drag coefficient.*

2. *For weakly shielded flow ($\chi < 1$), the sheath becomes thick and indirect charged aerodynamic forces dominate the total charged aerodynamic forces experienced by the*

Figure 6.35: Illustration of the link between plasma interaction phenomena and charged aerodynamic within the plasma interaction phase-space $\mathcal{P}\left(\alpha_k, \chi\right)$. Lines and location of labels are illustrative.

body.   Bounded growth in indirect charged aerodynamic forces is not observed for
increasing sheath thickness.

3. *Direct charged aerodynamic forces exhibit bounded growth as sheath thickness in-*
   creases ($\chi < 1$). This growth is limited by OML ion collection which is purely depen-
   dent on the relative kinetic energy of the ions compared to the potential energy of the
   body i.e. α_k.

4. *For sheath-limited flows ($\chi \approx 1$), indirect and direct charged aerodynamic forces are*
   observed to compete depending on the position in $\mathcal{P}(\alpha_k, \chi)$.   Bounded ion jets are
   observed to form, and ion collection becomes increasingly uniform about the surface
   with increasing α_k (ram dominated for small α_k).

These observations relate the plasma interaction phenomena described within $\mathcal{P}(\alpha_k, \chi)$
to charged aerodynamics. Viewed the other way, charged aerodynamic forces have been
linked to $\mathcal{P}(\alpha_k, \chi)$ through the associated plasma interaction phenomena. As a result,
$\mathcal{P}(\alpha_k, \chi)$ *now provides a two-dimensional framework within which to study the influence*
of charged aerodynamics on a variety of plasma systems - with the focus of this work being
ionospheric aerodynamics.

Chapter 7

Applying the Flow Physics: Effect of Charged Aerodynamics on Low Earth Orbit Objects

7.1 Introduction

The central thesis explored in this work is that ionospheric aerodynamic forces can become appreciable compared to neutral (thermospheric) aerodynamic forces in LEO. Previous chapters developed a physical framework to understand how the electrostatic interaction generated when a negatively charged body orbits through the ionosphere affects the body's non-conservative force vector, the focus here being on the drag force. The purpose of this chapter is to apply this framework to resolve the central thesis of this work by answering two fundamental questions:

1. Do there exist regions in LEO where ionospheric aerodynamics forces becomes significant compared to neutral aerodynamics forces?

2. If so, do ionospheric aerodynamic forces in these areas have an appreciable effect on the orbit of LEO objects.

Section 7.2 begins by collating results from previous chapters to develop a physics-based $C_{D,C}$ response surface defined by the dimensionless parameters χ and α_k. Section 7.3.1 then addresses the first question by considering the ratio of charged to neutral drag forces in LEO based on the IRI-2012 and NRLMSISE-00 atmospheric models. Taking these results, Section 7.3.2 then considers the perturbation caused by ionospheric drag forces for three representative objects (3U CubeSat, OneWeb MicroSat and ENVISAT LargeSat) at two different surface potentials ($-0.75V$ and $-30V$) for two representative orbits (equatorial and polar). In doing so, this work presents evidence that ionospheric aerodynamics forces can be appreciable compared to neutral aerodynamics forces in LEO.

7.2 Charged Aerodynamics:
A Physics-Based Response Surface

Section 4.4.1 attempted to predict the influence of ionospheric aerodynamics in LEO by following prior OML based arguments to develop an expression for the direct charged drag force ($(F_{D,d})_{OML}$) on a cylinder. Based on comparisons with numerical ionospheric aerodynamic predictions, the conclusion was drawn that OML does not provide an accurate prediction of ionospheric aerodynamics forces except under special circumstances where direct charged aerodynamics forces are OML and indirect aerodynamic forces are negligible. To develop a tool for predicting the influence of ionospheric aerodynamics requires an approach other than OML valid for all conditions.

The purpose of this section is to build a response surface (Θ) based on physical observations of plasma phenomena in Chapter 6 that yields the net charged drag coefficient $C_{D,C}$ as function of the ion deflection parameter α and general shielding ratio χ e.g.

$$C_{D,C} = \Theta\left(\alpha_k, \chi\right) \tag{7.1}$$

To construct the response function Θ, a *"coarse"* model based on physical observations in Chapter 6 is fitted against a *"fine"* model represented by the set of charged drag measurements made in simulations presented throughout this work. Section 7.2.1 begins by demonstrating that these simulations sufficiently resolve the space within $\mathcal{P}\left(\alpha, \chi\right)$ occupied by LEO plasma-body interactions i.e. the *"LEO plasma interaction envelope"*. Section 7.2.2 then develops physical arguments to construct the coarse model, which is in turn calibrated against the fine model to identify additional coupling terms and case specific constants.

It should be note that the response surface constructed in this section is based on data and observations of long cylindrical bodies (2D). Hence, while it may be applied to other objects, specific quantitative predictions should only be considered as representative (first-order) for 2D shapes other than cylinders. The important point is that the response surface will under-predict charged aerodynamic forces for compact (3D) objects i.e. predictions are conservative for 3D objects.

7.2.1 Fine Model: Distribution of Simulation Measurements

A Monte Carlo approach is applied here to investigate the region of the plasma interaction phase-space $\mathcal{P}(\alpha_k, \chi)$ occupied by LEO objects. The Monte Carlo method is relatively straightforward; an upper and lower bound of interaction quantities are specified, and conditions are drawn randomly based on a probability distribution function (pdf) within these bounds over a large number of samples. The interaction quantities are then plotted in $\mathcal{P}(\alpha_k, \chi)$ and compared against Cases 1-67 to determine whether the spread of points in Cases 1-67 is sufficient for LEO plasma-body interactions. Additional simulations are then added to supplement Cases 1-67 in $\mathcal{P}(\alpha_k, \chi)$ where appropriate.

The interaction quantities considered in the Monte Carlo analysis are: freestream ion density $n_{i,\infty}$, body potential ϕ_B, body velocity v_B and body radius r_B. Two single-species plasmas are considered; a monatomic oxygen plasma O^+ and a monatomic hydrogen plasma H^+. Table 7.1 lists approximate upper and lower limits on plasma and body parameters in the ionosphere (Wang and Hastings, 1992b; Wang et al., 1994; Hastings, 1995; Garrett and Whittlesey, 2000), the exception being ϕ_B which is restricted to the range of potentials considered in this work.

The relationship between the interaction quantities and scaling parameters is,

$$
\begin{aligned}
\alpha &= A\frac{\phi_B}{v_B^2} \\
\chi &= B\left(\frac{r_B n_{i,\infty}}{-\phi_B}\right)^{1/2}
\end{aligned}
\tag{7.2}
$$

where A and B are ion mass dependent constants.

In words, Eqn. 7.2 implies that,

- An increase in body potential ϕ_B will increase α_k (system becomes field dominated) and decrease χ (sheath thickness increases).

- An increase in body radius r_B or ion density $n_{i,\infty}$ will increase χ (sheath thickness decreases).

- An increase in body velocity v_B will decrease α_k (system becomes kinetic dominated).

- An increase in ion mass m_i will scale α_k (system becomes kinetic dominated) and χ (sheath thickness becomes thin).

Table 7.1: Upper and lower bounds of interaction quantities used in the Monte Carlo analysis. Note: Ion mass is discrete, instead the space in $\mathcal{P}(\alpha, \chi)$ occupied by O^+ and H^+ dominated plasmas are considered separately.
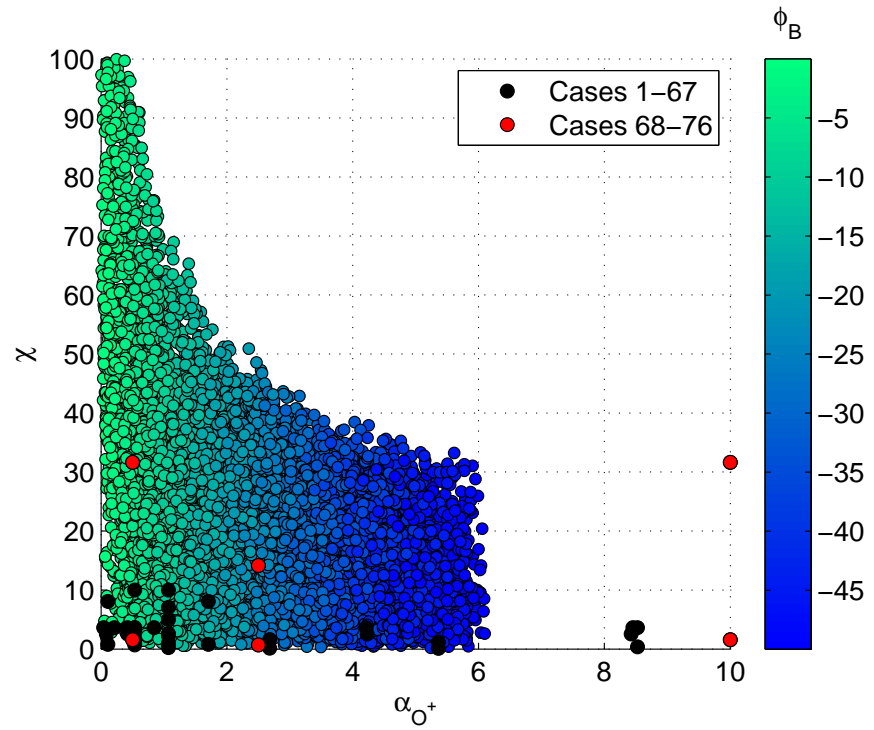
Parameter	Lower	Upper
n_∞ (m^{-3})	5×10^8	3×10^{12}
ϕ_B (V)	-50	0
v_B (ms^{-1})	7000	8000
r_B (m)	0.05	1

Table 7.2: Supplementary cases added to capture coupled extremes in $\mathcal{P}$.
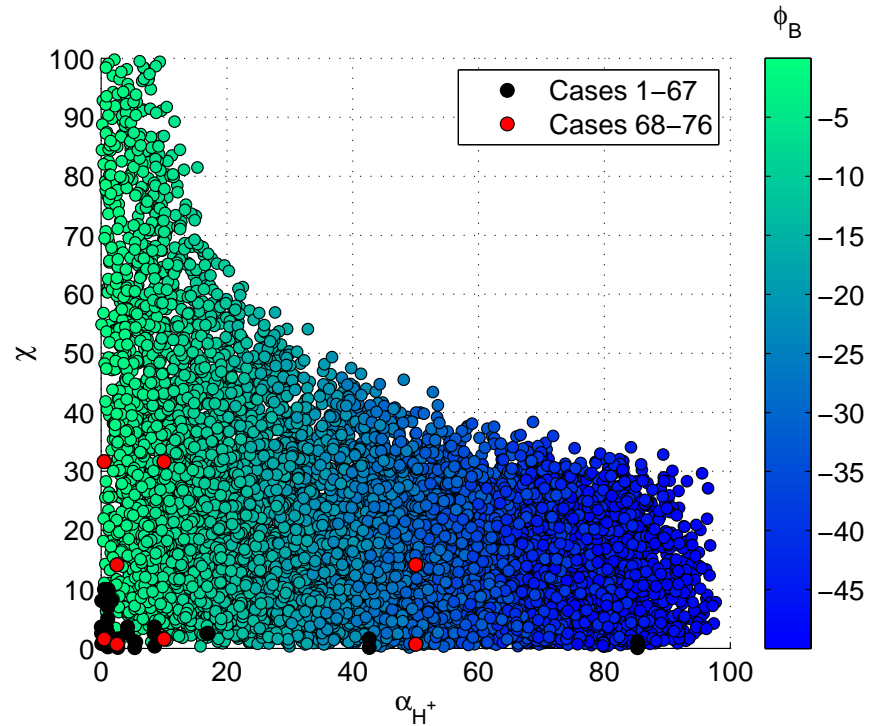
Case	68	69	70	71	72	73	74	75
$\phi_{(B)}$ (V)	-25	-25	-25	-25	-5	-5	-5	-5
$r_{(B)}$ (m)	0.3	0.3	0.3	0.3	0.3	0.3	0.3	0.3
$v_{(B)}$ (km/s)	7.768	1.737	7.768	1.737	7.768	1.737	7.768	1.737
m $(10^{-27}kg)$	26.55	26.55	26.55	26.55	26.55	26.55	26.55	26.55
n_∞ $(10^{10}m^{-3})$	0.7675	0.7675	307	307	0.7675	0.7675	307	307
T_e (K)	1997	1997	1997	1997	1997	1997	1997	1997
α	2.5	50	2.5	50	0.5	10	0.5	10
χ	$\sqrt{0.5}$	$\sqrt{0.5}$	$\sqrt{200}$	$\sqrt{200}$	$\sqrt{2.5}$	$\sqrt{2.5}$	$\sqrt{1000}$	$\sqrt{1000}$

These relationships can be seen in Figures 7.1 and 7.2, which plot the distribution of points in $\mathcal{P}(\alpha, \chi)$ for O^+ and H^+ plasmas, coloured by ϕ_B, for the range of interaction parameters specified in Table 7.2. Overlaid on Figures 7.1 and 7.2 are simulations 1-67 (shown in black). Supplementary simulations corresponding to Cases 68-76, shown in red and listed in Table 7.2, have been added to capture regions in $\mathcal{P}(\alpha_k, \chi)$ corresponding to coupled extremes, $\mathcal{P}(\alpha_k \gg 1, \chi \gg 1)$, $\mathcal{P}(\alpha_k \gg 1, \chi \ll 1)$, $\mathcal{P}(\alpha_k \ll 1, \chi \gg 1)$ and $\mathcal{P}(\alpha_k \ll 1, \chi \ll 1)$.

As will be shown in the following section, $C_{D,C}$ becomes limited by sheath thickness, which becomes very thin compared to the body for $\chi > 20$. Interpreted another way, when the sheath thickness is $1/20^{th}$ the body thickness, ion collection enhancement is negligible (direct charged drag equals neutral drag) and indirect aerodynamic forces are small. While this may not be true for all values of α_k, lacking any observations of physical mechanisms that would contradict this conclusion, we assume this is true for the range of ionospheric conditions considered. Therefore additional simulations, for example at $\mathcal{P}(10, 100)$ or $\mathcal{P}(80, 30)$, were not performed. Overall, the simulations presented throughout this work provide an adequate spread of measurements to construct a response surface to draw conclusions regarding the significance of ionospheric aerodynamics to LEO objects.

Figure 7.1: LEO plasma interaction envelope for O^+ plasmas. Coloured by ϕ_B.

Figure 7.2: LEO plasma interaction envelope for H^+ (right). Coloured by ϕ_B.

7.2.2 Coarse Model: A Physics-Based Response Surface

The previous chapter developed a map of plasma interaction phenomena and linked these phenomena to charged aerodynamic forces. Based on this map, three general behaviours were observed: (1) the ion deflection parameter α governs the direct collection of ions through the critical impact parameter b_*, while indirect charged aerodynamics forces counter a portion of the direct drag caused by this ion collection; (2) indirect charged aerodynamics scale with sheath thickness, so that as the sheath becomes thick, charged aerodynamic forces dominate the total drag; (3) there exists a region where direct, and indirect charged drag forces are coupled. As a result, this work hypothesises that a suitable charged aerodynamic response surface can be described by the following expression,
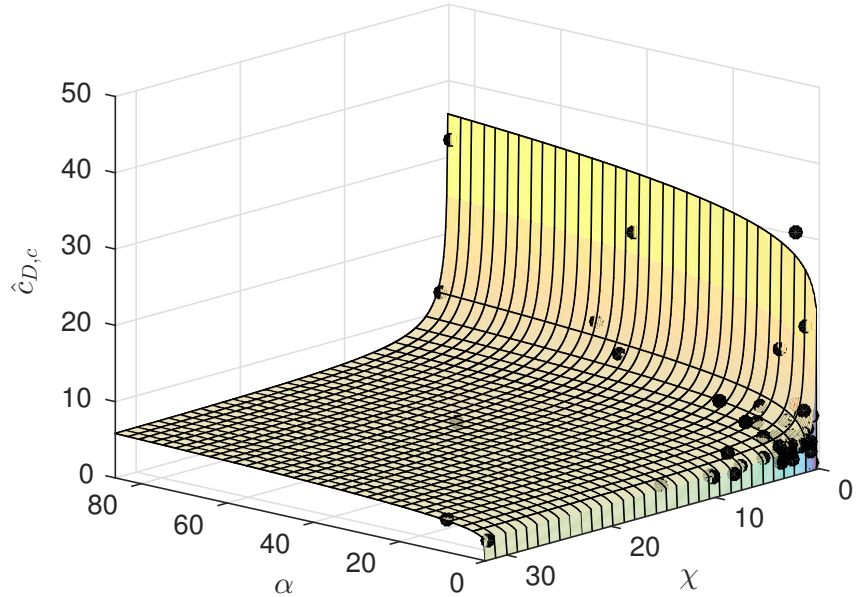
$$C_{D,C}\left(\alpha,\chi\right) = \underbrace{A(1+2\alpha)^{0.5-a}}_{\text{Direct Drag}} + \overbrace{B\chi^{-1}}^{\text{Indirect Drag}} + \underbrace{C\frac{2\alpha^c + D}{1+\chi}}_{\text{Coupling Term}} \tag{7.3}$$

where A, B, C, D, a and c are fitting constants.
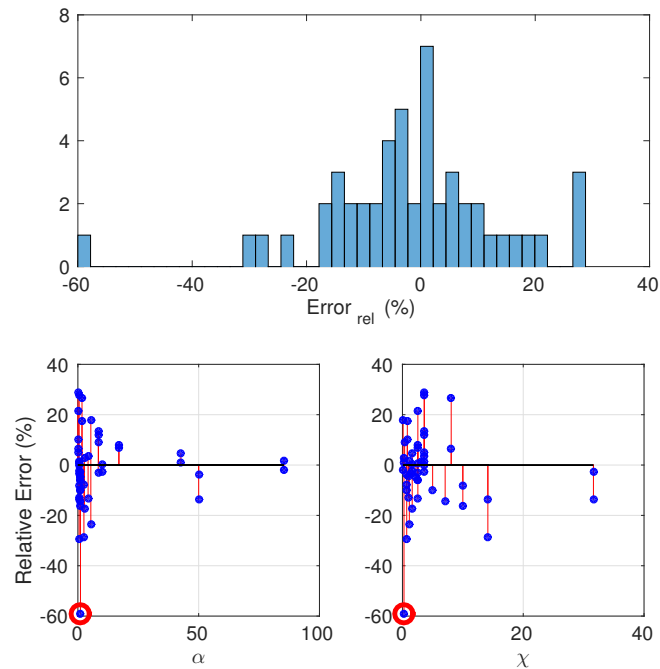
The first term on the right-hand side captures the ion collection enhancement using a similar form to b_{OML} where A is a geometric scaling constant, and a corrects for the direct charged drag reduction caused by indirect thrust on the body. The second term on the right-hand side captures the relationship between the sheath thickness and indirect charged drag forces. The third term captures the observed coupling between α_k and χ. Unlike the first two terms which are based on physical observations, the third term was selected to fit the observed coupling. It is worth noting that this last term might more appropriately take a form involving the Coulomb logarithm $\ln\Lambda$, such as found in analytical expressions in (Hutchinson, 2006) - this is something worth further investigation in future work.

Table 7.3: Fitting coefficients for Eqn. 7.3 based on $C_{D,C}$ for Cases 1-76.

Coefficient	Value	95% Confidence Interval
A	2.503	(1.978, 3.027)
B	1.973	(1.713, 2.232)
C	53.85	(-195.1, 302.8)
D	-1.996	(-2.03, -1.962)
a	0.3503	(0.2743, 0.4263)
c	0.02255	(-0.0797, 0.1248)

Figure 7.3: Visual comparison of fitted Eqn. 7.3 with $C_{D,C}$ measurements for simulations 1-76 (black dots).

Figure 7.4: Relative error between Eqn. 7.3 and the simulated total charged drag coefficients $C_{D,C}$.

The curve fitting toolbox in *MatLAB* (2014) was used to tune fitting constants in Eqn. 7.3 with $C_{D,C}$ measurements in Cases 1-76. These constants are shown in Table 7.3 along with a 95% confidence interval. Figure 7.3 overlays Eqn. 7.3 on the simulated data to illustrate qualitative agreement between Eqn. 7.3 and simulated $C_{D,C}$ measurements. The R-Squared[1] value that describes the fit between the response surface and the data is 99.07%.

To establish regions where the fit of Eqn. 7.3 breaks down, Figure 7.4 plots the spread of relative error between measured data and Eqn. 7.3. The top panel of Figure 7.4 shows a histogram of relative error and the bottom panels show the distribution of relative error with α_k (bottom left) and χ) (bottom right). An outlier corresponding to a 60% under-prediction of local $C_{D,C}$ is seen in Figure 7.4 (top). This point is highlighted in the bottom panels and corresponds to a weakly shielded case with intermediate ion coupling where indirect charged aerodynamic forces had a net positive contribution to total charged drag. Overall, Eqn. 7.3 captures the general variation of $C_{D,C}$ for the majority of conditions experienced by LEO objects and therefore is considered suitable for identifying general regions in LEO where ionospheric aerodynamics forces may become large.

7.3   Ionospheric Aerodynamics: Significant or Not?

Chapter 1 outlined the Space Situational Awareness (SSA) problem and the need for reliable and precise orbit prediction capabilities to maintain safe and secure access to LEO infrastructure. Uncertainties in force models limit these prediction capabilities. Among these forces, aerodynamic forces represent both the largest non-conservative force felt by LEO objects and the forces with the largest associated uncertainties. To date, the contribution of ionospheric aerodynamic to the aerodynamic force vector has not been considered based on the conclusions in Brundin, (1963) that ionospheric aerodynamic forces are negligible in LEO compared to neutral aerodynamic forces. The purpose of this section is to quantify the perturbation caused by ionospheric aerodynamics to the orbit of LEO objects using the IRI-2012 and NRLMSISE-00 atmospheric models to test this conclusion.

A variety of the gravitational and non-gravitational perturbations in LEO were outlined in Chapter 1. To isolate the effect of including ionospheric aerodynamics only the aerodynamic perturbation is modelled here. Three representative objects are considered: a CubeSat ($r_B = 0.05$ m), an object with a similar scale to those proposed for the OneWeb constellation ($r_B = 0.3$ m) and a large object representing satellites, such as ENVISAT

---

[1]R-Squared is a statistical measure of how close the data is to the fitted function, with 0% indicating that the model explains none of the variation about the mean, 100% indicating that the model explains all the variability about the mean.

($r_B = 5$) m. For compactness, these objects shall be referred to as *"CubeSat"*, *"SmallSat"* and *"LargeSat"*. All objects are assumed to be long and aligned perpendicular to the flow (2D) with uniform, fixed surface charge distributions. Two different surface potentials are considered: a surface potential of -0.75 V representative of natural floating potentials; and a moderate surface potential of -30 V representative of an artificially induced surface potentials.

To answer the question, is ionospheric aerodynamics appreciable to the motion of LEO objects compared to neutral aerodynamics, Section 7.3.1 begins by applying the response surface developed in Section 7.2.2 to determine the distribution of $F_{D,C}/F_{D,N}$ and, hence, whether there exist ionospheric aerodynamic dominated regions in LEO. The presence of charged dominated regions does not necessarily imply that ionospheric aerodynamic forces have a significant effect on the motion of LEO objects. To conclusively determine the significance of ionospheric aerodynamics, Section 7.3.2 considers the perturbation caused by ionospheric aerodynamic forces to the motion of LEO objects compared to neutral aerodynamics using General Mission Analysis Toolkit (GMAT) (Hughes, Parker, and Chavali, 2016)[2].
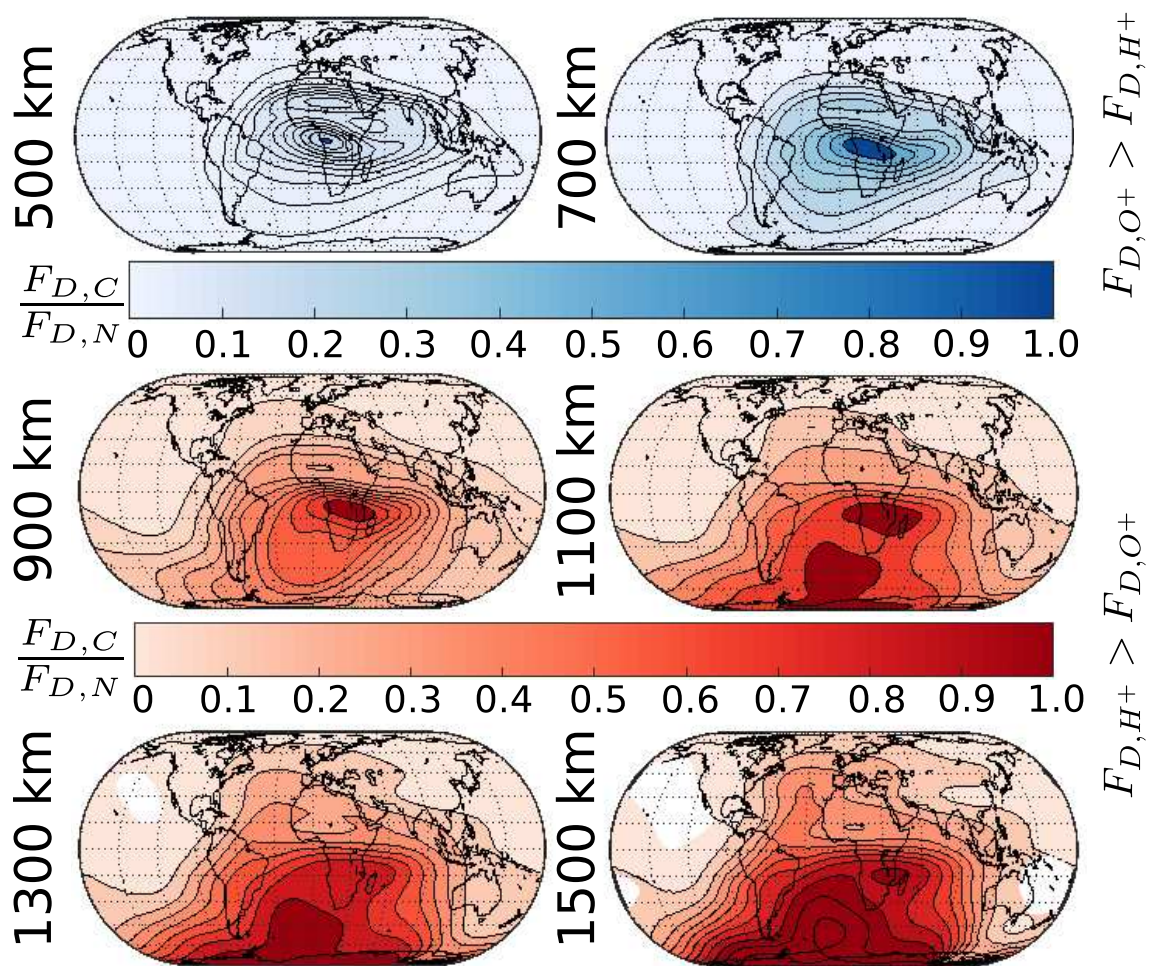
7.3.1 Identification of Charged Dominated Regions

Figures 7.5 and 7.6 plot the ratio of total charged drag ($F_{D,C} = F_{D,O^+} + F_{D,H^+}$) to neutral drag force ($F_{D,N} = F_{D,O} + F_{D,He} + F_{D,H}$) in the altitude range 500 km $< h <$ 1500 km based on the IRI-2012 (Bilitza et al., 2014) and NRLMSISE-00 (Picone et al., 2002) atmospheric models for a CubeSat ($r_B = 0.05$) floating at -0.75 V and a SmallSat ($r_B = 0.3$ m) with an artificial surface potential of -30 V. Atmospheric model conditions are for date 4/1/2007 UT 12:00:00 with solar indices $f_{10.7} = 87.7$, $f_{10.7a} = 83.35$ and using the daily magnetic index $a_p = [17.3750, 15.0, 20.0, 15.0, 27.0, 18.125, 21.75]$ (the same condition used in previous chapters). $F_{D,N}$ was calculated based on free molecular flow theory from Sentman, (1961) for a diffusely reflecting object with complete thermal accommodation to a 500 K wall (as in Chapter 4). $F_{D,C}$ was calculated from Eqn. 7.3 where IRI-2012 outputs were used to determine the local α_k and χ.
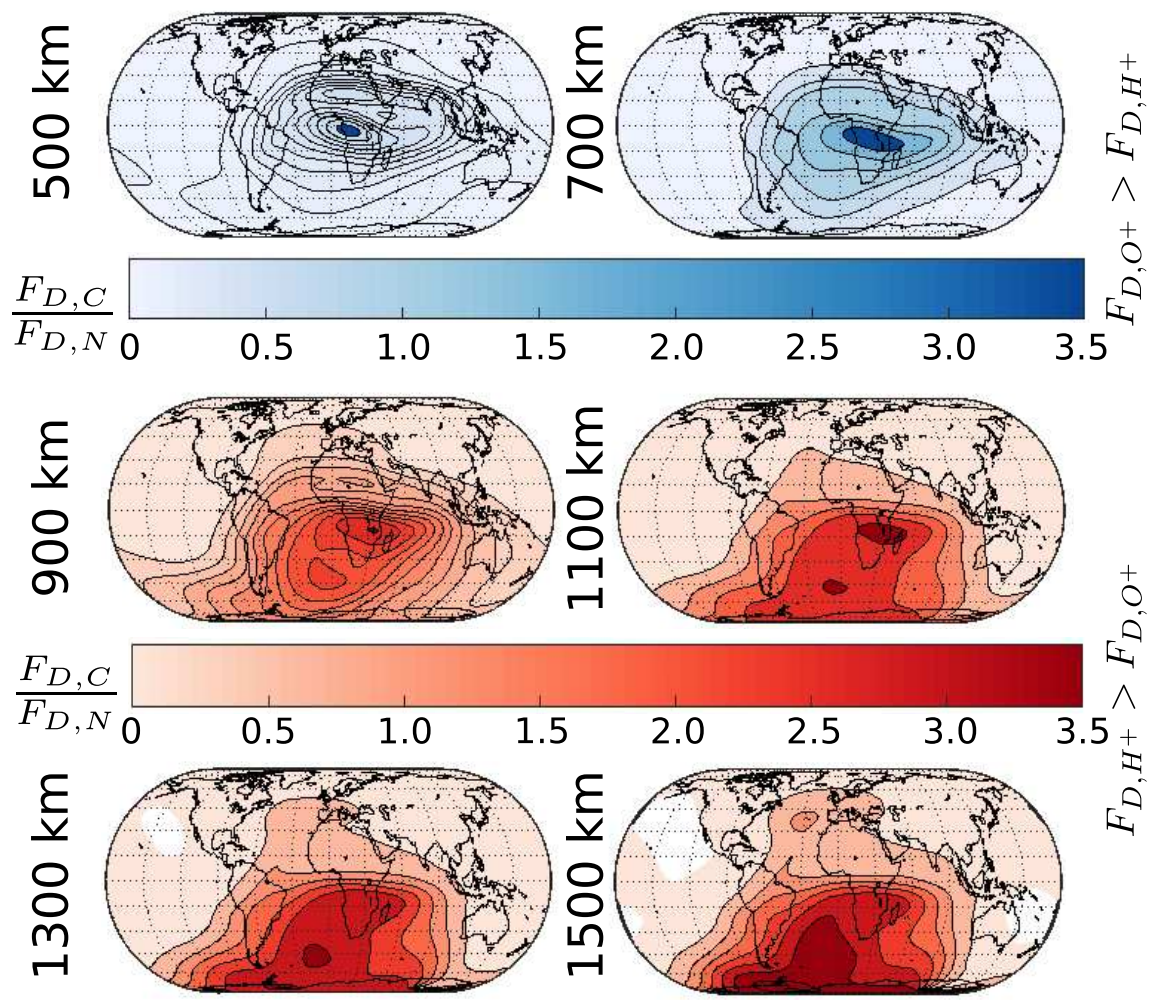
At 500 km altitude, the maximum and minimum $F_{D,C}/F_{D,N}$ ratios for the -0.75 V Cube-Sat case shown in Figure 7.5 at 500 km are 0.0005 and 0.11. Expressing ionospheric aerodynamics forces as a percentage of the total aerodynamic force experienced by the -0.75 V CubeSat, ionospheric aerodynamic forces account for between 0.05% to 10% of the aerodynamic forces experienced by this object at 500 km altitude. This proportion increases with altitude, ionospheric aerodynamic forces representing between 0.89% to 54.15% of

---

[2]Available from: https://gmat.gsfc.nasa.gov/.

Figure 7.5: Ratio of total charged to neutral drag for a small object ($r_B = 0.05m$) with a floating potential of -0.75 V. Blue regions represent O^+ dominated plasmas, red regions represent H^+ dominated plasmas.

Figure 7.6: Ratio of total charged to neutral drag for a large object ($r_B = 0.3m$) with an artificial surface potential of -30 V. Blue regions represent O^+ dominated plasmas, red regions represent H^+ dominated plasmas.

the total aerodynamic force of the -0.75 V CubeSat at 1500 km. Similarly, from Figure 7.6 considering the SameSat class object with a surface potential of -30 V, ionospheric aerodynamic forces represented between 0.18% to 18.35% of the total aerodynamic forces at 500 km, rising to between 1.11% to 78.68% at 1500 km. Framed another way, the above results imply that densities derived from satellite accelerations without accounting for ionospheric aerodynamics will be over-predicted by between $0.05 - 18.35\%$ at 500 km altitude increasing to $0.89 - 78.68\%$, the magnitude varying depending largely on latitude, longitude, surface potential and body size. While the exact value is sensitive to local space weather conditions and orbital location, these uncertainties appear consistent with those in atmospheric models, which have historically been developed based on satellite-derived density data.

A limitation of the approach used to generate these figures is the use of a fixed surface potential. While the SmallSat experienced a larger contribution from ionospheric aerodynamics than the CubeSat, this contribution stems from the assumption of a -30 V surface. This surface potential increased both the sheath thickness (χ) and potential dominated phenomena (increase in α_k), each of which enhance ionospheric aerodynamic forces. While this assumption may be appropriate for some objects, where high voltage power systems connect with the local plasma environment, it simplifies an important complexity of the problem where surface potentials should float and fluctuate based on local plasma parameters. Nevertheless, the purpose of Figures 7.5 and 7.6 is to determine whether ionospheric aerodynamic forces can become comparable to neutral aerodynamic forces; *they can.*

What these results do not achieve is to quantify the effect of ionospheric aerodynamics on the actual orbital motion of LEO objects. Though $F_{D,C}/F_{D,N}$ increases with altitude, the magnitude of forces decreases with decreasing density. Hence, at sufficiently high altitudes the contribution of $F_{D,C}$, while much larger than $F_{D,N}$, may still have no appreciable effect on the motion of orbiting objects - the definition of appreciable being dependent on specific mission requirements. The question then becomes, does there exists a window where the contribution of ionospheric aerodynamics is both significant compared to neutral aerodynamics and the magnitude of total forces is sufficient to have an appreciable effect on LEO orbital dynamics?

7.3.2 Perturbation to LEO Orbits caused by Ionospheric Aerodynamics

To answer this question, the perturbation to LEO orbits caused by charged aerodynamics is considered here using General Mission Analysis Toolkit (GMAT) (Hughes, Parker, and Chavali, 2016). Unfortunately, the IRI-2012 ionospheric model used in the previous section is currently not implemented in GMAT in such a way as to allow direct calculation of the local ion deflection parameter α and general shielding ratio χ, and therefore local charged aerodynamic forces using the response surface developed in Section 7.2. However, orbital dynamics simulations often use a constant neutral drag coefficient $C_{D,N}$, calculated from either DSMC simulations or mean accelerations measurements from LEO objects, or they use a constant neutral drag coefficient $C_{D,N}$ of 2.2. This work takes a similar approach, averaging $F_{D,C}/F_{D,N}$ over an orbit and adding it as a perturbation to a reference neutral drag coefficient $C_{D,N}$. Given its prevalence in the literature, $C_{D,N}$ is approximated as 2.2 here. While the exact value of $C_{D,N}$ will vary, its effect will be to scale the relative effect of the perturbation.

Numerical Setup

To isolate the effect of charged aerodynamics on the orbit of LEO objects compared to neutral aerodynamics, additional orbital perturbations are not considered here i.e. orbit simulations are for a two-body system. The effect of charged aerodynamics compared to neutral aerodynamics on an object's orbit is quantified as the relative drift in position (Δr) between the orbit of an object including neutral drag (N) and both neutral and charged drag $N + C$ forces i.e.

$$\Delta r = \sqrt{(x_N - x_{N+C})^2 + (y_N - y_{N+C})^2 + (z_N - z_{N+C})^2} \tag{7.4}$$

where x, y and z correspond to Cartesian co-ordinates in an Earth-Centred-Earth-Fixed inertial reference frame.

To quantify the effect of body size and surface potential the orbit of different objects in LEO, we shall match the area to mass ratio (A/m) in the ballistic coefficient ($\mathcal{B}$). The ballistic coefficient $\mathcal{B}$ comes from the aerodynamic acceleration equation,

$$a_D = -\frac{1}{2}\frac{C_{D,N+C}A}{m_B}\rho_m v_B^2 = -\frac{1}{2}\mathcal{B}\rho_m v_B^2 \tag{7.5}$$

By considering the relative motion of several different objects with the same ballistic properties, the influence different physical phenomena, such as sheath thickness, can be inferred.

Table 7.4: Ballistic properties of simulated objects. Note that area is calculated as $2r_B l_B$ i.e. r_B is a radius.

	r_B [m]	l_B [m]	m_B [kg]	A/m_B [kg/m²]
CubeSat	0.05	0.3	3	0.01
MicroSat	0.3	3	180	0.01
LargeSat	5	10	10000	0.01

Table 7.4 lists the ballistic properties (dimensions, mass and area to mass ratio) of the CubeSat, MicroSat and LargeSat considered in the previous section. To quantify the different contributions of charged aerodynamics based on different orbits, two mean charge to neutral drag ratios ($\langle F_{D,C}/F_{D,N} \rangle$) are considered; the equatorial average and the polar average. These measurements correspond to the lines indicated in Figure 7.7.

Figures 7.8 plots the variation of mean, minimum and maximum $F_{D,C}/F_{D,N}$ through altitude for the polar and equatorial cases. The shaded regions in these figures correspond to the maximum and minimum $F_{D,C}/F_{D,N}$ at given altitudes from Figures 7.5 and 7.6. Tables 7.6, 7.7 and 7.8 present a summary of the mean charge to neutral drag ratios used in GMAT. The total drag coefficient $C_{D,N+C}$ used in the GMAT simulations is based on these values and calculated as,

$$C_{D,N+C} = C_{D,N} \left(1 + \left\langle \frac{F_{D,C}}{F_{D,N}} \right\rangle \right) \tag{7.6}$$

Table 7.5: Orbital Propagation Settings used in GMAT.

GMAT Propergator Settings	
Integrator	RungeKutta89
Initial Step Size (s)	0.5
Min Step Size (s)	0.001
Max Step Size (s)	2700
Max Step Attempts	50
Atmosphere Model	MSISE90
Gravity Model	JGM-2
	Order 1
Solar Radiation Pressure	No
Relativistic Correction	No

Table 7.6: Mean ratio of charged to neutral drag forces for a small object ($r_B = 0.05$ m) in a polar and equatorial orbit.
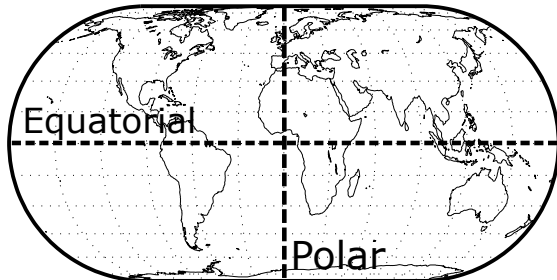
ϕ_B	-0.75		-30	
$\langle F_{D,C}/F_{D,N}\rangle$	Equatorial	Polar	Equatorial	Polar
Altitude (km)				
300	0.001	0.0013	0.0042	0.0047
500	0.0089	0.0244	0.0566	0.1192
700	0.0609	0.1169	0.5849	0.9446
900	0.2229	0.2316	2.4556	2.4289
1100	0.3648	0.3381	3.9024	3.6851
1300	0.4715	0.4541	4.7138	4/7154
1500	0.5648	0.5768	5.2573	5.5607

Table 7.7: Mean ratio of charged to neutral drag forces for a large object ($r_B = 0.5$ m) in a polar and equatorial orbit.
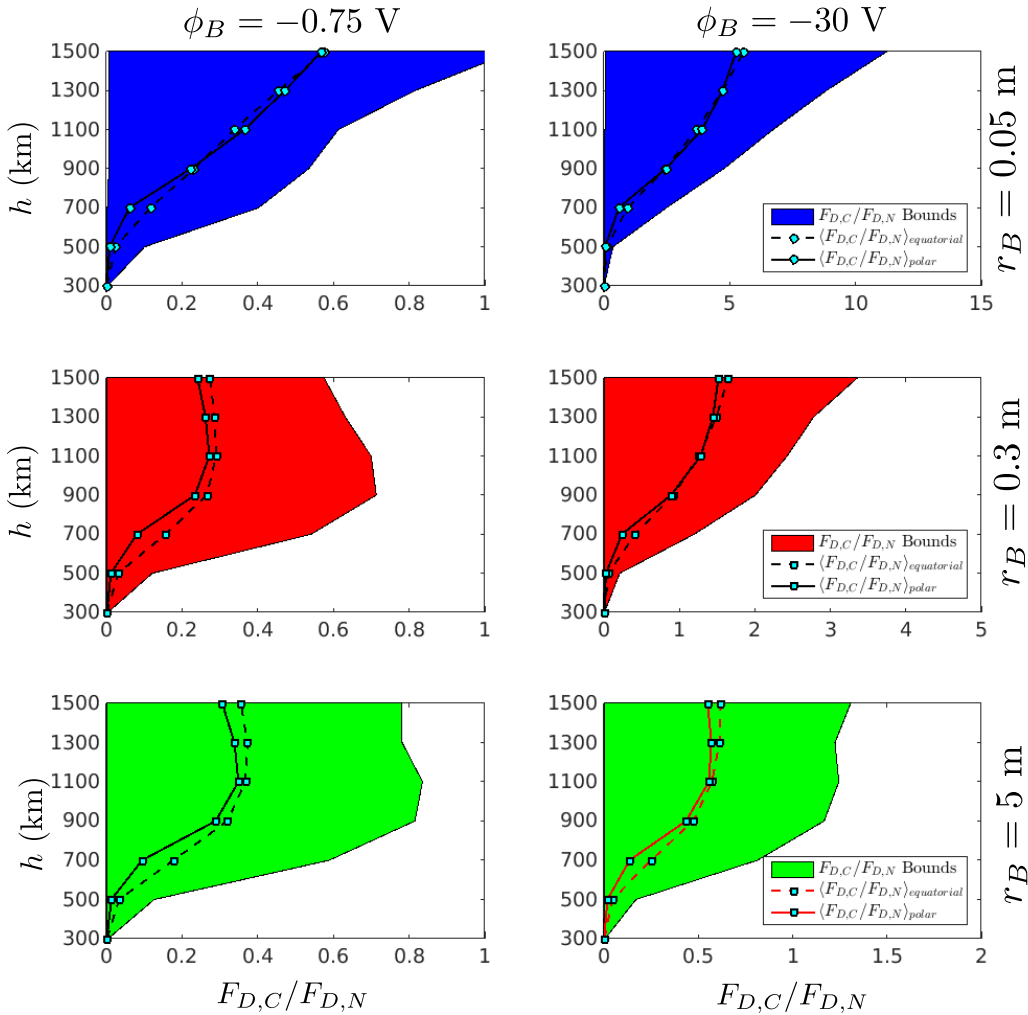
ϕ_B	-0.75		-30	
$\langle F_{D,C}/F_{D,N}\rangle$	Equatorial	Polar	Equatorial	Polar
Altitude (km)				
300	0.0013	0.0016	0.0023	0.0027
500	0.0122	0.0314	0.0271	0.0620
700	0.0814	0.1570	0.2397	0.4112
900	0.2339	0.2655	0.8895	0.9186
1100	0.2724	0.2904	1.2821	1.2588
1300	0.2622	0.2866	1.4443	1.4897
1500	0.2409	0.2731	1.5181	1.6466

Table 7.8: Mean ratio of charged to neutral drag forces for a large object ($r_B = 5$ m) in a polar and equatorial orbit.

ϕ_B	-0.75		-30	
$\langle F_{D,C}/F_{D,N}\rangle$	Equatorial	Polar	Equatorial	Polar
Altitude (km)				
300	0.0014	0.0016	0.0018	0.0022
500	0.0134	0.0336	0.0184	0.0456
700	0.0948	0.1775	0.1360	0.2507
900	0.2891	0.3200	0.4354	0.4740
1100	0.3490	0.3677	0.5559	0.5726
1300	0.3385	0.3727	0.5696	0.6122
1500	0.3063	0.3555	0.5489	0.6189

Figure 7.7: Illustration of orbits parameters considered.

Figure 7.8: Variation of $F_{D,C}/F_{D,N}$ with altitude for CubeSat ($r_B = 0.05$ m), SmallSat ($r_B = 0.05$ m) and LargeSat ($r_B = 0.05$ m) objects. Shaded regions correspond to the maximum and minimum $F_{D,C}/F_{D,N}$ at specific altitudes. Mean equatorial and polar $\langle F_{D,C}/F_{D,N}\rangle$ are listed in Table 7.7.

Results and Discussion

Starting with the trends shown in Figure 7.8, Figure 7.8 shows two distinct trends; a linear trend increasing with altitude, and a trend where $F_{D,C}/F_{D,N}$ peaks between $700 - 900$ km before stabilising and starting to decay.

The linear trend corresponds to the CubeSat cases (both the -0.75 V and -30 V cases) and the -30 V SmallSat case. All of these cases correspond to weakly shielded systems, the CubeSat's small size meaning the sheath thickness is appreciable compared to the body size for both potentials, while the SmallSat's sheath becomes significant compared to body size as the surface potential increases (λ_ϕ increases with ϕ_B). A distinct increase in the gradient of $F_{D,C}/F_{D,N}$ with altitude can be seen at 700 km. This is a reflection of the increasing dominance of H^+, the system also becoming potential dominated (increasing in both direct and indirect drag forces). A consequence of these mechanisms is that the contribution of ionospheric aerodynamics for these cases becomes large.

The second trend corresponds to the moderate to strongly shielded interactions of the -0.75 V SmallSat and the LargeSat. For these cases, the sheath thickness remains small compared to the body size. As a consequence, ionospheric aerodynamic forces are sheath-limited and primarily a reflection of the ion collection area enhancement (direct drag). Below $700 - 900$ km (but above 300 km) where O^+ ions dominate, this force is appreciable compared to the neutral environment and increases with altitude. When H^+ ions dominate however, while the system becomes more dominated by potential effects (α_k increases), the sheath-limited nature of the interaction means that indirect drag forces are small. As a result, ionospheric aerodynamic mechanisms are unable to sufficiently out-weigh neutral aerodynamic forces despite the increasing n_i/n_n ratio with altitude and the ratio of $F_{D,C}/F_{D,N}$ decays.

To quantify the effect of the ionospheric aerodynamic forces in Figure 7.8 on LEO objects, Figures 7.9 and 7.10 plot the error in position caused by ionospheric aerodynamics after one day for the equatorial and polar orbits respectively. Figures 7.11 and 7.12 then plot the error in position after ten days for equatorial and polar orbits respectively. Whether the effect of ionospheric aerodynamics is considered significant or not is then dependent on the application.
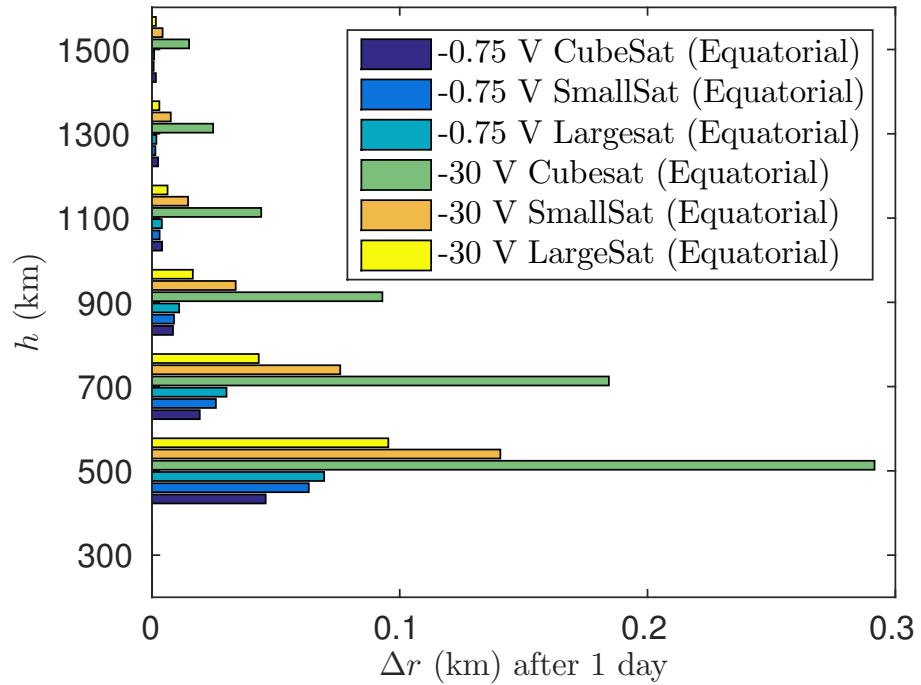
For example, Figures 7.9 and 7.10 illustrate that the error caused by not considering ionospheric aerodynamic forces will cause an uncertainty in position over one day between $0.05 - 0.15$ km at 500 km for the -0.75 V cases consider, and an uncertainty between $0.1 - 0.6$ km for the -30 V cases. Interestingly, for the -0.75 V cases, the CubeSat was the least effect at 500 km, the LargeSat the most, while for the -30 V case, the opposite trend is seen, the CubeSat almost double the distance from the -30 V SmallSat (the next highest position error). The question on whether these distances are significant depends on

the application. For active satellites that are observed multiple times per day for example, an error in position of 0.1 km caused by ionospheric aerodynamics will likely be masked by larger uncertainties in atmospheric models. However, for geodetic studies that attempt to infer environment properties based on satellite accelerations, neglecting ionospheric aerodynamic accelerations between 500 km and 900 km will cause non-negligible error in position (recall the discussion in Chapter 2 on the effort that went into understanding the cm change in semi-major axis of the LAGEOS-I and II).
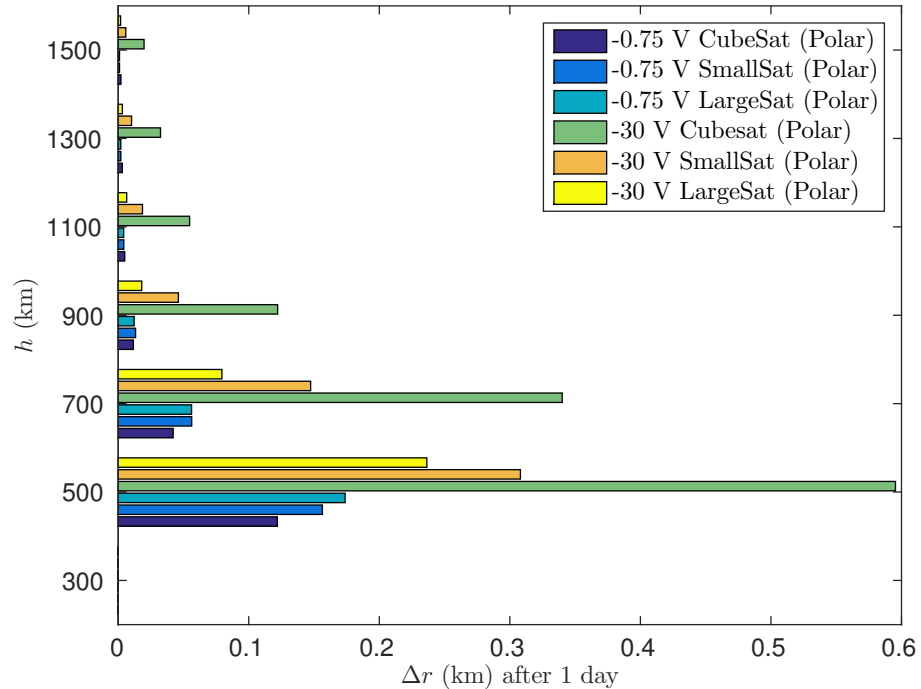
Considering observed uncertainties in atmospheric models as large as 100%, general atmospheric model uncertainties on the order of 10% and uncertainties in $C_{D,N}$ on the order of 5%, the predicted uncertainties caused by neglecting ionospheric aerodynamics are consistent with established trends. Importantly, ionospheric aerodynamics also provides a mechanism to explain the space weather dependent spikes in uncertainties discussed in Chapter 1 e.g. solar weather events cause temporary spikes in both interaction quantities and floating potentials that result in a net increase in ionospheric aerodynamic forces and therefore an over-prediction of neutral number density based on satellite accelerations. From an SSA perspective, Figures 7.11 and 7.12 are more useful.

Figures 7.11 and 7.12 show the evolution in position error over 10 days, error growth non-linear with time as differences in position also correspond to different local space environments and therefore aerodynamics forces. Figures 7.11 and 7.12 demonstrate that over a ten day period, not accounting for ionospheric aerodynamic forces on a -0.75 V objects can cause an uncertainty in position between $4 - 17$ km at 500 km ($10 - 60$ km for the -30 V cases). Further, these errors are high for all polar orbiting cases, the position error range $12 - 17$ km for the -0.75 V polar cases compared to $4 - 7$ km for the equatorial cases. These are significant errors in position; sufficient to make a repeated observations of an object difficult and large enough that the object's orbit may now represent a critical risk to an active satellite.
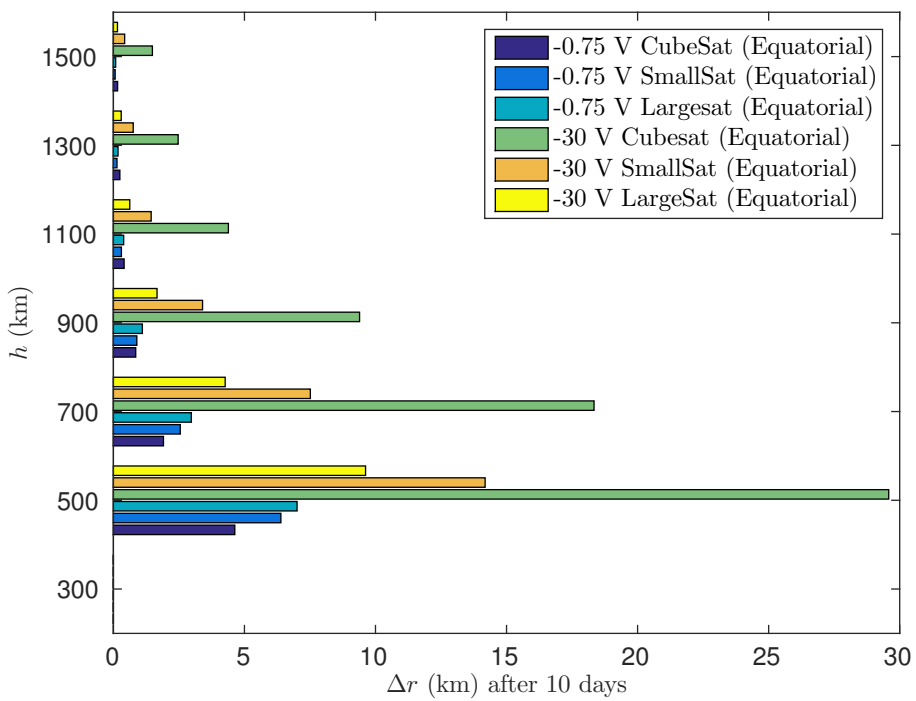
Based on these results therefore, we conclude that ionospheric aerodynamics forces may both become appreciable compared to neutral aerodynamic forces and that there exists conditions in LEO where these forces have a significant effect on the motion of LEO objects.
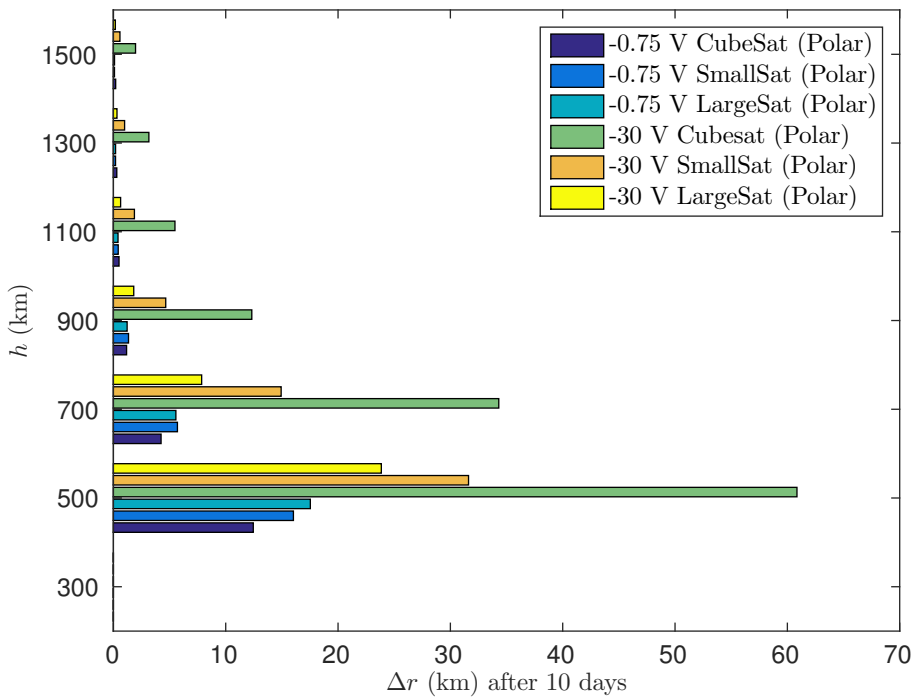
Figure 7.9: Δr caused by neglecting ionospheric aerodynamics over 1 day in a equatorial orbit.

Figure 7.10: Δr caused by neglecting ionospheric aerodynamics over 1 day in a polar orbit.

Figure 7.11: Δr caused by neglecting ionospheric aerodynamics over 10 day in a equatorial orbit.

Figure 7.12: Δr caused by neglecting ionospheric aerodynamics over 10 day in a polar orbit.

7.4 Summary

This chapter applies the framework developed in the preceding chapters to answer two key questions: (1) whether there exist regions in LEO where ionospheric aerodynamic forces are large compared to neutral aerodynamic forces in LEO; and (2) do these forces cause a significant perturbation to the predicted orbits of LEO objects.

Section 7.2 began by constructing a physics-based response surface to describe ionospheric aerodynamics in terms of the ion deflection parameter α_k and general shielding ratio χ. Applying this response surface, Section 7.3.1 predicted that neglecting ionospheric aerodynamics forces would result in an under-prediction of aerodynamic forces between 0.05% to 18.35% at 500 km altitude for objects with radii between 0.05 m to 5 m and surface potentials between -0.75 to -30 V, increasing to between 0.89% to 78.68% at 1500 km. Section 7.3.1 concluded however by pointing out that these ratios do not capture the net decrease in total number density and therefore force magnitude i.e. the significance of ionospheric aerodynamics forces on the motion of LEO objects could not be quantified.

Section 7.3.2 addressed this limitation by considering ionospheric aerodynamic forces as a perturbation to the orbit of LEO objects. By considering the motion of three representative objects (a 3U CubeSat, a OneWeb sized SmallSat and a ENVISAT sized LargeSat) with the same ballistic coefficient, *Section 7.3.2 demonstrated that small objects are more sensitive to ionospheric aerodynamic forces than large objects outside of the strongly shielded regime. Section 7.3.2 showed that ionospheric aerodynamics has a significant effect on the motion of LEO objects between $500km$ to 900 km and that the mean effect of ionospheric aerodynamics is larger in polar orbits than equatorial orbits for the conditions studied in this work.*

Based on these findings, this work concludes that ionospheric aerodynamic forces represent an non-negligible perturbation to LEO objects and that these effects are more significant between 500 km to 900 km altitude.

Chapter 8

Conclusion: Overview of Results, Contributions and the Implications of this Work

8.1 Summary of This Work

The exponential growth of space utilisation in recent years has seen the Low Earth Orbit (LEO) environment become increasingly congested. The risk of collision events increases year on year, which threatens important space infrastructure upon which society now relies. Successful space management policy, practices and the technical frameworks required to solve this problem, rest on the ability to obtain accurate knowledge of a given LEO object's orbit. Without precise information regarding a space object's orbit, the ability to take informed action to prevent, or mitigate the effects from, an on-orbit collision is severely degraded.

Orbital perturbations (accelerations experienced by a space object that perturbs it from pure 2-body motion) are a significant factor that drives the uncertainty of a given object's orbit. There are many sources of orbital perturbation, ranging from gravitational accelerations (from the non-spherical Earth, third bodies, tides), to solar radiation pressure, and atmospheric drag. Within the Low Earth Orbit regime, atmospheric drag is the largest non-conservative force exerted on the body. To date, the interaction of the neutral particles that form the thermosphere with the object has been considered the sole source of atmospheric drag on a LEO orbiting body. The subject of this thesis has been to challenge this understanding through examining the contribution that electrostatic forces play when the charged particles within the ionosphere interact with an orbiting body at a fixed negative surface potential with respect to a quasi-neutral charged environment. We refer to this effect as *"ionospheric aerodynamics"*.

A review of the ionospheric aerodynamic literature revealed that charged aerodynamic forces have historically been neglected in LEO based on the conclusions in the seminal work by Brundin, (1963). The conclusion that ionospheric aerodynamics is negligible was, however, founded on the assumptions that the maximum negative surface potential achieved by a body in LEO was on the order of -0.75 V and that the ion number density was never more than 10% of the neutral number density. These assumptions, while appropriate for the scope of space activities in the 1960s, are not valid for present space systems that regularly achieve natural floating potentials on the order of -100 V (and as high as -2000 V) and may have significant negative surface potentials as the result of high-voltage power systems. As a result, while the justification for surface potentials up to -60 V in Jastrow and Pearse, (1957) may have been inappropriate, their conclusions that ionospheric aerodynamics forces may represent between $10-150\%$ of the total aerodynamic force experienced by LEO objects is not necessarily invalid. This motivated the central research question explored throughout this thesis: can ionospheric aerodynamics have an appreciable effect on the non-conservative force vector experienced by a LEO object?

A key limitation of previous ionospheric analyses identified has been the use of assumptions regarding the structure of the plasma sheath resulting from the mesothermal interaction of a LEO object with the ionosphere. To capture the self-consistent sheath structure surrounding LEO objects the Particle-in-Cell method was implemented and validated in the code, pdFOAM; a PIC-DSMC code developed in this work in the open-source C++ library OpenFOAM as an extension of the DSMC code, dsmcFOAM. Confidence in the ability of pdFOAM to capture ionospheric aerodynamics was developed through code-to-code comparisons with the DSMC code, MONACO, and PIC code, PICLas along with the replication of fundamental plasma phenomena including the two-steam instability in Birdsall and Langdon, (1991), the 1D sheath structure near a flat plate and the oscillation of an electron about a stationary ion.

Using pdFOAM, the influence of self-consistent plasma interaction phenomena on charged aerodynamic forces was studied. A limitation of the analysis methods in Jastrow and Pearse, (1957) and Brundin, (1963) (and that in Andrés de la Fuente, (2007)) was the use of Orbital Motion Limited theory where the sheath structure is assumed to be spherically/cylindrically symmetric and thick with respect to the body. In the process of assessing the validity of previous conclusions regarding the significance of ionospheric aerodynamics in LEO, these assumptions were demonstrated not to capture the complexities of LEO plasma-body interactions. Kinetic phenomena resulting from the anisotropic nature of mesothermal sheath structures, such as bounded ion jets and ion pseudo-waves, were shown to have an appreciable effect on direct and indirect charged aerodynamic forces. Further, we demonstrated that not accounting for indirect thrust caused by ion accelerations would cause direct charged aerodynamic forces to be substantially over-predicted for most cases.

The most important observation was the significance of relative sheath thickness, with thick sheaths dominated by indirect charged aerodynamic forces, while thin sheaths are dominated by direct charged aerodynamic forces.

The picture built up from these observations is that of a complex, non-linear system defined by $4 + 5K$ independent dimensioned quantities (K being the number of species in the plasma). Even with advances in numerical methods and computational hardware, the characterisation of such a systems is not feasible. To resolve this challenge, we have reduced the $4 + 5K$ quantities that describe the electrostatic interaction of a K-species plasma with an arbitrarily charged body to $2 + 4K$ dimensionless parameters in this work. These parameters were shown to comprise a complete set of Π-groups predicted by the Buckingham Pi theorem. Knowing the influence of these dimensionless parameters on the electrostatic Vlasov-Maxwell equations means, however, that these parameters represent physically relevant scaling laws for electrostatic plasma interaction phenomena. We refer to scaling parameters as,

α_k: the ion deflection parameter, which describes the deflection of ions by electrical disturbances.

S_k: the ion thermal ratio, which describes the influence of ion thermal effects on the deflection of ions by electrical disturbances.

β_k: the ion coupling parameter, which describes the influence of ion species k to electrical disturbances.

Ω_k: the ion temporal parameter, which describes the scaling of transient phenomena.

μ_e: the electron energy coefficient, which describes the ability of electrons to penetrate negative electrical disturbances.

χ: the general shielding ratio, which describes the relative shielding thickness of a body with an arbitrary surface charge.

The identification of the general shielding length λ_ϕ in χ is a significant result, providing a link between the shielding of high and low-voltage plasma phenomena and resolves a key limitation of previous ionospheric studies, where scaling parameters were limited to low voltage systems (for example Knechtel and Pitts, (1965) and Stone, (1981a)). Drawing upon physical observations, the number of scaling parameters was further reduced, allowing the phenomena significant to charged aerodynamics to be represented in the two-dimensional *"plasma interaction phase-space"* $\mathcal{P}(\alpha, \chi)$.

Having reduced the $4 + 5K$ dimensions that describe plasma-body interactions in LEO to $\mathcal{P}(\alpha_k, \chi)$, a parametric study of collective and kinetic plasma phenomena within $\mathcal{P}(\alpha_k, \chi)$ was made to quantify the contribution of plasma phenomena to charged aerodynamic

forces. Based on observations, χ was shown to describe the relative thickness of the sheath; large values of χ corresponding to thin sheaths, small values of χ corresponding to thick sheaths. Similarly, α was shown to describe ion collection, correctly predicting the Orbital Motion Limited (OML) critical impact parameter for systems with thick sheaths ($\chi < 1$).

For thick sheath interactions, direct charged aerodynamic forces were shown to become OML while indirect forces increased unbounded for the presented simulations. A consequence of OML limited ion collection was that indirect charged thrust forces caused by the acceleration of fore-body ions were demonstrated to outweigh the direct charged aerodynamic contribution on the fore-body for a selection of interactions. The indirect drag caused by deflection of ions into the wake and the formation of ion pseudo-waves dominated these interactions, the charged aerodynamic force being a net drag. Similar behaviour was seen for sheath-limited interactions where the sheath thickness was smaller than the OML ion collection parameter. In these cases α was observed to describe the formation and extent of bounded ion jets and ion pseudo-waves, each having an appreciable and non-linear contribution to direct and indirect charged aerodynamic forces.

These observations were then collated into a map of plasma interaction phenomena in $\mathcal{P}(\alpha_k, \chi)$ and linked to charged aerodynamic forces. This map provides a physical link between charged aerodynamic forces and plasma interaction phenomena that may be used as a framework within which to understand the physics underpinning charged aerodynamics, ionospheric aerodynamics being one application.

Taking this framework, we then returned to the problem of ionospheric aerodynamics by developing a response surface based on physical observations and charged aerodynamic trends in $\mathcal{P}(\alpha_k, \chi)$. The resulting response surface captures the complexities of LEO plasma-body interactions including the relative contribution of indirect and direct charged aerodynamic forces with changing body size and surface potential.

Using this response surface, the influence of ionospheric aerodynamics on three representative objects were considered; a 3U CubeSat ($r_B = 0.05$ m), a OneWeb scale SmallSat ($r_B = 0.3$ m) and an ENVISAT LargeSat ($r_B = 5m$). Each object was set to have the same area to mass ratio of 0.01 m^2/kg, isolating ionospheric aerodynamic effects from ballistics and allowing a quantitative study of the significance of ionospheric aerodynamics to LEO objects. Ionospheric aerodynamic forces were shown to represent $0.05 - 18.35\%$ of the total aerodynamic force experienced by these objects at an altitude of 500 km for surface potentials between -0.75 V and -30 V, increasing to $0.89 - 78.68\%$ of the total aerodynamic force at 1500 km altitude. Using the General Mission Analysis Toolkit, the mean contribution of ionospheric aerodynamic forces on the orbit of LEO objects was quantified. At 500 km, ionospheric aerodynamic forces were demonstrated to cause an uncertainty in position on between $0.05 - 0.6$ km at 500 km over one day depending on

whether the system was small or large and at a natural floating potential (-0.75 V) or an artificial surface potential (-30 V). Over a ten day period, uncertainty in position caused by ionospheric aerodynamics for these objects was demonstrated to be between $4-60$ km at 500 km, reducing to a $0.1-12$ km uncertainty at 900 km altitude.

As a result, this work concludes that ionospheric aerodynamic forces have a measurable influence on the motion of LEO objects between $500-900$ km altitude and that this influence is governed primarily by the surface potential of the object and size of the body. Further, for geodetic studies that attempt to infer environment properties based on satellite accelerations, neglecting charged aerodynamic accelerations between 500 km and 900 km will cause non-negligible errors. In other words, this work has identified conditions that exist in LEO where unmodelled accelerations caused by ionospheric aerodynamic forces are on the order of (or greater than) the quoted uncertainties in atmospheric density predictions e.g. Vallado and Finkleman, (2014), Emmert, (2015). Therefore, improvement of atmospheric models must account for charged aerodynamic forces to achieve uncertainties smaller than those caused by ionospheric aerodynamics.

8.1.1   Summary of Major Contributions

- Development, implementation and validation of the open-source electrostatic PIC-DSMC code, pdFOAM, that may be applied to a wide of variety systems.

- Observations of self-consistent phenomena caused by the mesothermal interaction of a plasma with a negatively charged object.

- Derivation of physically relevant scaling laws that describe the electrostatic interaction of a multi-species plasma with an arbitrarily charged body.

- Construction of a map of plasma interaction phenomena in the two-dimensional phase-space $\mathcal{P}(\alpha_k, \chi)$ that may be applied to understand a variety of systems, such as ion collection (charging), with charged aerodynamics being only one application.

- Quantification of the significance of ionospheric aerodynamics to LEO objects.

8.2 Assumptions and Limitations of this Work

Assumptions in this work are categorised here as either physical or methodological. Physical assumptions are those that limit the scope of phenomena studied in this work. Methodological assumptions are those made during analyses to enable approximate conclusions. Where these assumptions have been made, they have been explicitly mentioned. The purpose of this section is to list these assumptions and discuss their implications to conclusions.

Physical Assumption: Two-dimensional flows are representative of ionospheric aerodynamic interactions   To isolate and understand the physics of LEO plasma-body interactions, this work focused on characterising the mesothermal interaction of a two-dimensional cylinder with a fixed, uniform surface potential. Two-dimensional flows were chosen to reduce computational costs and thereby allow a more comprehensive investigation of flow phenomena. A cylinder was chosen to enable a direct comparison with OML theory and prior ionospheric aerodynamic literature.

There is no reason the derived scaling parameters will be different for three-dimensional flows, the derivation of the scaling parameters being general. What will change is the distribution of surface forces and the relationship between interaction phenomena and scaling parameters. *The most important aspect of two-dimensional flows is that the reduction in degrees of freedom will cause an underestimation of the effective ion collection area of compact objects relative to the physical size of the object (this was discussed in Chapter 4).* In other words, results in Chapter 7 that are based on two-dimensional charged aerodynamic calculations will under-predict the influence of ionospheric aerodynamics on compact objects. *Therefore, conclusions in Chapter 7 regarding the significance of ionospheric aerodynamics to LEO objects can be considered conservative, and remain valid.*

Physical Assumption: Magnetism does not play a governing role in ionospheric aerodynamics   In general, the role of magnetism on ionospheric aerodynamics is not considered, either in this work or previous studies. The basis for this was discussed in Chapter 2; since the gyration radius of ions in LEO is so much greater than all but the largest objects (i.e. the International Space Station) that, in the frame of the objects, the ions will appear to travel in straight lines. While magnetic effects will play a role in other plasma perturbations, such as induction drag (Brundin, 1963), the assumption that they will have little effect on ionospheric aerodynamics is considered here to be physically reasonable.

Physical Assumption: The flow is collisionless (no binary particle collisions).
This work focused on ionospheric aerodynamics above $300km$ where the mean free path
of objects is on the order of kilometres i.e. the flow is collisionless for all LEO objects.
The DSMC portion of pdFOAM did not predict any collision events in the presented
simulations. Therefore, there is reasonable confidence that this assumption is appropriate.

**Methodological Assumption: Additional physical phenomena such as secondary
electron emission do not affect ionospheric aerodynamics.** The purpose of this
work was to determine whether ionospheric aerodynamics is significant in LEO compared to
neutral aerodynamics. Chapter 1 limited the scope of this work by considering the general
mesothermal interaction of LEO objects with the local plasma environment. Additional
phenomena, such as secondary electron emission, photoelectron emission, non-uniform sur-
face charge distributions, active emission of electron/ion beams from instruments, transient
phenomena, and so on, will affect the sheath structure surrounding LEO objects and there-
fore ionospheric aerodynamics forces. The inclusion of these phenomena however, would
cloud the underlying physics of the plasma-body interactions. *By developing an under-
standing of the underlying flow physics, this work has provided a framework upon which
future work may quantify the effect of these phenomena on ionospheric aerodynamic forces.*
This comprises one of our recommendations for future work in Section 8.3.

**Methodological Limitation: Mean charged to neutral drag forces remains con-
stant over the orbits considered in GMAT.** While investigating the perturbation
to LEO objects caused by ionospheric aerodynamics, Chapter 7 made the implicit assump-
tion that the mean charged to neutral drag ratio remains constant over the propagated
orbits.[ref] *Provided altitude did not substantially decrease during the orbit propagation,
the approach taken here can be considered reasonable - hence why orbits were propagated
for a maximum of ten days.* Studies that account for ionospheric aerodynamic contri-
butions based on local space environments parameters during orbital propagations is one
recommendation for future work in Section 8.3.

8.3 Recommendations for Future Research

8.3.1 To Address Limitations of this Work

Investigate the charged aerodynamics of three-dimensional objects   This work focused on studying the charged aerodynamics of cylindrical bodies. The reason for this was to isolate key physical phenomena and develop a framework for studying charged aerodynamics. As was noted, the extra degree of freedom for three-dimensional bodies should mean that the relative influence of charged aerodynamic forces compared to neutral aerodynamics forces is greater i.e. the predictions in this work are conservative. The next logical step for this work is to expand results presented here to three-dimensional bodies such as cubes and spheres. Comparison with spheres should also draw further upon dusty plasma work that has considered this problem within a region of $\mathcal{P}$ already.

Investigate whether ionospheric aerodynamics forces account force assumed to arise from the change in gas-surface interaction with altitude.   A fairly standard assumption is that neutral aerodynamic forces vary with altitude because the nature of the gas-surface interaction becomes increasingly specular. The mechanisms for this change revolves around atomic oxygen, at low altitudes it is argued that a layer of atomic oxygen that builds up on the surface making gas-surface interactions diffuse. As altitude increases, the atomic oxygen in the environment reduces and the surface becomes clean and gas-surface interactions are more appropriately modelled as specular (Moe and Moe, 2005; Pilinski, 2011). One possible avenue of future work is to compare ionospheric aerodynamic forces to forces caused by uncertainties in gas-surface interaction type to determine whether the change in force is more accurately a reflection of unmodelled ionospheric aerodynamics forces.

Investigate the influence of higher-order body phenomena on plasma-body interaction phenomena and ionospheric aerodynamics.   This work presented a physics-based argument that ionospheric aerodynamics can play a significant role in the motion of LEO objects. The scope of physical phenomena studied in this work was limited to isolating and understanding the underlying physics of these interactions. The reality of plasma interactions in LEO is more complicated, where phenomena such as secondary electron emissions, sputtering, non-uniform surface charged distributions, electron kinetics, and so on, will influence ionospheric aerodynamic forces. By developing a physical understanding of the underlying flow physics of these interactions in this work, the influence of these phenomena as perturbations to the underlying interaction may now be considered.

Account for local ionospheric aerodynamic perturbations in orbit propagations.
As noted in Section 8.2, orbital propagations in this work used a mean charged drag
coefficient to quantify the significance of ionospheric aerodynamics in LEO. Given the large
structural variations of the ionosphere with altitude, latitude and longitude, there will also
be large variations in ionospheric aerodynamic forces. To better quantify the influence
of ionospheric aerodynamics on the orbits of LEO objects requires an approach were the
charged aerodynamic coefficient is calculated based on local interaction parameters. This
will in turn aid in quantifying the regional significance of ionospheric aerodynamics to LEO
object e.g. how do ionospheric aerodynamics in polar regions influence the orbit of LEO
objects compared to equatorial regions?

Study regions of $\mathcal{P}(\alpha_k, \chi)$ outside the scope of this work. Intermediately coupled,
weakly shielded plasma-body interactions do not fit on the response surface used to in-
vestigate the influence of ionospheric aerodynamics on LEO objects. While it was argued
that these objects represent a small subset of those in LEO, they also represent a subset
most affected by ionospheric aerodynamics. It is possible there exist other regimes within
$\mathcal{P}(\alpha_k, \chi)$ not observed by the range of simulations presented in this work. Focused studies
of the different limits of $\mathcal{P}(\alpha_k, \chi)$ would aid in resolving this question and developing an
improved model of charged aerodynamics (including models for compact objects).

8.3.2 To Address Implications Outside the Scope of this Work

The word aerodynamics has two meanings. For the physicist, it refers to the study of flow
phenomena resulting from the interaction of an immersed object to quantify the momentum
exchange between flow and object. This has been the approach of this work, which has
studied the passive interaction of LEO objects with the LEO space environment from a
physical aerodynamic perspective. For an engineer, aerodynamics refers to the control of
forces, caused by the interaction of a flow with an immersed object, to influence a system.
This work has demonstrated that ionospheric aerodynamic forces can be significant in
LEO orbits. This has a variety of engineering implications. The following are two possible
applications of ionospheric aerodynamic control,

Active charge manipulation for the de-orbit applications. To mitigate the growth
of the debris population in LEO, organisations such as NASA and ESA have begun to
require LEO spacecraft at their end-of-life to be disposed by atmospheric re-entry within
25 years. Below 300 km where neutral aerodynamic forces have a significant influence on the
motion of LEO objects, proposed de-orbit methods centre around the deployment of high
area-to-mass ratio sails to maximise neutral drag forces. Another candidate technology

for de-orbit applications is the use of electrodynamic tethers which take advantage of the $q_e(v_B \times \mathbf{B})$ term in the Lorentz force (see for example Streetman and Peck, (2007) and Sanchez-Torres, (2016)). However, understanding charged aerodynamics in LEO is a pre-requisite for the use of electrodynamic tethers as they revolve around the electrical coupling between the satellite and the charged space environment - an understanding that was developed in this work.

Both of these approaches require the deployment of large, and at times, complex mechanical structures. Neutral aerodynamic methods are largely limited to low altitude applications, while there is yet to be successful demonstration of an electrodynamic tether for de-orbit applications.

One implication of this work is that, by manipulating the surface charge of an object, ionospheric aerodynamic forces may be maximised to significantly reduce de-orbit time at altitudes where neutral aerodynamic forces are small. For example, as shown in Chapter 7 at -30 V the mean ionospheric aerodynamic forces in equatorial orbits cause a $44 - 70\%$ increase in total drag forces at 900 km altitude. Larger negative surface potentials would cause corresponding increases in ionospheric aerodynamic forces. Therefore, without the need for large mechanical systems or propellant, ionospheric aerodynamic forces may be used to enhance aerodynamic forces and cause the rapid de-orbit of LEO object. The only requirement to achieve this is the availability of on-board power.

Contactless charge manipulation for debris removal. Following from the de-orbit concept, the natural progression is the contactless charging of local space debris using electron beam technologies to enhance the ionospheric drag of nearby debris and decrease their orbit lifetime. A similar proposal was made in Schaub et al., (2006), which proposed to use the Coulomb interaction between two charged objects (the charge maintained by electron beams) to manipulate their orbit for a variety of outcomes, de-orbit being one.

In LEO, the shielding length means that, unless the charge on the two objects is very large, they will not experience a force unless they are very close (approximately < 1 m). By manipulating charged aerodynamic forces, the proposed method does not require that the objects be close, the separation distance instead limited by the charging technique. High energy electron beams will penetrate a large distance into the surrounding plasma without significant attenuation. While more work is required to realise this concept, advantages over other debris removal concepts include:

- No need for complex orbital manoeuvres.

- No moving parts.

- Can be used on multiple nearby objects.

Appendix A

Derivation of the Maxwell Stress Tensor

Section 2.2.3 introduced the concept of the Maxwell Stress tensor $\bar{\mathbf{T}}$ to capture the momentum flux in a plasma. Specifically, when considering a volume of plasma, conservation of momentum gave,

$$\int_V n_i m_i \left(\mathbf{v} \cdot \nabla \right) \mathbf{v} dV + \int_V \nabla p_e dV - \int_V \epsilon_0 \left(\nabla \cdot \mathbf{E} \right) \mathbf{E} dV = 0 \tag{A.1}$$

Taking the last term, the following substitution was made,

$$\int_V \epsilon_0 \left(\nabla \cdot \mathbf{E} \right) \mathbf{E} dV = \int_V \nabla \cdot \bar{\mathbf{T}} dV \tag{A.2}$$

For completeness, this section derives $\bar{\mathbf{T}}$ to demonstrate that this substitution is appropriate. Derivation largely follows those listed in (Miller, Vandome, and John, 2010). We begin by considering the Lorentz force per unit volume $\mathbf{f}$,

$$\mathbf{f} = \rho_c \mathbf{E} + \mathbf{J} \times \mathbf{B} \tag{A.3}$$

where $\mathbf{B}$ is the magnetic field vector, $\mathbf{J}$ is the current density vector and ρ_c is the charge density.

Next we introduce Guass's law and Ampere's circuital law and express ρ_c and $\mathbf{J}$ in terms of $\mathbf{E}$ and $\mathbf{B}$.

$$\rho_c = \epsilon_0 \nabla \cdot \mathbf{E} \tag{A.4}$$

$$\mathbf{J} = \frac{1}{\mu_0} \left(\nabla \times \mathbf{B} \right) - \epsilon_0 \frac{\partial \mathbf{E}}{\partial t} \tag{A.5}$$

Substituting Eqn. A.4 and Eqn. A.5 into Eqn. A.3, $\mathbf{f}$ can be re-written,

$$\mathbf{f} = \epsilon_0 \left(\nabla \cdot \mathbf{E} \right) \mathbf{E} + \frac{1}{\mu_0} \left(\nabla \times \mathbf{B} \right) \times \mathbf{B} - \epsilon_0 \frac{\partial \mathbf{E}}{\partial t} \times \mathbf{B} \tag{A.6}$$

The time derivative can be written in terms of the Poynting vector $\mathbf{S} = \mathbf{E} \times \mathbf{B}$ using the product rule and Faraday's law of inductions,

$$\begin{aligned} \frac{\partial}{\partial t} \left(\mathbf{E} \times \mathbf{B} \right) &= \frac{\partial \mathbf{E}}{\partial t} \times \mathbf{B} + \mathbf{E} \times \frac{\partial \mathbf{B}}{\partial t} \\ &= \frac{\partial \mathbf{E}}{\partial t} \times \mathbf{B} - \mathbf{E} \times \left(\nabla \cdot \mathbf{E} \right) \end{aligned} \tag{A.7}$$

By collecting like terms, $\mathbf{f}$ can now be written as,

$$\begin{aligned} \mathbf{f} =& \epsilon_0 \left[\left(\nabla \cdot \mathbf{E} \right) \mathbf{E} - \mathbf{E} \times \left(\nabla \times \mathbf{E} \right) \right] \\ &+ \frac{1}{\mu_0} \left[\left(\nabla \cdot \mathbf{B} \right) \mathbf{B} - \mathbf{B} \times \left(\nabla \times \mathbf{B} \right) \right] \\ &- \epsilon_0 \frac{\partial}{\partial t} \left(\mathbf{E} \times \mathbf{B} \right) \end{aligned} \tag{A.8}$$

where the $\left(\nabla \cdot \mathbf{B} \right) \mathbf{B}$ term is inserted by applying Guass's law for magnetism to maintain symmetry of $\mathbf{B}$ and $\mathbf{E}$ terms i.e. absence of magnetic monopoles.

Applying the vector calculus identity,

$$\frac{1}{2} \nabla \left(\mathbf{A} \cdot \mathbf{A} \right) = \mathbf{A} \times \left(\nabla \times \mathbf{A} \right) + \left(\mathbf{A} \cdot \nabla \right) \mathbf{A} \tag{A.9}$$

The curls in Eqn. A.8 can be elminated such that,

$$\begin{aligned} \mathbf{f} =& \epsilon_0 \left[\left(\nabla \cdot \mathbf{E} \right) \mathbf{E} + \left(\mathbf{E} \cdot \nabla \right) \mathbf{E} \right] \\ &+ \frac{1}{\mu_0} \left[\left(\nabla \cdot \mathbf{B} \right) \mathbf{B} + \left(\mathbf{B} \cdot \nabla \right) \mathbf{B} \right] \\ &- \frac{1}{2} \nabla \left(\epsilon_0 E^2 + \frac{1}{2} B^2 \right) - \epsilon_0 \frac{\partial}{\partial} \left(\mathbf{E} \times \mathbf{B} \right) \end{aligned} \tag{A.10}$$

This expression represents all aspects of electromagnetism and momentum. It is written more compactly by introducing the maxwell stress tensor,

$$\bar{T}_i j = \epsilon_0 \left(E_i E_j - \frac{1}{2} \delta_{ij} E^2 \right) + \frac{1}{\mu_0} \left(B_i B_j - \frac{1}{2} \delta_{ij} B^2 \right) \tag{A.11}$$

where i and j are the tensor indices and δ_{ij} is the Krondecker delta

$$\delta_{ij} = \begin{cases} 0 \text{ if } i \neq j, \\ 1 \text{ if } i = j \end{cases} \tag{A.12}$$

f can now be written in a more compact form,

$$\mathbf{f} + \epsilon_0 \mu_0 \frac{\partial \mathbf{S}}{\partial t} = \nabla \cdot \bar{\mathbf{T}} \tag{A.13}$$

For a static, unmagnetised system, the **B** and time varying terms can be dropped and the $(E \cdot \nabla) \mathbf{E} = 0$. The momentum flux in a volume including mechanical momentum is then given by,

$$\int_V n_i m_i \left(\mathbf{v} \cdot \nabla\right) \mathbf{v} dV + \int_V \nabla p_e dV = \int_V \epsilon_0 \left(\nabla \cdot \mathbf{E}\right) \mathbf{E} dV = \int_V \nabla \cdot \bar{\mathbf{T}} dV \tag{A.14}$$

Q.E.D

Appendix B

Supplementary Validation Studies in pdFOAM

The cases presented in Section 3.4 were selected test the ability of pdFOAM to reproduce results predicted by independent DSMC and PIC codes i.e. demonstrating that all the modules within pdFOAM are integrated correctly. The following simulations present supplementary evidence to validate the implementation of individual modules described in Section 3.1.

B.0.1 Composite Linear Volume Method: Validation

Electron Oscillation
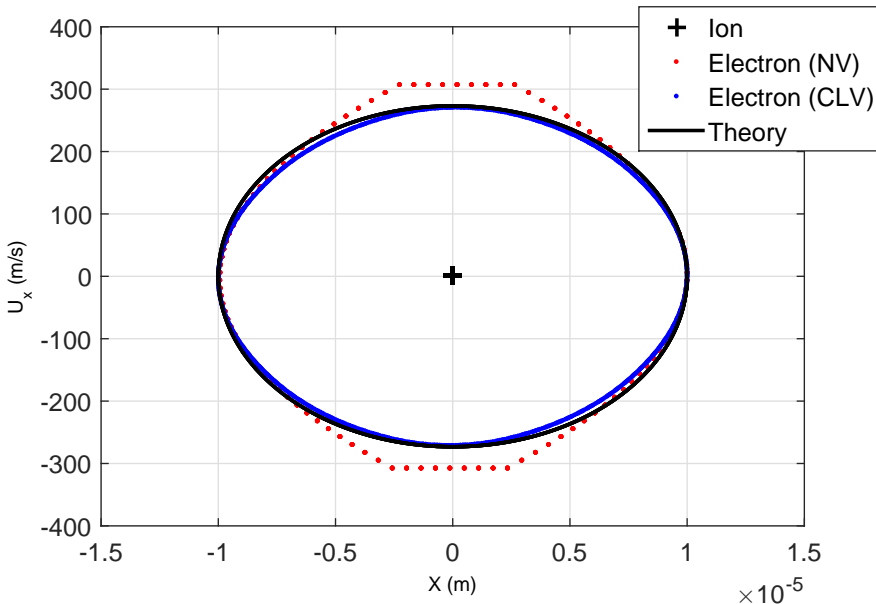
Ascribing finite-sizes through S to macro-particles may result in several numerical artifacts in PIC methods e.g. the addition of numerical energy. The idealised 1D oscillation of an electron about a stationary ion due to a small separation (Δx_{sep}) is a simple and instructive test shaping functions. The electron motion can be expressed as a simple harmonic oscillator described by,

$$X(t) = \Delta X_{sep}\cos(\omega_{pe}t)$$
$$U_x(t) = -\Delta X_{sep}\omega_{pe}\sin(\omega_{pe}t)$$

(B.1)

where ω_{pe} is the plasma oscillation frequency.

To test implementation of the NV and CLV method in pdFOAM, the oscillations of an electron about a fixed ion were investigated. A $1mm$ domain was sub-divided into 200 cells in x, an ion at 0.5025 mm (cell center) and a stationary electron at 0.5125. Figure B.1 plots the electron osculations through time with $\Delta t = 1 \times 10^{-9}s$ over a period of $1 \times 10^{-5}s$ (10000 steps) in position-velocity phase-space calculated using the NV and CLV shaping functions

respectively. Motion in X demonstrates that neither method adds a significant amount of numberical energy over the simulated period, the oscillation amplitude remaining constant. Motion in U_x illustrates the aliasing effect of the NV method, a_x constant throughout each cell and 0 in the central cell. Comparatively, the CLV method provides a significantly better approximation of the electron's motion, marginally under-predicting U_x compared to the NV method. Hence we conclude that both the NV and CLV methods don't add numerical energy, the CLV method providing a more physical approximation of plasma interactions. PIC simulations generally not interested in single particle motion, better suited to Molecular Dynamics (MD) methods, but in collective phenomena (Birdsall and Langdon, 1991).

Figure B.1: Theoretical 1D electron oscillation about stationary ion compared to observed oscillation in pdFOAM.

Two-Stream Instability

The two-stream instability problem is a well established plasma kinetic phenomenon (Birdsall and Langdon, 1991). It is a 1D problem involving the superimposition of two counter-streaming beams of charged particles e.g. electron-electron, positron-positron, or electron-positron beams. Given certain criteria, the response of these systems to an initial disturbance may result in a non-linear growth in position-velocity phase space (Birdsall and Langdon, 1991). Errors in shaping function will result in numerical self-forcing leading to the addition of non-physical energy to the system and the unbounded growth of such instabilities. This make it suitable for validating shaping functions.

Case 1 in Section 5.9 in (Birdsall and Langdon, 1991) is reproduced in Figure B.2 and
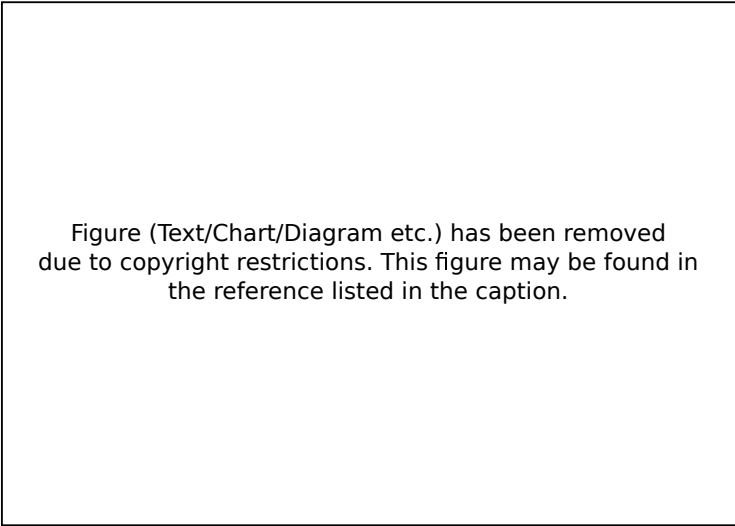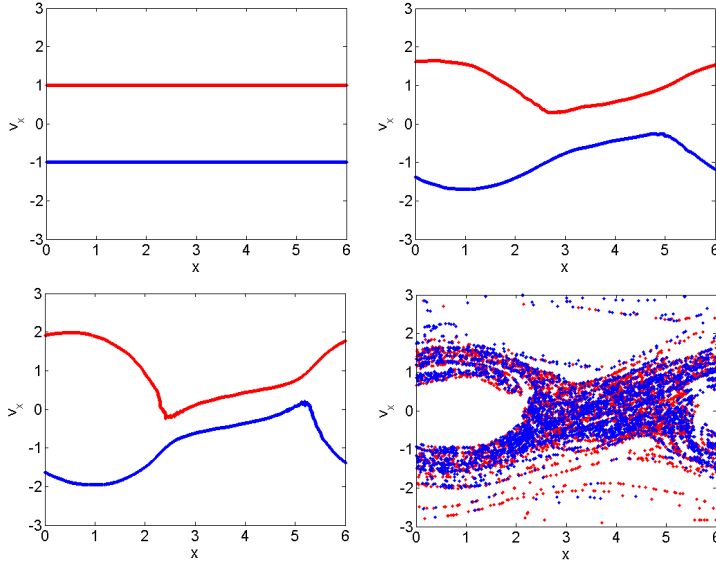
Figure B.2: Two-stream instability. Reproduced from Birdsall and Langdon, (1991).

shows the position-velocity phase-space evolution of an electron-electron two-stream instability. We have reproduced this interaction in Figure B.3 with a different initial disturbance source. Birdsall and Langdon, (1991)'s simulation uses a phase offset in velocity space between the electron beams as the initial disturbance, while the pdFOAM simulation disturbance is a result of small non-uniformities in an initial Maxwellian distribution. The latter representing a more realistic disturbance source. The disturbance source should have no effect on the transient growth dynamics of the instability but will change the initial growth rate e.g. a small disturbance will initially grow slower than a strong disturbance. Hence, snapshots in Figure B.2 and B.3 do not correspond to the same simulation time. The top left panel in Figure B.3 shows the initial position-velocity phase-space of the system; particles with an initial positive dimensionless velocity in x are colored red. The top right and bottom left panels in B.3 show the evolution of the instability, while the bottom right frame in both Figure B.2 and B.3 shows the systems at dynamic equilibrium, where there is no additional growth in phase-space. Comparing this last panel, we see the same phase-space void characteristic of the two-stream instability, which continues to move through time (hence why the voids are not at the same spot). Most importantly, the phase-space voids have a similar dimension in both simulations and the maximum particle velocity is similar. Therefore we conclude that pdFOAM has not added numerical energy to the system.

Figure B.3: Two-stream instability in pdFOAM.

B.0.2 Electron Fluid Model: Validation

The interaction of a plasma with an immersed object can be complex; ranging from surface absorption, deep penetration and neutralization, to the emission of other charged particles through secondary electron emission or sputtering (Whipple, 1981; Godd and Laframboise, 1983; Riemann, 1991). Before considering such phenomena, it is essential to demonstrate that the plasma-body interaction is modeled correctly; this applies to both FK and HK simulations. The shielding of a perfectly conducting wall in an unmagnetized, collisionless, flowing plasma, consisting of electrons and singly charged ions, is suitable for this purpose. The following discussion outlines the theory describing the general structure of a 1D plasma sheath for a fixed wall potential. For a detailed analysis, we refer the reader to (Riemann, 1991).

Consider a freestream plasma at $x = 0$ such that it is sufficiently far from a large flat plate with a fixed potential ϕ_p at $x = L$ that the freestream may be considered quasi-neutral i.e. $\phi(0) = 0$ and $\phi(x) = \phi_p$. In the region between $x = 0$ and $x = L$ there must then exist some potential structure or *"plasma sheath"* shielding the freestream plasma from the space-charge discontinuity at x. Given an ion drift velocity u_∞ and Boltzmann electrons, the dimensionless plasma sheath equation is described by (Riemann, 1991),

$$\frac{1}{2}\psi'^2 = M^2 \left[\left(1 + \frac{2\psi}{M^2}^{1/2} - 1 \right) \right] + exp\left[-\psi\right] - 1 \tag{B.2}$$

Equation B.2 can be expressed in closed form and solved numerically using the boundary

condition $\psi(L) = \psi_p$, where the dimensionless position (ξ), potential (ψ) and ion acoustic Mach number (M_i) are defined as,
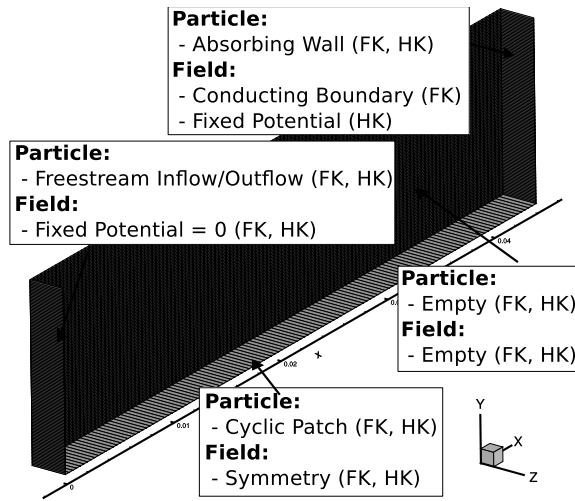
$$\xi = \frac{x}{\lambda_{D_e}}, \quad \psi(\xi) = -q_e\phi(\xi)/k_B T_e, \quad M_i = \frac{u_\infty}{(k_B T_e/m_i)^{1/2}} \tag{B.3}$$

To demonstrate the ability of pdFOAM to accurately reproduce sheath structure, we compare the sheath structure defined by Eqn. B.2 against pdFOAM for the conditions described in Table B.1 for a -0.1804 V wall. Maximum cell spacing was 1.7×10^{-5} m, while timestep was 1×10^{-9} s and 5×10^{-8} s for the FK and HK simulations respectively. Figure B.4 illustrates the numerical setup with particle and field boundary conditions.

Figure B.5 compares the theoretical and numerical sheath potential structure in a quasi-

Table B.1: Plasma sheath simulations parameters
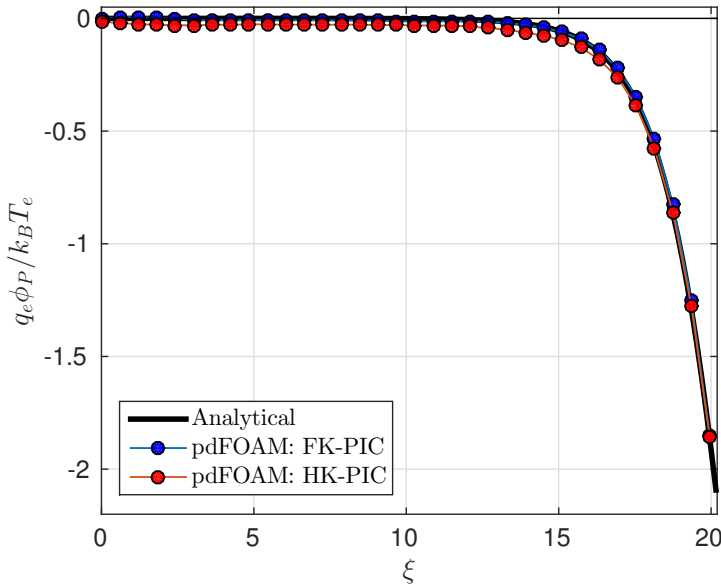
Plasma	Ions	Electrons
n_∞ (m^{-3})	1×10^{12}	1×10^{12}
m (kg)	1.67×10^{-27}	9.1×10^{-31}
T (K)	1000	1000
u_∞ (m/s)	$2.1u_{t,i}$	0

Figure B.4: Computational setup of planar sheath case

1D simulation. Motion is constrained in along the Z axis while retaining three velocity components. Figure B.5 shows that there is close agreement between FK, HK, and analytical ϕ distributions. The key difference being that the HK simulation does not exhibit an ion source sheath at the inlet as seen in the FK case (Schwager and Birdsall, 1990).

This is expected as the source sheath is a numerical product of re-fluxing electrons and the constant flux inlet boundary condition (Schwager and Birdsall, 1990).

Figure B.5: Comparison of numerical and analytical sheath structure (left) and computational setup (right)

B.0.3   Transient Conglomerated Cell: Validation
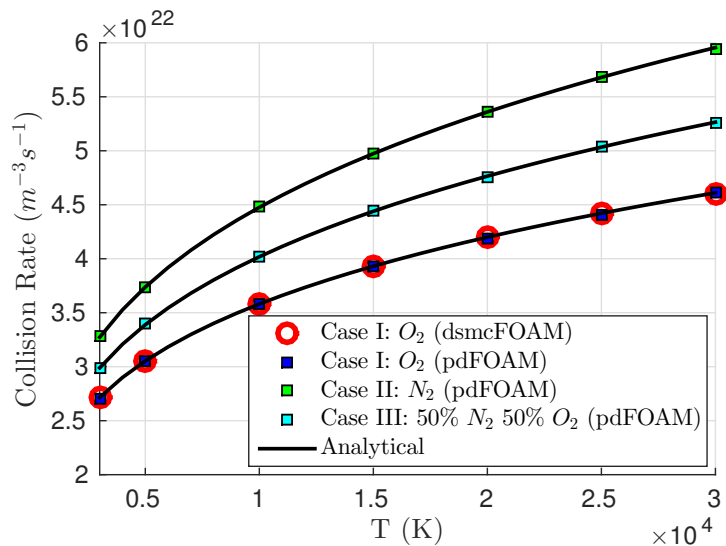
DSMC simulations model the evolution of a system's particle distribution function f_α through an approximation of the Boltzmann collision kernal. It is, therefore, essential that a DSMC code accurately reproduces collision rates described by kinetic theory (Bird, 1976). To ensure that the TCC method accurately captures collision rates consider a gas at thermal equilibrium with no gradients i.e. an adiabatic heat bath. The collision rates between species p and q is (Bird, 1976; Bird, 1994),

$$(N_{pq})_0 = 2\pi^{1/2}(d_{ref})^2_{pq} n_p n_q \left(\frac{T}{(T_{ref})_{pq}}\right)^{1-\omega_{pq}} \left(2k_B \frac{(T_{ref})_{pq}}{m_r}\right)^{1/2} \tag{B.4}$$

where d_{ref}, T_{ref} and ω are the VHS model parameters, reference diameter, reference temperature and viscosity component, respectively; n is the number density, k_B is the Boltzmann constant, T the overall temperature and m_r the reduced mass. The factor of 2 accounts for pq and qp collisions; for pp or qq collisions this must be removed.

To validate the TCC method, the collision rates of three different gas mixtures described by Eqn. B.4 were compared against those computed by pdFOAM at various temperatures.

Simulations used a $27x27x27$ mm cube with specular walls. The timestep was 1×10^{-7} s and cell spacing was 3×10^{-4} m. VHS collision properties are from (Bird, 2013). Cases I and II simulate the collision rates for a single species O_2 and N_2 gas respectively. Case III simulates a $50\%O_2 - 50\%N_2$ gas mixture. Figure B.6 shows that the TCC method accurately reproduces the increase in collision rate with temperature predicted by Eqn. B.4.

Figure B.6: Comparison of numerical and theoretical collision rates using the TCC method.

Appendix C

Summary of Simulation Parameters

Table C.1: Plasma interaction quantities and scaling parameters for cases 1-37.

	Plasma Interaction Quantities							Scaling Parameters			
#	ϕ_B (V)	r_B (m)	v_B (km/s)	m_i	n_∞ (10^{10}m^{-3})	T_i (K)	T_e (K)	α_k	χ	μ_e	S_i
1	0	0.3	7.5	O^+	4	1531	1997	0.00	0.0	0.0	1.48
2	-1	0.3	7.5	O^+	4	1531	1997	0.10	8.07	-5.81	5.93
3	-5	0.3	7.5	O^+	4	1531	1997	0.536	3.61	-29.05	5.93
4	-10	0.3	7.5	O^+	4	1531	1997	1.073	2.55	-58.1	5.93
5	-25	0.3	7.5	O^+	4	1531	1997	2.682	1.61	-145	5.93
6	-50	0.3	7.5	O^+	4	1531	1997	5.364	1.14	-290	5.93
7	0	0.3	7.5	H^+	4	1531	1997	0.000	0.0	0.0	1.48
8	-1	0.3	7.5	H^+	4	1531	1997	1.705	8.07	-5.81	1.48
9	-5	0.3	7.5	H^+	4	1531	1997	8.528	3.61	-29.0	1.48
10	-10	0.3	7.5	H^+	4	1531	1997	17.05	2.55	-58.1	1.48
11	-25	0.3	7.5	H^+	4	1531	1997	42.63	1.61	-145	1.48
12	-50	0.3	7.5	H^+	4	1531	1997	85.28	1.14	-290	1.48
13	0	0.03	7.5	O^+	4	1531	1997	0.000	0.0	0.0	5.93
14	-1	0.03	7.5	O^+	4	1531	1997	0.107	0.807	-5.81	5.93
15	-5	0.03	7.5	O^+	4	1531	1997	0.536	0.361	-29	5.93
16	-10	0.03	7.5	O^+	4	1531	1997	1.073	0.255	-58.1	5.93
17	-25	0.03	7.5	O^+	4	1531	1997	2.682	0.161	-145	5.93
18	-50	0.03	7.5	O^+	4	1531	1997	5.364	0.114	-290	5.93
19	0	0.03	7.5	H^+	4	1531	1997	0.000	0.0	0.0	1.48
20	-1	0.03	7.5	H^+	4	1531	1997	1.705	0.807	-5.81	1.48
21	-5	0.03	7.5	H^+	4	1531	1997	8.528	0.361	-29	1.48
22	-10	0.03	7.5	H^+	4	1531	1997	17.05	0.255	-58.1	1.48
23	-25	0.03	7.5	H^+	4	1531	1997	42.63	0.161	-145	1.48
24	-50	0.03	7.5	H^+	4	1531	1997	85.28	0.114	-290	1.48
25	-50	0.3	7.5	O^+	4	1531	1997	5.36	1.14	-290	5.93
26	-50	0.3	7.5	H^+	4	1531	1997	85.27	1.14	-290	1.48
27	-50	0.3	29.9	H^+	4	1531	1997	5.36	1.14	-290	5.93
28	-25	0.3	7.5	O^+	4	1531	1997	2.68	1.61	-145	5.93
29	-25	0.03	7.5	O^+	4	1531	1997	2.68	0.16	-145	5.93
30	-25	0.03	7.5	O^+	400	1531	1997	2.68	1.61	-145	5.93
31	-25	0.3	7.5	O^+	4	1531	1997	2.68	1.61	-145	5.93
32	-10	0.3	7.5	O^+	4	1531	1997	1.07	2.55	-58.1	5.93
33	-10	0.3	4.73	O^+	1.6	1531	798.8	2.68	1.61	-145	3.74
34	-25	0.3	7.5	O^+	4	1531	1997	2.68	2.82	-145	5.93
				H^+	4	1531		85.38			1.48
35	-25	0.3	7.5	O^+	4	1531	1997	2.68	2.7	-45	5.93
				H^++	4	1531		85.27			1.58
36	-50	0.3	10.6	O^+	4	1531	3994	2.68	2.28	-145	8.38
				He^++	4	1531		42.69			2.97
37	-50	0.3	10.6	O^+	4	3074	3994	2.68	2.28	-145	5.92
				He^++	4	6124		42.69			1.48

Table C.2: Plasma interaction quantities and scaling parameters for cases 38-75.

#	Plasma Interaction Quantities							Scaling Parameters			
	ϕ_B (V)	r_B (m)	v_B (km/s)	m_i	n_∞ (10^{10}m^{-3})	T_i (K)	T_e (K)	α_k	χ	mu_e	S_i
38	-10	0.3	26.76	O^+	4	1531	1997	0.084	2.55	-58	21.16
39	-10	0.3	11.97	O^+	4	1531	1997	0.42	2.55	-58	9.46
40	-10	0.3	7.5	O^+	4	1531	1997	1.072	2.55	-58	5.93
41	-10	0.3	3.78	O^+	4	1531	1997	4.227	2.55	-58	2.98
42	-10	0.3	2.676	O^+	4	1531	1997	8.426	2.55	-58	2.12
43	-10	0.3	1.889	O^+	4	1531	1997	16.90	2.55	-58	1.49
44	-10	0.3	7.5	O^+	0.307	1531	1997	1.072	0.7	-58	5.93
45	-10	0.3	7.5	O^+	0.614	1531	1997	1.072	1	-58	5.93
46	-10	0.3	7.5	O^+	3.07	1531	1997	1.072	2.55	-58	5.93
47	-10	0.3	7.5	O^+	15.35	1531	1997	1.072	5	-58	5.93
48	-10	0.3	7.5	O^+	30.7	1531	1997	1.072	7.07	-58	5.93
49	-10	0.3	7.5	O^+	61.4	1531	1997	1.072	10	-58	5.93
50	-10	0.3	7.5	O^+	4	5802	1997	1.072	2.55	-20	5.93
51	-10	0.3	7.5	O^+	4	2901	1997	1.072	2.55	-40	5.93
52	-10	0.3	7.5	O^+	4	1934	1997	1.072	2.55	-60	5.93
53	-10	0.3	7.5	O^+	4	1450	1997	1.072	2.55	-80	5.93
54	-10	0.3	7.5	O^+	4	1160	1997	1.072	2.55	-100	5.93
55	-10	0.3	7.5	O^+	4	580	1997	1.072	2.55	-200	5.93
56	-5	0.3	26.76	O^+	4	1531	1997	0.042	3.6	-29	21.16
57	-5	0.3	11.97	O^+	4	1531	1997	0.201	3.6	-29	9.46
59	-5	0.3	8.46	O^+	4	1531	1997	0.421	3.6	-29	6.69
60	-5	0.3	5.98	O^+	4	1531	1997	0.842	3.6	-29	4.72
61	-5	0.3	2.67	O^+	4	1531	1997	4.213	3.6	-29	2.12
62	-5	0.3	1.89	O^+	4	1531	1997	8.451	3.6	-29	1.49
63	-5	0.3	7.5	O^+	0.153	1531	1997	0.5	0.7	-29	5.93
64	-5	0.3	7.5	O^+	0.307	1531	1997	0.5	1	-29	5.93
65	-5	0.3	7.5	O^+	0.614	1531	1997	0.5	1.41	-29	5.93
66	-5	0.3	7.5	O^+	3.07	1531	1997	0.5	3.61	-29	5.93
67	-5	0.3	7.5	O^+	30.7	1531	1997	0.5	10	-29	5.93
68	-25	0.3	7.77	O^+	0.767	1531	1997	2.5	0.707	-145	6.09
69	-25	0.3	1.73	O^+	0.767	1531	1997	50	0.707	-145	1.36
70	-25	0.3	7.77	O^+	307	1531	1997	2.5	14.14	-145	6.09
71	-25	0.3	1.73	O^+	307	1531	1997	50	14.14	-145	1.36
72	-5	0.3	7.77	O^+	0.7675	1531	1997	0.5	1.58	-29	6.09
73	-5	0.3	1.73	O^+	0.7675	1531	1997	10	1.58	-29	1.36
74	-5	0.3	7.77	O^+	307	1531	1997	0.5	31.62	-29	6.09
75	-5	0.3	1.73	O^+	307	1531	1997	10	31.62	-29	1.36

Bibliography

Allen, J. E. (1992). "Probe theory - the orbital motion approach". In: *Physica Scripta* 45.5, p. 497. ISSN: 0031-8949. DOI: 10.1088/0031-8949/45/5/013.

– (2007). "On the drag on an object immersed in a flowing plasma: The control surface approach". In: *Journal of Plasma Physics* 73, pp. 773–783. ISSN: 0022-3778. DOI: Doi10.1017/S0022377806006246.

Al'Pert, Ya. L., A. V. Gurevich, and L. P. Pitaevskii (1965). *Space Physics with Artificial Satellites*. New York: Consultants Bureau. DOI: 10.1119/1.1973101.

Amos, Jonathan (2015). *OneWeb satellite operator eyes huge rocket campaign.* URL: http://www.bbc.com/news/science-environment-33268180 (visited on 01/10/2017).

Anderson, John D. et al. (2009). *Computational Fluid Dynamics: An Introduction*, p. 332. ISBN: 9783540850557. DOI: 10.1007/978-3-540-85056-4. URL: http://www.bidyut.yolasite.com/resources/WendtJ.F.(ed.)ComputationalFluidDynamics..AnIntroduction(3ed.,Springer,2008)(ISBN3540850554)(333s){_}PCfm{_}.pdf.

Anderson, Phillip C. (2012). "Characteristics of spacecraft charging in low Earth orbit". In: *Journal of Geophysical Research* 117.A7, pp. 1–11. ISSN: 0148-0227. DOI: 10.1029/2011JA016875.

Andrés de la Fuente, Jose (2007). *Enhanced Modelling of LAGEOS Non-Gravitational Perturbations*. Turbineweg, Delft: Sieca Repro. ISBN: 9789056230814.

Auweter-Kurtz, Monika et al. (2005). "Development of a hybrid PIC/DSMC Code". In: *29 th International Electric Propulsion Conference,* pp. 1–15.

Bachmat, Yehunda and Jacob Bear (1987). *On the Concept and Size of a Representative Elementary Volume*. Springer Netherlands, pp. 3–20. ISBN: 978-94-009-3625-6. DOI: 10.1007/978-94-009-3625-6_1.

Barenblatt, G. I. (1996). *Self-similarity: Dimensional Analysis, and Intermediate Asymptotics*. Ed. by D. G. Crighton. Cambridge University Press. ISBN: 0521435226.

Barnes, Michael S. et al. (1992). "Transport of dust particles in glow-discharge plasmas". In: *Physical Review Letters* 68.3, pp. 313–316. ISSN: 00319007. DOI: 10.1103/PhysRevLett.68.313.

Barrie, Alexander (2006). "Modeling Differential Charging of Composite Spacecraft Bodies Using the Coliseum Framework". PhD thesis. Virginia Polytechnic Institute.

Beard, David B and Francis S Johnson (1960). "Charge and Magnetic Field Interaction with Satellites". In: *Journal of Geophysical Research* 65.1. ISSN: 0028-0836. DOI: 10.1038/088331a0.

Beiser, A. and B. Raab (1961). "Hydromagnetic and Plasma Scaling Laws". In: *Physics of Fluids* 4.2, p. 177. ISSN: 00319171. DOI: 10.1063/1.1724425. URL: http://scitation.aip.org/content/aip/journal/pof1/4/2/10.1063/1.1724425.

Belyaev, Mikhail A. (2015). "PICsar: A 2.5D axisymmetric, relativistic, electromagnetic, Particle in Cell code with a radiation absorbing boundary". In: *New Astronomy* 36, pp. 37–49. ISSN: 13841076. DOI: 10.1016/j.newast.2014.09.006. arXiv: 1407.1810.

Benilov, M S (2008). "The Child–Langmuir law and analytical theory of collisionless to collision-dominated sheaths". In: *Plasma Sources Science and Technology* 18.1, p. 014005. ISSN: 0963-0252. DOI: 10.1088/0963-0252/18/1/014005.

Bilitza, Dieter et al. (2014). "The International Reference Ionosphere 2012 – a model of international collaboration". In: *Journal of Space Weather and Space Climate* 4, A07. ISSN: 2115-7251. DOI: 10.1051/swsc/2014004. URL: https://www.researchgate.net/publication/261016440{_}The{_}International{_}Reference{_}Ionosphere{_}2012-A{_}model{_}of{_}international{_}collaboration.

Bird, G. A. (1962). "The Flow About a Moving Body in the Upper Ionosphere". In: *Journal of the Aerospace Sciences* 29.7, pp. 808–814.

– (1976). *Molecular Gas Dynamics.* Oxford: Clarendon Press.

– (1977). "Direct Molecular Simulation of a Dissociating Diatomic Gas". In: *Journal of Computational Physics* 25.4, pp. 353–365. ISSN: 00219991.

– (1994). *Molecular Gas Dynamics and Direction Simulation of Gas Flows.* Clarendon Press.

– (2007). "Sophisticated DSMC". In: *Notes prepared for a short course at the DSMC07 meeting.* Santa Fe, pp. 1–49.

– (2013). *The DSMC Method.* 1.1. Sydney: CreateSpace. ISBN: 1492112909.

Birdsall, Charles K. and A. B. Langdon (1991). *Plasma physics via computer simulation.* Vol. 42. New York: Adam Hilger Press. ISBN: 0750301171. DOI: 10.1016/0010-4655(86)90240-7.

Blau, Patrick (2017). *Update: High-Risk Satellite Conjunction passes without Incident.* URL: http://spaceflight101.com/close-orbital-encounter-january-7-2017/ (visited on 01/10/2017).

Boerner, Jeremiah and Iain D. Boyd (2007). "Numerical Simulation of Probe Measurements in a Non-equilibrium Plasma , Using a Detailed Model Electron Fluid". In: *AIAA Aerospace Science Meeting and Exhibit* 2007-995.January, pp. 1–12.

Boltzmann, L. (1872). "Weitere StudiEn fiber das WSxmegleichgewicht unter Gasmolek-filen". In: *Wien. Ber.*

Brundin, C L (1963). "Effects of Charged Particles on the Motion of an Earth Satellite". In: *AIAA Journal* 1.11, pp. 2529–2538. ISSN: 0001-1452. DOI: 10.2514/3.2105.

Burgess, David and Manfred Scholer (2015). *Collisionless Shocks in Space Plasmas: Structure and Accelerated Particles*. Cambridge: Cambridge University Press. ISBN: 978-0-521-51459-0.

Cairns, Iver (1999). *Earth's Atmosphere*. URL: http://www.physics.usyd.edu.au/{~}cairns/teaching/lecture16/node2.html (visited on 01/10/2017).

Call, Stephen. M. (1969). *The Interaction of a Satellite with the Ionosphere*. Tech. rep. COLUMBIA UNIV NEW YORK PLASMA LAB.

Chandrasekhar, S. (1943). "Dynamical Friction". In: *Astrophysical Journal* 97, p. 255.

Choi, Seung J and Mark J Kushner (1994). *Particle-in-cell simulation of dust charging and shielding in low pressure glow discharges*. DOI: 10.1109/27.279017.

Choinière, Éric and Brian E. Gilchrist (2007). "Self-consistent 2-D kinetic simulations of high-voltage plasma sheaths surrounding ion-attracting conductive cylinders in flowing plasmas". In: *IEEE Transactions on Plasma Science* 35.1, pp. 7–22. ISSN: 00933813. DOI: 10.1109/TPS.2006.889300.

Chopra, K. P. (1961a). "Errata: Interactions of Rapidly Moving Bodies in Terrestrial Atmosphere". In: *Review of Modern Physics* 33.2.

– (1961b). "Interactions of Rapidly Moving Bodies in Terrestrial Atmosphere". In: *Review of Modern Physics* 33.2.

Chopra, K. P. and S. F. Singer (1958). "Drag of a Sphere Moving in a Conducting Fluid in the Presence of Magnetic Field". In: *Heat Transfer and Fluid Mechanics Institute*.

Cook, G.E. (1965). "Satellite drag coefficients". In: *Planetary and Space Science* 13.10, pp. 929–946. ISSN: 00320633. DOI: 10.1016/0032-0633(65)90150-9.

Council, National Research (2012). *Continuing Kepler's Question: Assessing Air Force Space Commands Astrodynamics Standards*. Tech. rep. Washington: TThe National Academies Press. DOI: https://doi.org/10.17226/13456.

Davis, A. H. and I Harris (1961). *Interaction of a charged satellite with the ionosphere*. Washington, D.C.: National Aeronautics and Space Administration.

Deforest, Sherman E (1972). "Spacecraft Charging at Synchronous Orbit". In: *Journal of Geophysical Research* 77.4, pp. 651–659.

Delzanno, Gian Luca et al. (2013). "CPIC: A curvilinear particle-in-cell code for plasma-material interaction studies". In: *IEEE Transactions on Plasma Science* 41.12, pp. 3577–3587. ISSN: 00933813. DOI: 10.1109/TPS.2013.2290060. arXiv: 1311.2286.

Dietrich, Stefan and Iain D. Boyd (1996). "Scalar and Parallel Optimized Implementation of the Direct Simulation Monte Carlo Method". In: *Journal of Computational Physics* 126.2, pp. 328–342. ISSN: 00219991. DOI: 10.1006/jcph.1996.0141. URL: http://www.sciencedirect.com/science/article/pii/S0021999196901412.

Doornbos, E. and H. Klinkrad (2006). "Modelling of space weather effects on satellite drag". In: *Advances in Space Research* 37.6, pp. 1229–1239. ISSN: 02731177. DOI: 10.1016/j.asr.2005.04.097.

Doornbos, E., H. Klinkrad, and P. Visser (2005). "Atmospheric density calibration using satellite drag observations". In: *Advances in Space Research* 36.3, pp. 515–521. ISSN: 02731177. DOI: 10.1016/j.asr.2005.02.009.

Emmert, J. T. (2015). "Thermospheric mass density: A review". In: *Advances in Space Research* 56.5, pp. 773–824. ISSN: 18791948. DOI: 10.1016/j.asr.2015.05.038. URL: http://dx.doi.org/10.1016/j.asr.2015.05.038.

Engwall, E., a. I. Eriksson, and J. Forest (2006). "Wake formation behind positively charged spacecraft in flowing tenuous plasmas". In: *Physics of Plasmas* 13.6, pp. 1–10. ISSN: 1070664X. DOI: 10.1063/1.2199207.

Enloe, C L et al. (1995). "The Charging Hazards and Wake Studies (CHAWS) Experiment". In: *33rd Aerospace Sciences Meeting and Exhibit*.

ESA (2008). *Debris objects in low-Earth orbit (LEO)*. URL: http://www.esa.int/spaceinimages/Images/2008/03/Debris{_}objects{_}in{_}low-Earth{_}orbit{_}LEO (visited on 01/10/2017).

Evans, Robin et al. (1989). "A Preliminary Spacecraft Charging Map for the Near Earth Environment". In: *Spacecraft Charging Technology Conference*. Jet Propulsion Laboratory. URL: http://holbert.faculty.asu.edu/eee460/spacecharge.html.

Fahleson, U (1967). "Laboratory Experiments with Plasma Flow Past Unmagnetised Obstacles". In: *Planetary and Space Science* 15.10, pp. 1489–1497.

Fehske, H., Rudolf Schneider, and A. Weibe (2008). *Computaional Many-particle Physics*. New York: Springer. ISBN: 9783540746850.

Feller, Willy (1940). "On the Integro-Differential Equations of Purely Discontinuous Markoff Processes". In: *Transactions of the American Mathematical Society* 48.3, pp. 488–515.

Fortov, V. E. et al. (2005). "Complex (dusty) plasmas: Current status, open issues, perspectives". In: *Physics Reports* 421.1-2, pp. 1–103. ISSN: 03701573. DOI: 10.1016/j.physrep.2005.08.007.

Fournier, G. (1970). "Electric drag". In: *Planetary and Space Science* 18.7, pp. 1035–1041. ISSN: 00320633. DOI: 10.1016/0032-0633(70)90105-4.

Garrett, Henry B. (1981). "The charging of spacecraft surfaces". In: *Review of Geophysics and Space Physics,* 19.4, pp. 577–616. ISSN: 8755-1209. DOI: 10.1029/RG019i004p00577.

Garrett, Henry B. and Albert C. Whittlesey (2000). "Spacecraft charging, an update". In: *IEEE Transactions on Plasma Science* 28.6, pp. 2017–2028. ISSN: 00933813. DOI: 10.1109/27.902229.

Gilles, M, David Vokrouhlick, and J Eanes (1997). "Nongravitational effects and the LAGEOS eccentricity excitations". In: *Journal of Geophysical Research: Solid Earth* 102.96, pp. 2711–2729.

Godd, R. and J. G. Laframboise (1983). "Total current to cylindrical collectors in collisionless plasma flow". In: *Planetary and Space Science* 31.3, pp. 275–283. ISSN: 00320633. DOI: 10.1016/0032-0633(83)90077-6.

Gurevich, A. V., L. V. Pariiskaya, and L. P. Pitaevskii (1966). "Self-similar motion of rarefied plasma". In: *Journal of Experimental and Theoretical Physics* 22.2, pp. 449–454.

Gurevich, A. V., L. P. Pitaevskii, and V. V. Smirnova (1970). "Ionospheric Aerodynamics". In: *Soviet Physics Uspekhi* 99.1, pp. 3–49. ISSN: 00386308. DOI: 10.1007/BF00226263.

Gussenhoven, M. S. et al. (1985). "High-Level spacecraft charging in the low-altitude polar auroral environment.pdf". In: *Journal of Geophysical Research* 90.A11, pp. 11009–11023. DOI: 10.1029/JA090iA11p11009.

Hall, D. F. et al. (1963). "Plasma-Vehicle Interaction in a Plasma Stream". In: *AIAA Electric Propulsion Conference,* 2.6, pp. 1032–1039. ISSN: 0001-1452. DOI: 10.2514/3.2495.

Hastings, D. E. (1995). "A review of plasma interactions with spacecraft in low Earth orbit". In: *Journal of Geophysical Research* 100.A8, pp. 14457–14483. ISSN: 0148-0227. DOI: 10.1029/94JA03358.

Heatley, A. H. (1937). "Collector Theory for Ions with Maxwellian Drift Velocities". In: *Physical Review* 52.3, p. 235.

Hester, S. D. and Ain. A. Sonin (1969). "A laboratory study of the electrodynamic influences on the wakes of ionospheric satellites". In: *2nd Fluid and Plasma Dynamics Conference* 8.6, pp. 1090–1098. DOI: doi:10.2514/6.1969-673. URL: http://dx.doi.org/10.2514/6.1969-673.

Hockney, R W and J W Eastwood (1988). *Computer Simulation Using Particles*. Abingdon: Taylor & Francis Group. ISBN: 0852743920. DOI: 10.1137/1025102. URL: http://link.aip.org/link/SIREAD/v25/i3/p425/s1{\&}Agg=doi.

Hoegy, W. R. and L. E. Wharton (1973). "Current to a moving cylindrical electrostatic probe". In: *Journal of Applied Physics* 44.12, pp. 5365–5371. ISSN: 00218979. DOI: 10.1063/1.1662157.

Horányi, Mihály (1996). "Charged Dust Dynamics in the Solar System". In: *Annu. Rev. Astron. Astrophys* 34, pp. 383–418. ISSN: 0066-4146. DOI: 10.1146/annurev.astro.34.1.383.

Hughes, Steven, Joel Parker, and Deepa Chavali (2016). *General Mission Analysis Toolkit*. URL: https://gmat.gsfc.nasa.gov/.

Hutchinson, I H (2002). "Principles of plasma diagnostics". In: *Plasma Physics and Controlled Fusion* 44.12, p. 2603. DOI: https://doi.org/10.1017/CBO9780511613630.

– (2005). "Ion collection by a sphere in a flowing plasma: 3. Floating potential and drag force". In: *Plasma Physics and Controlled Fusion* 47.1, pp. 71–87. ISSN: 0741-3335. DOI: 10.1088/0741-3335/47/1/005.

Hutchinson, I H (2006). "Collisionless ion drag force on a spherical grain". In: *Plasma Physics and Controlled Fusion* 48.2, pp. 185–202. ISSN: 0741-3335. DOI: 10.1088/0741-3335/48/2/002.

Hutchinson, I. H. (2011). "Forces on a small grain in the nonlinear plasma wake of another". In: *Physical Review Letters* 107.9, pp. 2–5. ISSN: 00319007. DOI: 10.1103/PhysRevLett.107.095001.

Hutchinson, I H and C B Haakonsen (2013). "Collisional effects on nonlinear ion drag force for small grains". In: *Phys.\ Plasmas* 20.8, p. 83701. ISSN: 1070664X. DOI: 10.1063/1.4818144. arXiv: arXiv:1305.6944v3. URL: http://link.aip.org/link/?PHP/20/083701/1.

Ikkurthi, V. R. et al. (2010). "Computation of charge and ion drag force on multiple static spherical dust grains immersed in rf discharges". In: *Physics of Plasmas* 17.10. ISSN: 1070664X. DOI: 10.1063/1.3499356.

Jasak, Hrvoje, Aleksandar Jemcov, and Zeljko Tukovic (2007). "OpenFOAM : A C ++ Library for Complex Physics Simulations". In: *International Workshop on Coupled Methods in Numerical Dynamics* 1000, pp. 1–20.

Jastrow, R. and C. A. Pearse (1957). "Atmospheric Drag on the Satellite". In: *Journal of Geophysical Research* 62.3. URL: http://onlinelibrary.wiley.com/doi/10.1029/JZ062i003p00413/pdf.

Jeong, Hyunju (2008). "Kinetic Simulations of Spacecraft Charging and Plasma Interactions in the Solar Wind". PhD thesis. Virginia Tech.

Khrapak, S. and G. Morfill (2009). "Basic processes in complex (dusty) plasmas: Charging, interactions, and ion drag force". In: *Contributions to Plasma Physics* 49.3, pp. 148–168. ISSN: 08631042. DOI: 10.1002/ctpp.200910018.

Khrapak, S. A. (2008). "Ion drag force acting on an absorbing body in highly collisional plasmas". In: *Ukrainian Journal of Physics* 53.11, pp. 1062–1065. ISSN: 05031265. DOI: 10.1063/1.2464187.

Khrapak, S. A. et al. (2005). "Hybrid approach to the ion drag force". In: *Physics of Plasmas* 12.4, pp. 1–8. ISSN: 1070664X. DOI: 10.1063/1.1867995.

Khrapak, Sergey A., Manis Chaudhuri, and Gregor E. Morfill (2009). "Ion drag force in collisional plasmas". In: *IEEE Transactions on Plasma Science* 37.4 PART 1, pp. 487–493. ISSN: 00933813. DOI: 10.1109/TPS.2008.2011803.

Kiel, R. E. and F. C. Gey (1968). "Electrostatic potential fields of an ionospheric satellite." In: *AIAA Journal* 6.4, pp. 690–694. ISSN: 0001-1452. DOI: 10.2514/3.4564.

Kiel, Roger E (1968). "Electrostatic Probe Theory for Free Molecular Cylinders". In: *AIAA Journal* 6.4, pp. 708–712. ISSN: 00011452.

Knechtel, D and William C Pitts (1965). "Experimental Investigation of Electric Drag on Spherical Satellite Models". In: *AIAA Aerospace Sciences Meeting* 2.February, pp. 1148–1151.

Kolobov, V. I. and R. R. Arslanbekov (2012). "Towards adaptive kinetic-fluid simulations of weakly ionized plasmas". In: *Journal of Computational Physics* 231.3, pp. 839–869. ISSN: 00219991. DOI: 10.1016/j.jcp.2011.05.036. URL: http://dx.doi.org/10.1016/j.jcp.2011.05.036.

Kraus, Lester and Kenneth M. Watson (1958). "Plasma Motions Induced by Satellites in the Ionosphere". In: *Physics of Fluids* 1.6, p. 480. ISSN: 00319171. DOI: 10.1063/1.1724371. URL: http://link.aip.org/link/PFLDAS/v1/i6/p480/s1{\&}Agg=doi.

Lacina, J (1971). "Similarity rules in plasma physics". In: *Plasma Physics* 13, pp. 303–312.

Laframboise, J. G. and J. Luo (1989). "High-voltage polar-orbit and beam-induced charging of a dielectric spacecraft: A wake-induced barrier effect mechanism". In: *Journal of Geophysical Research* 94.A7, p. 9033. ISSN: 0148-0227. DOI: 10.1029/JA094iA07p09033. URL: http://doi.wiley.com/10.1029/JA094iA07p09033.

Laframboise, J. G. and L. W. Parker (1973). "Probe design for orbit-limited current collection". In: *Physics of Fluids* 16.5, p. 629. ISSN: 00319171. DOI: 10.1063/1.1694398. URL: http://link.aip.org/link/PFLDAS/v16/i5/p629/s1{\&}Agg=doi.

Lam, S. H. (1969). "Collisionless flow of a plasma mixture". In: *7th Aerospace Sciences Meeting* 7.11, pp. 2094–2098. ISSN: 00011452. DOI: doi:10.2514/6.1969-78. URL: http://dx.doi.org/10.2514/6.1969-78.

Lapenta, Giovanni (2011). "DEMOCRITUS: An adaptive particle in cell (PIC) code for object-plasma interactions". In: *Journal of Computational Physics* 230.12, pp. 4679–4695. ISSN: 00219991. DOI: 10.1016/j.jcp.2011.02.041. URL: http://dx.doi.org/10.1016/j.jcp.2011.02.041.

Leeuw, J. H. de (1966). "A Brief Introduction to Ionospheric Aerodynamics". In: *Rarefied Gas Dynamics*. Ed. by C. L. Brundin. New York: Academic Press.

Li, Lin Sen (2011). "Perturbation effect of the Coulomb drag on the orbital elements of the earth satellite moving in the ionosphere". In: *Acta Astronautica* 68.7-8, pp. 717–721. ISSN: 00945765. DOI: 10.1016/j.actaastro.2010.11.004. URL: http://dx.doi.org/10.1016/j.actaastro.2010.11.004.

Liu, Chia-Han (1972). "Forces and Energy Tranfer Induced by Rarefied Plasma Flows Past Solid Bodies". PhD thesis. University of Oklahoma.

Liu, V C (1975). "On ionospheric aerodynamics". In: *Progress in Aerospace Sciences* 16.3, pp. 273–297. ISSN: 03760421. DOI: 10.1016/0376-0421(75)90017-2.

Lofthouse, Andrew J. (2008). "Nonequilibrium Hypersonic Aerothermodynamics Using the Direct Simulation Monte Carlo and Navier-Stokes Models". PhD thesis, p. 231. URL: http://deepblue.lib.umich.edu/bitstream/handle/2027.42/58370/ajloft{_}1.pdf?sequence=1.

Lofthouse, Andrew J., Iain D. Boyd, and Michael J. Wright (2007). "Effects of continuum breakdown on hypersonic aerothermodynamics". In: *Physics of Fluids* 19. DOI: 10.1063/1.2710289.

Macpherson, Graham B., Nordin Niklas, and Henry G. Weller (2009). "Particle tracking in unstructured, arbitrary polyhedral meshes for use". In: *International Journal for Numerical Methods in Biomedical Engineering* 25, pp. 263–273. ISSN: 20407939. DOI: 10.1002/cnm. URL: http://onlinelibrary.wiley.com/doi/10.1002/cnm.1494/full.

Maldonado, Carlos A. and Andrew D. Ketsdever (2015). "Drag Measurements in a Simulated Low-Earth Orbit Environment". In: *53rd AIAA Aerospace Sciences Meeting* January. DOI: 10.2514/6.2015-1392. URL: http://arc.aiaa.org/doi/10.2514/6.2015-1392.

Martin, Anthony R (1974). "Numerical Solutions to the problem of charged particle flow around an Ionospheric Spacecraft". In: *Planetary and Space Science* 22, pp. 121–141.

MatLAB (2014). Natick, Massachusetts, United States. URL: https://www.mathworks.com/products/matlab.html.

Maxwell, J Clerk (1867). "On the Dynamical Theory of Gases". In: *Philosophical Transactions* January, pp. 49–88.

Mclaughlin, Craig A, S. Mance, and T. Lechtenberg (2011). "Drag Coefficient Estimation in Orbit Determination". In: *Journal of Astronautical Sciences* 58.3, pp. 513–530.

McMahon, J. C., G. Z. Xu, and J. G. Laframboise (2005). "The effect of ion drift on the sheath, presheath, and ion-current collection for cylinders in a collisionless plasma". In: *Physics of Plasmas* 12.6, pp. 1–11. ISSN: 1070664X. DOI: 10.1063/1.1924392.

Measick, S. et al. (1991). "Temporal Study of Wake Formation Behind a Conducting Body". In: *Journal of Geophysical Research: Space Physics* 96.A8, pp. 13985–13995.

Mehta, Piyush M, Andrew Walker, and Josef Koller (2014). "Comparing Physical Drag Coefficients Computed with Direct Simulation Monte Carlo Using Different Gas – Surface Interaction Models". In: *Journal of Spacecraft and Rockets* 51.3, pp. 873–883. ISSN: 0022-4650. DOI: 10.2514/1.A32566.

Melzani, Mickaël et al. (2013). "Apar-T: code, validation, and physical interpretation of particle-in-cell results". In: *Astronomy & Astrophysics* 558, A133. ISSN: 0004-6361. DOI: 10.1051/0004-6361/201321557. arXiv: 1308.5892. URL: http://www.aanda.org/10.1051/0004-6361/201321557{\%}5Cnhttp://arxiv.org/abs/1308.5892{\%}5Cnhttp://www.aanda.org/10.1051/0004-6361/201321557.

Mignard, F et al. (1985). "Re-assessment of the charge and neutral drag of LAGEOS and its Geophysical implications". In: *Journal of Geophysical Research: Solid Earth* 90.B11, pp. 9381–9398.

Miller, Frederic P., Agnes F. Vandome, and McBrewster John (2010). *Maxwell Stress Tensor*. VDM Publishing. ISBN: 9786132848321.

Miloch, W. J., M. Kroll, and D. Block (2010). "Charging and dynamics of a dust grain in the wake of another grain in flowing plasmas". In: *Physics of Plasmas* 17.10. ISSN: 1070664X. DOI: 10.1063/1.3488252.

Moe, Kenneth and Mildred M Moe (2005). "Gas – surface interactions and satellite drag coefficients". In: *Planetary and Space Science* 53, pp. 793–801. DOI: `10.1016/j.pss.2005.03.005`.

Northrop, T G and T J Birmingham (1990). "Plasma Drag on a Dust Grain Due to Coulomb Collisions". In: *Planetary and space science* 38.3, pp. 319–326.

Olsen, R C and C K Purvis (1983). "Observations of Charging Dynamics". In: *Journal of Experimental and Theoretical Physics* 88, pp. 5657–5667.

Olson, Spencer E and Andrew J Christlieb (2008). "Gridless DSMC". In: *Journal of Computational Physics* 227.17, pp. 8035–8064. DOI: `10.1016/j.jcp.2008.04.038`.

Parker, Lee W. (1976). *Computation on collisionless steady-state plasma flow past a charged disk*. Tech. rep. February 1976. Concord, Massachusetts: NASA. URL: `http://ntrs.nasa.gov/search.jsp?R=19760011843`.

Parker, Lee W (1978). "Differential Charging and Sheath Asymmetry of Non-conduction Spacecraft Due to Plasma Flows". In: *Journal of Geophysical Research: Space Physics* 83.A10, pp. 4873–4876.

Pelton, Joseph (2016). *Handbook of Satellite Applications*. Ed. by Joseph Pelton, Scott Madry, and Sergio Camacho-Lara. Springer New York. ISBN: 978-1-4614-6423-5. DOI: `10.1007/978-1-4614-6423-5_106-2`.

Pfeiffer, M, A Mirza, and S Fasoulas (2013). "A grid-independent particle pairing strategy for DSMC". In: *Journal of Computational Physics* 246, pp. 28–36. ISSN: 0021-9991. DOI: `10.1016/j.jcp.2013.03.018`. URL: `http://dx.doi.org/10.1016/j.jcp.2013.03.018`.

Picone, J. M. et al. (2002). "NRLMSISE-00 empirical model of the atmosphere: Statistical comparisons and scientific issues". In: *Journal of Geophysical Research: Space Physics* 107.A12, pp. 1–16. ISSN: 21699402. DOI: `10.1029/2002JA009430`.

Pilinski, M D (2011). *Dynamic Gas-Surface Interaction Modeling for Satellite Aerodynamic Computations*.

Pilinski, Marcin D., Brian M. Argrow, and Scott E. Palo (2011). "Drag Coefficients of Satellites with Concave Geometries: Comparing Models and Observations". In: *Journal of Spacecraft and Rockets* 48.2, pp. 312–325. ISSN: 0022-4650. DOI: `10.2514/1.50915`.

Prieto, David Mostaza, Benjamin P. Graziano, and Peter C.E. E Roberts (2013). "Spacecraft drag modelling". In: *Progress in Aerospace Sciences*, pp. 1–10. ISSN: 0376-0421. DOI: `10.1016/j.paerosci.2013.09.001`. URL: `http://dx.doi.org/10.1016/j.paerosci.2013.09.001`.

Ridley, A J, Y Deng, and G To (2006). "The global ionosphere – thermosphere model". In: 68, pp. 839–864. DOI: `10.1016/j.jastp.2006.01.008`.

Riemann, K U (1991). "The Bohm criterion and sheath formation". In: *Journal of Physics D: Applied Physics* 24.4, pp. 493–518. ISSN: 0022-3727. DOI: `10.1088/0022-3727/24/`

4/001. URL: http://stacks.iop.org/0022-3727/24/i=4/a=001?key=crossref.8ef018f33cb54573928abc7217c3932b.

Rubincam, Parry (1980). "On the secular decrease in the semimajor axis of Lageos's orbit". In: *Celestial Mechanics* 26.4, pp. 361–382. DOI: 10.1007/BF01230417.

– (1990). "Drag on the LAGEOS Satellite". In: *Journal of Geophysical Research: Solid Earth* 95.89, pp. 4881–4886.

Sadarjoen, I Ari et al. (1994). *Particle Tracing Algorithms for 3D Curvilinear Grids*. Tech. rep. Delft.

Samir, U., K. H. Wright, and Nobie H Stone (1983). "The expansion of a plasma into a vacuum - Basic phenomena and processes and applications to space plasma physics". In: *Reviews of Geophysics and Space Physics* 21.7, pp. 1631–1646. ISSN: 8755-1209. DOI: 10.1029/RG021i007p01631.

Sanchez-Torres, Antonio (2016). "Drag and propulsive forces in electric sails with negative polarity". In: *Advances in Space Research* 57.4, pp. 1065–1071. ISSN: 18791948. DOI: 10.1016/j.asr.2015.12.013. URL: http://dx.doi.org/10.1016/j.asr.2015.12.013.

Scanlon, T. J. et al. (2010). "An open source, parallel DSMC code for rarefied gas flows in arbitrary geometries". In: *Computers and Fluids* 39.10, pp. 2078–2089. ISSN: 0045-7930. DOI: 10.1016/j.compfluid.2010.07.014. URL: http://dx.doi.org/10.1016/j.compfluid.2010.07.014.

Scanlon, T. J. et al. (2015). "Simulation of Rarefied and Continuum Hypersonic Flow over Re-Entry Objects". In: *8th European Symposium on Aerothermodynamics for Space Vehicles*. ISBN: 8789809289. DOI: 10.1016/j.buildenv.2006.10.027. arXiv: 0812.0143v2.

Schaub, Hanspeter et al. (2006). *Final Report for Coulomb Thrusting Application Study Program : Next Generation Space Technologies & Systems*. Tech. rep.

Schwager, L. a. and Charles K. Birdsall (1990). "Collector and source sheaths of a finite ion temperature plasma". In: *Physics of Fluids B: Plasma Physics* 2.5, pp. 1057–1068. ISSN: 08998221. DOI: 10.1063/1.859279. URL: http://link.aip.org/link/?PFB/2/1057/1.

Selding, Peter B. de (2015). *SpaceX To Build 4,000 Broadband Satellites in Seattle*. URL: http://spacenews.com/spacex-opening-seattle-plant-to-build-4000-broadband-satellites/ (visited on 01/10/2017).

Senbetu, Legesse and John R. Henley (1989). "Distribution of Plasma Density and Potential Around a Mesothermal Ionospheric Object". In: *Journal of Geophysical Research* 94.89, pp. 5441–5448.

Sentman, Lee H. (1961). *Free Molecule Flow Theory and its application to the determination of Aerodynamic Forces*. Tech. rep. California: Lockheed Aircraft Corporation.

Sentoku, Y. and A. J. Kemp (2008). "Numerical methods for particle simulations at extreme densities and temperatures: Weighted particles, relativistic collisions and reduced

currents". In: *Journal of Computational Physics* 227.14, pp. 6846–6861. ISSN: 00219991. DOI: 10.1016/j.jcp.2008.03.043.

Shaw, Graeme (1993). "Analysis of the Ion Current Collection in the Plasma Wake During the Charging Hazards and Wake Studies (CHAWS) Experiment". PhD thesis. Massachusetts Institute of Technology.

Stone, Nobie H (1981a). *The Aerodynamics of Bodies in a Rearefied Ionized Gas with Applications to Spacecraft Environmental Dynamics*. Tech. rep. Alabama: Marshall Space Flight Center, p. 319.

– (1981b). "The plasma wake of mesosonic conducting bodies . Part 1 . An experimental parametric study of ion focusing by the plasma sheath". In: *Journal of Plasma Physics* 25, pp. 351–371.

Streetman, Brett and Mason A Peck (2007). "New synchronous orbits using the geomagnetic lorentz force". In: *Journal of Guidance, Control, and Dynamics* 30.6, pp. 1677–1690. ISSN: 0731-5090. DOI: 10.2514/1.29080. URL: http://dx.doi.org/10.2514/1.29080.

Troy, Ballard. E., E. J. Maier, and U. Samir (1975). "Electron Temperatures in the Wake of an Ionospheric Satellite". In: *Journal of Geophysical Research* 80.7, pp. 993–997.

Turansky, Craig P. and Brian M. Argrow (2014). "Rigid-Body Dynamics in Free-Molecular and Transition Flow". In: *Journal of Spacecraft and Rockets* 51.1, pp. 239–252. ISSN: 0022-4650. DOI: 10.2514/1.A32441. URL: http://arc.aiaa.org/doi/abs/10.2514/1.A32441.

Uglov, A A and AG Gnedovets (1991). "Effect of particle charging on momentum and heat transfer from rarefied plasma flow". In: *Plasma chemistry and plasma processing* 11.2, pp. 251–267. URL: http://www.springerlink.com/index/W818014518V61PH2.pdf.

Vaglio-Laurin, R and G Miller (1969). "Electrostatic field in the trail of ionospheric satellites". In: *AIAA Journal* 8.6, pp. 1098–1103. DOI: doi:10.2514/6.1969-674. URL: http://dx.doi.org/10.2514/6.1969-674.

Vallado, D. A. and D. Finkleman (2014). "A critical assessment of satellite drag and atmospheric density modeling". In: *Acta Astronautica* 95.1, pp. 141–165. ISSN: 00945765. DOI: 10.1016/j.actaastro.2013.10.005. URL: http://dx.doi.org/10.1016/j.actaastro.2013.10.005.

Vay, Jean Luc and Brendan B. Godfrey (2014). *Modeling of relativistic plasmas with the Particle-In-Cell method*. DOI: 10.1016/j.crme.2014.07.006.

Wagner, Wolfgang (1992). "A convergence proof for Bird's direct simulation Monte Carlo method for the Boltzmann equation". In: *Journal of Statistical Physics* 66.3-4, pp. 1011–1044. ISSN: 00224715. DOI: 10.1007/BF01055714.

Walker, A., P Mehta, and J Koller (2013). "A Quasi-Specular Drag Coefficient Model using the Cercignani-Lampis-Lord Gas-Surface Interaction Model". In: *Journal of Spacecraft and Rockets*. ISSN: 00224650. DOI: 10.2514/1.A32677. URL: http://www.impact.lanl.gov/docs/Walker2013b.pdf.

Walker, Andrew, Piyush Mehta, and Josef Koller (2014). "Drag Coefficient Model Using the Cercignani – Lampis – Lord Gas – Surface Interaction Model". In: *Journal of Spacecraft and Rockets* 51.5, pp. 1544–1563. ISSN: 0022-4650. DOI: 10.2514/1.A32677.

Wang, Joseph (1991). "Electrodynamic Interactions Between Charged Space Systems and the Ionospheric Plasma Environment". PhD thesis. Massachusetts Institute of Technology.

Wang, Joseph and D. E. Hastings (1992a). "Ionospheric plasma flow over large high-voltage space platforms. I : Ion-plasma-time scale interactions of a plate at zero angle of attack". In: *Phys. Fluids B* 4.6, pp. 1597–1614. ISSN: 08998221. DOI: 10.1063/1.860069.

– (1992b). "Ionospheric plasma flow over large high-voltage space platforms. II: The formation and structure of plasma wake". In: *Phys. Fluids B* 4.6, pp. 1597–1614. ISSN: 08998221. DOI: 10.1063/1.860069.

Wang, Joseph, J W Qiu, and X G Qin (2008). "PIC Simulation of Surface Charging in the Wake Zone". In: *PIERS Proceedings*. Hangzhou, China, pp. 518–521.

Wang, Joseph et al. (1994). "Multibody-Plasma Interactions : Charging in the Wake". In: *Journal of Spacecraft and Rockets* 31.5, pp. 5–10.

Whipple, E. C. (1981). "Potentials of surfaces in space". In: *Reports on Progress in Physics* 44.11, pp. 1197–1250. ISSN: 0034-4885. DOI: 10.1088/0034-4885/44/11/002. URL: http://iopscience.iop.org/0034-4885/44/11/002.

Whipple, Elden Cole (1965). "The Equilibrium Electric Potential of a Body in the Upper Atmosphere and in Interplanetary Space". PhD thesis. George Washington University.

White, Craig et al. (2013). "Rarefied gas effects on the aerodynamics of high area-to-mass ratio spacecraft in orbit". In: *Advances in Space Research* 51.11, pp. 2112–2124. ISSN: 02731177. DOI: 10.1016/j.asr.2013.01.002. URL: http://dx.doi.org/10.1016/j.asr.2013.01.002.

Wiedemann, C. et al. (2001). "Modeling of copper needle clusters from the West Ford Dipole experiments". In: *Proceedings of the Third European Conference on Space Debris* 1, pp. 315–320.

Wyatt, P. J. (1960). "Induction Drag on a Large Negatively Charged Satellite Moving in a Magnetic Field Free Ionosphere.pdf". In: *Journal of Geophysical Research* 65.6, pp. 1673–1678.